Interdisciplinary Investigation of CO_2 Sequestration in Depleted Shale Gas Formations

Final Report

September 15, 2010 through September 30, 2013

Mark D. Zoback, PI, Department of Geophysics
Anthony R. Kovscek, co-PI, Energy Resources Engineering
Jennifer Wilcox, co-PI, Energy Resources Engineering

December 31 2013

DE-FE-0004731

Stanford University
367 Panama Street
Stanford, CA 94305

SUBMITTED TO

U.S. Department of Energy
National Energy Technology Laboratory

NETL contact:
Joshua Hull
joshua.hull@netl.doe.gov

Disclaimer

Executive Summary

This project investigates the feasibility of geologic sequestration of CO_2 in depleted shale gas reservoirs from an interdisciplinary viewpoint. It is anticipated that over the next two decades, tens of thousands of wells will be drilled in the 23 states in which organic-rich shale gas deposits are found. This research investigates the feasibility of using these formations for sequestration. If feasible, the number of sites where CO_2 can be sequestered increases dramatically. The research embraces a broad array of length scales ranging from the ~10 nanometer scale of the pores in the shale formations to reservoir scale through a series of integrated laboratory and theoretical studies.

There are four main focus areas: I. Physical and chemical aspects of CO_2/shale interactions at the pore scale, II. Transport processes of critical state CO_2 in hydrofracs, natural fractures and pores, III. Chemical interactions with ground water, and IV. Trap and seal mechanisms of CO_2 in shale gas reservoirs. These four areas address the principal scientific objectives of this work which are to determine how the physical and chemical processes associated with CO_2 interaction with organic-rich shales affects CO_2 injectivity over long periods of time, and the ability of the shale to store CO_2 as both a free phase and an adsorbed phase for thousands of years. We are studying shales derived from a number of U.S. basins where shale gas is to be produced, including the Barnett, Haynesville, and Eagle Ford shale.

In this final report of the project, we provide an overview of all research carried out as part of this project. The primary conclusions and observations are as follows:

- Imaging of the in-situ porosity that carries gas within low permeability media was accomplished and enhanced by implementing a high X-ray contrast gas imaging technique. Hence, it is possible to obtain sub-millimeter resolution images and 3D reconstructions that represent the average porosity spatial distribution of the sample.
- Excess sorption measurements carried out with N_2, CH_4, and CO_2 confirmed the preferential sorption of CO_2 in shales compared to other gases. N_2 and CH_4 sorption were fitted with a Langmuir. CO_2 sorption isotherms did not follow the standard Langmuir model and were fitted with an N-BET model indicating multilayer sorption.
- CO_2 sorption measurements confirmed a large potential storage capacity for carbon in shale reservoirs. It is important to note that large reductions in permeability and effective pore radius occurred in some cases, but not all, as CO_2 saturated the pore space. Significant CO_2 sorption likely impacts the flow mechanism in shale reservoirs.
- Dual control volume molecular dynamics simulations were carried out for methane and CO_2 transport in pores with diameters between 10 to 100s of nm and it was found that the no-slip boundary condition does not apply to the transport of these compounds on carbon surfaces and that the velocity profile is plug flow rather than the traditional parabolic, which is the case of Darcy flow.
- Through Grand Canonical Monte Carlo simulations it was found that the CO_2 and methane densities are up to several orders of magnitude higher in nanoconfined

carbon pores compared to their densities in their bulk phase. In addition, molecular simulation investigations show that the viscosity of these fluids changes significantly to bulk viscosities.

- Darcy permeability relationships, including taking into account gas slippage (ie., the Klinkenberg effect) were applicable to all core samples examined.
- Permeability determination using a history-match method for low permeability transient pressure decay experiments provides reliable measurement when exactly matched to the experimental pressure history. Such numerical models incorporate gas sorption, pressure-dependent gas properties, and non-ideal phase behavior including the case of CO_2 as the saturating gas.
- We conducted pulse-decay and steady-state flow experiments on Eagle Ford Shale samples, using adsorbing gas (CO_2) and non-adsorbing gas (Helium) as pore fluids. We found that the adsorption of CO_2 molecules reduced the permeability normal to bedding by about an order of magnitude. However, the permeability reduction parallel to bedding decreased by only about 10%. In both cases, the permeability reduction was reversible. That is, when the CO_2 was desorbed, the He permeability returned to its initially higher values. As the tests with both types of gases were performed at the same mean free path, the observed difference in permeability anisotropy is due to the adsorption of CO_2.

As the project has progressed, we have made significant effort for transfer of project results and learnings to the scientific and engineering community as follows. All work acknowledges DOE funding.

- A manuscript entitled "CT Imaging of Low Permeability, Dual-Porosity Systems Using High X-Ray Contrast Gas," was revised and accepted for publication in journal *Transport in Porous Media.*
- A manuscript entitled "Molecular Simulation of Adsorption in Micro- and Mesoporous Carbons with Applications to Coal and Gas Shale Systems," was published in the *International Journal of Coal Geology*.
- A manuscript entitled "Molecular modeling of carbon dioxide transport and storage in porous carbon-based materials," was published in *Micro and Mesoporous Materials*.
- A manuscript entitled "Slippage and viscosity predictions in carbon micropores and their influence on CO_2 and CH_4 transport," was published in *Journal of Chemical Physics*.
- A paper entitled "Experimental Investigation of Matrix Permeability of Gas Shales" will be published in early 2014 in the AAPG Bulletin.
- A manuscript entitled "Adsorption of Methane and Carbon Dioxide on Gas Shale and Pure Mineral Samples" is in review at The Journal of Unconventional Oil and Gas Resources.
- A manuscript entitled "Klinkenberg Effect on Predicting and Measuring Helium Permeability in Gas Shales" was submitted, revised, and accepted for publication in the J. Coal Geology.

- We wrote a manuscript entitled "In-Depth Experimental Investigation of Shale Physical and Transport Properties" and presented the work orally at the Unconventional Resources Technology Conference held in Denver, Colorado, USA, 12-14 August 2013.
- We wrote a manuscript entitled "Experimental and Numerical Analysis of Gas Transport in Shale Including the Role of Sorption" and presented the work orally at the SPE Annual Technical Conference and Exhibition, New Orleans, LA 30 Sep to 2 Oct 2013.
- A manuscript entitled "Frictional Properties of Shale Reservoir Rocks", has been published in the *Journal of Geophysical Research, Solid Earth*

Approach

The over-arching objective of this project is to conduct a multiscale, multiphysics, interdisciplinary shale characterization and laboratory study that assesses the feasibility of depleted organic-rich gas shale reservoirs for large-scale CO_2 sequestration. The principal scientific objectives of this work are to determine how the physical and chemical processes associated with CO_2 storage in organic-rich gas shales affect injectivity and storage capacity (over long periods of time), and the ability of the gas shale to sequester CO_2 (as both a free and adsorbed phase) for thousands of years. We are delineating the physical and chemical aspects of CO_2/shale interactions, characterizing transport processes and mobility of supercritical CO_2 in hydrofracs, natural fractures, shale matrix, pores, probe potential interactions of stored CO_2 with ground water, and developing a trap and seal framework/workflow for CO_2 storage in gas shale reservoirs.

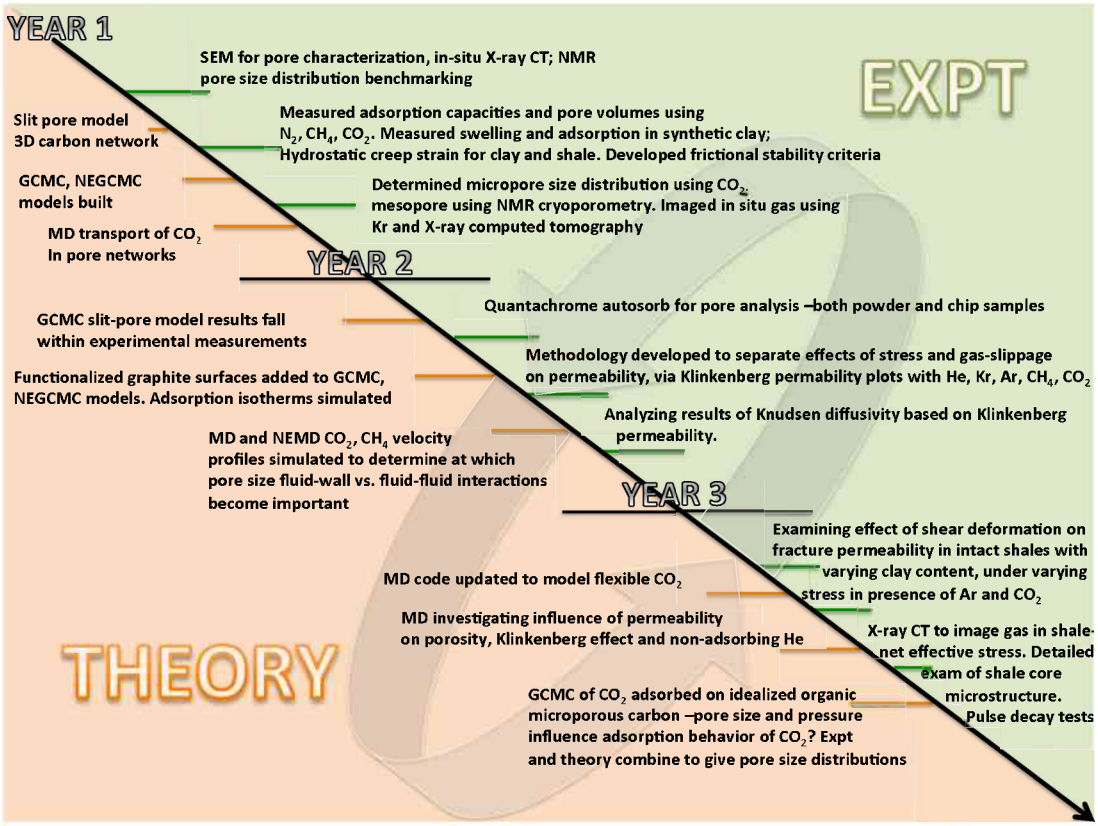

Figure 1 Timeline showing some theoretical and experimental research developments during the course of this project

2.0: Physical and chemical CO_2/shale interactions

2.1: Surface and bulk characterization experiments

Pore characterization and sizing began by using SEM. Scanning electron microscopy presents images in 2D and permits identification of organic and inorganic constituents. In terms of understanding methane and CO_2 adsorption and transport phenomena in gas shale, however, it is crucial to characterize shale pore-size and pore-shape distributions together with connectivity. We continue to explore whether SEM can provide images sufficient for quantitative image analysis (see for instance, Jia et al. 2007).

To date, X-ray CT experiments have focused on image quality tests and nondestructive characterization of Barnett shale samples. We have two X-ray CT scanners at our disposal, but each has different capabilities. Hence, image quality tests were conducted. Our GE Lightspeed scanner yields reasonable resolution of in-situ fine-scale details as shown in Figs. 2 and 3 that contrast CT scan images and standard photographs. Dense calcite layers are evident in both views. Note the white striations in photographs and the red planar structures in the CT images. The spatial resolution of the CT-scan images is 0.25 mm by 0.25 mm by 2 mm. Red corresponds to large CT number and correspondingly large density. For reference, the CT number of air is defined as -1000 and the CT number of water is 0. The large CT numbers in Figures 2(b) and 3(b) indicate that the samples are quite dense.

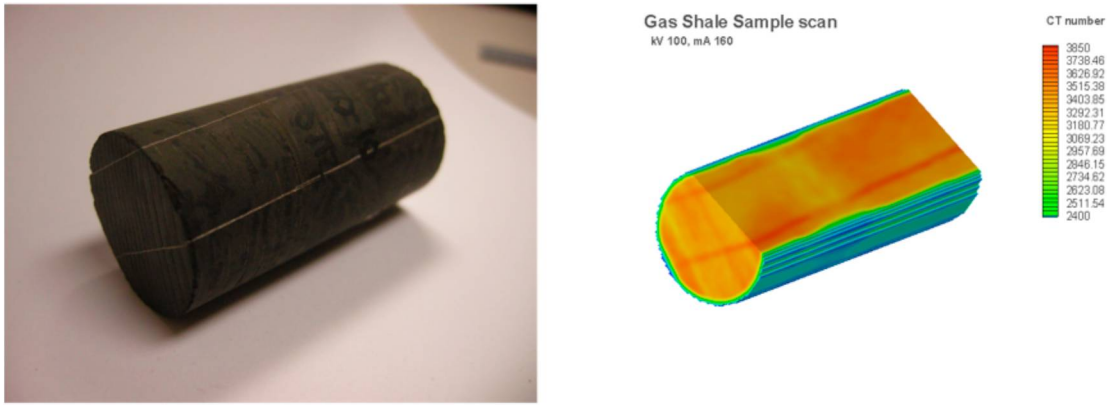

(a) (b)

Figure 2. Characterization of shale sample (a) photograph of core and (b) tomographic reconstruction of core. CT scanner settings are tube voltage and current of 100 kV and 160 mA, respectively.

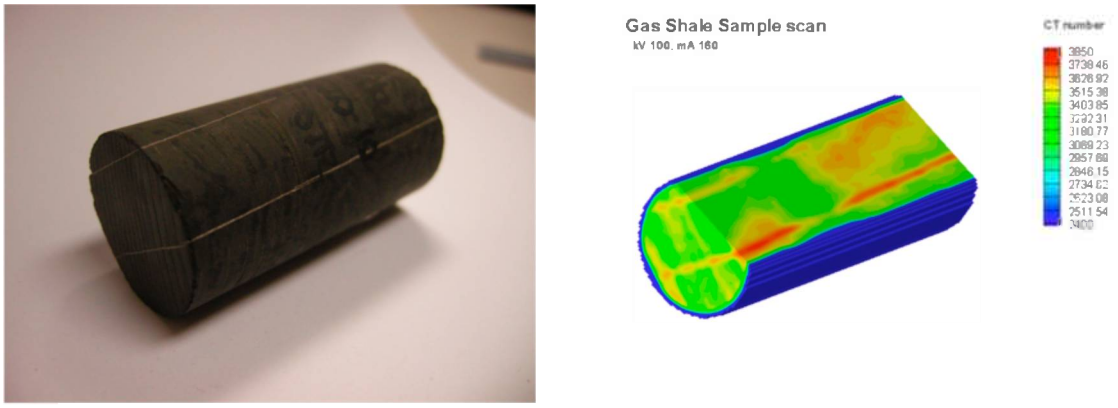

(a) (b)

Figure 3. Characterization of shale sample (a) photograph of core and (b) tomographic reconstruction of core. CT scanner settings are tube voltage and current of 100 kV and 160 mA, respectively.

Bulk characterization studies to determine pore size distributions were undertaken. NMR was attempted to determine the pore size distribution of the gas shale samples. To benchmark the technique of NMR cryoporometry, we carried out experiments on porous glasses with known pore size distributions. We were able to reproduce the pore size distrubution of porous glasses that have been determined previously and available in the literature (Sagidullin and Furo, 2008). Figure 4 shows the pore size distribution comparison of a controlled porous glass sample with an average pore diameter of 72.9 nm.

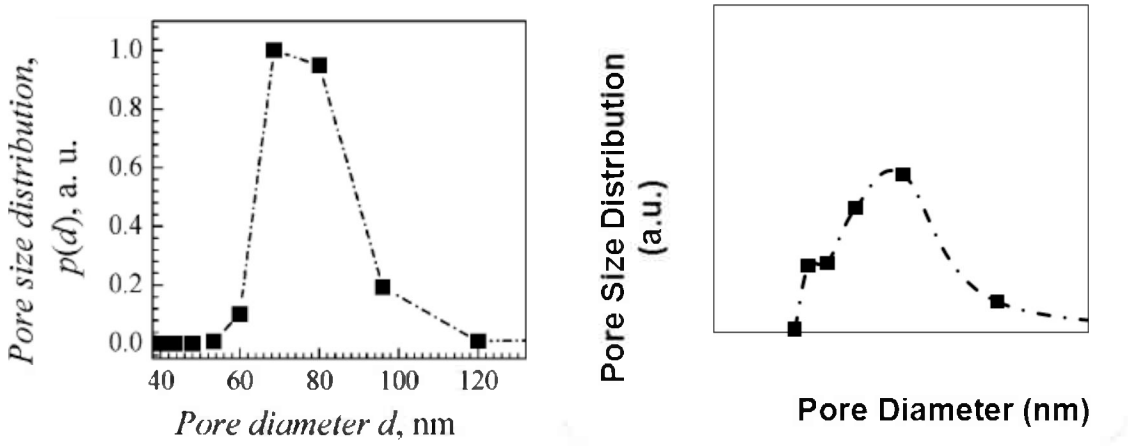

Figure 4. Comparison (left, Sagidullin and Furo, 2008 and right, Stanford) of pore size distribution of controlled porous glass with average pore size of 72.9 nm.

With confidence from the agreement with the literature on the pore size measurements using NMR cryoporometry with controlled glass, experiments were begun with gas shale samples. Due to the heterogeneity of gas shale rock we tested other materials such as coal and activated carbon for comparison. Figure 5 shows results of pore size obtained from DARCO activated carbon (left) and the Barnett shale (right).

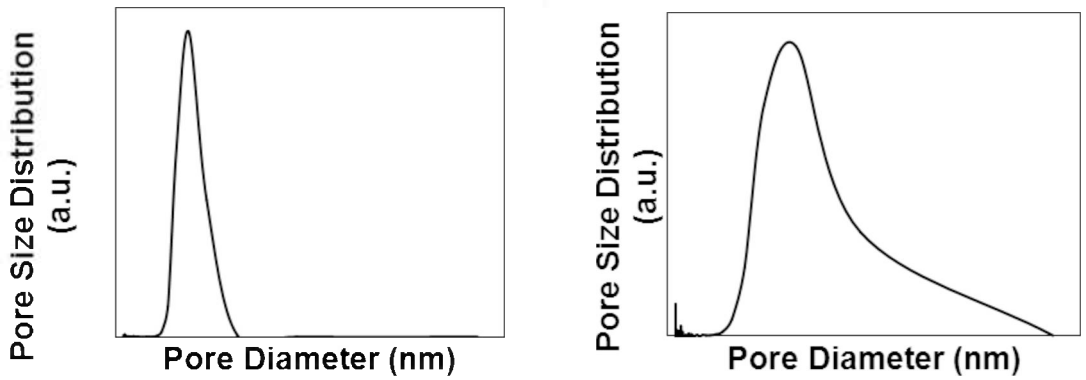

Figure 5. Comparison of pore size distribution of DARCO activated carbon from Norit (left) and pore size distribution of a Barnett shale sample (right).

These experiments were continued to achieve reproducibility of the results and also to apply BET nitrogen adsorption isotherm experiments as a comparison, although we were initially unable to use this technique to characterize smaller pores in the meso and micropore range. The next steps were to carry out pore size distribution of gas shale samples using N_2 and CO_2 BET adsorption isotherm experiments.

Micropore Size Distribution using CO_2 Probe gas and the Dubinin-Astakhov Model

Pore size distributions in samples of the Montney and Barnett shales using CO_2 as the probe gas with the Dubinin-Astakhov (DA) model and a Micromeritics ASAP 2020 instrument. The DA model combined with the use of CO_2 as a probe gas allows for the determination of the micropores (i.e., < 2 nm) within a given material. Based upon the previous NMR cryoporometry experiments it is clear that these materials are comprised of both micro and mesopores.

The DA isotherm model is applicable to the determination of only micropores, in which the adsorption mechanism reflects a continuous filling process with adsorption enhanced due to the overlapping potential fields of the pore walls. The properties (*e.g.*, density and packing) of the condensed phase in micropores are assumed to be similar to those of the fluid particles of the bulk liquid phase. At temperatures less than the fluid critical temperature, T_c, (*e.g.*, $T \leq 0.8T_c$), it is assumed that the pore volume is strictly a liquid with an approximate volume of $V = W/\rho$, such that W and ρ are the fluid weight and density, respectively. The energy, E, associated with micropore filling is equivalent to the

isothermal work required to compress a vapor from its equilibrium pressure, p, to its saturation pressure, p_0 in the micropore, *e.g.*, $E = RT \ln p_0/p$.

Both of the shale samples were roughly ground to small chunks with weights of 0.3627 g and 0.6323 g for the Barnett and Montney, respectively and low-pressure adsorption isotherms were measured. The value n in the Dubinin-Astakhov equation (2) is optimized to fit the low-pressure adsorption isotherm using a linear regression.

$$ln(W)=ln(V\rho)-K[ln(p_0/p)]^n \qquad (2)$$

such that n is approximately 1.001 for both samples, in which the square of the sample correlation coefficients, R^2, are approximately 0.996. The plot of ln(W) as a function of $\left[\ln\left(p_0/p\right)\right]^n$ is shown in Figure 6:

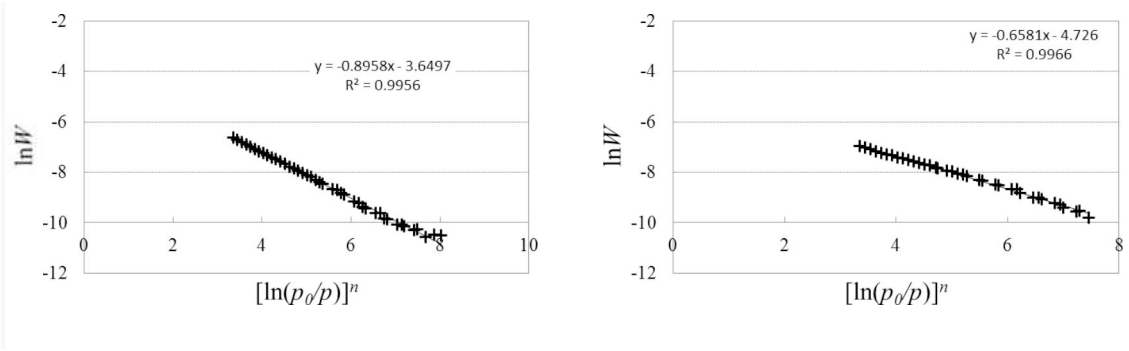

(a) Barnett shale (b) Montney shale

Figure 6. Optimize the value n in the Dubinin

Based upon the parameter estimates of Eq. (2) and Figure 4, the pore volumes, V, of the two different shale samples are:

$$V_{Barnnet}=e^{-3.6497}/\rho=e^{-3.6497}/1.023\ kg/m^3=0.0254\ cm^3$$

$$V_{Montney}=e^{-4.726}/\rho=e^{-4.726}/1.023\ kg/m^3=0.00866\ cm^3$$

where ρ is the adsorbed liquid density of CO_2 at 273 K. The specific pore volume of the two shale samples are:

$$V_{Barnnet}/m_{Barnnet}=0.0254\ cm^3/0.3627\ g=0.07\ cm^3/g$$

$$V_{Montney}/m_{Montney}=0.00866\ cm^3/0.6323\ g=0.013\ cm^3/g$$

Based on the assumption that the micropores are cylindrical-shaped pores, and if the fluid weight of the micropore filling is expressed as a function of pore radii, r, then the DA equation can be written as:

$$\theta = exp[-(k/E)^n r^{-3n}] \quad (3)$$

where θ represents the extent of micropore filling, n is the fitting parameter in the DA equation determined by linear regression of $ln(W)$ versus $[ln(p_0/p)]^n$, and k is interaction constant of fluid molecule in units of J·Å^3.

Based upon a Gaussian distribution assumption, and assume that no perturbation takes place in the adsorbed phase, from Eq. (3):

$$dV/Vdr = d\theta/dr = d\theta/(d(d/2)) = 3n(k/E)^n r^{-(3n+1)} exp[-(k/E)^n r^{-3n}] \quad (4)$$

where θ represents the extent of micropore filling. The quantities V, E, and n have been determined from the linear regression discussed previously, such that n = 1.001

$$E_{Barnet} = RTK^{-1/n} = 8.315\ JK^{-1}mol^{-1} \cdot 273\ K \cdot 0.8958^{-1/1.001} = 2534.07\ J/mol$$

$$E_{Montney} = RTK^{-1/n} = 8.315\ JK^{-1}mol^{-1} \cdot 273\ K \cdot 0.6581^{-1/1.001} = 3449.46\ J/mol$$

The pore size distributions are then determined as shown in Figure 7.

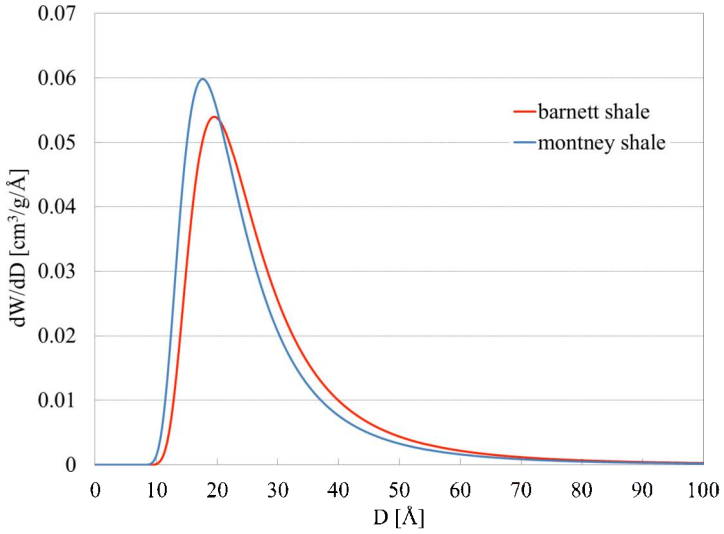

Figure 7. Micropore size distribution determined by DA model

As indicated by Figure 7, the micropores of the two gas shale samples are both concentrated near 20 Å, which means most micropores are ~2 nm. Although the application of the DA model combined with the assumption of Gaussian distribution has limitations to predict the real pore size distribution, i.e., only one main peak can be captured even if multiple pore size distributions exist.

The direct CO_2 adsorption isotherm measurements in the gas shale samples at low-pressure are shown in Figure 8. To compare with the Grand Canonical Monte Carlo (GCMC) modeling work, a 20-Å slit-pore model with perfect graphite surfaces (3 layers on each wall) was employed in the molecular simulation work. It can be observed that the

GCMC prediction of the low-pressure adsorption isotherm falls within the range of the experimental measurements of the two different gas shale samples. The discrepancies between the theoretical and experimental predictions are most likely because of the following factors: (1) pore size distribution predicted is not necessarily identical to the real system due to the Gaussian distribution used in the experimental-based model; (2) surface functionalities and structural heterogeneities exist in the gas shale samples that were not considered in the GCMC modeling work.

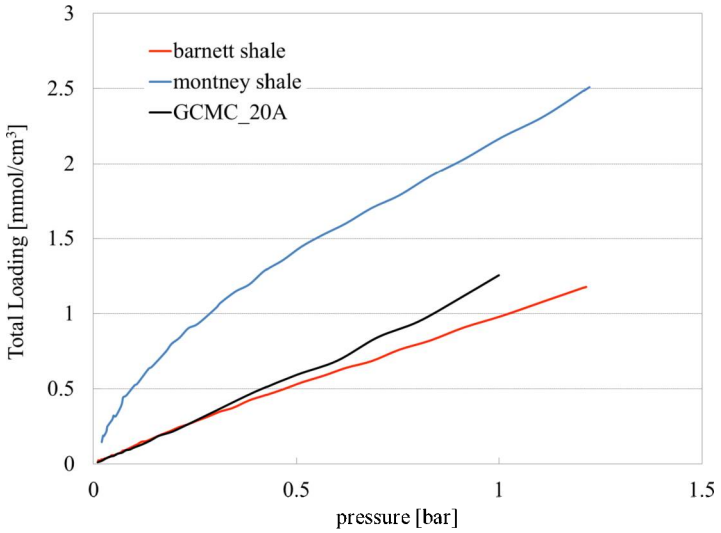

Figure 8. Comparison of the GCMC simulation and the adsorption isotherms of CO_2 in two gas shale samples

Mesopore Size Characterization using NMR Cryoporometry

In addition to micropores, it is anticipated that mesopores exist in shale. Nuclear Magnetic Resonance (NMR) cryoporometry has been carried out to determine the mesopore size distribution of the gas shale samples. The mesopore size distribution of the Barnett shale sample is shown in Figure 5.

Since it is clear that both micro and mesopores exist within the gas shale samples under investigation, future work will involve the use of N_2 and the BET adsorption model using the Micromeretics instrument to validate the NMR cryoporometry data associated with the mesopore size distribution in the various shale samples.

Pore Size Distribution using N_2 and Ar as Probe Gases using Low-Pressure Adsorption

Three shale samples were chosen for pore analysis using a Quantachrome Autosorb iQ_2 low pressure adsorption instrument. The three shale reservoirs are: Haynesville (identifier – Stanford 76), Barnett (18 Ha) and Eagle Ford (176 Ha). Each sample was ground into a powder using a chalcedony mortar and pestle and then sieved to between 45 and 63 μm using USA Standard Test Sieves No. 230 and No. 325, with ASTM E-11 Specification. The analyzed samples were approximately 90 mg after the outgas procedure, with little weight change from the pre-outgas sample. The outgas procedure is as follows: ramp to

110 °C at 2 °C min^{-1}, hold for 60 minutes, ramp to 140 °C at 5 °C min^{-1}, hold for 180 minutes and test for pressure change (which signifies continued outgassing). If the test passes (indicating minimal pressure change), the sample is dropped to room temperature and backfilled with He. If the test fails, the temperature is maintained at 140 °C for up to 180 minutes more, with tests every 15 minutes.

The samples are analyzed in 99.999% N_2 at 77 K at a P/P_0 range of 10^{-7} to 0.995 and in 99.999% Ar at 87 K at a P/P_0 range of 10^{-6} to 0.995. The same sample of each of the shale reservoirs was used for both the N_2 and Ar analyses, with an outgas procedure run between the two gases. Nitrogen isotherms were performed with 47 adsorption points and 20 desorption points. Argon isotherms were performed with 46 adsorption points and 20 desorption points. The results were analyzed using non-localized density functional theory (NLDFT) with cylindrical pores for pore size distribution using the adsorption isotherm.

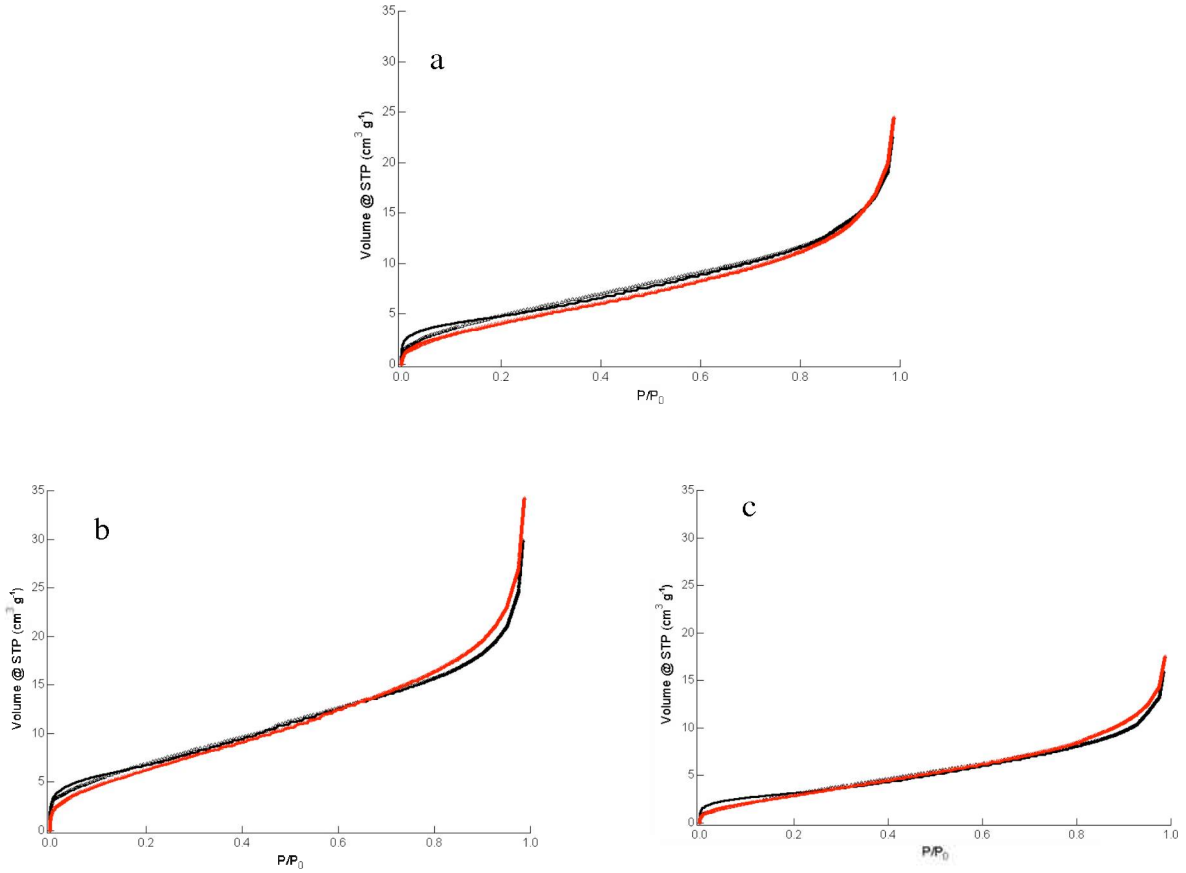

Figure 9. a) Haynesville; b) Eagle Ford; c) Barnett. Black lines are N_2 adsorption isotherms and black triangles are the DFT fits. Red lines are Ar adsorption isotherms and red triangles are the DFT fits.

The adsorption isotherms for each of the 3 shale samples can be see in Figure 9. There is superb agreement between N_2 and Ar isotherms for each of the samples. The Haynesville reservoir sample is observed to have the largest pore volume, at approximately 33 cm^3 g^{-1}. The Barnett samples has slightly less at 25 cm^3 g^{-1}, but the Haynesville sample has double

the pore volume at P/P_0 below 0.1, indicating an increased micro- to low mesopore volume. The Eagle Ford sample has the lowest pore volume (18 cm^3 g^{-1}) but a similar amount of micro- to low mesopore volume as the Barnett sample.

The pore size distribution estimates using the NLDFT methods are seen in Figure 10. The fits for the data are seen in the open triangles in Figure 10a-c. The fit refers to an estimated isotherm based on the pore size distribution (data → PSD → fit). A better match between the data and the estimated isotherm indicate a more realistic pore size distribution. The cylindrical pore adsorption branch was chosen due to better overall fits than other methods, including a slit pore adsorption branch. Differences between the actual data and the fitted isotherm typically occurred at $P/P_0 < 0.1$, which include the micropore volume.

The average pore size for each of the 3 shale reservoirs was approximately 4 to 5 nm, although the Haynesville sample had significant pore volume below 4 nm, more so than the other samples. The majority of all pore volume is found below 10 nm, specifically between 4 and 8 nm. Only the Haynesville sample had a high level of pore volume in the classical micropore range (< 2 nm). The 3 samples pore size distributions corresponded to the pore volume seen in Figure 10a-c.

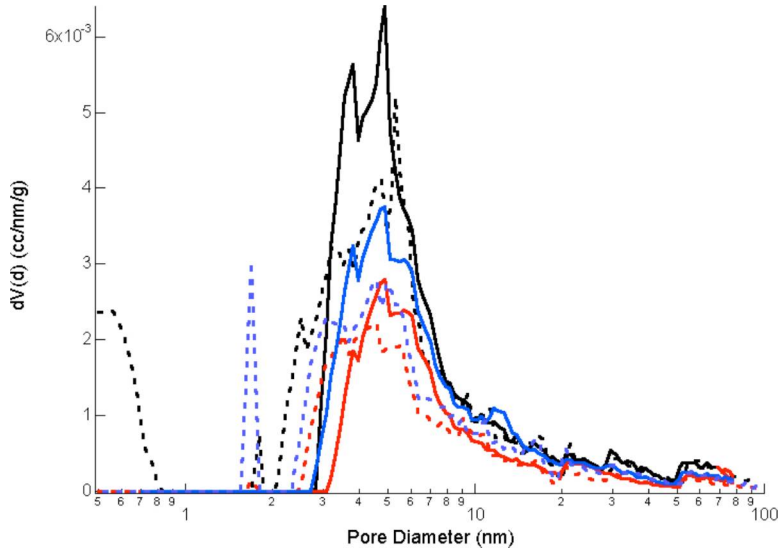

Figure 10. a) Haynesville - Black; b) Eagle Ford – Red; c) Barnett - Blue. Solid lines are determined using N_2 isotherms and dotted lines are determined using Ar isotherms.

The pore volume of 3 shale reservoir samples was analyzed, indicating that there is a wide range between different reservoirs. The largest shale (Haynesville) had over double the pore volume of the smallest shale (Eagle Ford). Each sample was analyzed with both N_2 and Ar, with great correspondence between the two samples. Non-localized DFT based on silica and cylindrical pores appears to be a valid way of estimating pore size distribution of shale samples.

In addition, work was conducted to study the pore-size differences between shale samples in chip and powder form. The transport of gas through the pore network of consolidated rock yields lower gas accessibility than in crushed samples. The weights of all the samples used are about 90 mg and they were treated as described earlier. The gases used here are N_2, Ar and CO_2. CO_2 has the tendency to occupy micro-pores over meso- and macro-pores. Experiments run with CO_2 gas were conducted at 273 K. The atmospheric pressure of the experiment was corrected to 5.2 atm. The chip-versus-powder study was conducted on Barnett sample, 20Ha.

Additionally, further work was performed on an Eagle Ford shale sample. The sample was ground into a powder using a chalcedony mortar and pestle. The shale material is then sieved to below 350 μm and re-ground until the entire sample was below the 350 μm limit. Using the N_2 adsorption procedure described earlier in this section, isotherms were run on the entire sample, and on 4 separate bins of the material: < 50 μm, 50-150 μm, 150-250 μm and 250-350 μm. This procedure was followed in an attempt to highlight heterogeneities in the material, and determine where the pore space exists. Hypothetically, the softer material in the shale will end up in the smaller bins, and a difference in the isotherms can help signify this difference. The pore-size distributions for each of the bins can be seen in Figure 11.

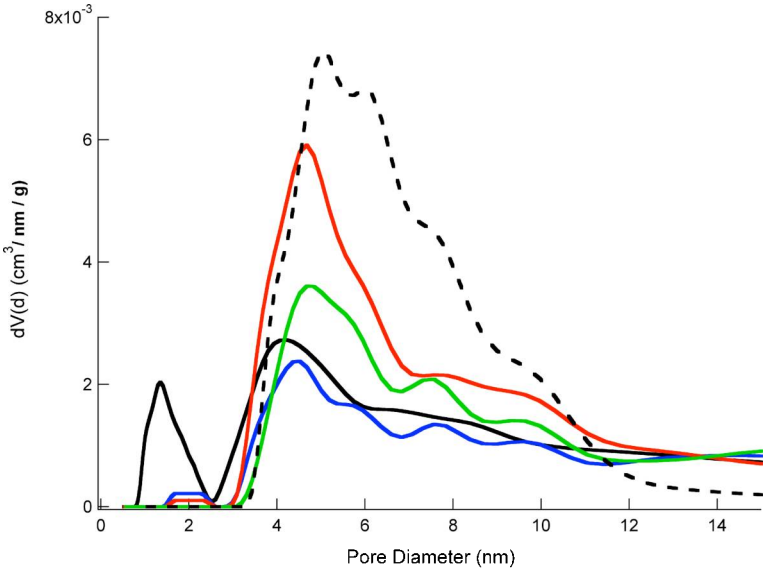

Figure 11. Eagle Ford <350 μm – Black; 250-350 μm – Blue; 150-250 μm – Red; 50-150 μm – Green; <50 μm - Dashed

Figure 12 shows the isotherms of a Barnett sample, in powder and chip form, using N_2, Ar and CO_2. The pore volume of the powder sample occupied by N_2 and Ar is again very similar and has a value of 25.8 $cm^3 g^{-1}$. The hysteresis measured with Ar is greater than with N_2 and generally appears very similar to a type 4 adsorption isotherm. The chips also have some hysteresis but it is masked by the scale difference. The pore volume of the chip sample is 3.5 $cm^3 g^{-1}$ with N_2 and 6.7 $cm^3 g^{-1}$ with Ar. The isotherms of the chip sample are lower indicating access limitation to pore networks that is mainly governed in this case by the conductive conduits. Crushing the sample exposes all various pore size

scales within the inner fabric of the rock. This indicates that the absolute pore sizes measured for the chip sample indicate the well-connected pore sizes. The resolution of pore-size measurements for the chip samples depends on the time required for pressure in the pore to equilibrate. Because shale has a substantial amount of micro-pores, it would be quite time consuming for pressure to equilibrate within the very small pore volumes. Also, The diffusional limitation of N_2 and Ar at the low temperatures of 77K and 87K, respectively, might affect to some degree the isotherms.

In CO_2 isotherms, the powder sample has a pore volume of about 3 $cm^3 g^{-1}$ while the chip has a greater value of 5.8 $cm^3 g^{-1}$. This indicates that the chip sample has greater pore volumes between the micro-pore and lower meso-pore region than the powder chip. This difference in pore volume accessibility is explained later in the next figure.

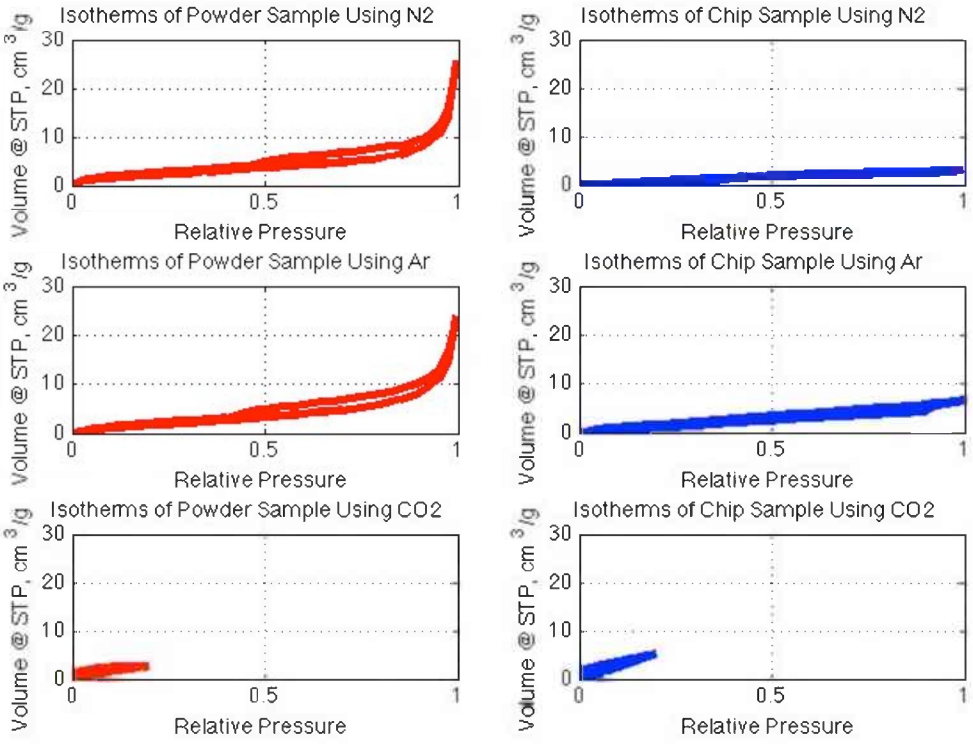

Figure 12. Adsorption/desorption isotherms for powder and chip samples of Barnett shale, 20Ha sample.

Figure 13 shows a collapse of three pore size distribution (PSD) methods: BJH, DA and NLDFT. The three methods are used to indicate the uniformity of PSD obtained for the chip sample, as they yield very similar pore volumes. The powder sample shows different pore volumes and pore diameters associated with each method used. Although the DA method is widely used for micro-pore characterizations, it enforces a Gaussian distribution and suppresses any other peak. The extreme heterogeneity of shale rocks may suggest several peaks at micro- and ultra micro-pores. The BJH method is used to describe capillary condensation at meso- and macro-pore characterizations (Ravikovitch and Neimark, 2001). The NLDFT method is more reliable to describe the micro-pores as

well as it signifies multiple peaks at ultra micro-pore scale (Jagiello and Thommes, 2004), as shown in the pore volume using CO_2 in Figure 13.

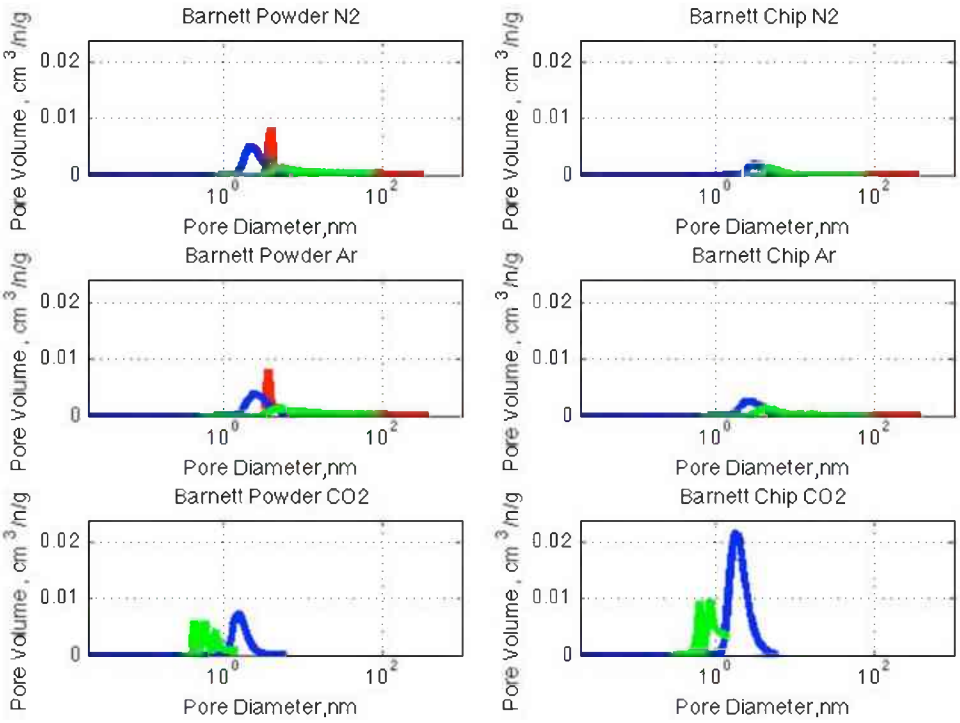

Figure 13. Pore size distribution plots using BJH, DA and NLDFT methods for N_2, Ar and CO_2 gases in powder and chip shale samples.

Table 1 provides a summary of the most prominent pore volumes and the associated pore sizes of each method for the three gases used in powder and chip samples. As Figure 13 indicates, the pore size distribution of the powder sample is quite different for every method used where DA method shows the smallest pore size, yet this method is only accurate at micro-pores which both N_2 and Ar have limited access to. The chip sample, on the other hand, has very similar pore volumes for every method used. This confirms the concept of limited access because of the low pore volume resolution detected by N_2 and Ar gases.

The pore-size distribution obtained using CO_2 is dissimilar from the other gases. Higher pore volume is measured using DA in the chip than in the powder. Bearing in mind that CO_2 has access to micro-pores only, this might be due to the accumulation of the gas at the available micro-pores and possible micro-cracks. The powder sample has a better exposure of the micro-pores causing CO_2 to adsorb at various pore sizes within that pore-scale. This micro-pore access capability by CO_2 is attributed to the high diffusivity of the gas compared to N_2 and Ar. The NLDFT method shows multiple peaks, as mentioned previously, at lower pore sizes allowing more accurate description of micro- and ultra micro-pores characterization. In the powder sample, the gas access smaller pore volumes at smaller pore sizes compared to the chip for the same reasons mentioned previously.

Table 1: Summary of pore volumes and diameters for N_2, Ar and CO_2 gases in powder and chip samples.

Barnett Sample				
Using N_2 Gas				
	Powder		Chip	
PSD Method	Pore Volume, cm^3/g	Pore Diameter, nm	Pore Volume, cm^3/g	Pore Diameter, nm
BJH	0.039	3.93	0.004	3.702
DA	0.008	2.24	0.004	3.14
NLDFT	0.03	4.887	0.004	4.728
Barnett Sample				
Using Ar Gas				
	Powder		Chip	
PSD Method	Pore Volume, cm^3/g	Pore Diameter, nm	Pore Volume, cm^3/g	Pore Diameter, nm
BJH	0.031	3.704	0.007	3.491
DA	0.009	2.52	0.006	2.64
NLDFT	0.025	5.514	0.008	4.575
Barnett Sample				
Using CO_2 Gas				
	Powder		Chip	
PSD Method	Pore Volume, cm^3/g	Pore Diameter, nm	Pore Volume, cm^3/g	Pore Diameter, nm
DA	0.006	1.54	0.026	1.82
NLDFT	0.002	0.438	0.004	0.859

The PSD was determined using Quenched Solid Density Functional Theory (QSDFT) assuming N_2 adsorption on carbon in slit, cylindrical and spherical pores. The QSDFT method is beneficial because it accounts for surface heterogeneities, although it will not account for material heterogeneities, such as silica and clay materials. Early results indicate that there is a difference in the pore-size distribution.

The pore-size distributions determined by low-pressure gas adsorption and the computed pore-size distributions of the 3-D pore network model for the Eagle Ford shale and a lignite coal sample are shown in Figures 14 and 15, respectively. In Figure 14 the size of the initial graphite cell in the modeling is 102, 103, and 103Å in x-, y-, and z- directions, respectively. The carbon atoms were packed with 31 layers of graphite. The total initial number of carbon atoms in each graphite layer and the simulation cell were 4,032 and 124,992, respectively. The porosity is 15% and the pores are selected randomly, with average pore sizes of 1.6 nm. The total number of carbon atoms in generated 3-D pore network matrix is 105,813. The PSDs and their averages that are generated resemble to the experimental PSD obtained for Eagle Ford by gas adsorption. As can be seen in Figure 14, the experimental PSD for Eagle Ford also shows a peak around 1.5 nm. In Figure 15 the size of the initial graphite cell in our modeling is 302, 303, and 301Å in x-, y-, and z- directions, respectively. The carbon atoms were packed with 90 layers of

graphite. The total initial number of carbon atoms in each graphite layer and the simulation cell were 34,932 and 3,143,880 respectively. The porosity is 15% and the pores are selected randomly, with average pore sizes of 5.0 nm. The total number of carbon atoms in generated 3-D pore network matrix is 2,673,343. The PSDs and their averages that are generated resemble the experimental PSD obtained for lignite by gas adsorption. As can be seen in Figure 13, the experimental PSD for Eagle Ford also shows a peak around 5.4 nm. The experimental distributions presented in Figures 13 and 14 are a small portion of the complete distribution, which can be seen in Figure 12.

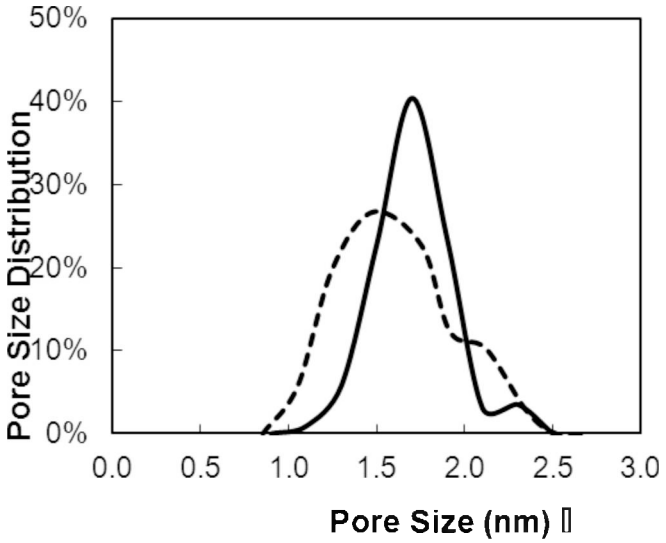

Figure 14. Computed pore size distribution of the 3-D pore network (solid curve) and pore size distribution determined by low-pressure gas adsorption (dotted curve) for Eagle Ford shale

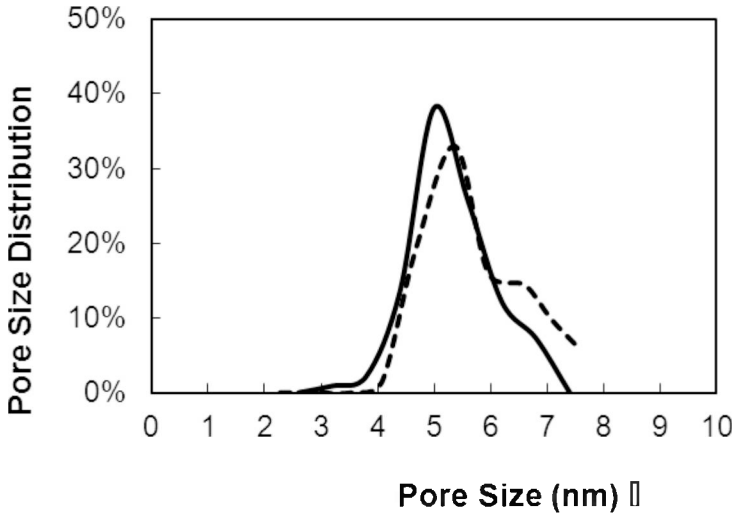

Figure 15. Computed pore size distribution of the 3-D pore network (solid curve) and pore size distribution determined by low-pressure gas adsorption (dotted curve) for North Dakota lignite.

The conclusion about the pore accessibility for different gases in the powder and chip samples is supported by a histogram plot, Figure 16, constructed on the basis used in the NLDFT method. The figure shows that the gas accesses various pore-scales, micro-, meso- and macro-pores and shows very limited access to upper meso- and macro-pores in the chip sample. Therefore, using powder in the PSD analysis exposes original pore volumes at various scale while the chip indicates only the conductive pore volumes. In powder samples, Ar gas accesses more macro-pores than N_2 gas. In the chip sample, Ar gas accesses greater pore volumes at the lower meso-pores and shows two peaks at that scale.

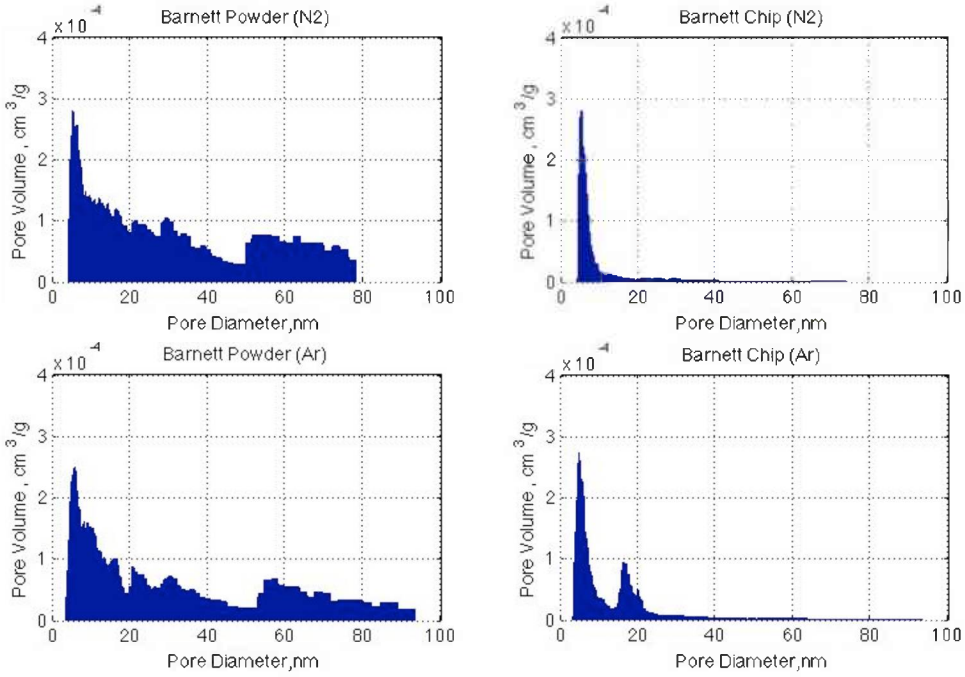

Figure 16. Histogram plot of pore volume vs. pore diameter for N_2 and Ar in powder and chip shale samples

The histogram plot of CO_2 access in powder and chip samples is depicted in Figure 17. Larger pore volumes are accessed in the chip sample at pore diameters greater than 1 nm. In the powder sample, however, larger pore volumes are accessed below 1 nm (ultra micro-pores).

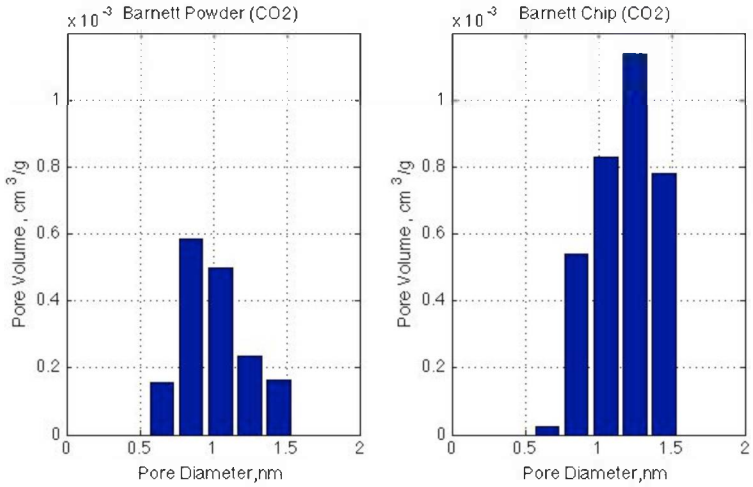

Figure 17. Histogram plot of pore volume vs. pore diameter for CO_2 gas in powder (left) and chip (right) shale samples.

In summary, pore-size distribution analysis of shale rocks is essential to reveal the various pore-scales that influence gas transport mechanisms in these types of rocks. Processes such as Knudsen diffusion, hopping and adsorption contribute largely to gas flow and knowledge of pore size distribution allows one to define the physical regimes at every pore-scale. Gases such as N_2 and Ar have access to meso- and macro-pores making them effective indicators to pore volumes in that region. CO_2, on the other hand, is more effectively employed to reveal micro- and ultra micro-pores due to its diffusive nature. The nature of the sample used in the analysis can either reveal the interconnected pathways in the pore networks such as in chips, or reveal the true inner pore structures of the shale that are not necessarily interconnected as found in powder. Powder might be more useful to define pore volume differences between different shale rocks, for example Barnett and Eagle Ford.

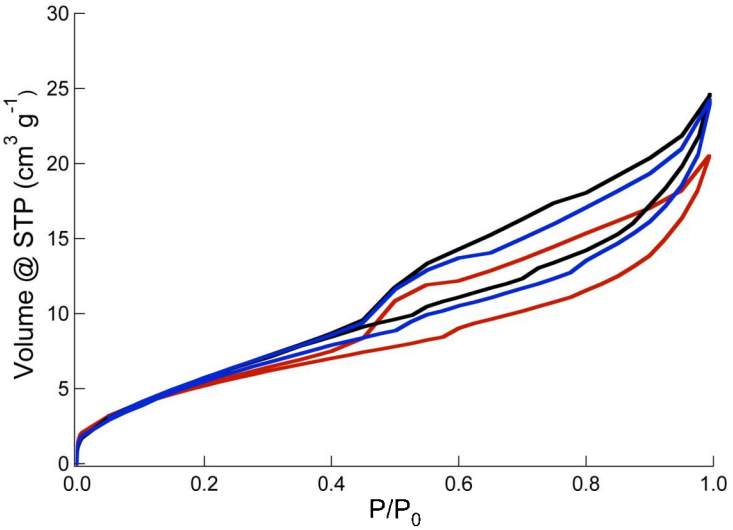

Figure 18. Eagle Ford 176 Ha isotherms with high-temperature outgassing. Sample 1 – Black; Sample 2 – Blue; Sample 3 – Red.

Pore size distributions are a portion of the information that is desired from low-pressure adsorption isotherms. Shale materials create several complications for traditional PSD methods due to high material heterogeneity and complicated pore networks, as evident in the isotherms presented in Figure 18, where the hysteresis loops close late at a P/P_0 near 0.4, a classic indication of complex pore networks and ink-bottle shaped pores. The traditional method of Barrett-Joyner-Halenda is poorly suited for shale materials, since the complex pore network effects are evident in the desorption isotherm. Modern DFT methods may be effective, but they still rely on defined pore shapes and adsorbent surfaces. However limited they may be, the transparency of the method allows for some conclusions about the shale PSDs to be drawn.

Figure 19 shows a number of pore size distributions for the same isotherm (Sample 3 in Figure 18) using a variety of assumptions. These assumptions range from DFT method (quenched solid (QSDFT) vs. non-localized (NLDFT)), isotherm branch (adsorption vs. desorption, adsorbent material (carbon vs. silica) and pore geometry (slit vs. cylindrical vs. spherical, and combinations of those). It is clear that the assumptions that lead into the pore size distribution can greatly affect the result. There are tri-modal (QSDFT adsorption on carbon with slit/cylindrical/spherical pores), bi-modal (QSDFT desorption on carbon with slit/cylindrical/spherical pores; NLDFT adsorption on silica with cylindrical/spherical pores) and uni-modal (NLDFT adsorption on silica with cylindrical pores; NLDFT desorption on silica with cylindrical pores) distributions, all of which could be taken as "reality". In addition, due to the complex pore networks, desorption isotherms tend to overestimate the mesopore volume. Any pore size distribution based off of low-pressure gas adsorption should clearly state the assumptions behind the model and indicate that the distribution is, at best, an interpretation of the actual pore distribution within the sample.

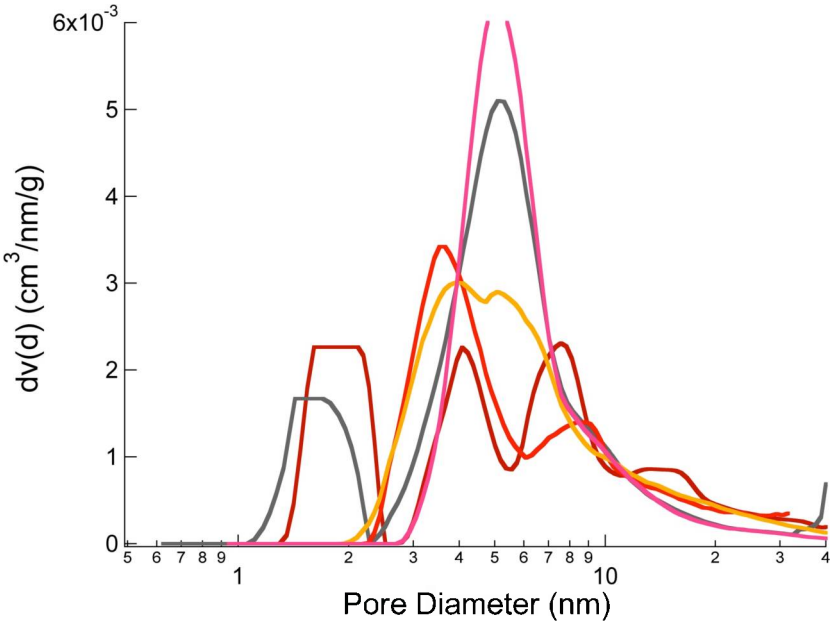

Figure 19. Pore size distribution results for Eagle Ford 176 Ha, Sample 2 from Figure 14. QSDFT Adsorption on C – Dark Red. QSDFT Desorption on C – Grey. NLDFT Adsorption on Si (Cyl/Sph) – Red. NLDFT Desorption on Si – Pink. NLDFT Adsorption on Si (Cyl) – Yellow.

Analysis of Low Pressure Adsorption for Pore Analysis

Eagle Ford (identifier – 176 Ha) was chosen for pore analysis using a Quantachrome Autosorb iQ_2 low-pressure adsorption instrument. The initial sample was ground to less than 355 μm, and separated into three samples between 50 and 355 μm with each sample weighing approximately 60 mg. Due to concerns with previous low-pressure analysis, primarily isotherms that are of insufficient quality for analysis, each sample was tested twice, with different outgassing procedures. The low-temperature outgas procedure, the same as in previous work, is: ramp to 110 °C at 2 °C min^{-1}, hold for 60 minutes, ramp to 140 °C at 5 °C min^{-1}, hold for 180 minutes and test for pressure change (which signifies continued outgassing). If the test passes (indicating minimal pressure change), the sample is dropped to room temperature and backfilled with N_2. If the test fails, the temperature is maintained at 140 °C for up to 180 minutes more, with tests every 15 minutes. Discussions with Quantachrome have indicated that the outgassing pressure test may not reliably indicate that the sample has finished outgassing. The sample was analyzed with N_2 adsorption. An improperly outgassed sample will lead to isotherms that cannot be properly analyzed. To check for this, the sample was then subjected to the following high temperature outgassing procedure, taken from the protocol for zeolite 13X regeneration: ramp to 80 °C at 1 °C min^{-1}, hold for 30 minutes, ramp to 110 °C at 1 °C min^{-1}, hold for 30 minutes, ramp to 300 °C at 5 °C min^{-1}, hold for 480 minutes, ramp to 350 °C at 5 °C min^{-1} and hold for 180 minutes. The pressure test is not performed at the end of this outgas procedure.

The samples were analyzed in 99.999% N_2 at 77 K at a P/P_0 range of 10^{-7} to 0.995. Nitrogen isotherms were performed with 47 adsorption points and 20 desorption points. The results of the analysis performed after the low-temperature outgassing procedure can be seen in Figure 20. There are a few key indicators that the samples were improperly outgassed prior to analysis: a) poor loop closing following hysteresis, b) choppy isotherms, which indicate that the samples had difficulty reaching equilibrium and c) the hysteresis loops for sample 1 cross. These results would indicate that the three arbitrarily chosen samples from the same small chip have very different pore properties.

The same samples were then subjected to the high-temperature outgassing procedure, which can be seen in Figure 21. There is a distinct improvement in the isotherm shapes and consistency between the samples. The hysteresis loops are now closing within the capabilities of the instrument and the isotherms have smoothed slightly. The samples are now indicating a very consistent micropore volume (as seen in the isotherms below 0.2 P/P_0) and increased consistency in the mesopore range. This is what should be expected, as the samples are from the same source. These results indicate that an improper outgassing may lead to incorrect conclusions, both within the same sample and across different shale types. It would be difficult to draw conclusions across different shale samples if the outgas procedure is not sufficient.

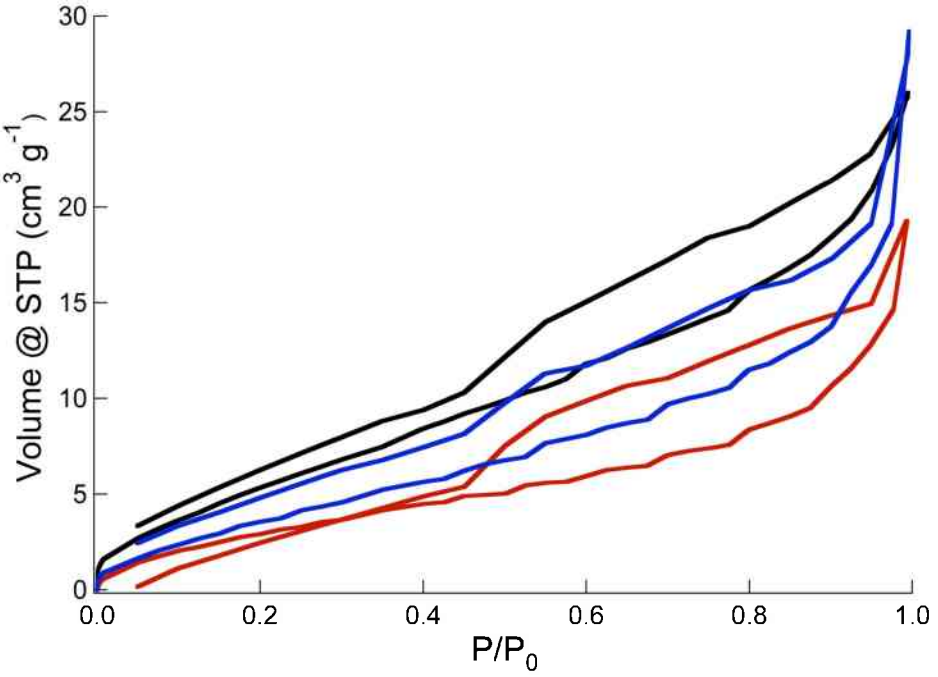

Figure 20: Eagle Ford 176 Ha with low-temperature outgassing. Sample 1 – Black; Sample 2 – Blue; Sample 3 – Red.

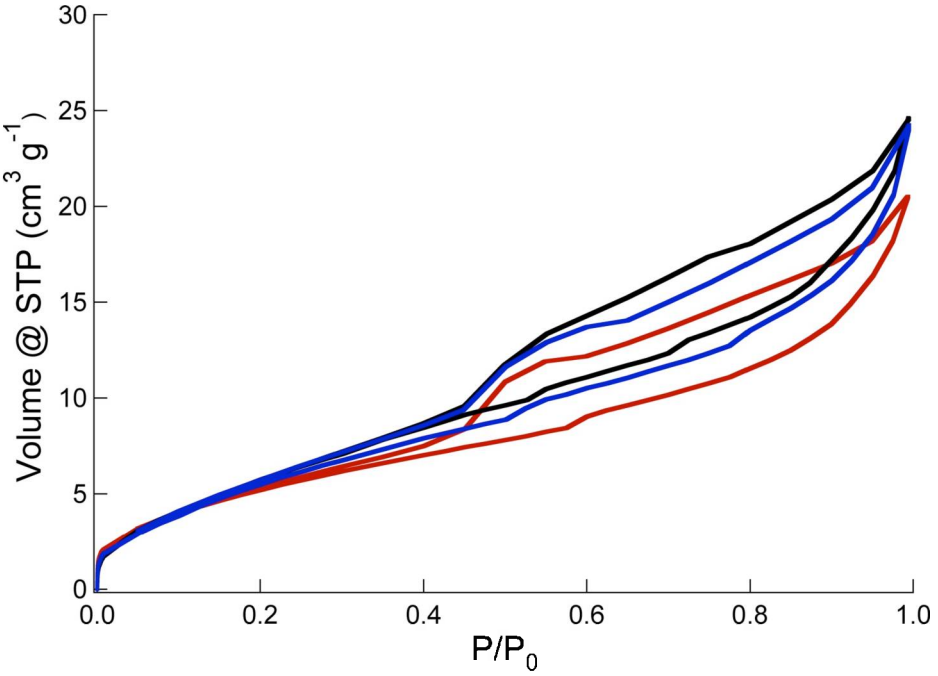

Figure 21: Eagle Ford 176 Ha isotherms with high-temperature outgassing. Sample 1 – Black; Sample 2 – Blue; Sample 3 – Red.

2.2: Development of model systems for adsorption and transport simulations

Development of these model systems is discussed within the text as it aligns with the molecular simulation predictions compared to experimental measurement.

2.3: Adsorption simulations using Grand Canonical Monte Carlo (GCMC)

A slit-pore model based upon graphite with and without surface functional groups has been employed along with grand canonical Monte Carlo to predict adsorption isotherms representative of the carbon-based constituents in gas shale. Figure 22 shows the predicted CO_2 density within an 8-nm carbon pore at varying pressures spanning to supercritical CO_2 conditions. It is anticipated that micropores (less than 2 nm) in addition to the mesopores (2 – 50 nm) measured using NMR cryoporometry comprise the pore network of gas shales. Although not pictured here, our results indicate that the adsorption mechanism of supercritical CO_2 differs in micropores from mesopores. In micropores the CO_2 exists only as an adsorbed phase, where in the mesopore there is a coexistence between an adsorbed and bulk phase. Notice in Figure 22 that the isothermal (305K) density profiles change by increments of 10 bar, with a jump existing between 90 and 100 bar. Bulk CO_2 is supercritical at 305K and pressures of approximately 70 bar. From these results it is suggested the CO_2 is supercritical at elevated pressures than its bulk phase, i.e., above 90 bar, where clearly there is a substantial increase in CO_2 density within the pore.

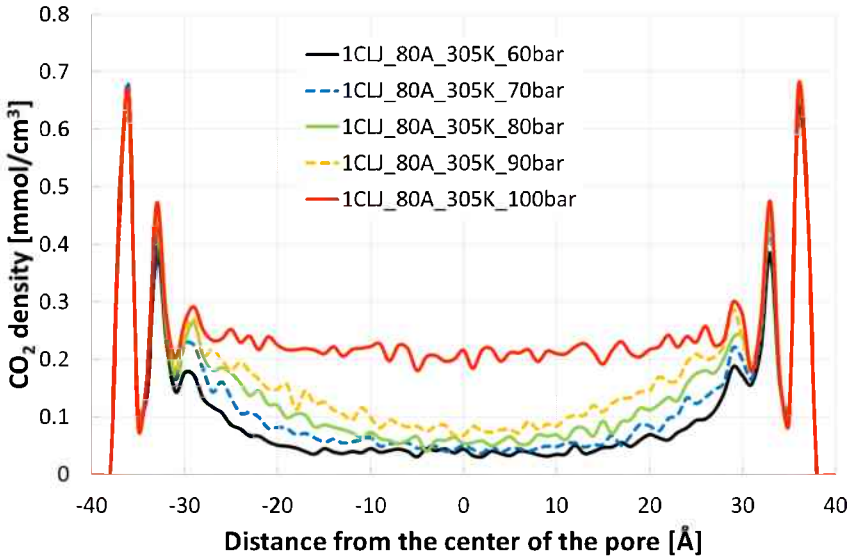

Figure 22. Comparison of CO_2 density within an 8nm pore representative of the organic matrix with gas shale.

The adsorption of CO_2 in micropores is different than that of mesopores. For instance, in micropores only several molecular layers of CO_2, at the most, can be contained. The energy associated with adsorption in these systems is enhanced through the inclusion of wall-wall interactions of the pore since the size of micropores is less than 2 nm in diameter. The wall-wall interaction is included along with CO_2-surface interactions and CO_2-CO_2 interactions to obtain the total potential energy of the system. In a mesopore,

there exists ordered molecular layers of CO_2 adsorbed to the pore walls, with the packing or CO_2 density decreasing toward the core of the pore. In mesopores there exists two types of sorbate particles, i.e., 1) CO_2-surface interactions are the major contribution to the potential energy of adsorption and 2) CO_2-CO_2 interactions are the major contribution to the potential energy of adsorption, with the second interaction type occurring toward the core of the pore. In mesopores, the pore walls are far enough apart such that wall-wall interactions are a negligible contribution to the adsorption energy. Through our simulations we are interested in predicting the excess CO_2 density, which is defined as the density difference between the density of total adsorbed CO_2 (surface + core) and the density of CO_2 in its pure bulk liquid phase. The excess adsorption and corresponding density of CO_2 at the surface of the pore and its change as a function of distance away from the pore will provide insight into its stability as a function or pore size.

The top images of Figure 23 show total loading and excess density as a function of pressure. Examination of the top left image reveals the early supercritical CO_2 transition that occurs in mesopores as a function of pore size. The presence of CO_2-CO_2 interactions in the pore's core is what drives the density changes from the phase transition. As adsorption is investigated in micropores, i.e., pores less than 2 nm, the density of CO_2 is fairly consistent as a function of pressure as shown in the top right image of Figure 23. Only in mesopores does the phase transition influence the CO_2 packing and subsequent adsorption mechanism. The bottom images of Figure 23 show the total loading and excess loading as a function of the bulk CO_2 density.

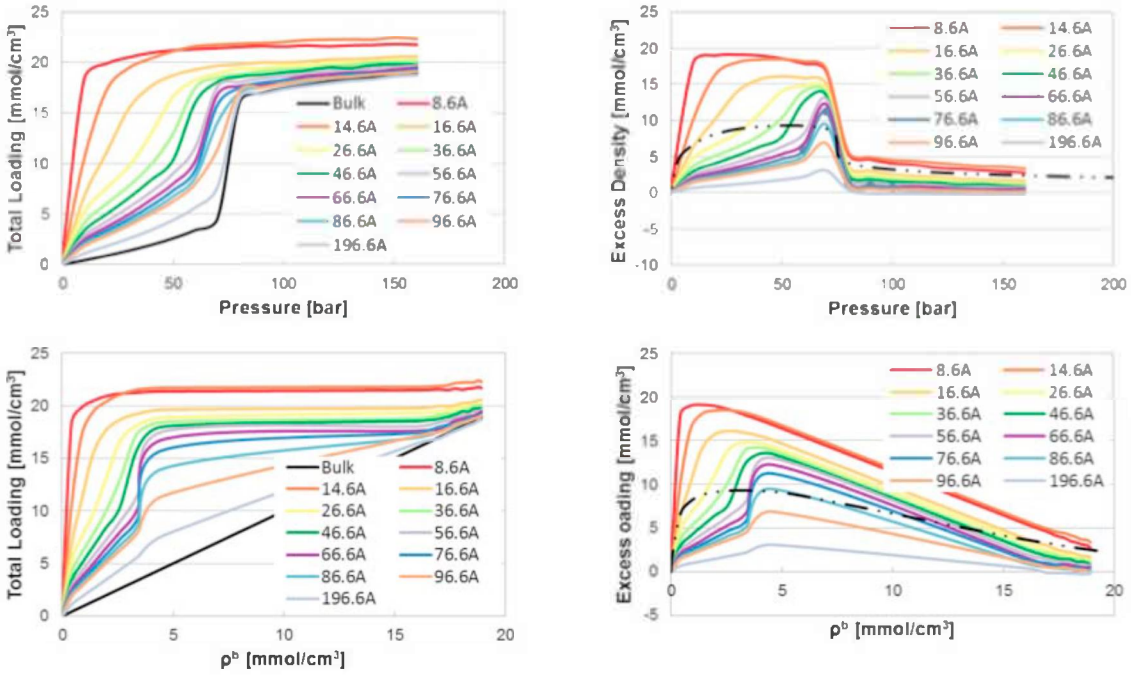

Figure 23. Total loading (top left) and excess density (top right) as a function of pressure and total loading (bottom left) and excess loading (bottom right) as a function of density.

Figure 24 shows the total CO_2 loading in carbon-based micro and mesopores at 318 K as a function of increasing pressure. Bulk CO_2 is represented by the solid black line, with the

phase change to supercritical evident at approximately 74 bar (~7.4 MPa) and 318 K. The loading of CO_2 in a pore increases steadily with pressure in pores greater than 40 Å (4 nm) up to a pressure of approximately 74 bar, after which the loading sharply increases over a narrow pressure range, followed by a plateau in loading after approximately 100 bar. As the pore size increases, the behavior of CO_2 becomes more representative of the bulk behavior of CO_2. In pores less than 40 Å (4 nm), the phase transition to supercritical does not exist. Rather, the CO_2 loading in the smaller sized pores increases steadily as pressure increases and begins to plateau between approximately 40 to 50 bar in pores between 20 and 40 Å (2 and 4 nm) and between 10 to 20 bar in pores less than 20 Å (2 nm).

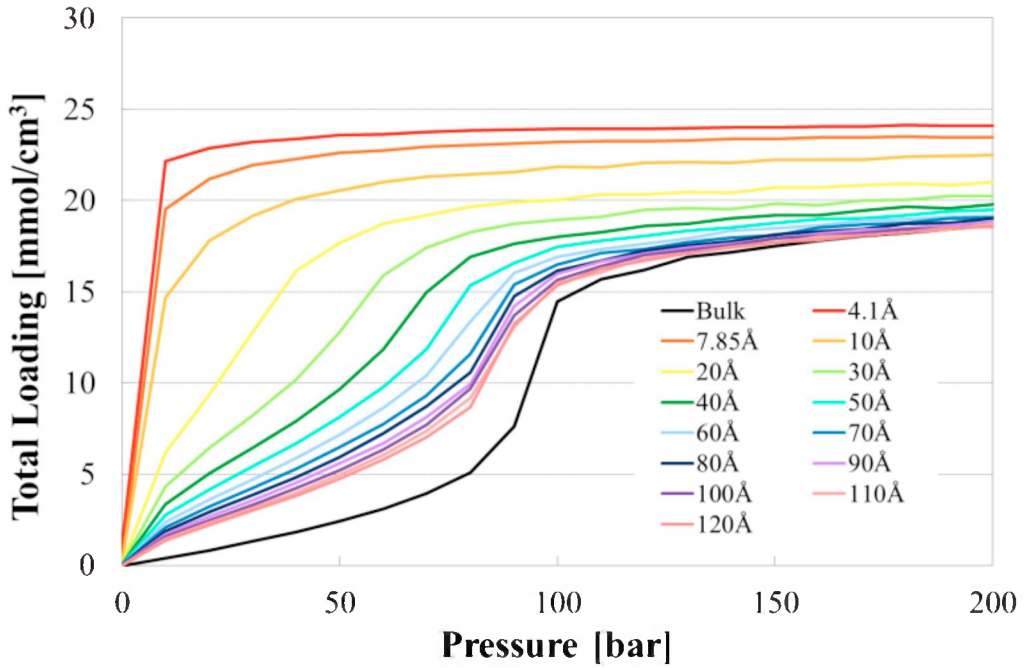

Figure 24. Total CO2 loading in carbon-based micro and mesopores at 318 K as a function of pressure.

The pore occupancy at 318K and 200 bar, representative of the plateau region from Figure 24, has also been investigated as a function of pore size as illustrated in Figure 25. The energy associated with adsorption in micropores is enhanced through the inclusion of wall-wall interactions of the pore since the size of micropores is less than 2 nm in diameter. The wall-wall interaction is included along with CO_2-surface interactions and CO_2-CO_2 interactions to obtain the total potential energy of the system. In a mesopore, there exists ordered molecular layers of CO_2 adsorbed to the pore walls, with the packing or CO_2 density decreasing toward the core of the pore. In mesopores there exists two types of sorbate particles, i.e., 1) CO_2-surface interactions are the major contribution to the potential energy of adsorption and 2) CO_2-CO_2 interactions are the major contribution to the potential energy of adsorption, with the second interaction type occurring toward the core of the pore. In mesopores, the pore walls are far enough apart such that wall-wall interactions are a negligible contribution to the adsorption energy. From Figure 26 it is evident that the pore occupancy is highest in pores less than 10 Å (1 nm), and fairly

constant in greater pores. Additionally, pores greater than 20 Å (2 nm) exhibit a second-layer of CO_2, with the core of the pores greater than this size comprised of CO_2 behaving as that of the bulk fluid.

Through our simulations we are interested in predicting the excess CO_2 density, which is defined as the density difference between the density of total adsorbed CO_2 (surface + core) and the density of CO_2 in its pure bulk liquid phase. The excess adsorption and corresponding density of CO_2 at the surface of the pore and its change as a function of distance away from the pore will provide insight into its stability as a function or pore size.

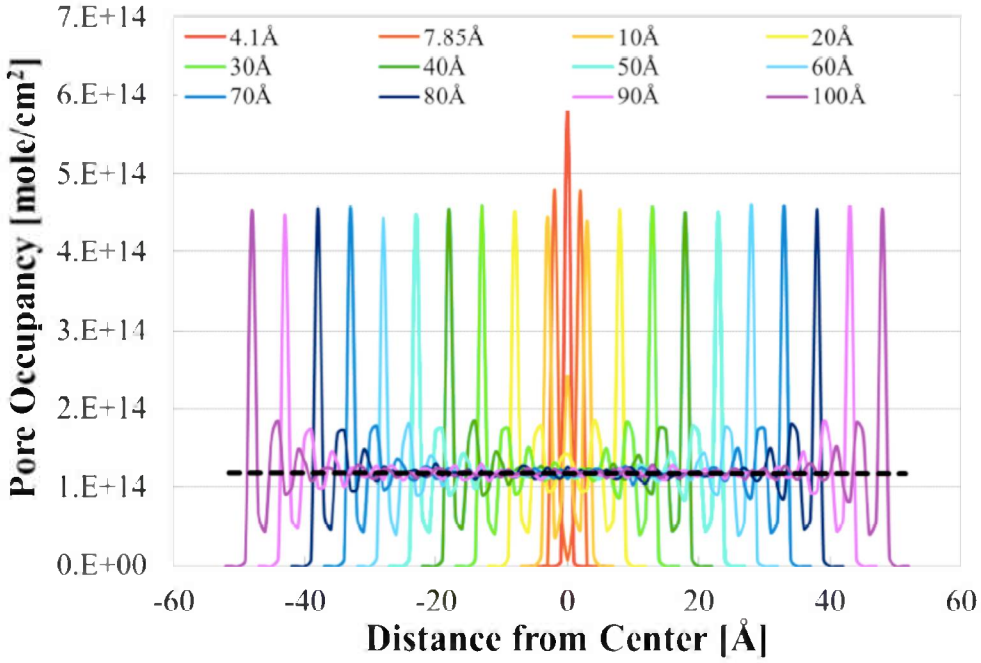

Figure 26. Pore occupancy as a function of pore size at 200 bar. Pore size (x-axis) is measured in terms of distance from the center of the pore.

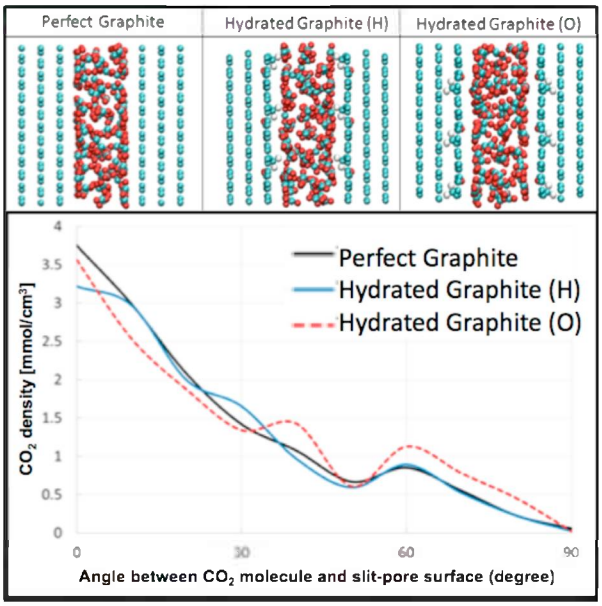

Figure 27. Snapshots and orientation distribution of CO_2 in graphitic slit-pores.

To begin our investigation on the influence of water on CO_2 adsorption, modeling of CO_2 has also been carried out on hydrated graphite pore surfaces as shown in Figure 26. Similar to our previous work (Liu and Wilcox, 2011), ab initio thermodynamics and electronic structure calculations were applied to determine the most stable configuration of dissociated water on the carbon surface in equilibrium with water vapor, which is likely in the systems present in the Earth's subsurface. Therefore, it is quite likely that CO_2 will "see" a carbon surface functionalized rather than clean, which will have an effect on its sorption behavior, with a more pronounced effect in smaller pores where the surface chemistry will dictate. The interaction between surface dangling bonds and volatile components (such as H_2O) creates chemical and structural heterogeneity on the graphitic surface. The partial charges in this system redistribute making it either passivating or enhancing the CO_2-surface adsorption. To investigate the surface heterogeneity effect a Bader charge map was created for the surface from the electronic structure output so that Columbic interactions could be added to the L-J potential to determine the system potential energy and the TraPPE (Potoff and Siepmann, 2001) model was employed for CO_2. From Figure 27, it can also be seen that when the surface functional group involves oxygen, CO_2 will change its alignment thereby influencing its density in the pore. This result is consistent with the Bader charge analysis, which predicts that the electronegative surface atoms (e.g., oxygen atoms) are more likely to serve as basic sites for CO_2 adsorption, with the carbon atom of CO_2 serving as the acid component. With the strong CO_2-CO_2 and CO_2-surface interactions, the bulk gas-phase of CO_2 in micro-pores does not exist. In fact, the role of supercritical CO_2 is fairly insignificant at this scale, while it may be quite significant at the meso- and macropore scales. This characteristic can be applied for detecting micro-pores in porous materials. For instance, if the gas density profile varies compared to the standard bulk gas, the existence of micropores is likely.

Since the pore space in gas shale systems is comprised primarily of clay and carbon (kerogen)-based networks, modeling the surface chemistry and structure of the pores is required for accurately predicting their capacity and the mechanism of gas adsorption as a function of temperature and pressure. Previous experimental studies provide indication that the natural carbon-based systems include both aromatic and aliphatic structures, as well as a variety of surface functional groups (Van Krevelen, 1991; Haenel, 1992; Smith et al. 1994; White et al. 2005), including volatile components such as water vapor, methane, nitrogen- and sulfur-containing compounds. Such chemical heterogeneity may play an important role in determining the adsorption capacity and adsorbed/gas phase equilibrium properties such as density, heat of adsorption and packing within the pore. In addition, embedded functional groups will change the electrostatic properties of the pore surface, and thus are expected to play an important role in the adsorption mechanisms associated with CO_2 in these systems depending on the temperature and pressure conditions. As shown in Figure 28, the graphite surface functional groups of the following types are considered: mono-vacancy (Hashimoto et al., 2004) with dissociated H_2O (Kostov et al., 2005); epoxy functionalized (Kudin et al., 2008); hydroxyl functionalized (Kudin et al., 2008; Bagri et al., 2010), carbonyl functionalized (Bagri et al., 2010), carboxyl functionalized, and combined hydroxyl-carbonyl functionalized (Bagri et al., 2010).

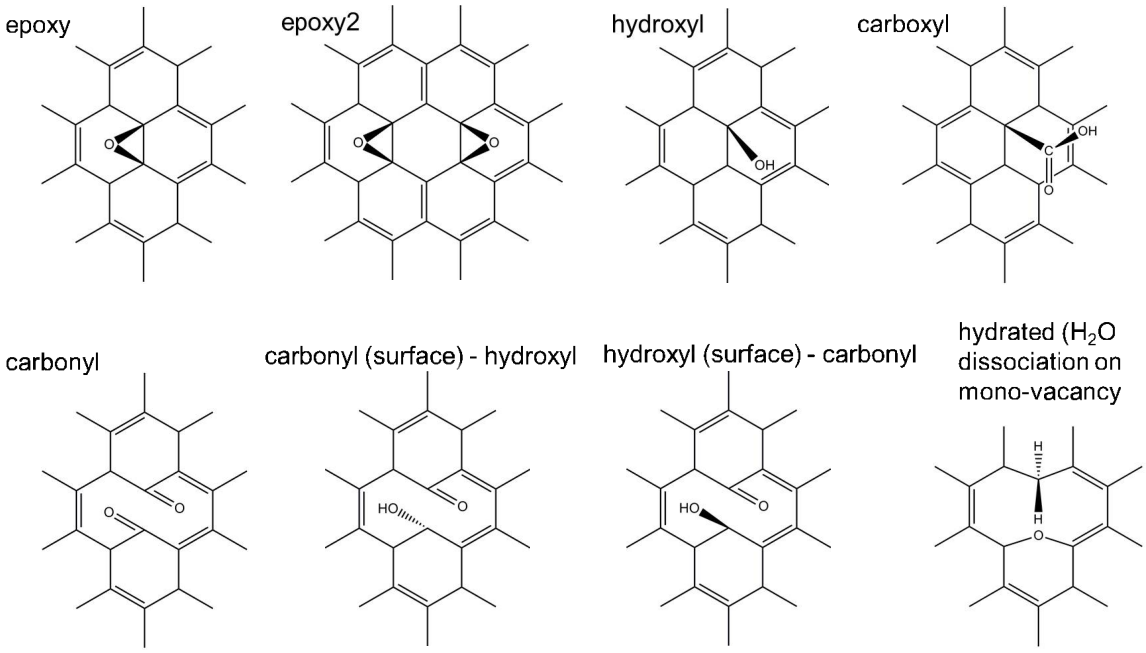

Figure 28. Functionalized graphitic surfaces investigated in the current work. These functional groups are positioned in the center of the top layer of the periodic graphite slabs.

Grand canonical Monte Carlo (GCMC) simulations of CO_2 adsorption in idealized organic microporous carbons were carried out in the μVT ensemble. The Peng-Robinson equation of state was used to relate the bulk experimental pressure with the chemical potential required in the GCMC simulations. A total of approximately 100 million GCMC moves were attempted during each GCMC simulation. The implementation of the GCMC method yields the adsorption isotherms of a given adsorbent-adsorbate interaction in micro- and meso-slit pores: the total and the excess adsorption isotherms were

predicted and the effects of pore size and surface functionality have been investigated. Total adsorption represents the total amount of CO_2 adsorbed per unit pore volume, including CO_2 in both condensed surface-bound adsorbed phase and weakly surface-bound gas phases. The excess adsorption is the additional amount of CO_2 adsorbed per unit pore volume compared with the amount of CO_2 in the same volume as the pore without the pore walls. The conversion from total to excess adsorption bridges the molecular simulation results to the direct experiment measurements.

Figure 29 shows a complete comparison of pore volumes with different surface functionalities for both 9.2 Å and 20 Å pores.

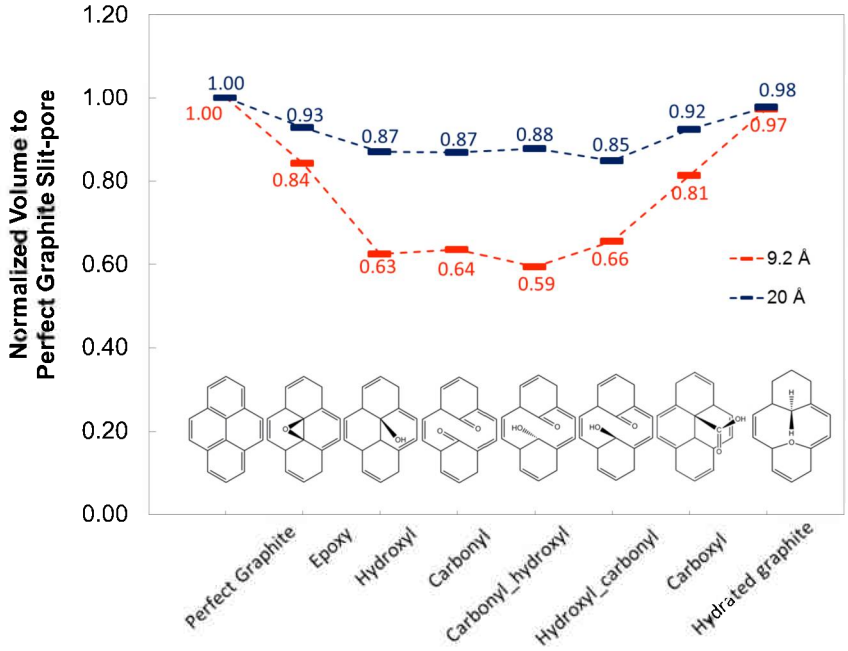

Figure 29. Comparison of the pore volumes with different surface functionalities.

To have an improved understanding of the CO_2 packing in the pores, packing configuration snapshots of CO_2 in the functionalized graphitic surfaces at 250 bar are shown in Figure 30. Linear CO_2 molecules are represented by the red line segments. The CO_2 molecules are more organized and aligned when they are adsorbed in the functionalized slit pores, and thus the adsorption capacity is enhanced by the higher efficient side-by-side packing. In the ultramicropores, due to the overlapping potentials from the strong pore wall-wall interactions and the strong CO_2-wall interaction, the CO_2 density of the condensed phase is even higher than that of the larger pores. In general, as the pore width decreases, the surface functionalities dictate the adsorption, and thus the surface functionalities play more of a role in enhancing the CO_2 adsorption capacity. The surface heterogeneity changes the adsorbates' accumulation configuration by changing the geometry of the pore surface and the charge distribution of the surface,

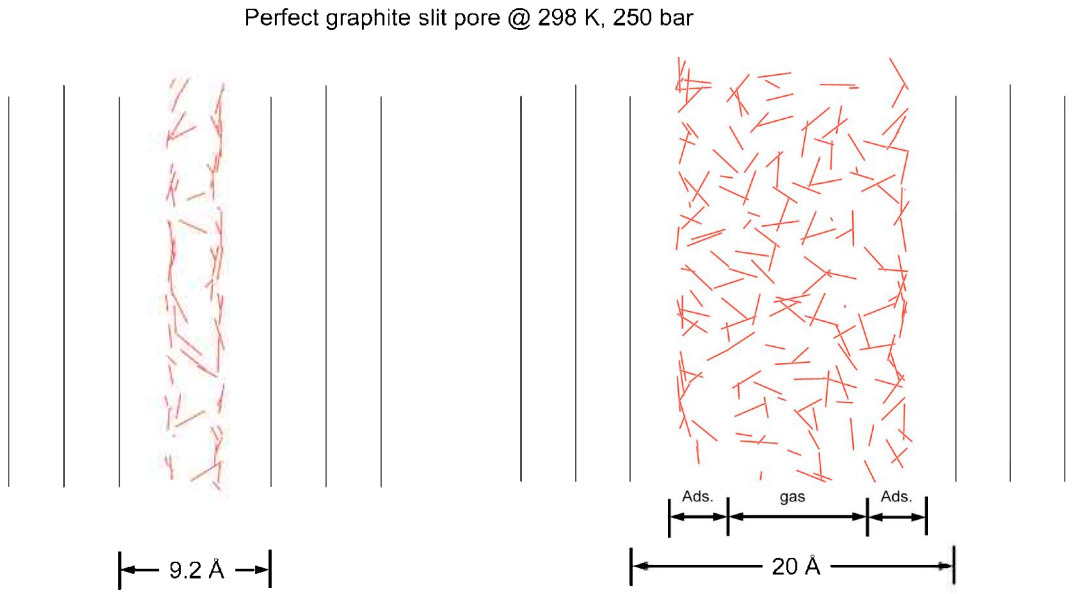

(a) Perfect graphite slit pore

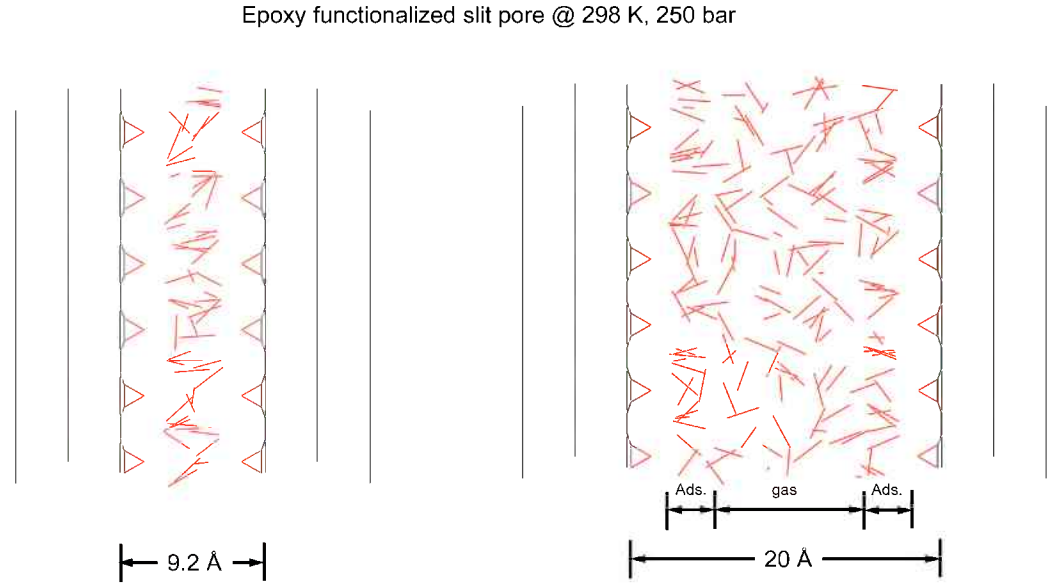

(b) Epoxy functionalized slit pore

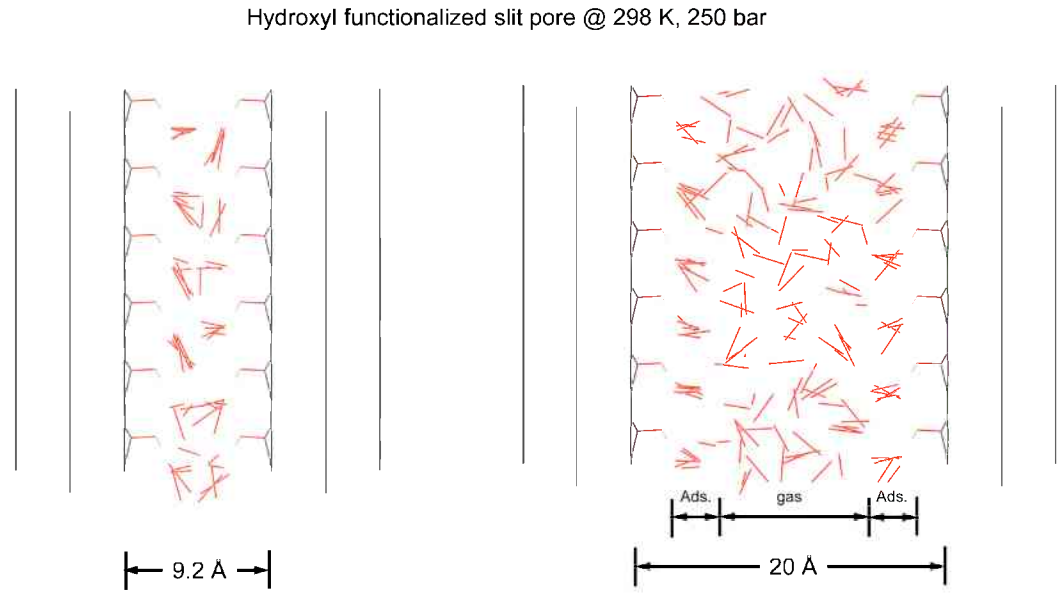

(c) Hydroxyl functionalize slit pore

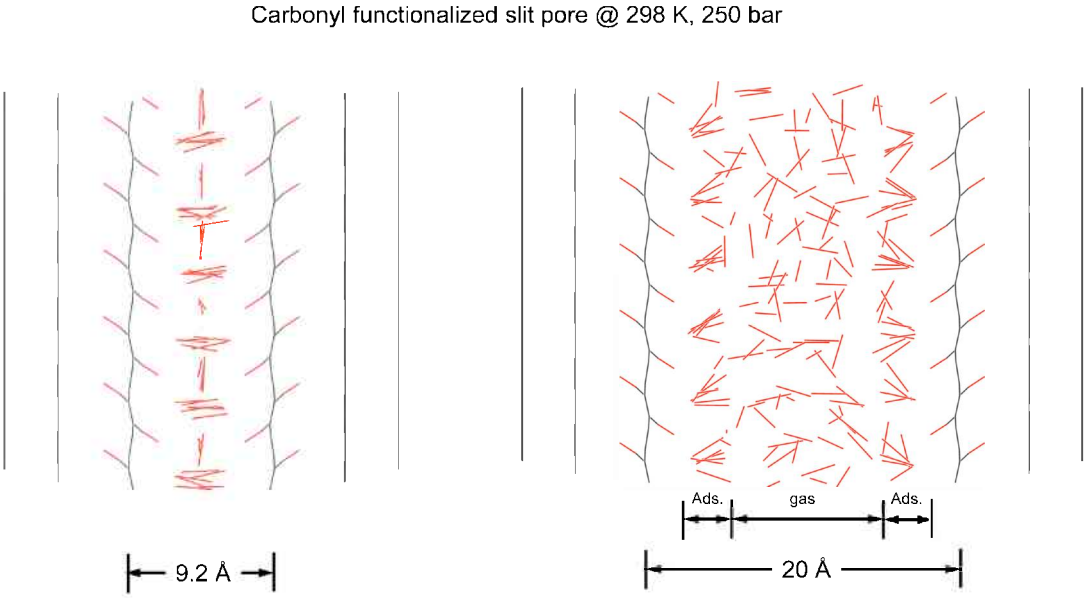

(d) Carbonyl functionalized slit pore

Figure 30. Packing configurations of CO_2 in functionalized micropores. Left: side views of adsorbed CO_2 in various functionalized graphite slit pores with the pore width of 9.2 Å; Right: side views of adsorbed CO_2 in various functionalized graphite slit pores with the pore width of 20 Å.

Figure 31 shows the local density distribution of CO_2 in the investigated functionalized slit pores with different pore widths at conditions of 298 K and 250 bar. The bulk CO_2 density at the same pressure and temperature is also illustrated in all of the figures, in addition to the density of dry ice, which is perceived to be the most efficient packing of

CO_2. Both the bulk CO_2 density and dry ice density is homogeneous in the pore space; however, the local density distributions of CO_2 in the slit pores are far from uniform. In the case of the 9.2 Å pores, due to the overlap of the strong surface-surface and the CO_2-surface interactions, the condensed phases of CO_2 are concentrated in the middle of the pores, with an even higher density than that of bulk CO_2 or dry ice.

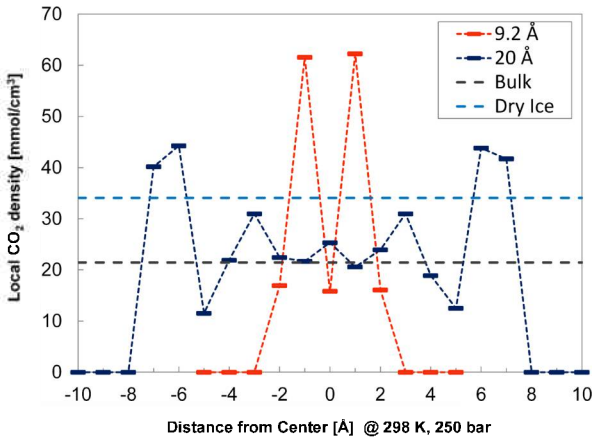

(a) Perfect graphite (PG)

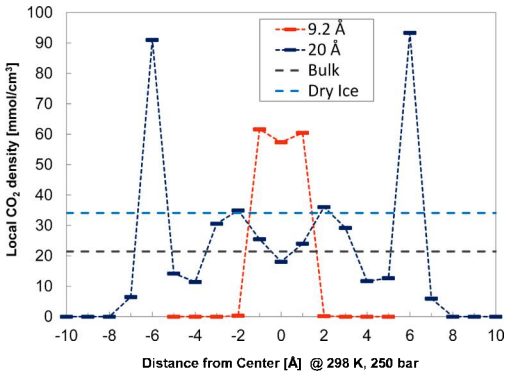

(b) Epoxy functionalized (OX)

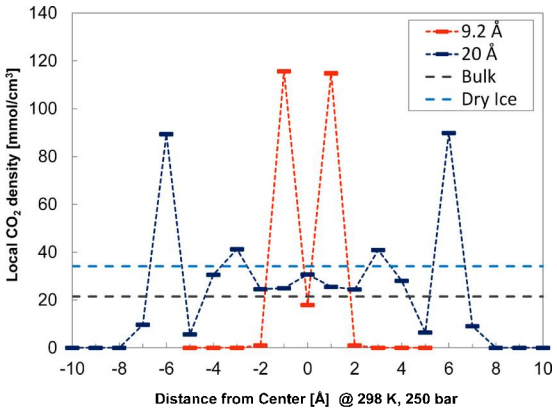

(c) Hydroxyl functionalized (OH)

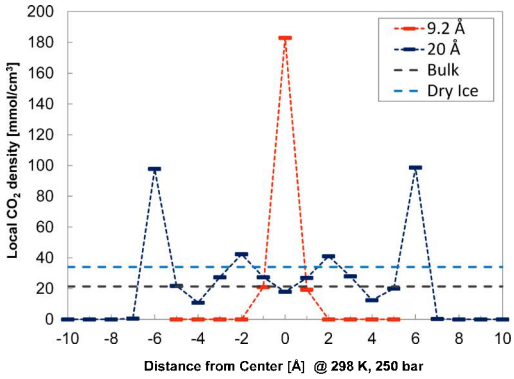

(d) Carbonyl functionalized (C=O)

Figure 32. Local CO_2 density distribution in various functionalized slit pores of two widths: 9.2 Å and 20 Å.

Comparison of Adsorption Isotherm Prediction by Theoretical and Experimental Work

For the adsorption prediction in this work, carbon-slit pores ranging from micropores (i.e., < 2nm) to mesopores (between 2 and 10 nm) have been modeled with the space between sheets of graphite representing the pore diameters. Lennard-Jones potentials are used to describe CO_2-wall and CO_2-CO_2 fluid interactions. A statistical sampling approach based upon Grand Canonical Monte Carlo was employed to test various particle

configurations in a given pore, with the minimum energy configuration providing knowledge of particle number and position within the pore. Based upon this information, total adsorption, excess adsorption, and absolute adsorption isotherms have been generated.

In the molecular simulation work, the direct results are expressed as "total adsorption," which takes all the gas molecules into account, including the gas phase and adsorbed phase. The excess adsorption can be measured directly by lab experiments based on a volumetric balance. The absolute amount of adsorption, $n_{ads,absolute}$, can then be calculated according to eqn. (1):

$$n_{ads,absolute}=n_{ads,excess}/(1-\rho_{gas}/\rho_{ads}) \qquad (1)$$

where $n_{ads,excess}$ is the excess adsorption, ρ_{ads} is the density of the adsorbed phase, and ρ_{gas} is the density of the free gas phase. To be consistent with the experiment measurement, the density of the adsorbed phase can be estimated using the hard sphere term, b, from the Redlich-Kwong-Soave equation of state, which is equivalent to the density of the fluid at the critical temperature and pressure.

The adsorption measurements were carried out for four Barnett shale samples labeled 19HVab, 22Vab, 26Vab, and 31Vcde, which were pulverized with ultimate particle sizes of between 100 and 250 microns. The pore volume and porosity were measured using helium and then corrected by additional changes by the direct measurement with N_2, CH_4, and CO_2 during adsorption measurements. It was reported that the corrections of the pore volume measurements never exceeded 2% of that measured with helium, and were generally well under 1%. For consistency, the simulated temperature is 298.15 K, which is the same as the lab measurement.

Using the measured material density and porosity, the GCMC simulated adsorption isotherms can be converted for direct comparison against the experimental measurements. Assuming a porosity of approximately 8%, yields GCMC adsorption predictions in the range of experimental measurements carried out in the Zoback lab as shown in Figure 33. Additional pore size distribution measurements of these shale samples will be required for accurately predicting the adsorption behavior using GCMC simulations as the adsorption represented by the GCMC simulations in Figure 10 are for discrete pore sizes.

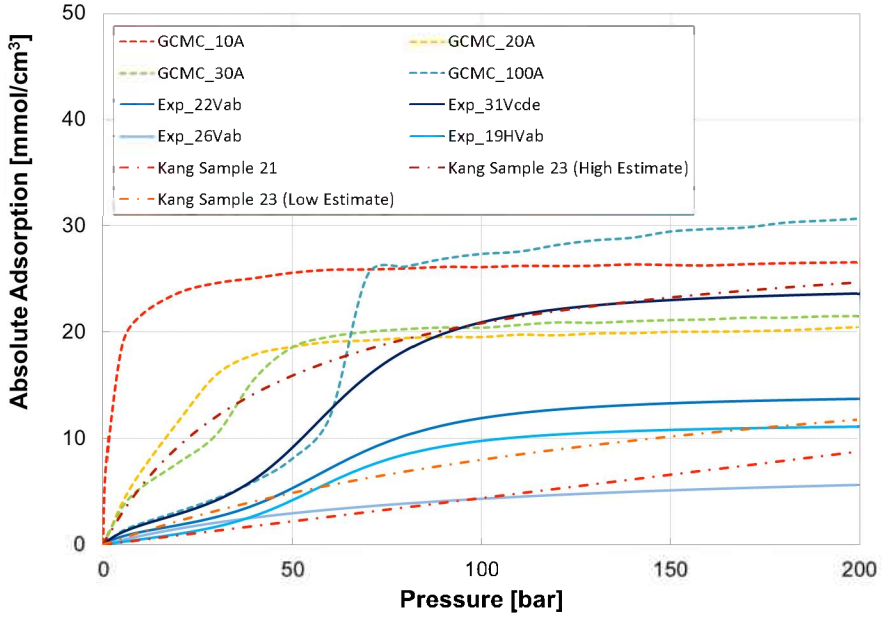

Figure 33. Comparison of the adsorption isotherms predicted by the GCMC simulations for various discrete pore sizes to the lab measurement of four different Barnett gas shale samples. The porosity used to convert the GCMC simulation results is φ=0.08

Molecular Simulation of CO_2 Adsorption on Graphite Slit Pore

To understand the interaction between CO_2 and carbon-based material at a molecular level, simulation of adsorption properties using statistical modeling based on the Grand Canonical Monte Carlo method (GCMC) of CO_2 adsorption in idealized organic microporous carbons has been performed in the μVT ensemble. Similar to previous research carried out by Liu and Wilcox, the 1C-LJ intermolecular model was applied on CO_2 molecule in the simulation. The collision diameter σ and the reduced well-depth of the interaction energy ε are tuned to be 3.750Å and 235.00 K, respectively, by comparing with NIST data (experimental data) as shown in Figure 34.

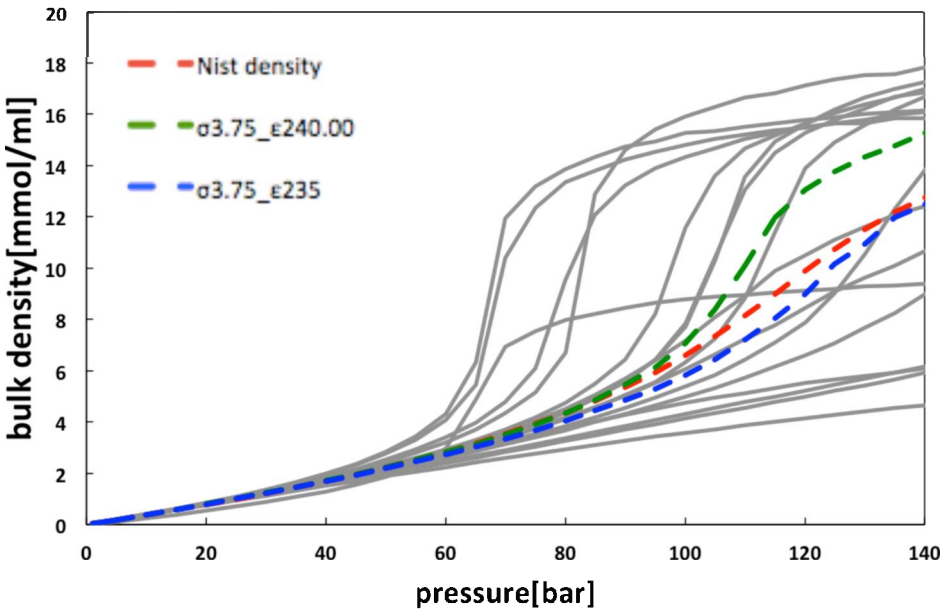

Figure 34. Parameter Tuning for LJ model. Simulation result by tuning collision diameter σ within a range from 3.454 Å to 4.486 Å, and reduced well-depth of the interaction energy ε within a range from 189K to 250K.

To investigate how the pore size and pressure can influence the adsorption behavior of CO_2 in shale, a three-layered graphite model was used to simulate the carbon-based material. A total of approximately 50 million GCMC moves were attempted during each GCMC simulation. Results are shown in Figure 12.

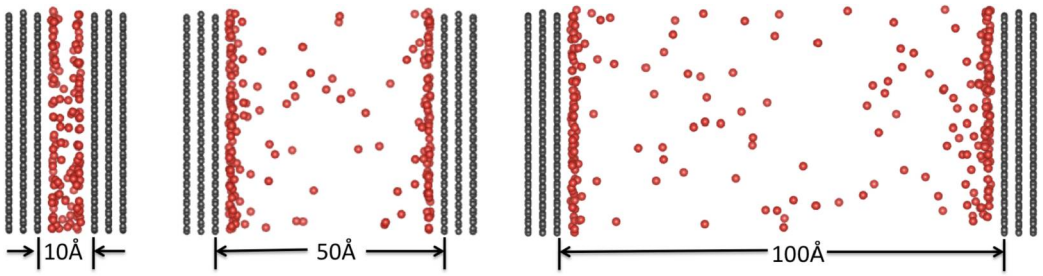

(a)

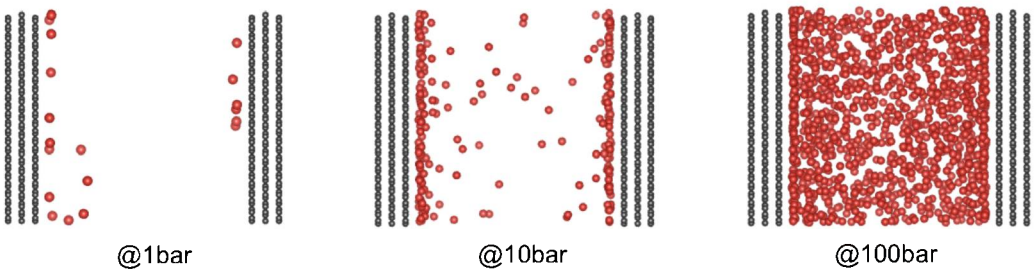

(b)

Figure 35. (a) Comparative side views of adsorbed CO_2 in graphite slit pores with varying pore width at 333K and 10 bar; (b) Comparative side views of adsorbed CO_2 in graphite slit pores with pore width of 50Å at 333K and varying pressure.

Predicted excess adsorption isotherms of CO_2 from molecular simulation are compared to experimental excess adsorption isotherms on an activated carbon sample with a known PSD. To this aim, the experimentally measured pore size distribution was truncated to include only the micropore and lower mesopore range since it is likely that for the density of CO_2 in pores greater than 20 nm, the density can simply be estimated as that of the bulk-phase CO_2 at the same temperature and pressure conditions. PSD of activated carbon is shown in Figure 35(a), and it was truncated at 20 nm and normalized as shown in Figure 36(b).

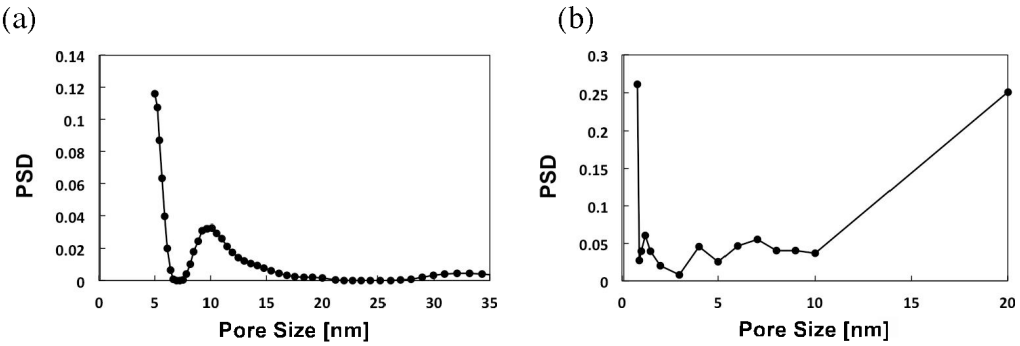

Figure 36. (a) Measured PSD for activated carbon; (b) PSD cutoff at 20 nm for simulation

Based on the assumption that the real porous system is a linear combination of slit pores with varying widths, the predicted excess adsorption isotherm is then calculated as the weighted average of the excess isotherms obtained from density estimates of single pores at the various sizes of the PSD, as shown in Figure 37.

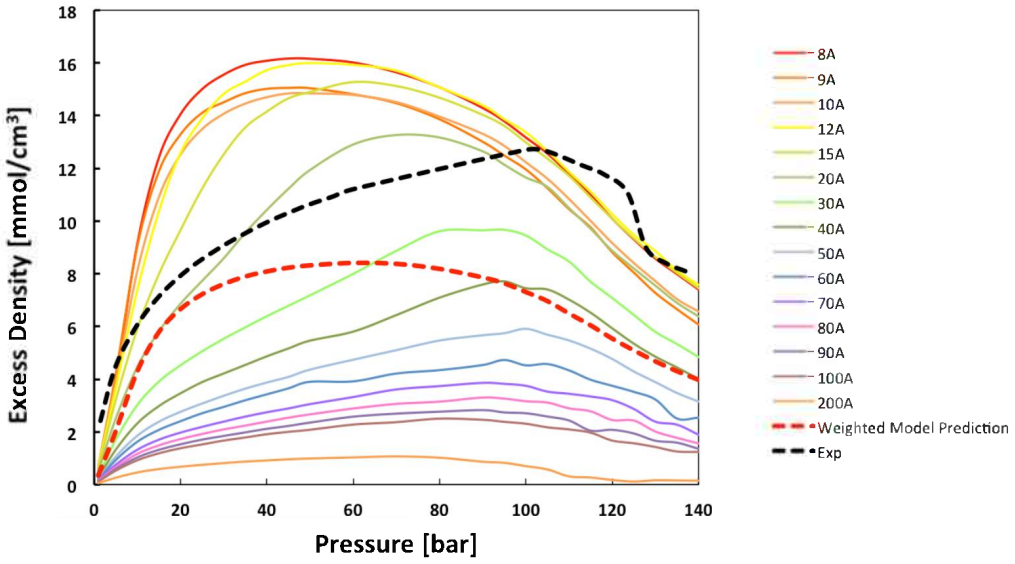

Figure 37. Comparison of the simulated adsorption isotherm with the experimental measurement at 333 K

The simulated adsorption isotherm is fairly consistent with the lab measurement, especially in the low-pressure region. At high-pressure conditions, the molecular simulation results under predict the adsorption. To investigate whether the surface

functionality of the pore is the cause of the discrepancy, we introduced hydroxyl functional groups within the graphite model. As shown in Figure 38, the gas capacity increases in the hydroxyl-functionalized model in the low-pressure range, but in the high-pressure range still underestimates adsorption. Clearly more work is required to determine the reason for disagreement between the model prediction and experiment at high pressure.

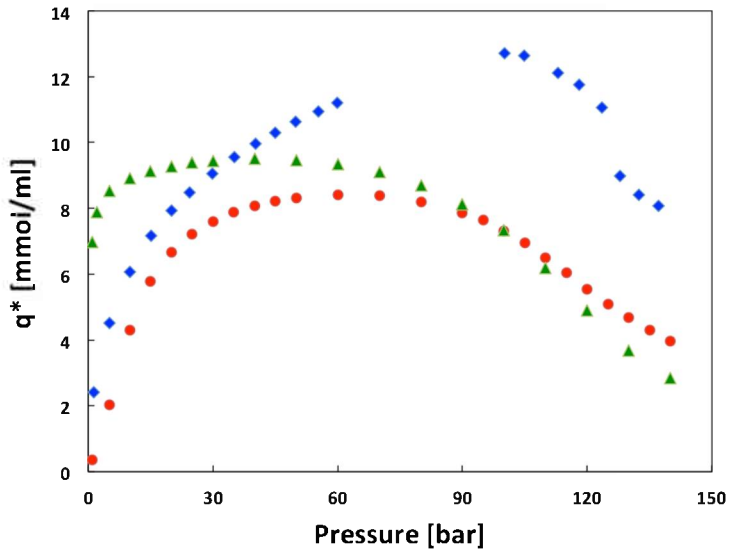

Figure 38. Comparison of experimental measurement (shown blue) with simulated isotherm on perfect carbon pores (shown in red) and hydroxyl functionalized carbon pores (shown in green).

2.4: Physical property measurements

Research on the relative adsorption of various gases has been carried on four samples of Barnett shale. Isotherms for rocks like coal or a gas shale are often fit by a Type I, or Langmuir, isotherm (Figure 39). The Langmuir isotherm represents the adsorption of a monolayer of molecules on the inner surfaces of the material (Langmuir, 1916). It can be fit with a two-parameter equation:

$$V(P) = \frac{V_L P}{P_L + P}$$

where $V(P)$ is the volume of adsorption at pressure P, V_L is the Langmuir volume, representative of total adsorption at infinite pressure, and P_L is the Langmuir pressure, which is the pressure at which half of the maximum amount has adsorbed. If multi-layer adsorption occurs, then a Type II, or BET, adsorption curve is used to fit the data. As with a Langmuir isotherm, a BET isotherm can also be fit with a two parameter equation (Brunauer et al., 1938):

$$V(P) = \frac{V_m C P}{(P_0 - P)\left[1 + (C-1)P/P_0\right]}$$

where P_0 is the vapor pressure of the gas, V_m is the maximum monolayer adsorption and C is a parameter that controls the shape of the adsorption curve at low pressure.

However, the standard BET isotherm assumes that an infinite number of adsorption layers are possible as pressure increases, despite the finite volume of free space in a rock and the finite capacity of a surface to adsorb gas layers. Thus, it is common to use an "N-layer" BET isotherm which assumes that there are a maximum N layers that can be adsorbed onto the internal surfaces:

$$V(P) = \frac{V_m C P_R}{1-P_R} \frac{1-(N+1)P_R^N + N P_R^{N+1}}{1+(C-1)P_R - C P_R^{N+1}}$$

where P_R is the ratio of the measured pressure (P) to the vapor pressure (P_0), and N is the maximum number of adsorption layers.

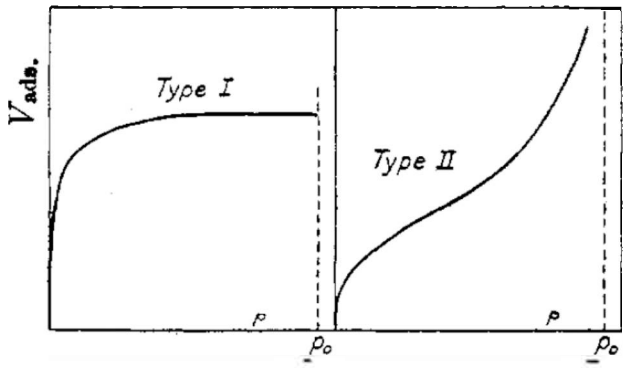

Figure 39: Type I (Langmuir) adsorption curve, representing monolayer adsorption, and Type II (BET) adsorption curve, representing multi-layer adsorption. Source: Brunauer et al. [1940]

Our measured adsorption capacities varied by as much as 50% among the four samples (Fig. 40). It is likely that composition was the major controlling factor on these differences. Sample 31Vcde had the highest amount of TOC (5.7%) of any tested sample and also the largest measured adsorption capacity. This sample may also have exhibited "molecular sieving" of the different gases, perhaps caused by the pore size distribution in this high TOC sample.

Due to limitations of our modified tri-axial system, our adsorption studies were conducted at pressures well below the in situ pressures found in the Barnett shale. Nevertheless, the results are consistent with studies on gas shales conducted at both high and low pressure. Nuttall et al. (2005) found average CO_2 adsorption of 25-60 scf/ton on Appalachian gas shale samples. Our Barnett results show similar magnitudes within this pressure range, except with 3 out of 4 samples exhibiting BET-like adsorption isotherms, in contrast to the Langmuir behavior found by Nuttall et al. (2005). While we were running our experiments, Kang et al. (2010) published results of Barnett CH_4 and CO_2 adsorption at high pressures. As seen in Figure 3 if we extrapolate our own low pressure results out to the in situ pressures found in the Barnett, we find that for CO_2 our results are reasonably predictive of the same adsorption capacities found by Kang et al. When extrapolated out to Barnett reservoir pressures, our N-BET models of CO_2 adsorption behave similarly to Langmuir-type models. Thus, it is possible that Kang et al. would

have also found BET behavior had they measured adsorption at low pressures and not assumed a priori that adsorption would demonstrate Langmuir-type behavior. Studies that measure adsorption at both low and high pressures on the same samples would be beneficial in clarifying the full behavior of CO_2 adsorption in the Barnett shale.

Figure 40. Adsorption isotherms for four different samples of Barnett shale. Note that CO_2 is always preferentially adsorbed to CH_4 and N_2. In all samples, CH_4 and N_2 are characterized by Langmuir adsorption. While sample 26Vab (lower left) appears to be characterized by Langmuir adsorption, samples 19HVab (upper left), 22Vab (upper right) and 31Vcde (lower right) are characterized by BET adsorption.

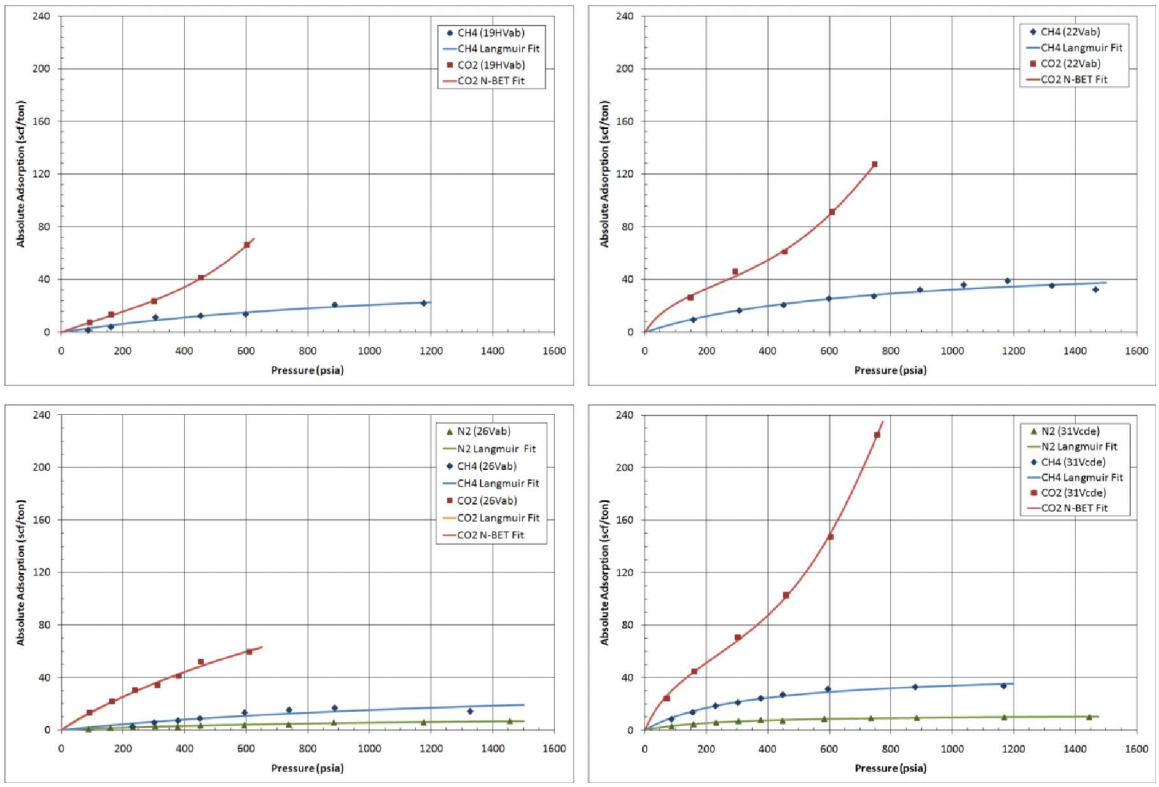

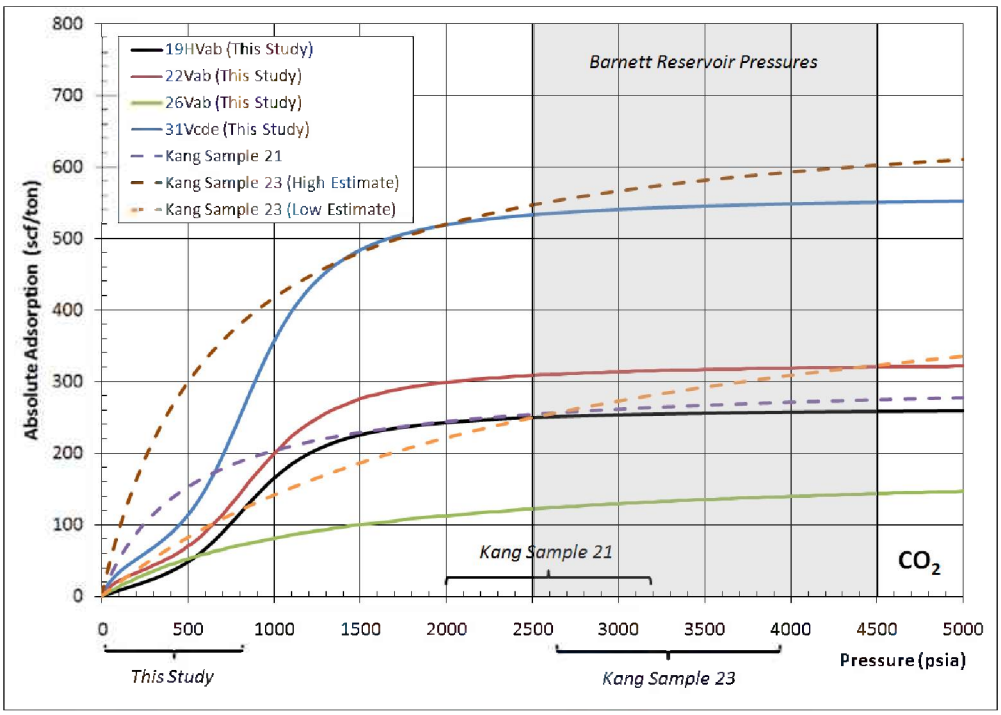

Figure 41. Comparison of CO_2 adsorption results from this study with Barnett shale adsorption results reported in Kang et al. (2010). The ranges on the bottom axis show the spread of actual pressures measured for each tested sample. The extrapolation of our low-pressure results to in situ Barnett pressures lies within the same region as directly measured by Kang et al.

Measuring Adsorption of Methane and CO2 in Organic-Rich Rocks

We measured adsorption on Barnett shale samples. Our adsorption measurements focused on N_2, CH_4, and CO_2 with implications for potential storage of CO_2 and enhanced recovery of CH_4. We successfully measured adsorption on four Barnett shale samples. CH_4 and N_2 demonstrated Langmuir-type adsorption at magnitudes consistent with previous studies of the Barnett shale. Three of our samples demonstrated BET-type adsorption of CO_2 and one demonstrated Langmuir-type adsorption of CO_2, in contrast to all previous studies on CO_2 adsorption in gas shales that have found Langmuir-adsorption. At low pressures (600 psi) we found preferential adsorption of CO_2 over CH_4 ranging from 3.6x to 5.5x. While our measurements were conducted at low pressures (up to 1500 psi), when our model fits are extrapolated to reservoir pressures they suggest similar adsorption magnitudes as have been found in previous studies. At these high reservoir pressures, there is very large preferential adsorption of CO_2 over CH_4 (up to 5-10x) suggesting a significant potential for CO_2 storage in gas shales like the Barnett if practical problems of injectivity and matrix transport can be overcome.

The Barnett shale is a complex rock, making accurate analysis of its geological, geophysical, petrophysical, and transport properties an ongoing challenge. The Barnett shows heterogeneity in composition and structure at all scales, from the basin-scale geology down to the nanometer-scale pore structure. Similarly, the production of natural gas from the Barnett and other gas shales is controlled by phenomena acting at many

different scales, as has been recently reviewed by several authors [Bustin *et al.,* 2008; *Loucks et al.,* 2009; *Sondergeld et al.,* 2010a; *Sondergeld et al.,* 2010b; *Wang and Reed,* 2009].

One important property impacting production in the Barnett is the pressure-dependent adsorption of CH_4, which is controlled by the composition and microstructure of the rock. Gas is stored in the Barnett in both a free phase and a dense adsorbed phase, allowing for much greater total storage of gas than if there was a free phase alone. The amount of adsorption has a major impact on the total gas-in-place in the reservoir and therefore its potential as an economic producer. If preferential adsorption of CO_2 over CH_4 occurs in the Barnett, there may be the potential for enhanced recovery of CH_4 and sequestration of CO_2 in the reservoir, providing increased production of the cleanest fossil fuel and sequestration of the primary greenhouse gas. To investigate these questions, we have conducted adsorption tests on a series of Barnett samples.

Adsorption is the attraction of gas molecules to the surface of a solid, creating a high-density phase that is distinct from the surrounding free gas molecules. Microporous materials commonly exhibit high adsorption potential due to their significant internal surface area. Gas shales are composed of several percent microporous organic kerogen, and thus have been shown to adsorb reservoir gases like CH_4. Due to the high density of the adsorbed phase, adsorption is an important storage mechanism in gas shales.

To quantify the adsorption potential for a material, the amount of adsorption is measured at many different pressures, keeping temperature constant to generate an adsorption isotherm. The generation of CH_4 adsorption isotherms is important for gas-in-place calculations and reservoir modeling, and thus has been assessed previously for gas shales including the Barnett. Lu et al. [1995a; 1995b] found Langmuir-type adsorption of CH_4 for samples from Appalachian Devonian shales and from the Antrim shale. Similarly, for Barnett shale samples, Montgomery et al. (2005) found Langmuir-type adsorption of CH_4.

While CH_4 adsorption has long been seen as important for gas production in unconventional reservoirs, CO_2 adsorption has only recently been studied in the context of enhanced recovery and sequestration. CO_2 adsorption in coal has been studied extensively, with researchers finding significant preferential adsorption of CO_2 over CH_4 and thus the potential for enhanced recovery and sequestration [Kovscek *et al.,* 2005]. To date there have been only two published papers on CO_2 adsorption in gas shales. Nuttall et al. [2005] found Langmuir-like adsorption of CO_2 that was five times greater than the amount of CH_4 adsorption. Kang et al. [2010] studied CO_2 adsorption on two Barnett shale samples, finding five to ten times greater adsorption of CO_2 than CH_4. However, Kang et al. [2010] only took five adsorption measurements per sample, all at high pressures above 2000 psi. They also assumed a priori that there would be Langmuir-like adsorption as part of their experimental method, while other authors have found non-Langmuir adsorption of CO_2 on coal and shale rocks [Busch *et al.,* 2008; *Lin,* 2009]. Thus, to further our understanding of adsorption in the Barnett shale, we have conducted adsorption experiments using N_2, CH_4, and CO_2 on four Barnett shale samples.

The samples we have used are from a Barnett shale well drilled in 2008 and then cored

through the reservoir interval. We evaluated well logs and inspected the core in person to identify locations that were representative of the rock property diversity seen in the core. 1-inch diameter plugs were then drilled from these locations to be used for our adsorption experiments and also complementary mechanical experiments by Stanford colleagues. In the following sections we provide context on the geologic properties of the samples and also discuss the results of a compositional analysis on the sample set.

We analyzed each core plug visually for fractures or heterogeneities, and selected samples to represent different compositions found in the well. The samples were analyzed by ConocoPhillips for mineral composition using standard XRD methods [Warren, 1969]. Pyrolysis and TOC were conducted by Weatherford Laboratories using Rock-Eval methods [K. *E. Peters,* 1986; *K.E. Peters and Cassa,* 1994]. The mineralogical properties of the samples used for laboratory students are presented below in Table 2. All samples show high quartz concentration (43.5-56.7%) as is typical of the productive areas of the Barnett shale. TOC varies from 3.0% to 5.7% in the sample set, while total carbonate content varies from 0.4% to 14.3%. Clay minerals vary from a low of 23.8% to a high of 39.6%. There is minor pyrite in nearly every sample. All samples are in the oil window for maturity based on pyrogram peak temperatures. Kerogen type is between Type III (gas-prone) and Type II-III (oil-gas prone) for all samples except 21Ha, which is closer to Type IV (inert) based on its low hydrogen index and high oxygen index.

Table 2: Adsorption samples mineralogical properties.

	19Hvab	**22Vab**	**26Vab**	**31Vcde**
Depth (ft)	8560.0	8592.0	8628.2	8641.8
Depth (m)	2609.1	2618.9	2629.9	2634.0
Mass (g)	22.6	34.3	31.6	34.6
TOC (%)	3.4	3.6	4.0	5.7
Quartz (%)	49.2	48.8	43.5	48.2
Plagioclase Feldspar (%)	3.7	4.2	5.3	4.3
Calcite (%)	4.2	10.7	11.3	0.3
Dolomite (%)	10.1	1.1	2.3	0.2
Ankerite (%)	0.0	0.8	0.0	0.1
Illite (%)	21.9	19.0	19.3	25.2
Illite/Smectite (%)	6.1	9.3	8.4	13.6
Pyrite (%)	1.3	1.6	2.0	1.8

Apatite (%)	0.0	0.9	4.1	0.5
S1 (mg HC/g rock)	3.3	5.1	6.2	4.2
S2 (mg HC/g rock)	4.1	4.1	4.3	6.9
S3 (mg HC/g rock)	0.3	0.4	0.5	0.6
Tmax (°C)	452.0	450.5	447.0	452.3
HI (mg HC/g TOC)	119.5	112.3	109.0	119.8
OI (mg CO_2/g TOC)	10.5	11.2	12.0	9.8

To carry out these experiments we have specially modified an NER Autolab 2000 tri-axial press to measure adsorption at a range of confining and pore pressures. While this machine is typically used for rock mechanics experiments, we have found the confining pressure control and precise tracking of deformation to be beneficial in investigating the mechanical effects of adsorption on the sample. We use a Quizix QX-1500 to control and precisely record gas pressures. Valves are used to deliver gas from a known upstream

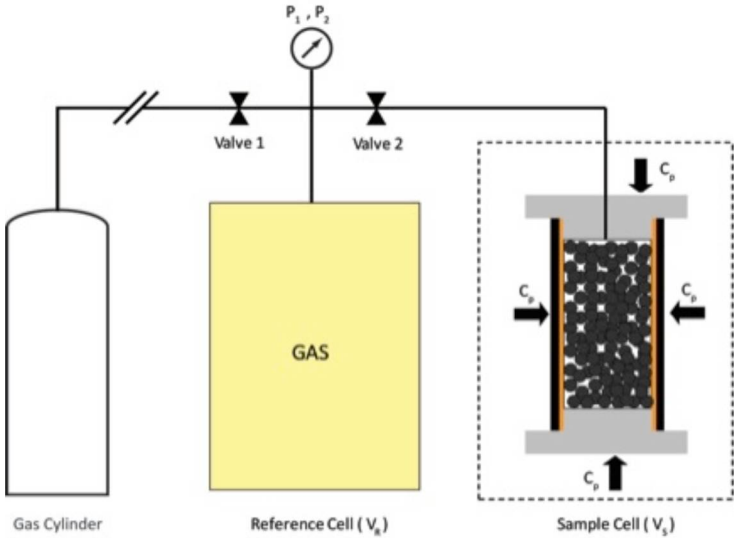

Figure 42: Schematic of system used for adsorption experiments. For the reference cell (VR), one cylinder the Quizix pump is used. The sample cell (VS) is shown on the right, encased by a copper and viton jacket to isolate the sample and pore fluid from the confining fluid. Pressure is measured by a digital transducer within the Quizix pump. Gas temperature is measured close to where the gas lines enter the tri-axial press.

reference volume to the downstream sample volume. A simplified schematic of the

reference and sample volumes is shown in Figure 4. We have measured gas leakage rates at a range of pressures in this system and corrected our adsorption calculations for this loss. We also record the temperature in the gas lines for use in equation of state calculations.

We performed our adsorption experiments on crushed, dried Barnett shale samples. As is common in adsorption experiments, the samples were crushed to speed up adsorption equilibrium and dried to remove the effect of open storage conditions. After crushing the sample to between 100 and 250 microns, it was dried under vacuum at 105°C for at least three days, or until the weight of the sample stabilized. Approximately 30g of the crushed sample were placed into a 1-inch diameter copper jacket that had been soldered into a cylinder and placed on top of a stainless steel coreholder. Copper was used as the material next to the sample to prevent CO_2 interaction with an outer, heat-shrinkable viton jacket. Fine mesh screens were placed between the core holders and the sample to ensure that no particles were lost into the pore lines. After loading the second core holder on top of the sample, the viton was shrunk with a heat gun and o-rings and hose clamps were used to seal the jacket against grooves in the core holder. After loading the sample into the tri-axial system, the confining pressure was cycled up and down to 30 MPa until the sample exhibited only elastic deformation. A new viton jacket was then shrunk around the compressed sample. After loading the system again, the sample was placed under vacuum to remove water and gas that may have contaminated the sample during the final preparation.

The first step in the adsorption test was to measure the pore volume of the sample. The calibrated upstream reference cell, with volume V_R, was filled with He (a non-adsorbing gas) at a given pressure. After waiting for equilibrium pressure, P_1, valve 2 was opened and the pressure dropped and stabilized at a lower pressure, P_2 . The volume of the downstream sample cell V_S, which includes both the sample pore volume and the volume in the lines and core holders, was calculated as follows:

$$n_{total} = \frac{P_1 V_R}{Z_1 R T_1}$$

$$V_S = \frac{n Z_2 R T_2}{P_2} - V_R$$

where n is the total number of moles of H_e, Z is the compressibility factor, R is the universal gas constant, and Z is the temperature.

Having previously measured the volume in the pore lines and the core holders, the pore volume itself could be backed out. This process of gas expansion was repeated until a curve of pore volume vs. pressure was generated for the entire pressure range to be measured for adsorption. While the difference in the confining pressure and the pore pressure was held constant at 3 MPa throughout all experiments, the pore volume changes as pressure increases because the Biot coefficient for the compacted sample is less than 1. Ross and Bustin [2007] have found a pressure-dependent increase in pore

volume in gas shales due to what they argue is increased access to low aperture pores at higher pressures. With these two impacts potentially counteracting each other, it is important to directly measure pore volume at all pressures. We also corrected the helium-based pore volumes for additional changes in sample volume as measured by our mechanical sensors. We adjusted the pore volume vs. curve with the differences in sample volume measured at a gas pressure with helium and the sample volume measured at the same pressure with a deforming gas. These deformations can be caused by additional permanent plastic strain of the compacted sample, swelling during gas adsorption, or temperature variations within the pressure vessel. In our experiments these corrections never exceeded 2% of the pore volume as measured with helium, and were generally well under 1%, indicating that the sample did not significantly deform during the tests.

Having measured the sample pore volume, it is possible to measure the amount of adsorption by expanding a known quantity of gas into the sample chamber and calculating the expected pressure, P_{exp} (if there were no adsorption) with the measured pressure, P_{meas} . If adsorption occurs, P_{meas} will be less than P_{exp} due to the high-density of the adsorbed phase. The amount of adsorption, n_{ads} is calculated as follows:

$$n_{ads}^{excess} = n_{total} - n_{unads}$$

$$n_{ads} = n_{exp} - \rho(P_{meas}, T_{meas})(V_R + V_S)$$

where n_{exp} is the known quantity of gas first measured in the reference cell, n_{meas} is the calculated quantity of gas using P_{meas} , and ρ is the molar density of the gas at pressure P_{meas} and temperature T_{meas}.

The procedure above will calculate the excess, apparent adsorption. To calculate the absolute amount of adsorption, $n_{ads,absolute}$, we correct for the effect of the adsorbed phase reducing the available free pore space:

$$n_{ads}^{absolute} = \frac{n_{ads}^{excess}}{1 - \frac{\rho_{gas}}{\rho_{ads}}}$$

where $n_{ads,apparent}$ is the apparent adsorption, ρ_{ads} is the density of the adsorbed phase, and ρ_{gas} is the density of the free gas phase. To estimate the density of the adsorbed phase, we use the hard sphere term, b , in the Redlich-Kwong-Soave equation of state, which is equivalent to the density at the critical temperature and pressure.

All molar densities were calculated using NIST's REFPROP program [NIST, 2007], which includes tables of the most accurate equations of state available for each of the gases used. After calculating the adsorption at the first pressure, the same procedure is repeated at a higher pressure each time, thus generating an entire adsorption isotherm. We have measured adsorption isotherms on multiple samples using N_2, CH_4, and CO_2, the most relevant gases for the issues of production performance, enhanced recovery, and

greenhouse gas sequestration. We have measured adsorption on four Barnett samples: 19HV ab, 22V ab, 26V ab, and 31Vcde. Adsorption of CH_4, CO_2, and N_2 were measured on samples 26Vab and 31Vcde, while only CH_4 and CO_2 were measured on 19HVab and 22Vab. Fitted adsorption parameters are shown below in Table 3. Plots of measured absolute adsorption and model fits are shown below in Figures 4a-d.

Table 3: Adsorption results.

	19HVab	**22Vab**	**26Vab**	**31Vcde (adjusted)**
Nitrogen				
PL (psia)	-	-	1087	244
VL (scf/ton)			11.8	12.0
Methane				
PL (psia)	1281	702	1596	335
VL (scf/ton)	47.4	55.0	39.2	45.4
Carbon Dioxide				
PL (psia)	-	-	1254	-
VL (scf/ton)	-	-	183.6	-
Vm (scf/ton)	27.9	35.3	37.5	55.5
C	2.7	10.1	4.0	9.0
N	9.5	9.3	3.4	10.2

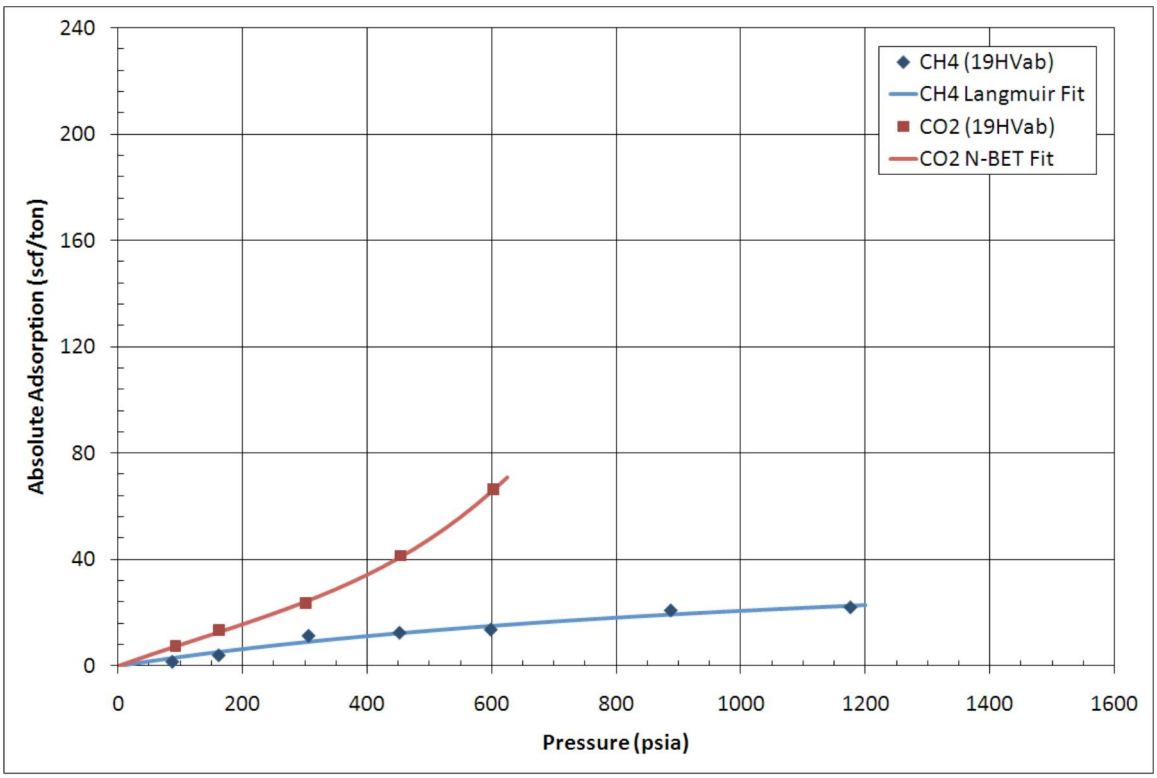

Figure 43a: Absolute adsorption of CH4, and CO2 for sample 19HVab. Measured data shown as points; fitted models shown as lines.

Figure 43b: Absolute adsorption of CH4, and CO2 for sample 22Vab.

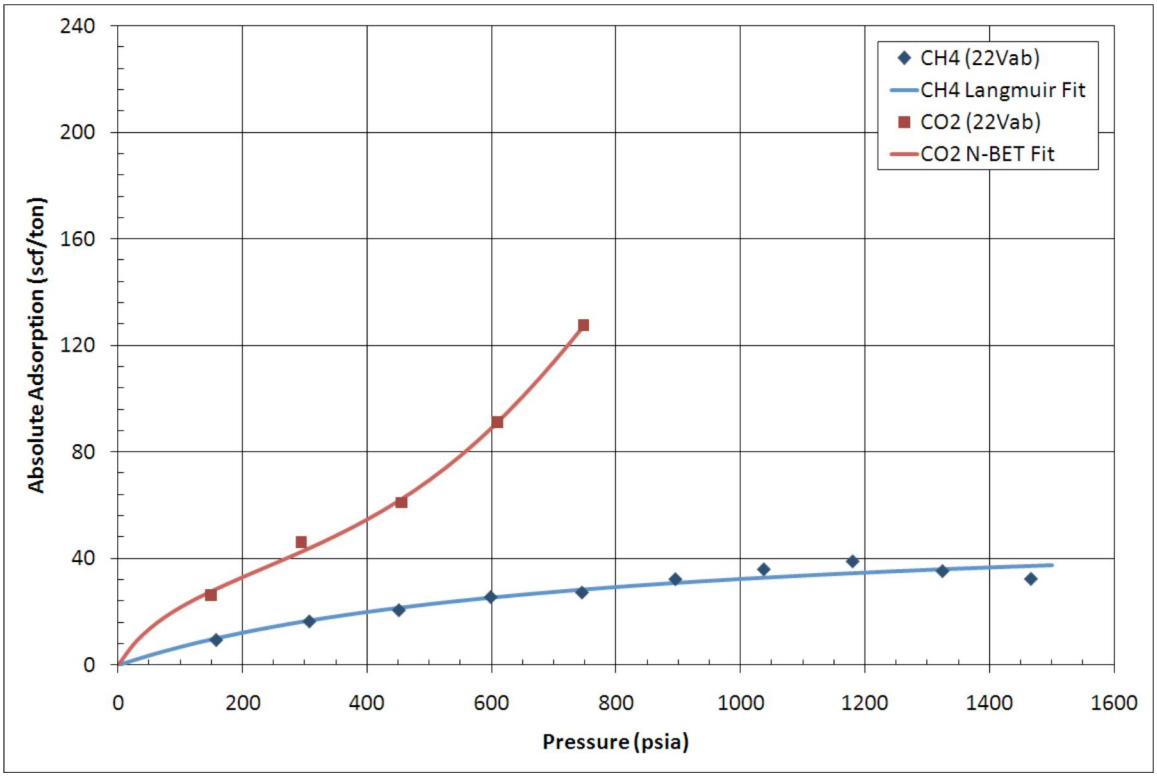

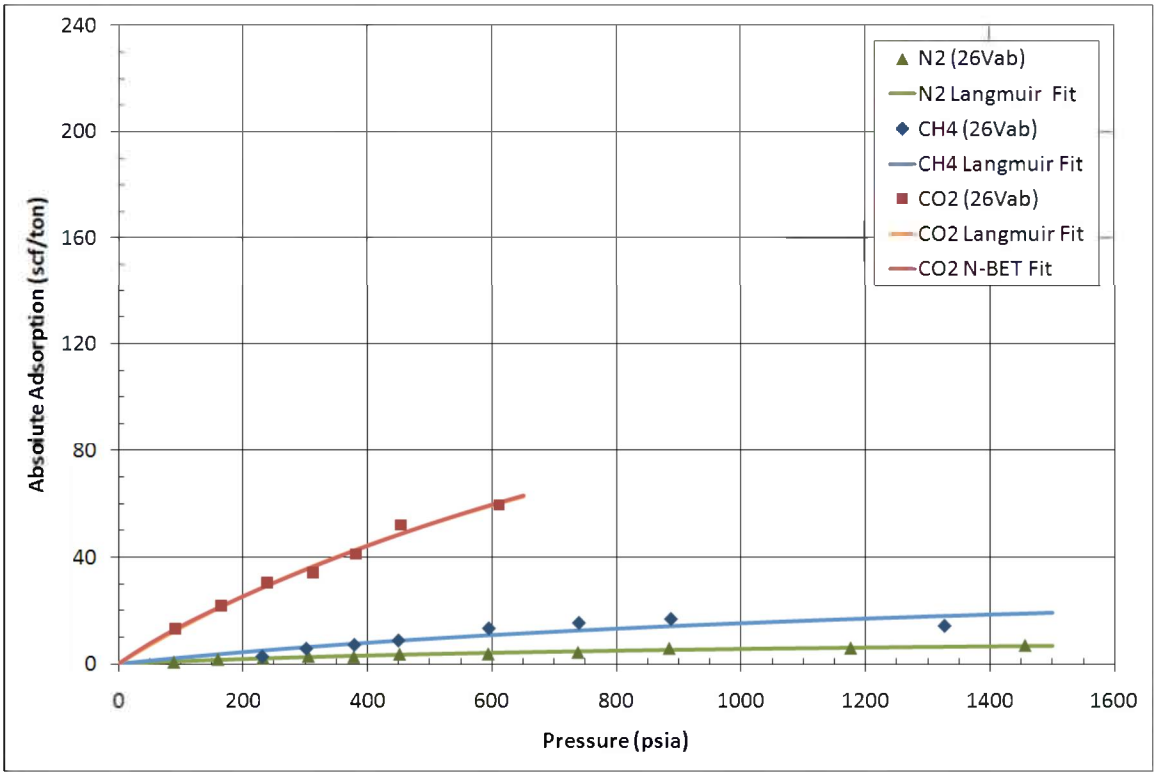

Figure 43c: Absolute adsorption of N2, CH4, and CO2 for sample 26Vab.

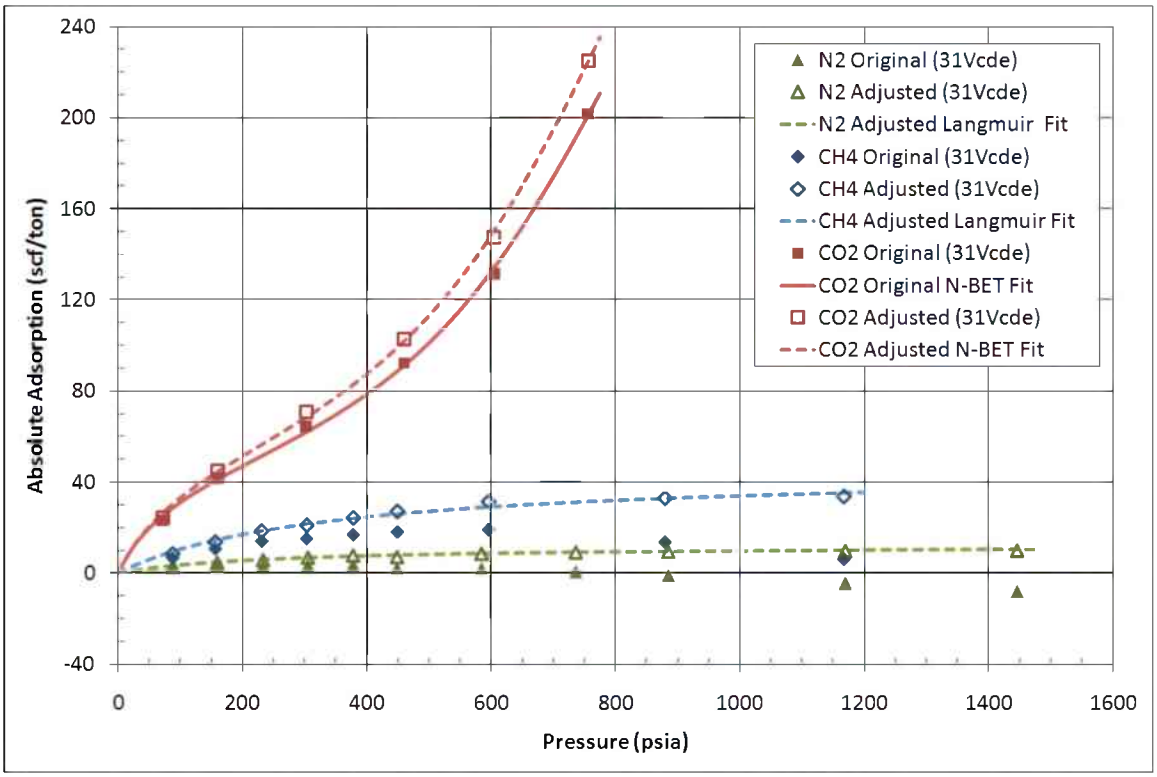

Figure 44d: Absolute adsorption of N2, CH4, and CO2 for sample 31Vcde. Measured data shown as solid points; data adjusted with pore volume correction shown as hollow points. Fitted models of the adjusted data shown in dashed lines.

Sample 19HVab

As seen in Figure 4a, we were able to successfully measure adsorption of both CH_4 and CO_2 on sample 19HVab. The sample demonstrated Langmuir-type adsorption of CH_4 and BET-type adsorption of CO_2, which we fit to an N-BET model. At 600 psi, 4.8x more CO_2 was adsorbed than methane.

Sample 22 Vab

Sample 22Vab is shown in Figure 44b. It too exhibited Langmuir-type adsorption of CH_4 and BET-type adsorption of CO_2. However, the total magnitude of adsorption was greater than for sample 19HVab. At 600 psi, sample 22Vab adsorbed 1.9x more CH_4 than sample 19HVab and 1.4x more CO2 than sample 19HVab. However, at this pressure sample 22Vab adsorbed only 3.6x more CH_4 than CO_2, demonstrating less preferential adsorption of CO_2 than for sample 19HVab.

Sample 26Vab

We measured N_2, CH_4, and CO_2 adsorption on sample 26Vab. Adsorption of N_2 was of fairly weak Langmuir-type, less than 4 scf/ton at 600 psi. In contrast to samples 19HVab and 22Vab, CO_2 demonstrated Langmuir-type adsorption over the measured pressure ranges. At 600 psi, sample 26Vab adsorbed 5.5x more CO_2 than CH_4, the largest difference in preferential adsorption of the four tested samples.

Sample 31Vcde

We calculated negative amounts of CH_4 and N_2 adsorption when using the original helium-derived pore volumes for Sample 31Vcde. Negative adsorption calculation has no physical meaning, so we spent significant time processing and analyzing the data from this sample to ensure that there were no measurement errors or sample volume changes during the test. Unable to create realistic adsorption curves despite this careful review, we sought explanations from the literature as to why apparent negative adsorption could occur. Ross and Bustin [2007] also found apparent negative adsorption. They suggested could be the results of "molecular sieving", where the pore space is not equally accessible to all molecules, in particular to CO_2 and CH_4 which have a larger molecular diameter than He. Kang et al. [2010] also report a possibly similar effect in a Barnett shale sample.

In the molecular sieving model, the pore volume that is available to He can be much larger than the pore volume accessible to an adsorbing gas. When using He-derived values of pore volume, adsorption will be cumulatively underestimated, especially if at high pressures He gains significant access to pore spaces that aren't accessible to an adsorbing gas. At a given pressure the pore volume available to an adsorbing gas like CH_4 would be lower than was available to He during calibration. Thus, the measured pore pressure of CH_4 after reaching equilibrium would be higher than expected, leading to a lower estimate of adsorbed gas, and perhaps even negative.

Ross and Bustin [2007] suggested that the pore volume estimate for the adsorbing gas tests could be adjusted until the measured adsorption reaches an expected shape, such as

a Langmuir-type isotherm. Following this suggestion, we have adjusted the estimated pore volumes until reaching Langmuir-type isotherms. Figure 44d shows both the original data for sample 31vcde as well as the corrected data points and curve fits. For the N_2 experiment, the pore volume estimate for the sample was reduced by 5.7%. For the CH_4 and CO_2 experiments, the pore estimate was reduced by 9.3%. As seen in Figure 44d, these corrections create Langmuir-type results for the N_2 and CH_4 experiments, as well increase the total adsorption quantity for the CO2 experiment. After the adjustments, sample 31Vcde shows greater N_2, CH_4, and CO_2 adsorption than any other sample. At 600 psi, 4.7x more CO_2 adsorbs than CH_4. Given the speculative nature of these corrections, the quantitative adsorption results for sample 31Vcde are accordingly more uncertain than for the other samples.

Our measured adsorption capacities varied by as much as 50% among the four samples. It is likely that composition was the major controlling factor on these differences. Sample 31Vcde had the highest amount of TOC (5.7%) of any tested sample and also the largest measured adsorption capacity. As discussed above, this sample may also have exhibited "molecular sieving" of the different gases, perhaps caused by the pore size distribution in this high TOC sample.

If the extrapolations of our adsorption measurements are correct, we've demonstrated significant preferential adsorption of CO_2 over CH_4 at reservoir pressures. For example, at 4000 psi, sample 19HVab would show 7.1x preferential adsorption of CO_2, sample 22Vab would show 6.8x preferential adsorption, sample 26Vab would show 5.0x preferential adsorption, and sample 31vcde would show 13.1x preferential adsorption. With Kang et al. [2010] showing similar 5-10x preferential adsorption of CO_2, (Figure 5) there is likely very significant capacity for CO_2 storage in the Barnett shale. With these promising adsorption capacity results, further work on the practical feasibility of CO_2 injection and storage in the Barnett is necessary. Additional confirmation adsorption experiments are needed to determine if reservoir temperatures will significantly decrease the amount of adsorption or if water in situ moisture inhibits or enhances the amount of adsorption. Important questions, such as the permeability of CO_2 in the Barnett and the time scale over which adsorption of CO_2 and replacement of CH_4 occurs, will need to be answered before the potential of the Barnett as a carbon storage reservoir is proven.

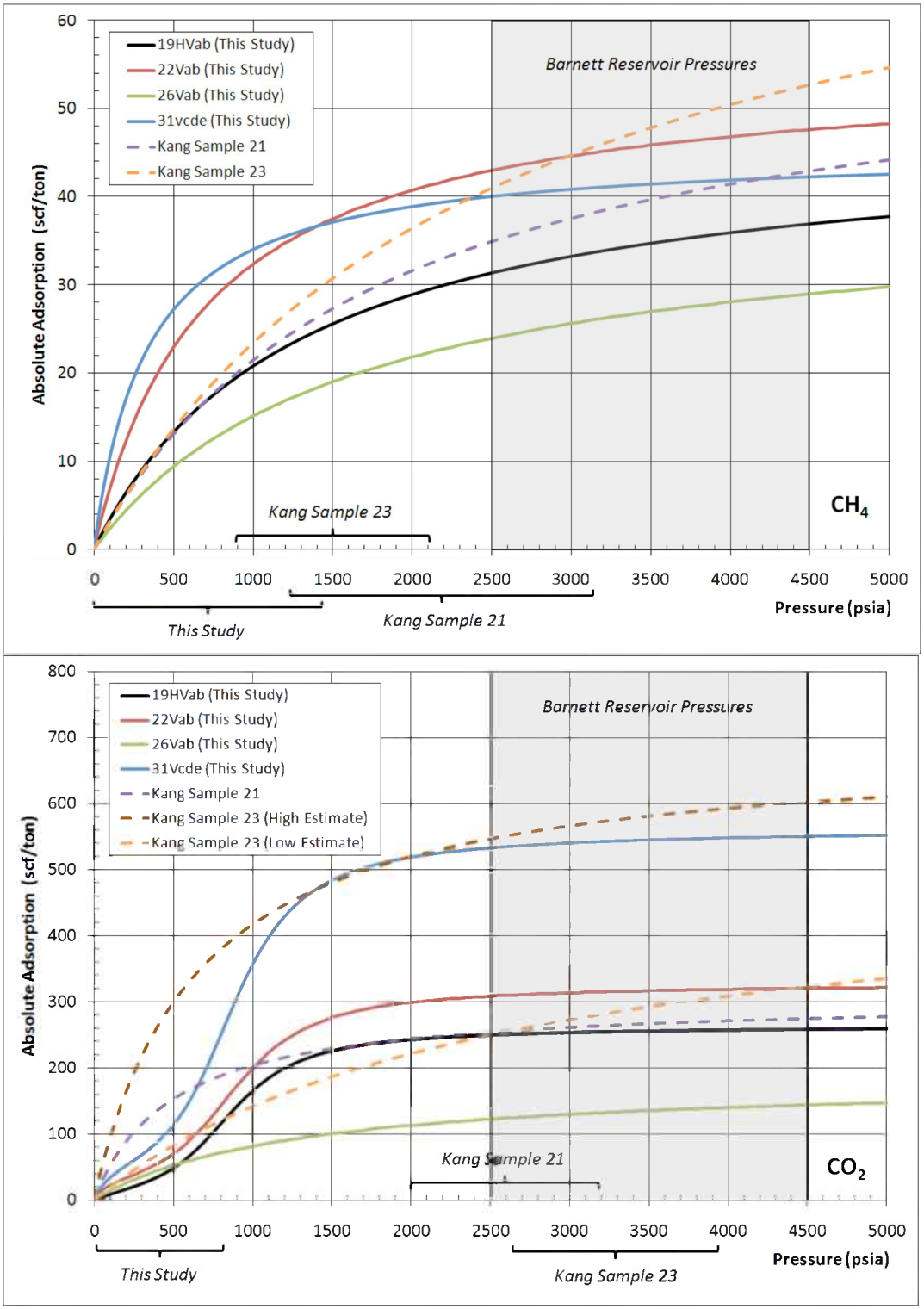

Figure 45: Comparison of adsorption results from this study with Barnett shale adsorption results reported in Kang et al. [2010]. The ranges on the bottom axis show the spread of actual pressures measured for each tested sample. The extrapolation of our low-pressure results to in situ Barnett pressures lies within the same region as directly measured by Kang et al. for both CH_4 (top) and CO_2 (bottom).

CO_2 Adsorption Isotherms of Gas Shales at Subsurface T and P Conditions

The adsorption of CO_2 on a gas shale sample has been measured under subsurface temperature and pressure (pore pressure only, neglecting confinement) conditions, using a Rubotherm microbalance (Fig. 46) recently made available in the Wilcox lab. The heart of a Rubotherm instrument is a magnetic suspension balance that can measure weight with an absolute accuracy of 0.01 mg. A heat jacket is used to keep the balance at constant temperature. Compared to a conventional balance, the Rubotherm provides an enclosed system, causing no air flow inside, thus maintaining a constant pressure and temperature to a very accurate level.

The steps to calculating the CO_2 equilibrium loading in shale sample are as follows:

First, we evacuate the magnetic suspension balance and measure the weight of the metallic component, including the basket of the balance, which will hold our sample in the next measurement.

$$M_0^1 = m_{metal} \quad (1)$$

Then, after shale sample is placed in the basket, the balance is evacuated again and the weight $\square_0$ is measured.

$$M_0 = m_{metal} + m_{shale} \quad (2)$$

Thus the weight of the shale sample can be calculated as

$$m_{shale} = M_0 - M_0^1 \quad (3)$$

Then the system is filled with He and the volume of the metallic component and the shale sample can be calculated from the measured weight M_1, assuming He is not adsorbing onto the shale sample.

$$M_1 = M_0 - r_{He} V_0 \quad (4)$$

Where V_0 is the volume of the metallic component and the shale sample, ρ_{He} is the density of He at the experimental pressure and temperature. By plotting ρ_{He} vs. $\square_1$, the slope, V_0 may be obtained.

Finally, the system is filled with the adsorbing gas after evacuating again. The excess gas adsorption can be calculated at the desired pressure and temperature by:

$$m_{CO2}^{adsorbed} = M_p - M_0 + r_{CO2}^{bulk} V_0 \quad (5)$$

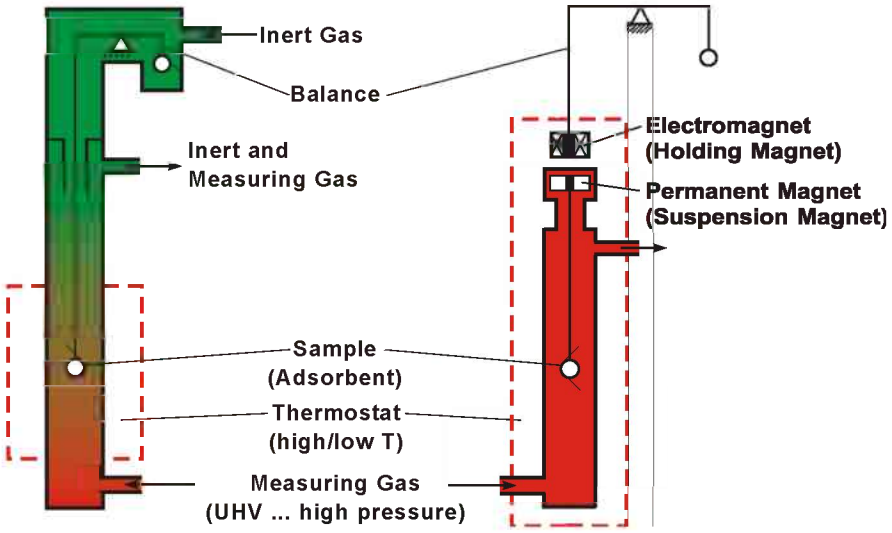

Figure 46: Rubotherm (left) compared to a conventional magnetic suspension balance (right).

Where $m_{CO2}^{adsorbed}$ is the amount of adsorbed CO_2, □□ is the measured weight at the desired pressure and temperature, ρ_{CO2}^{bulk} is the CO_2 density at the experimental conditions. Here we make the assumption that the density of adsorbed CO_2 is much larger than that of CO_2 in the bulk phase.

The excess CO_2 adsorption isotherm for the Eagle Ford 174HA shale sample has been carried out in this study. The measurement was carried out on a particle chip. We set the temperature to 125°C, which is indicative of the subsurface temperature for the shale sample under realistic conditions, and measured adsorption under a series of pressure conditions as shown in Figure 47.

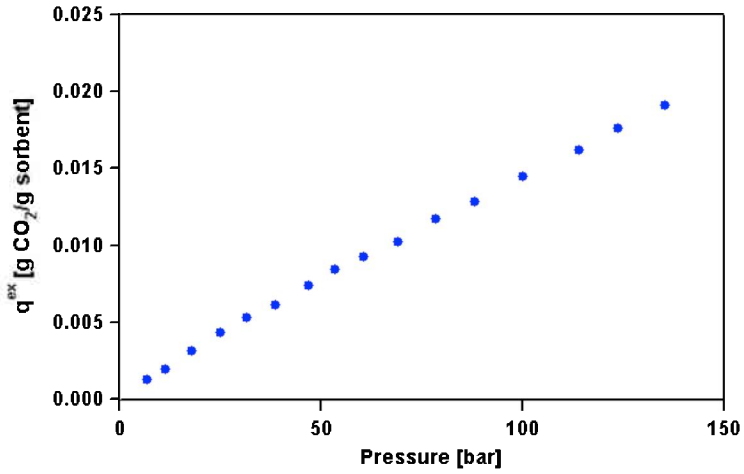

Figure 47: CO_2 adsorption isotherm on particle shale sample Eagle Ford 174HA at 125°C

Following the experiment on the shale chip, we crushed the sample into a powder and repeated the procedure to determine if the pore structure was compromised upon pulverizing. The temperature was set to 125°C and the adsorption was measured again at

a series of pressures as shown in the isotherm plotted in Figure 48. A comparison of Figures 47 and 48 show that crushing the sample indeed leads to increased adsorption, which is consistent with the low-pressure measurements using the Autosorb instrument that was used for PSD analysis. Crushing the shale sample likely enhances the connectivity of the sample on the macroscale allowing more of the pore space/volume to be accessed by the adsorbing gas.

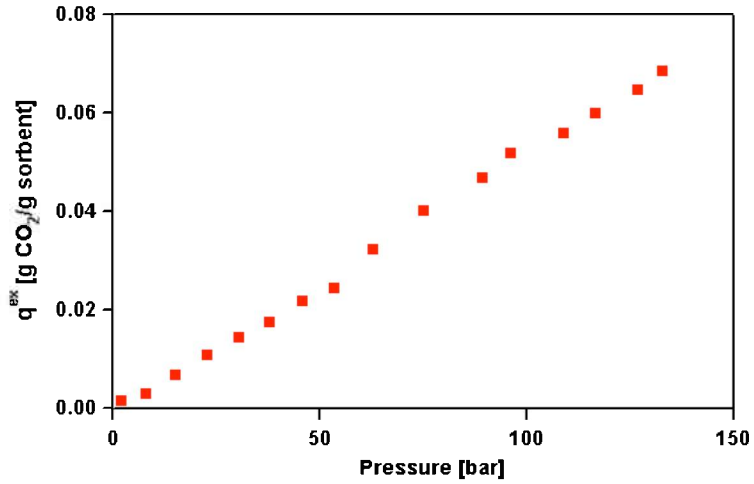

Figure 48: CO_2 adsorption isotherm on powder shale sample Eagle Ford 174HA at 125°C

To compare directly the CO_2 adsorption on the shale particle vs. the powder sample, we plotted both isotherms as shown in Figure 49.

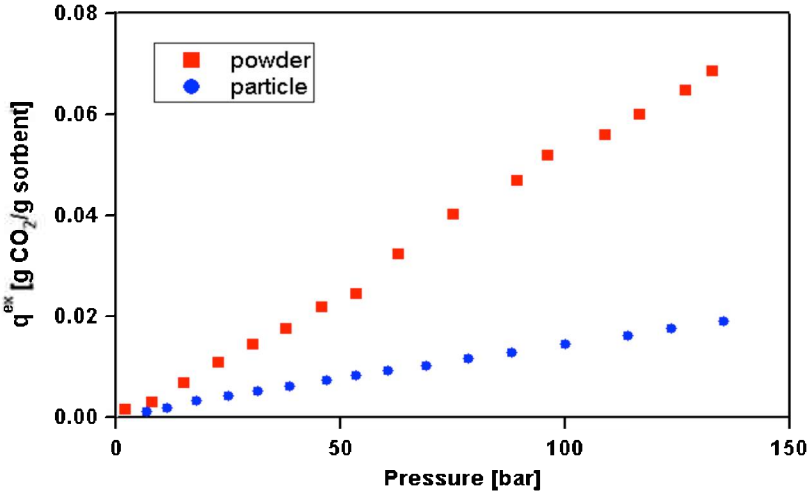

Figure 49: CO_2 adsorption isotherm on powder and particle shale sample Eagle Ford 174HA at 125°C

It is important to note that the isotherms measured as described thus far are not typical Langmuir isotherms. We hypothesized that if we could carry our experiments to higher pressures, i.e., greater than 150 bar, that we would begin to see the adsorption plateau and begin to look Langmuir-like. To test this hypothesis, rather than going to higher pressures we decided to investigate CO_2 adsorption at lower temperature, i.e., 50 °C as shown in Figure 50.

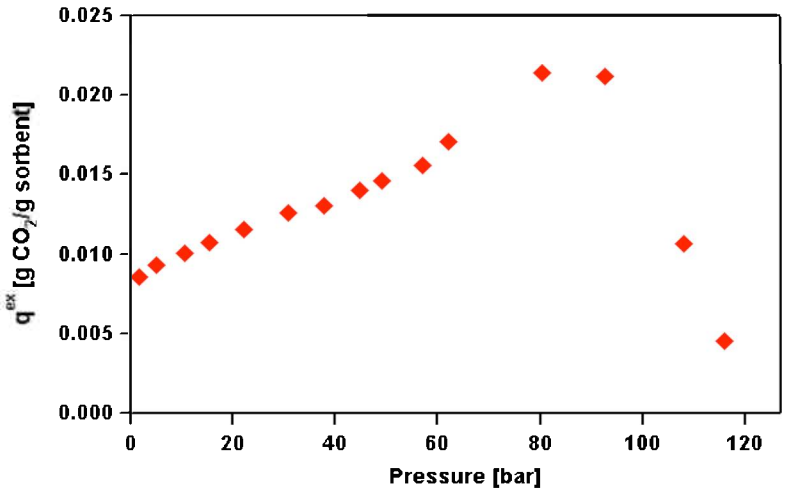

Figure 50: CO_2 adsorption isotherm on powder shale sample Eagle Ford 174HA at 50°C

At the lower temperature, the characteristic excess adsorption plot can be observed. The plot obtained previously is actually only the linear part of the extended isotherm. Hence, at the high temperature, the experiment requires very high pressure for the curvature to be exhibited.

The adsorption of CO_2 on gas shale sample from the Barnett Formation under subsurface temperature and pressure (pore pressure only, neglecting confinement) conditions has been conducted, using a Rubotherm Magnetic Suspension Balance. The sample is originally from a formation with a depth of 8611.85 ft corresponding to a temperature of approximately 80 °C. Thus, the CO_2 adsorption isotherm at 80 °C has been performed and is shown in Figure 51. The measurement was carried out on a particle chip shale sample of proximately 2 cm^3. The sample is regenerated under vacuum at 120 °C before measuring the CO_2 adsorption isotherm.

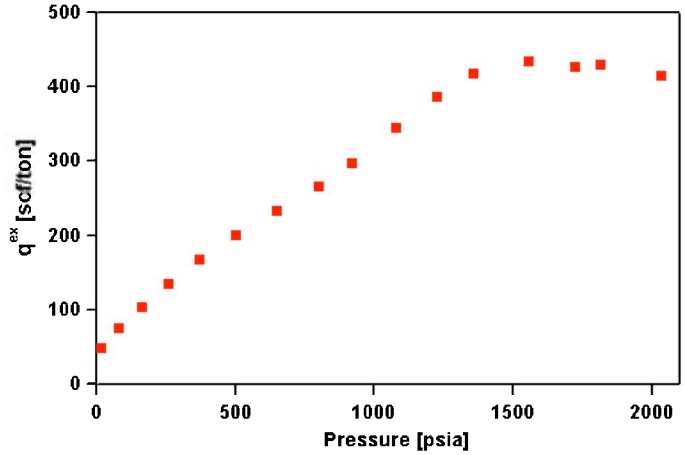

Figure 51: CO_2 adsorption isotherm on Barnett shale sample at 80°C

Compared to Figure 72 (Section 3.2), the shale sample shows significant larger adsorption capacity of CO_2 over CH_4.

Since kerogen and clay are the major parts that contribute to the adsorption behavior in gas shale, adsorption isotherm measurements for carbon-based and clay-based model materials are underway. XRD results of the Barnett sample indicate that it has the composition as shown in Table 4.

Table 4: XRD, Pyrolysis Compositional Data of Barnett shale sample (wt%)

Quartz	*Feldspar*	*Calcite*	*Pyrite*	*Clay*	*TOC*	*Other*
38.00	2.80	2.20	1.80	39.00	16.00	0.20

To investigate the relative roles that each of these kerogen and clay materials play in determining the adsorption mechanism and subsequent capacity estimates, we first analyzed the pore size distribution (PSD) of kerogen and clay using the Quantachrome instrument with N_2 as probe gas. The results were analyzed using non-localized density functional theory (NLDFT) and more information of PSD analysis on shale can be found in Section 2.1: "Pore Size Distribution using N_2 and Ar as Probe Gases using Low-Pressure Adsorption." The kerogen has been isolated from the same Barnett shale sample by the National Petrographic Service, Inc. (NPS), and the model clay sample investigated is illite originally separated from the Green shale formation. The results are presented in Figures 52 and 53, in which the kerogen shows a wider pore size distribution within the mesopore range, while the clay shows three main peaks at 1.9nm, 4.2nm and 7.5nm. Results also indicate that kerogen has a pore volume of 0.068 cc/g, larger than pore volume of clay, which is 0.020 cc/g.

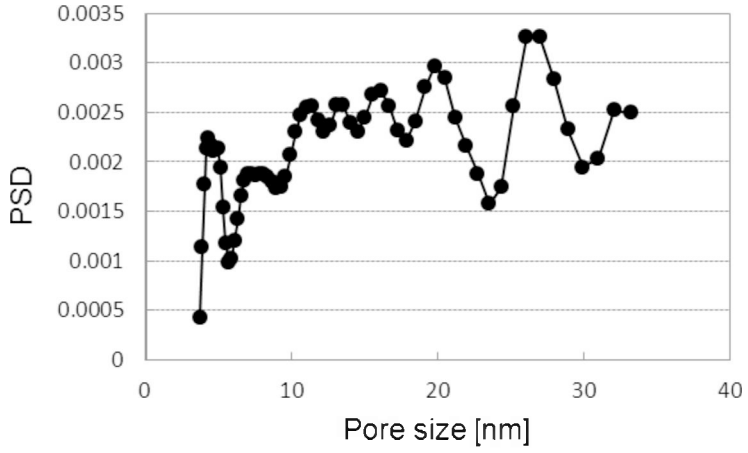

Figure 52. Pore size distribution of kerogen

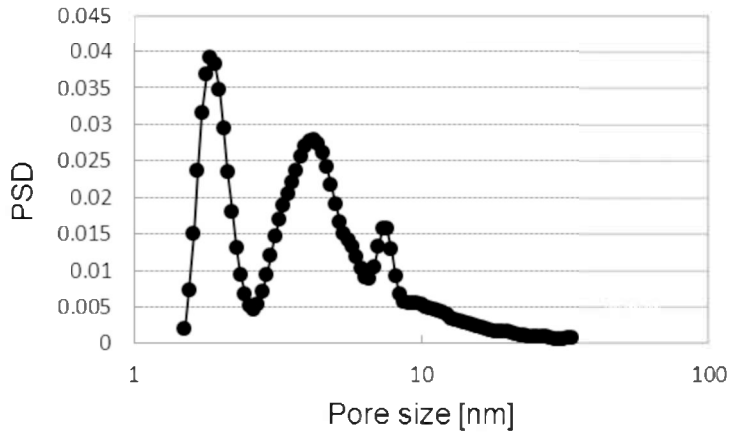

Figure 53: Pore size distribution of clay(illite)

More characterization and isotherm measurements will be performed, including pore size distribution of shale, as well as gas capacity measurement of kerogen and clay systems, to fully understand the mechanism of adsorption in gas shales and how the composition in the shale system contributes to the overall gas capacity and adsorption mechanism.

To investigate the relative roles that kerogen and clay play in determining the adsorption mechanism and subsequent capacity estimates, we first analyzed their pore size distributions (PSD) using the Autosorb Quantachrome instrument with N_2 as a probe gas. The results were analyzed using non-localized density functional theory (NLDFT). The kerogen was isolated from a Barnett shale sample by the National Petrographic Service, Inc. (NPS), and the model clay sample investigated is illite originally separated from the Green shale formation. The results are presented in Figure 54, in which the kerogen shows a wider pore size distribution within the mesopore range, while the clay shows three main peaks at 1.9nm, 4.2nm and 7.5nm, and shale sample shows its peaks at 5nm, 7.5nm and up to 20nm. Results also indicate that the shale has a pore volume of 0.058 cc/g, smaller than kerogen's pore volume of 0.068 cc/g, but larger than pore volume of the clay, which is 0.020 cc/g.

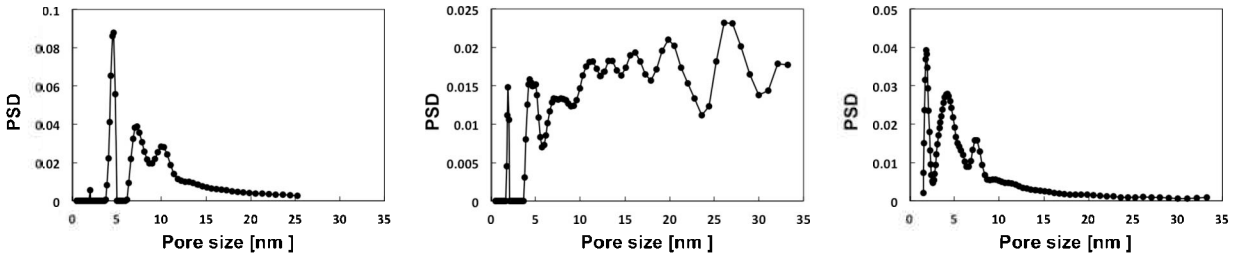

Figure 54: Pore size distribution of shale (left), kerogen (middle) and clay (right).

SEM analysis of the Barnett sample, isolated kerogen and clay have been carried out and are shown in Figure 55.

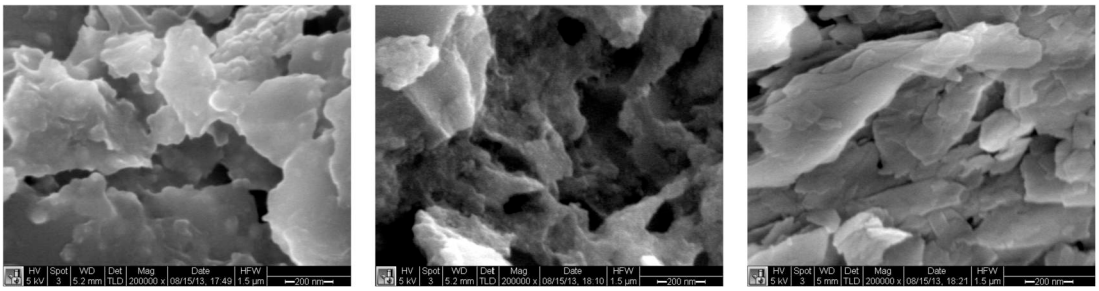

Figure 55: SEM image of shale (left), kerogen (middle) and clay (right).

Friction Experiments on Shale Gas Rocks

The inherent low permeability of shale gas reservoirs necessitates enhancement by hydraulic fracturing and stimulation of existing faults through fluid pressurization in order to achieve gas production. Hydraulic stimulation of these faults lowers the effective normal stress on the fault planes, inducing microseismic events around the hydraulic fracturing stages, which enhance permeability through shear slip and result in damage processes in the surrounding rock. These microearthquakes have magnitudes generally less than -1.5 and require seismometer arrays in wells adjacent to the hydraulic fracturing stages in order detect and locate the events. Recent hydraulic fracturing operations and accompanying seismic studies in the Barnett Shale, TX show microseismic events clustered within 1000 feet of each corresponding stage, which define a stimulated reservoir volume (SRV) around the stage. In addition to these microseismic events that resemble the form of tectonic microearthquakes, recent analysis of the waveform dataset reveals longer period, longer duration, stable slip events, indicating that hydraulic stimulation of existing faults in the reservoir can induce distinct slip behaviors (*Das and Zoback*, 2011). These long period long duration (LPLD) events are not necessarily correlated with pumping history, and in some cases actually contain small microseismic events, implying a related mechanism to transient fluid pressurization.

Understanding the conditions responsible for induced seismic and stable slip events during stimulation stages requires the development of frictional stability criteria for shale gas reservoir rocks. Previous fault mechanics studies examining frictional stability have focused on clay-rich gouges, which are hypothesized to control the transition from seismic to stable slip in the Earth through changes in mechanical and hydrologic properties with depth (*Bird*, 1984; *Saffer and Marone*, 2003). The results of these studies are particularly relevant to the frictional behavior of shale gas reservoir rocks due to their significant clay content and the transient hydrologic conditions experienced in reservoir stimulation. Initial laboratory studies have characterized the basic frictional strength of clay-rich gouges and demonstrate significant weakness relative to Byerlee's Law (*Byerlee*, 1978) in samples with clay contents as low as 15% (*Shimamoto and Logan*, 1981). More detailed studies vary clay mineralogy in order to correlate the conditions for transformation of 'swelling' to 'non-swelling' clays in the Earth with the transition from unstable to stable slip behavior, but find that the combined effects of stress state, water

content, and mineralogy are significantly more complex than the transition between clay types (*Saffer and Marone*, 2003; *Ikari et al.*, 2007, 2008).

The schematic drawing in the upper part of Figure 56 illustrates stable sliding – as sliding velocity increases, friction evolves to a level higher than the initial value (a-b > 0). The schematic drawing in the upper right shows unstable sliding – when the sliding velocity increases, friction evolves to a level lower than the initial value (a-b< 0), allowing slip to accelerate. The experiments carried out to date show that as clay content increases, the coefficient of friction reduces from ~0.6 (a typical value for most rock) to about 0.35. At the same time the parameter a-b is less than 0 for low clay fractions (indicating that the faults slide unstably) to values greater than 0 for high clay (indicating stable sliding). This indicates that fault slip as clay content in the shale increases, faulting becomes easier, but it is more likely for the sliding to be aseismic. Thus, the occurrence of micro earthquakes during hydraulic fracturing may be limited to portions of the shale with relatively low clay.

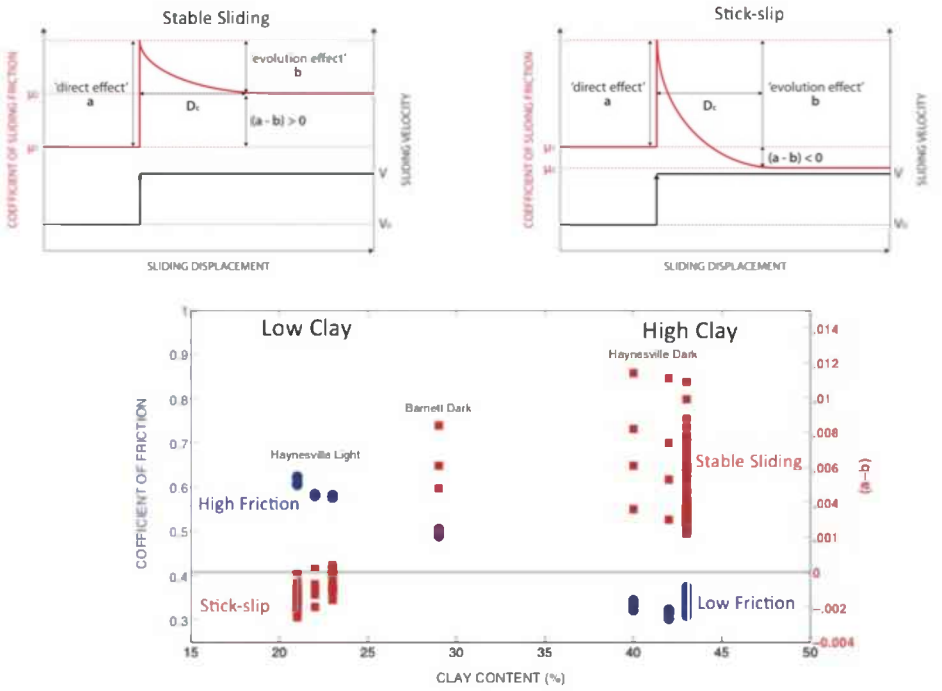

Figure 56. Schematics illustrating velocity strengthening behavior where the parameter a-b >0 (upper left) and velocity weakening behavior where a-b < 0 (upper right). Our rate and state measurements show that as clay content in shales increase, there is a monotonic decrease in frictional strength and a transition from unstable sliding to stables sliding.

Although many of these studies assess the frictional stability of clay-rich rocks under quite specific conditions, no systematic investigations under the conditions relevant to reservoir stimulation have yet been presented. In addition, most existing studies consider only a small range of the parameter space, and do not employ the most recent rate and state friction models, which are able to reproduce more complex frictional responses such

as tectonic tremor and slow slip (*Liu and Rice*, 2006; *Shibazaki and Shimamoto*, 2007; *Rubin*, 2008; *Segall et al.*, 2010). These models of slip behavior are particularly relevant to the frictional response of shale gas reservoir rocks, because reservoir stimulation produces similar dynamic fluid pressurization changes that are invoked to explain stable slip in tectonic settings. The role of these changes in producing conditions for stable frictional responses in the Earth is yet to be determined; however, the results of rate and state friction modeling and seismic studies suggests that the dynamic interactions of frictional response and pore pressure must be responsible (*Beroza et al.*, 2009).

Application of Rate and State Constitutive Law

In order to understand the observed slip behaviors during hydraulic fracturing operations in shales, a frictional constitutive law over the conditions of the reservoir is necessary. The Dietrich-Ruina rate and state (RS) constitutive laws (*Ruina*, 1983) have shown strong agreement with the results of laboratory rock friction studies on simulated fault gouge (*Segall and Rice*, 1995, 2006), motivating the use of inverse modeling of experimental friction data to determine the parameters of the model (*Reinen and Weeks*, 1993, *Blanpied et al.*, 1998). In addition, RS constitutive laws represent the foundation of recent representations of frictional stability criteria, which account for the effects of both mechanical and hydrologic behavior (*Segall et al.*, 2010). The single-state variable form of the Dietrich-Ruina constitutive model is as follows:

$$\mu(V, \theta) = \mu_0 + a\ln(V/V_0) + b\ln(V_0\theta) \tag{6}$$

$$d\theta/dt = (1 - V\theta/D_c) \tag{7}$$

$$(a - b) = \Delta\mu_{ss}/\ln(V/V_0) \tag{8}$$

in which μ_0 is the initial coefficient of friction, $\Delta\mu_{ss}$ is the change in the steady state coefficient of friction, a and b are material parameters representing the frictional evolution over a velocity step, V is the sliding velocity, V_0 is the initial sliding velocity, and θ is the state variable, which is sometimes represented as the average sliding contact lifetime at steady state. These changes are modeled to occur over a slip evolution displacement D_c, which represents the slip distance required to reach a new frictional steady state. In this formulation, the friction parameter $(a-b)$ is diagnostic of frictional evolution over a step-wise change in sliding velocity, with $(a-b) > 0$ describing a velocity-strengthening or stable response and $(a-b) < 0$ describing a velocity-weakening or potentially unstable response. In addition to the effect of frictional evolution, the slip behavior will be dependent on the effects of fluid pressure changes in the slipping zone. These effects have been quantified in the previous experimental studies (*Saffer and Marone*, 2003; *Ikari et al.*, 2008) by the dilatancy parameter, α, which describes the resultant change in fault normal displacement, Δw, to a change in slip rate.

$$\alpha = \Delta w/\ln(V/V_0) \tag{9}$$

Recent work in modeling the transition between different slip regimes attempts to integrate the effects of dilatancy and frictional weakening, combining poroelasticity, RS

friction, and a dilatancy law incorporating α, so that both the frictional coefficient and the porosity evolve to steady-state values in a displacement, D_c (*Segall et al.*, 2010). Linearized stability analysis of these relations reveals the relevant nondimensional parameter to frictional stability, ε, which defines the boundary between slip regimes by comparing the relative importance of dilatancy (which scales by $\mu_0 \alpha K$) to frictional weakening (which scales by $b\sigma_n$).

$$\varepsilon = \mu_0 \alpha K / b\sigma_n \tag{10}$$

Here, σ_n represents the effective normal stress and K is the combined bulk modulus of the fluid and the pore space. For this form of the constitutive relations, *Segall et al.*, determine the boundaries of unstable and stable slip behavior, based on the relative importance of dilatant strengthening to frictional weakening. For $\varepsilon < 1$- *(a-b)*, slip accelerates to instability for sufficiently large faults; for $\varepsilon > 1 - (a-b)$, slip speeds remain stable and quasi-static. No current studies have applied this dilatant strengthening model to laboratory frictional stability analysis, although many previous studies have employed only *(a-b)* as a proxy for frictional stability; however, given the wide observations of stable slip events in regions with high interpreted pore pressures, mostly notably in the SRV of shale gas reservoirs, the application of a coupled mechanical and hydrologic framework to slip behavior appears pertinent.

Methodology of Friction Experiments

Friction experiments were performed in an NER Autolab 2000 Triaxial press on two 1 X 2 inch core samples from the Haynesville Shale reservoir as part of a complete methodology to measure static moduli, as well as intact and frictional strength. The Haynesville Light sample is more calcareous, less clay rich, and less porous than the Haynesville Dark sample; the mineral compositions of each are given in Table 5. An example of the experimental procedure is represented in Figure 57, showing how axial load and confining pressure were maintained over time. Axial load is increased while confining pressure is held constant at 20 MPa from the beginning of the experiment until the strength of the rock is reached and failure occurs, at which point the sample is unloaded. The sample is then reloaded until the frictional strength is reached, at which point the axial ram is servo-controlled by displacement rate to perform the velocity-stepping friction test. The geometry of the frictional sliding test is represented schematically in Figure 58; σ_a and σ_c are the axial and confining pressures respectively, w and L are the dimensions of the sample, θ is angle of the laboratory fault plane to the horizontal, and σ_n and τ are fault normal and shear stress. Sliding velocities ranging 0.1 – 100 μm/s were implemented in approximately even displacement increments up to 5 mm, which represents the maximum allowed sliding displacement in this experimental geometry due to the presence of a Viton sample jacket around the core. After each experiment was completed, the two halves of the laboratory fault were separated and ~ 1 mm pieces were removed from the sliding surface in a manner that did not disturb the surface itself. These pieces were filed flat from below and mounted on aluminum sample post with colloidal silver adhesive as preparation for scanning electron microscopy (SEM). Imaging of these samples was conducted in an FEI XL30 SEM with a field emission gun source.

Table 5: Mineral composition data [%] for Haynesville Shale samples

Sample	QFM	Carbonate	Clay	Other	Porosity
Haynesville Light	28	48	22	2	5.3-5.7
Haynesville Dark	45	13	39	3	9.1-9.4

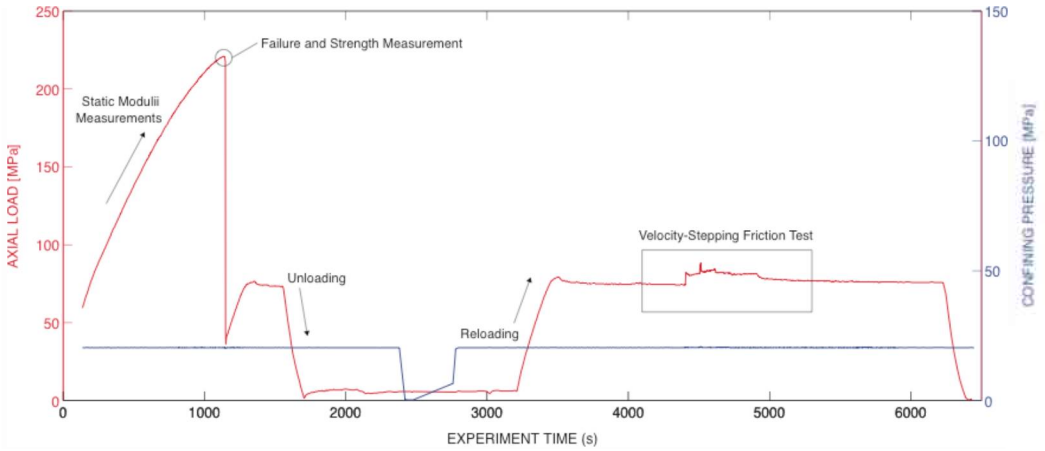

Figure 57. Experimental procedure for measuring static moduli, frictional and intact rock strength in the triaxial apparatus geometry. The velocity-stepping portion of the test is highlighted above in the black bounding box.

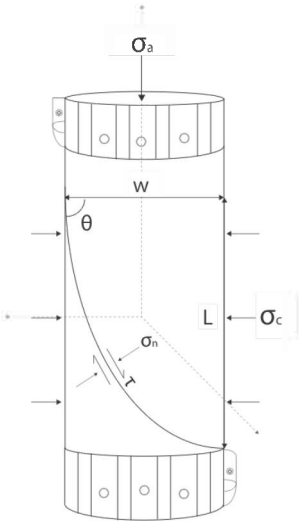

Figure 58. Experimental set-up and sliding geometry for triaxial apparatus faults.

The results of the two velocity-stepping friction tests performed on the Haynesville Shale samples are shown in Figure 59; in each figure, the coefficient of sliding friction is plotted in red and the sliding velocity in m/s is plotted in black. The dotted lines denote

implemented velocity steps with the corresponding sliding velocities are listed above in μm/s. Figure 59a shows the test performed on the Haynesville Light sample; the initial coefficient of sliding friction is ~0.75 along the laboratory generated failure plane at a sliding velocity of 0.5 μm/s. In the first velocity up-step to 5 μm/s, frictional resistance rises sharply from 0.74 to 0.76 and then decays over less than 0.2 mm of slip to 0.75. Slight strengthening is observed over the rest of the 5 μm/s increment. Sliding velocity is subsequently stepped to 50 μm/s, causing another increase in frictional resistance, which continues to a value of 0.81 over the interval relatively constant velocity. Sliding velocity is then dropped back to 0.5 μm/s in two steps, causing corresponding drops in frictional resistance, but slight strengthening at 5 μm/s constant velocity. Friction returns to the starting value of 0.75 at 0.5 μm/s at the end of the test.

Figure 59b shows the test performed on the Haynesville Dark sample; the initial friction strength is ~0.82 at sliding velocity of 1.0 μm/s. In the first velocity up-step to 10 μm/s, frictional resistance to rises sharply to 0.84 and then decays to 0.83 over less than 0.05 mm of slip, but subsequently strengthens back to a frictional coefficient of 0.84 in 0.1 mm of slip at constant velocity. With increasing slip at 10 μm/s, significant weakening is observed to a frictional coefficient of 0.78 until sliding velocity is stepped to 100 μm/s, at which point a direct strengthening response is observed. The friction coefficient rises immediately to 0.81 at this velocity step, with no subsequent evolution or decay. Slight weakening is again observed over the remainder of the constant velocity segment. Sliding velocity is subsequently dropped back to 10 μm/s, causing an instantaneous decrease in frictional resistance, again with no evolution behavior, and significant weakening over the constant velocity segment at 10 μm/s. Sliding velocity is then dropped back to 1.0 μm/s, causing a similar decrease in frictional resistance accompanied by the consistently observed weakening effect at constant sliding velocity. At the end of the test, sliding velocity is stepped back up to 10 μm/s, and friction increases from 0.7 to 0.72 instantaneously, with a slight decay in 0.1 mm of slip, and minor weakening to a final friction coefficient of 0.7.

Figure 60 shows a mid-range magnification view of a piece of Haynesville Light sample from off the fault surface to establish a basis for which to compare the morphologies of the fault sliding surface. The sample has been coarsely surface ground and has distributed, ~ 10 μm patches between the flats from which material has been removed by the grinding process. Figure 61 shows a series of images at increasing magnification of the experimental fault 'footwall' sliding surface from the velocity-stepping friction experiment on the Haynesville Light sample (see Figure 59a); the sample is oriented such that the slip direction is N-S in these views. Figures 62a – c highlight the significant production of comminuted clay gouge, which is evident from comparing the morphology of the fault surface to the unslid piece imaged in Figure 60. Figures 61d, e reveal more details of the structure of the produced gouge, illustrating its platy or flake-like appearance and ~ 1 μm average size for individual gouge aggregates. Figure 61e gives a perspective cross section on a stacked configuration of these gouge aggregates showing increased comminution between the aggregates below the surface layer of gouge. Figure 61f shows a high magnification view through the surface gouge layer revealing the some

of the internal rock structure, which seems to be comprised of stacked, sheet-like aggregates of clay.

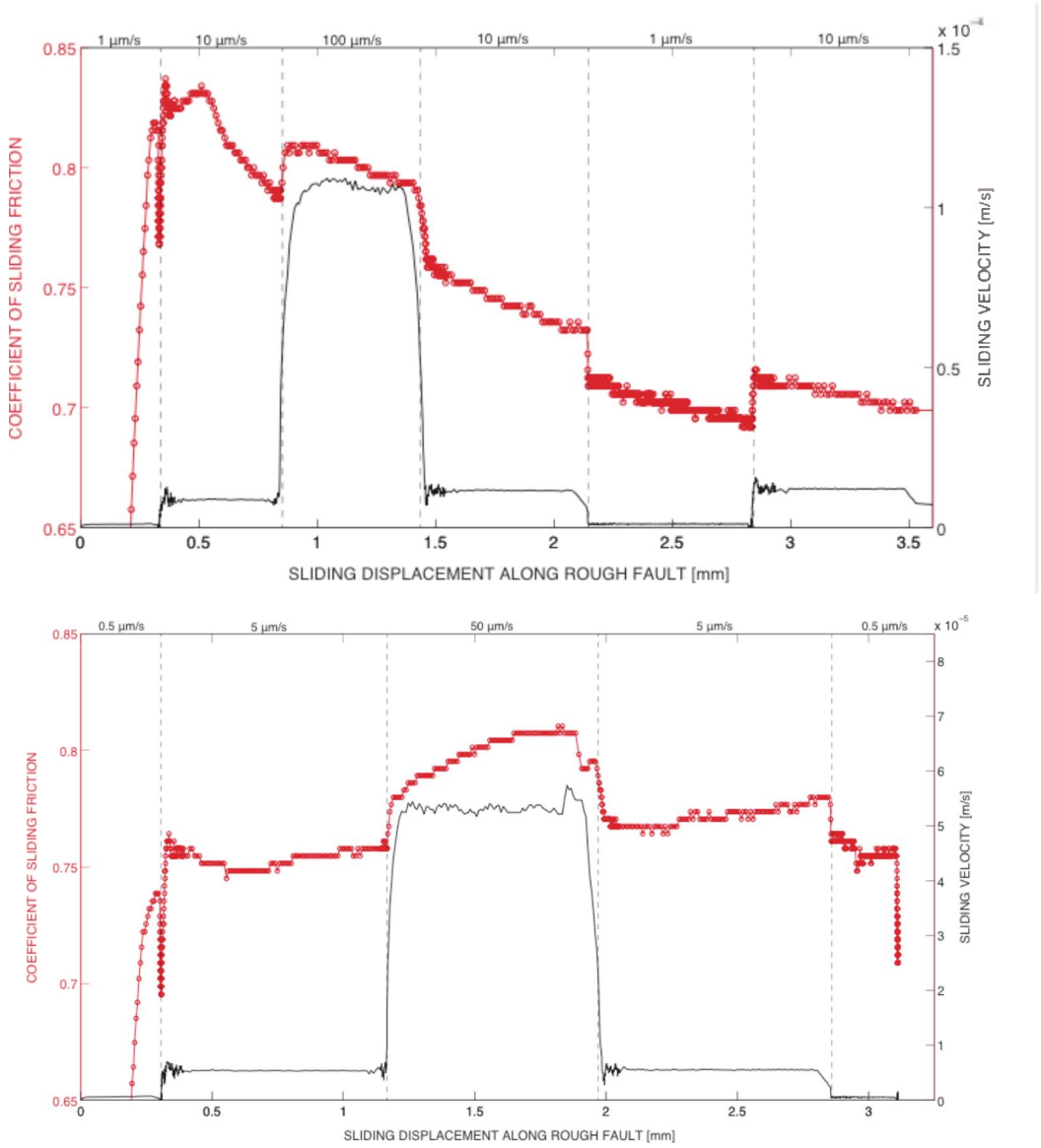

Figure 59. (a) Velocity-stepping friction test on Haynesville Light shale sample; sliding velocities range from 0.5 – 50 µm/s. (b) Velocity-stepping friction test on Haynesville Dark shale sample; sliding velocities range from 1.0 – 100 µm/s.

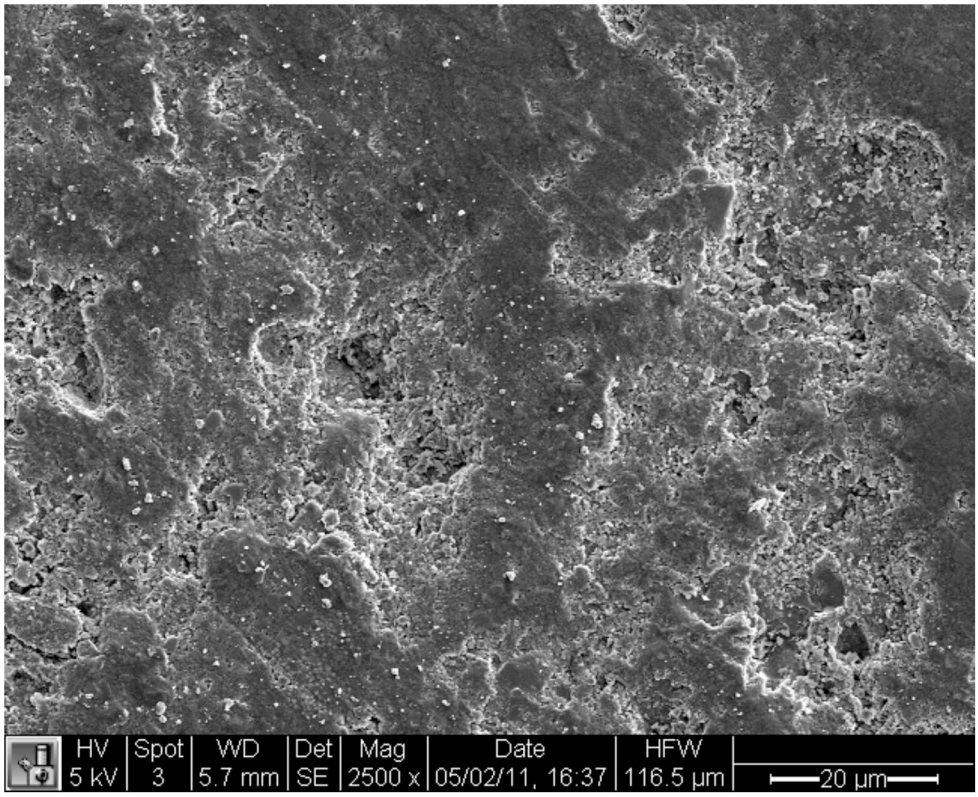

Figure 60. Secondary electron image of Haynesville light from the unslid part of the tested core at 2500X magnification.

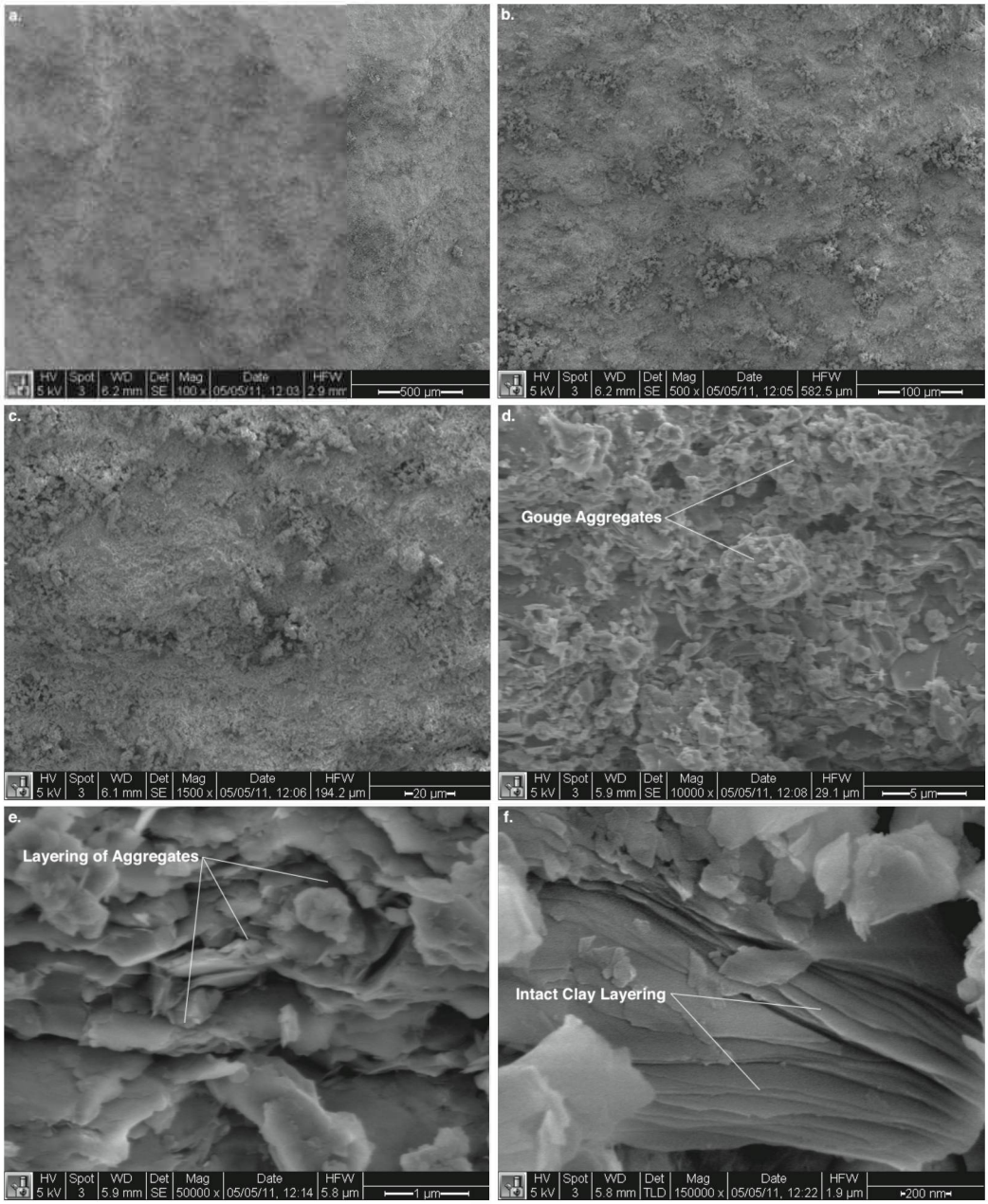

Figure 61. (a) Lowest magnification overview of sample sliding surface. (b) Lower magnification view of the dispersed gouge aggregates on the sliding surface of the experimental 'footwall'. (c) Low magnification view of platy gouge aggregates. (d) High magnification view of gouge aggregates. (e) Higher magnification view of gouge aggregates, showing internal structure and layer. (f) High magnification view of the intact rock beneath the accumulation of clay gouge.

Figure 62 shows another series from the same sample; Figure 62a shows a low magnification view of a horseshoe-shaped ridge in the upper half of the image, which is 'down-step' feature on the fault sliding surface consistent with slip on the 'footwall' and N-S oriented slip. Down the slip direction from this feature is a significant accumulation of aggregated clay gouge, indicating that the feature experienced significant slip and wear during the experiment. Figure 62b displays a closer view of this feature, revealing

consistent linear topographic features in the direction of slip with produced gouge to the side of the 'tracks'. A higher magnification view of these features is shown in Figure 62c, illustrating a pattern of microfractures below in the intact surface and confirming slickensides to be in the direction of slip. Figure 62d gives an even closer view of this bare surface, which displays similar 'down-step' features on to the macroscopic surface (Figure 62a), which trend along the direction of slip that have an approximate wavelength of 1 μm.

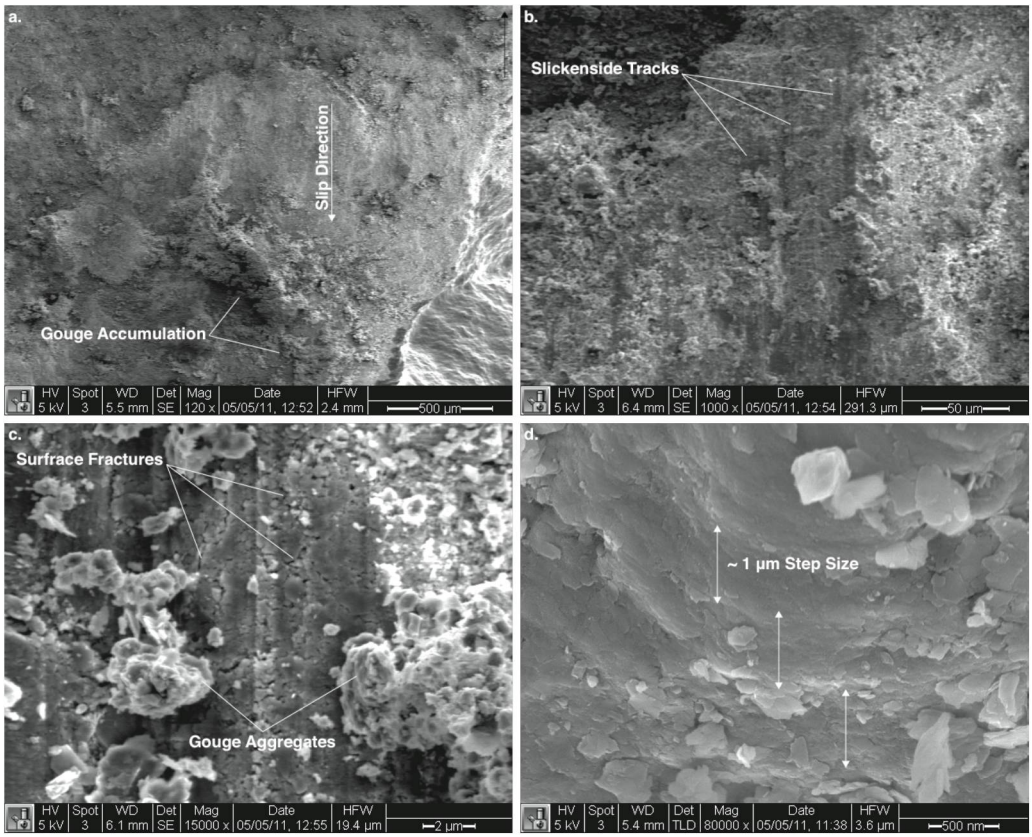

Figure 62. (a) Low magnification view of horseshoe-shaped, 'down step' feature with significant gouge accumulation adjacent. The white arrow shows the relative slip direction and the black arrow in the corner denotes the actual direction of motion for the footwall block. (b) Higher magnification view of the 'down-step' feature, showing slickensides in the direction of slip. (c) Higher magnification view of the slickensides with accompanying gouge aggregates to the sides of the track. (d) Highest magnification view of the slickenside track. Similar 'down-step' features to the macroscopic ones on the sample surface can be seen and step size can be estimate as ~ 1 μm.

Discussion of Friction Experiments

The results of the two velocity-stepping friction tests on Haynesville Shale are generally consistent with previous measurements of frictional strength on samples from the same reservoir (*Sone and Zoback*, 2010), showing frictional coefficients ~0.7-0.8. Both samples show strongly velocity-strengthening frictional behavior over the range of sliding velocities tested. The velocity-strengthening response of these samples also shows little to no evolution for most velocity steps; however, a resolvable decay in the

instantaneous strengthening response is evident in the first velocity steps of both tests. In addition to the responses to changes in sliding velocity, significant frictional evolution is observed during the constant velocity segments of both tests. In the Haynesville Light test, slight strengthening is observed during the constant velocity segments and is more pronounced for the largest sliding velocities. In the Haynesville Dark test, a more complex response occurs in the first constant velocity segment at 10 μm/s. Apparent strengthening after the velocity step effects proceeds for 0.1 mm, at which point sudden weakening occurs, dropping the friction coefficient by 0.05 in 0.25 mm of slip. Throughout the rest of the test, friction continues to drop slowly during the constant velocity segments, seemingly at constant rate, independent of the magnitude of the sliding velocity in this range.

SEM imaging of the experimental sliding surface from the Haynesville Light reveals significant heterogeneity and complexity in post-experiment microstructures. Comparison of the slid and unslid surfaces in the same sample (Figures 60, 61b) highlight the production of comminuted clay gouge, which is dispersed throughout the sliding surface, but also localized around slip-indicating microstructural features such as slickensides (Figure 62). Higher magnification views of gouge accumulations show the development of an internal structure, defined by ~ 1 μm stacked, platy aggregates of clay particles (Figure 61e), suggesting that the wear and comminution processes may play a significant role in the evolution of sliding surface strength.

Although these observations suggest that shales are capable of complex frictional behavior even under relatively simple experimental conditions, the results of these preliminary velocity-stepping experiments cannot be directly interpreted in terms of rate and state friction models due to the roughness of the laboratory generated fault planes. Examination of the faulted cores after each friction experiments reveals wavelengths of macroscopic roughness on the order of the sample dimension, which would most likely contribute to the frictional resistance in a manner localized to various points on the slipping surface, and therefore not resolvable in the experimental data. Due to these unquantifiable effects on the frictional behavior in the case of a rough sliding plane, RS constitutive parameters cannot be determined from friction or dilatancy data from these initial experiments. Previous laboratory experiments that invoke RS constitutive laws to describe observations of velocity-stepping friction employ 'straight' laboratory fault configurations and detrend friction data to exclude the effects of any evolution behavior at constant sliding velocities (e.g. *Saffer and Marone*, 2003; *Ikari et al.*, 2007, 2008; *Noda and Shimamoto*, 2009). These analyses are practiced in order to produce more robust results when inverting for the parameters of the RS constitutive model: a, b, and D_c. Although we do not invert for these parameters for the two experiments presented here, the form of frictional evolution over the velocity steps can be described by a RS model to show an example of how similar data can be analyzed in future trials with pre-fabricated, 'straight' slip planes. Figure 63 illustrates this application in the case of a velocity step of 0.5 – 5 μm/s from the Haynesville Light experiment.

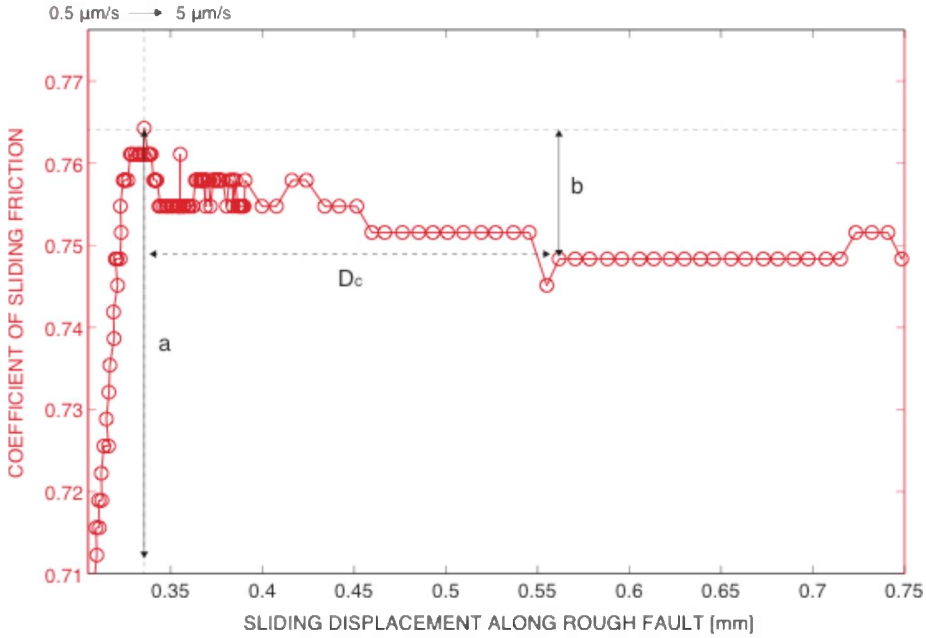

Figure 63. Zoom-in view of the first velocity up-step from the test on the Haynesville Light sample. The rate and state constitutive parameters are illustrated schematically for this example in order to show what must be determined in an RS inversion.

Outstanding Questions - Future studies will need to connect laboratory friction behaviors over a range of experimental conditions to the processes of unstable and stable slip observed in shale gas reservoir stimulation stages through rate and state constitutive laws and to examine the friction behavior of these shales with CO_2 as a pore fluid.

In order to contextualize these experiments to hydraulic stimulation in shale gas reservoirs, pore fluids will be introduced into the sample in a 'drained' configuration, so changes in permeability and fluid pressure dilatancy can be measured and related to the micromechanical details of slip processes. For the triaxial apparatus geometry, application of the RS constitute model requires determining the stiffness of the apparatus, so that the elastic interactions of machine-rock system can be accounted for. The apparatus stiffness can be determined experimentally by conducting stick-slip experiments to examine that critical stiffness required for the rock sample to unload faster than the apparatus, which can be related to the machine stiffness by the Dietrich-Ruina constitutive model (*Ruina*, 1983). This is important for evaluating friction data using the RS formulation because constraining this parameter has been shown to be very significant in the results of model inversions for the RS parameters (*Noda and Shimamoto*, 2009). Also, future friction experiments will need to employ pre-fabricated or saw-cut cores that are pre-positioned in the sample jacket such that frictional sliding may occur on a 'straight' surface (with and without CO_2). This will eliminate significant uncertainty in distinguishing changes in frictional behavior with changes in the slip geometry along a rough fault plane, allowing for measurement of sliding surface dilatancy, application of the RS framework and possibly decreased effects of frictional evolution at constant sliding velocity. In addition, although detrending evolution

behaviors during the constant velocity segments of the velocity-stepping experiments is necessary to find RS parameters, future work will be needed to attempt to understand these effects through constant sliding velocity

Effect of Shear Deformation on Fracture Permeability in Shales

The experimental study discussed in this section will examine the effect of shear deformation on fracture permeability in intact shales with varying clay contents, under varying stress conditions, and in the presence of different gases. Experiments will be needed to be carried out for three different types of samples: 1) shale cores with saw cuts; 2) shale cores naturally broken along fractures; and 3) shale wafers between aluminum forcing blocks. Fracture permeability will be measured after individual shear deformation increments using steady state Darcy flow. The nature of the fault damage zones is controlled by two processes governed by grain size and composition that strongly influence fracture permeability: 1) formation of fault smear, a relatively impermeable membrane seal where clay particles preferentially align with the shear direction; and 2) formation of a relatively permeable fault gouge where grains and grain fragments are plucked off the sliding surfaces and crushed.

We hypothesize that during stable sliding in high clay samples, fracture permeability will decrease with increasing shear deformation due to the formation of a fault smear, whereas during unstable, stick-slip sliding in samples with low clay content, fracture permeability will first decrease followed by an increase due to the combined effects of smear and gouge layer.

Petrographic analysis of thin sections and scanning electron microscope images as well as fracture roughness measurements will provide insights into the microstructure of fractures in the various shale samples. The relationship between shear deformation and fracture permeability is important to understand how shear slip, induced by injection of CO_2, slickwater, or wastewater from the drilling and fracturing process, may affect the seal integrity of CO_2 repositories.

Because of their low permeability, shales serve as unconventional reservoirs for natural gas as well as repositories for CO_2, waste material, and flowback water from shale gas production. It is shown through laboratory experiments on granitic rock that shear displacements of only a few millimeters are capable of enhancing fracture and joint permeability by one order of magnitude (Chen et al., 2000), which could improve shale gas production and worsen seal integrity of CO_2 reservoirs by creating pathways for leakage. Thus, it is very important to understand how permeability of pre-existing faults/fractures evolves during shearing of low-permeability and organic-rich shales in order to predict shale gas production and seal integrity of a CO_2 reservoir.

Small-magnitude earthquakes are often associated with hydraulic fracturing operations in shale gas reservoirs. Das and Zoback (2013) showed a cloud of microseismic events surrounding hydraulic fractures in the Barnett Shale indicating the occurrence of shear slip on pre-existing fractures and faults distributed around the induced hydraulic fractures. However, of greater concern are earthquakes triggered by the injection of wastewater

from the drilling and fracturing process or by the injection of CO_2. These small- to moderate-sized earthquakes, if triggered in formations that were intended to sequester CO_2 or waste material for hundreds and thousands of years, can threaten the seal capacity of such a repository (Zoback & Gorelick, 2012). In a critically stressed crust, where a subset of pre-existing fractures in the crust is potentially active in the current stress field, it only takes very small pressure perturbations caused by the injection of CO_2 or wastewater to trigger slip on unidentified faults (Chiaramonte et al., 2008) at pressures far below that at which hydraulic fractures would form (Zoback and Gorelick, 2012).
Several studies discussed below have been published on shear-induced fracture permeability. However, these consider either fault gouges/smears or joints/fractures in rocks other than shales, which represent the candidate storage reservoirs for CO_2 or waste material. The study proposed here will examine the effect of shear deformation on fracture permeability in intact shales with varying clay contents, under varying stress conditions, and in presence of different gases such as CO_2 and Ar. These different inert gases are chosen to address the adsorption effect on fracture permeability as some gases adsorb and others do not. In addition, we will perform surface roughness measurements and microscale imaging in order to investigate the fundamental mechanisms driving the fracture permeability behavior.

There are many remaining questions regarding potential CO_2 leakage and seal integrity in the field of carbon capture and storage as well as enhanced gas recovery from shale gas reservoirs. The questions we will address with this research study are the following:

1. Does a pre-existing fracture in shale seal itself during shear slip or does it open up a pathway for potential CO_2 leakage or enhanced gas recovery from shale gas reservoirs?
2. How does the fracture permeability in shale change during shearing?
3. How does the rock clay content affect the fracture permeability?
4. How does adsorption of CO_2/CH_4 affect leakage pathways/gas production and its permeability?
5. What does the fault damage zone look like?
6. What is the range of slip displacements on natural faults?

Considerable experimental work has been undertaken concerning the effect of shear displacement on permeability of a rock fracture. Chen et al. (2000) investigated hydraulic behavior of natural fractures/joints in granite samples through shear deformation and steady state flow experiments, in particular, relationships between fracture offset and mechanical and hydraulic apertures under varying stress conditions. They found that shear dilation induced by shear displacement could significantly enhance the permeability of fractures in granite samples even at high normal stresses (Figure 64).

Similarly, Esaki et al. (1999) showed an overall increase in fault/joint permeability with increasing shear deformation. They performed coupled shear-flow tests with an artificially created granite joint sample and found that the change in permeability is similar to that of dilatancy. Esaki et al. (1999) reported an initial decrease in permeability with shear displacement (Figure 65) from the onset of shearing until the peak shear stress was reached, which they attributed to asperities on both joint surfaces locking up. A steep

increase in permeability followed (Figure 65) caused by dilatancy that occurred due to the upper asperities sliding over the lower ones and being worn down by the stresses concentrated on them (Esaki et al., 1999). At high shear displacements, permeability gradually approached a constant value (Figure 65). This change in permeability was due to the wearing down of asperities and further shearing, which created gouge material within the joint, thereby blocking flow paths (Esaki et al. 1999). Thus, the mechanism for the observed permeability evolution during shearing in both of these studies is an asperity-mismatch between rough surfaces.

Based on reverse shearing experiments, Esaki et al. (1999) documented a large residual aperture, which resulted in permeability after shearing that was about one order of magnitude larger than that prior to shearing. They also compared their results to Barton's model (Barton et al., 1985) and found fault permeabilities based on their experiments that were up to two orders of magnitude lower than the theoretical calculations by Barton. Esaki et al. (1999) argue that this discrepancy is due to the development of gouge material that blocks flow paths and consequently reduces permeability. Barton's model does not include the effect of such gouge production on flow path and permeability. Therefore, we do not consider Barton's model as applicable to shales in our proposed research study.

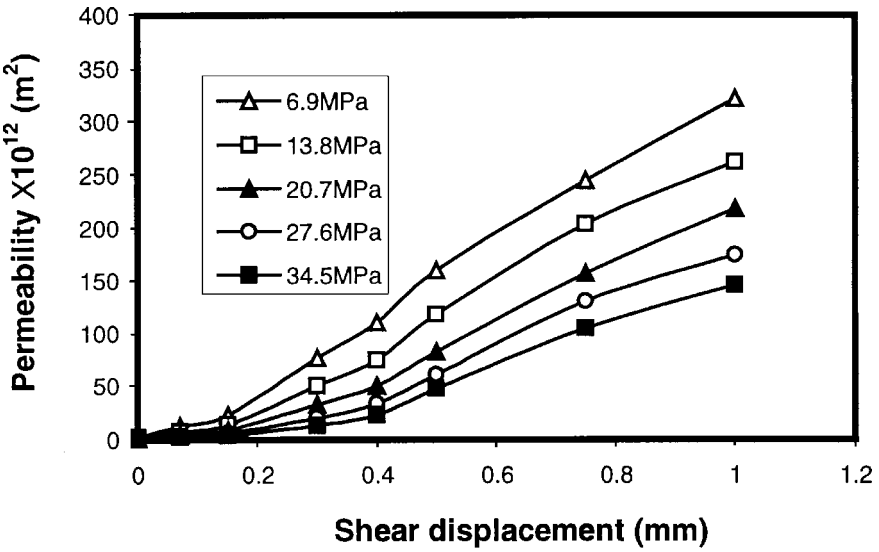

Figure 64. Permeability as a function of shear displacement at different confining pressures for jointed granite samples from the subsurface at Olympic Dam, a mining site in Central Australia (Chen et al., 2000).

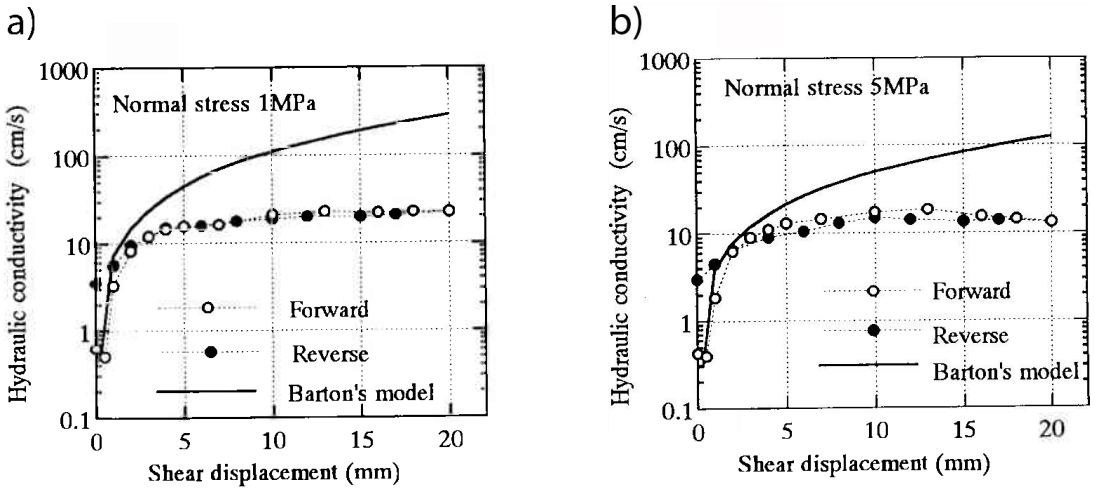

Figure 65. Shear-flow coupling test results for granite joints (Esaki et al., 1999). Hydraulic conductivity versus shear displacement curves for normal stresses of (a) 1 MPa and (b) 5 MPa. Dots are experimental results and solid lines represent Barton's model (Barton et al., 1985).

In contrast to the observed increase in fracture permeability during shearing, a few studies documented the opposite trend (Okazaki et al., 2013; Teufel, 1987). Teufel (1987) investigated the effect of shear deformation on permeability of pre-fractured samples of Coconino sandstone and found that permeability perpendicular to the fracture decreased with increasing shear deformation (Figure 66). Teufel (1987) showed that the generation of a gouge zone came along with a reduction in grain size and porosity during shear thus explaining the observation that permeability decreased normal to the fault plane during shearing. He also showed that the permeability perpendicular to the fracture decreased with increasing confining pressure (Figure 66).

Takahashi (2003) described a more complicated permeability trend with shear deformation than the steady permeability increase or decrease as indicated in the previous studies. Takahashi (2003) performed shear-flow experiments on specimens consisting of interlayered Byoubugaura siltstone, comprised of quartz, feldspar, calcite, illite, smectite-chlorite mixed-layer clays, kaolinite, zeolite, hornblende, pyrite, and opal CT, and Berea sandstone. Takahashi (2003) categorized the permeability changes in three distinct regimes (Fig. 67): 1) rapid reduction until the yield point due to compaction of siltstone layer prior to fault movement; 2) constant and minimum permeability while the smear developed, a membrane seal where clay particles preferentially align with the shear direction by entraining a primary unit with the shale or clay into the fault zone during fault movement (Peacock et al., 2000); and 3) permeability recovery caused by smear thinning and loss of smear continuity (Figure 63). Takahashi (2003) concluded that the thickness and continuity of the smear are important factors in fluid flow across the fault.

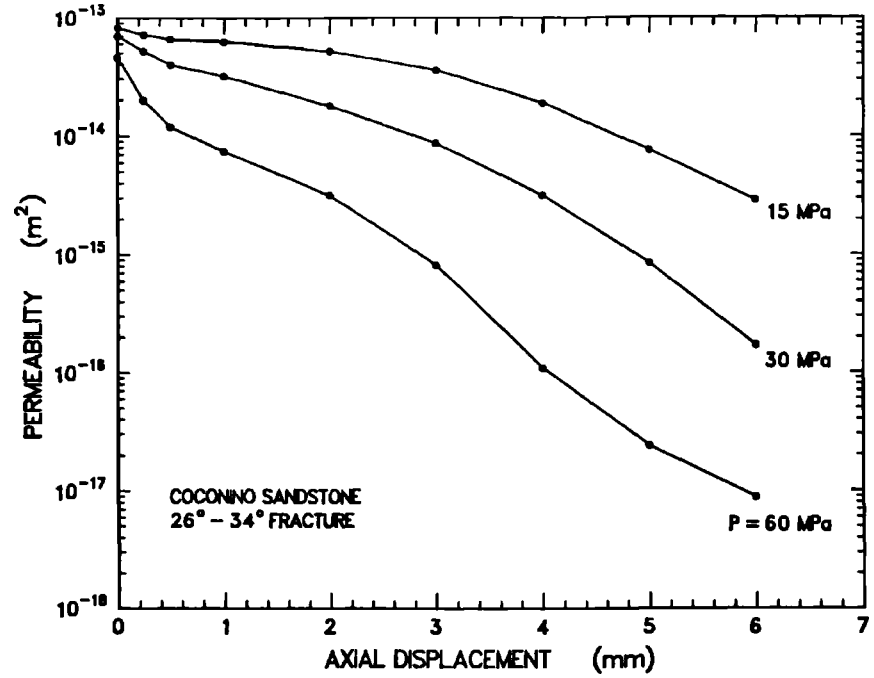

Figure 66. Fracture-perpendicular permeability versus axial displacement as a function of confining pressure for pre-fractured samples of Coconino sandstone (Teufel, 1987).

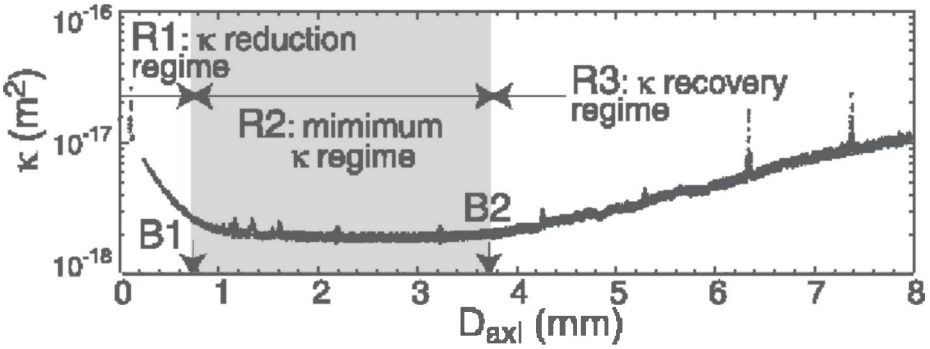

Figure 67. Fracture-perpendicular permeability versus axial displacement obtained during deformation in a simulated smear experiment using Berea sandstone and interlayered Byoubugaura siltstone (Takahashi, 2003).

A few studies are published on different types of fault gouges as opposed to joints in intact rocks (Crawford et al., 2008; Okazaki et al., 2013). Okazaki et al. (2013) measured shear-induced permeability of antigorite serpentinite gouges in three orthogonal directions during triaxial friction experiments. All three directional permeabilities decreased with increasing axial displacement with the permeability perpendicular to the fault decreasing the most (Figure 68, orange and red lines). Permeability normal to the shear plane reduced to one order of magnitude lower than in the other orthogonal directions when the shear stress reached a steady state (Okazaki et al., 2013). Observed microstructures indicated shear deformation being accommodated on the R1 and Y shear bands, and P foliation. R1 represents the classic Riedel shears, Y-shears form parallel to

the boundaries, and P-shears are conjugate to the R1-shears (Paterson and Wong, 2005). The shear bands can be viewed as representing localization instabilities in the deformation of the gouge layer.

Crawford et al. (2008) studied strength and fluid flow properties of fault gouges composed of varying fractions of fine-grained quartz and kaolinite during hydrostatic and shear loading. However, synthetic binary fault gouges are not necessarily the same as natural shale gouge at the same clay content. Crawford et al. (2008) concluded that clay mineralogy may be as significant as clay content in controlling fault rock permeability and that the accumulation of slip displacement or strain magnitude is believed to be of secondary importance with regard to evolution of permeability magnitude in clay-bearing gouges. This conclusion directly contradicts Takahashi's (2003) results described previously.

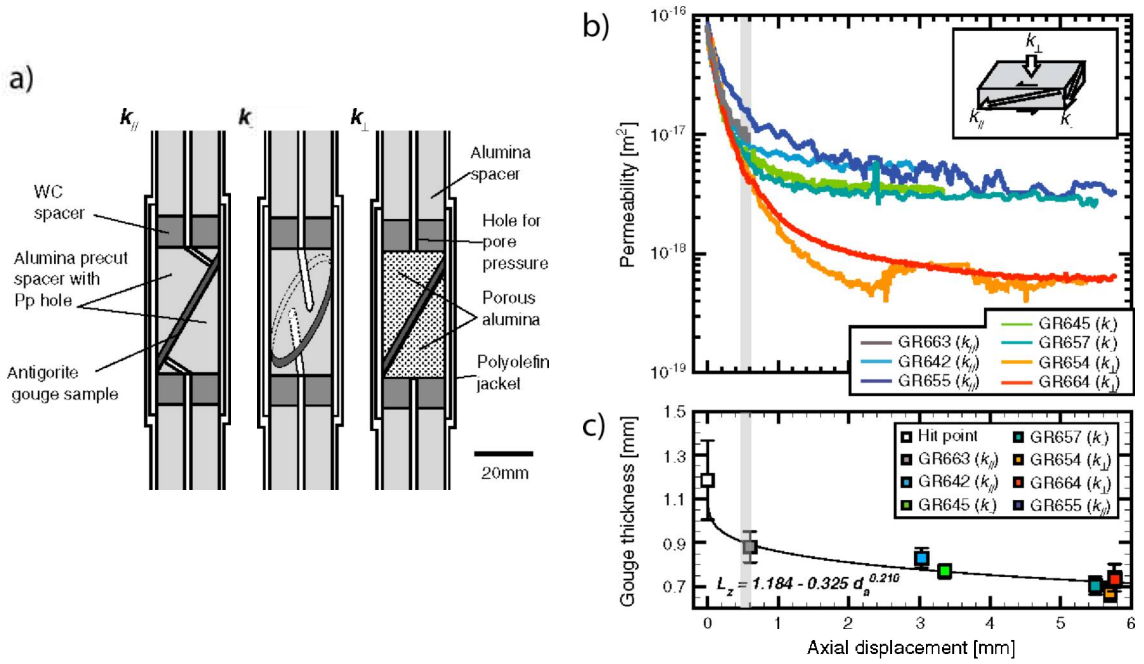

Figure 68. a) Schematic diagram of sample assemblies for measuring fracture permeability in the slip direction, normal to the slip direction in the fault, and normal to the fault (respectively, from left to right). b) Permeabilities in the slip direction (gray, light blue, and dark blue; top three lines), normal to the slip direction in the fault (green and teal; middle two lines), and normal to the fault (orange and red; bottom two lines). c) gouge thickness as a function of axial displacement during shear experiments. (after Okazaki et al., 2013)

Slip on faults can propagate unstably generating conventional microseismic events or slowly, which is a process that does not generate high frequency seismic waves, and thus is often not detected in conventional microseismic monitoring (Das and Zoback, 2013). Kohli and Zoback (2013) showed based on rate and state friction experiments using shale samples with different lithologies that where the clay content is approximately < 30%, slip is expected to be unstable (stick-slip), and where the clay content is approximately > 30%, slip on faults is expected to be stable. The size, style, and location of the damage

zone within the fault, which has an effect on the fault permeability, might be different from fast slip to slow slip. Under slow slip, we expect the damage zone to be reduced to the fault plane because of the formation of a thin clay-rich smear layer, whereas under fast slip, a low-permeability layer might develop in the fault with a damage zone including microfractures adjacent to it. The hypotheses agree with the argument by Tembe et al. (2010) that a weaker clay mineral such as montmorillonite (compared to illite or quartz) organizes into localized, thin slip surfaces and dominates the shearing micromechanics. These microstructural processes will affect the fault permeability evolution during shearing and need to be considered in this study.

Planned Studies - Three different types of samples will be tested in this study: (1) cores with fresh saw cuts at 30° to the cylindrical core axis, (2) cores that naturally broke in shear deformation tests (Sone and Zoback, 2013a, b), and (3) core wafers sandwiched between aluminum forcing blocks at 30° to the cylindrical axis (Figure 69). For the saw cut samples, intact cores of the Haynesville and Eagle Ford shales will be used as material. A saw cut jig that will be added to a precision saw has been designed and completed to cut the intact shale cores at exactly 30° to the cylindrical core axis. The saw cut surfaces will have to be roughened with 100 grit Silicon Carbide to avoid predominant stick-slip behavior during shearing. The naturally broken samples are cores from the Haynesville shale. We have four cores available that are suitable for these coupled shear-flow experiments, of which two are of great quality and two of poor quality. The core wafers will be cut with the modified IsoMet© 1000 Precision Saw to a thickness of a few millimeters. The exact thickness will be determined after initial experiments to test the setup. Both ellipsoidal faces will be attached to aluminum forcing blocks with epoxy resin. For this purpose an aluminum adhesive with high tensile strength and shear force resistance, as used in the aerospace industry, is needed; an example is EP17. The sides of the aluminum forcing blocks, that are to be attached to the core wafer, will have to be cleaned and roughened in order to bond with the epoxy resin. Haynesville and Eagle Ford shales will also be used as material for the wafers.

Pore fluid will be introduced through two small holes (approximately 1mm in diameter) drilled parallel to the cylindrical axis down to the fault plane. Depending on the stability of the core and the drilling setup, the holes may have to be drilled perpendicular to the fault plane. Initial experiments testing different drill bit sizes will determine the ideal borehole diameter, which should allow steady state flow from the inlet/outlet to the fault but avoid clogging. Filling the holes loosely with fibrous alumina as performed by Crawford et al. (2008) may inhibit fault material extruding into the holes. Before starting the experiments on shale, we will use Berea sandstone to test the experimental setup.

Coupled shear-flow experiments on shales with varying compositions will be conducted in a conventional triaxial configuration under varying confining pressures using different gases such as argon and carbon dioxide. The testing setup for all three different sample types is shown in Figure 69. The core sample or aluminum forcing blocks with the core wafer will be jacketed in polyolefin tubing and placed in an annealed 0.25 mm wall thickness copper jacket. Crawford et al. (2008) successfully used this arrangement to reduce the possibility of fluid pathways short-circuiting the fault layer between the core

sample/aluminum forcing blocks and the copper jacket and minimized the likelihood of rupture of the jacket at high strain. The sample or forcing blocks will be sealed around the edge on either end with steel platens, which allow the pore fluid to be radially distributed towards the small holes drilled in the samples, and placed in the triaxial pressure vessel.

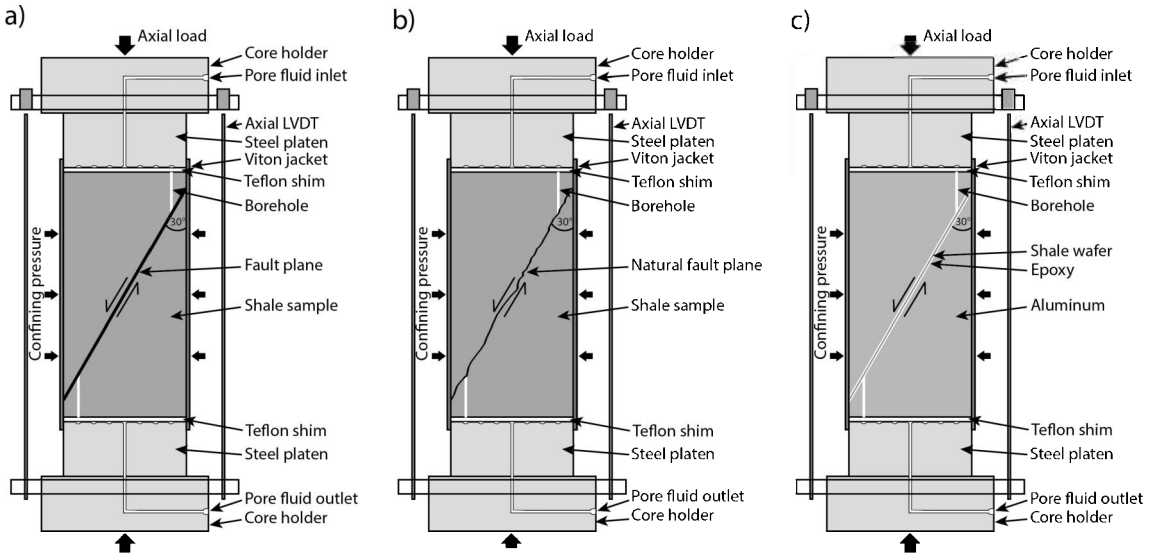

Figure 69: Experimental testing setup for a) a saw-cut shale sample, b) a naturally broken shale sample, and 3) a shale wafer in between aluminum forcing blocks.

The full stress path for all samples consists of hydrostatic loading followed by shear loading. During hydrostatic loading, the samples will be loaded to an effective pressure of 5 MPa (5 MPa pore fluid pressure), for example, by careful synchronous ramping of confining and pore pressure. From this point on permeability will be measured at constant pore fluid pressure after individual, small increments in shear displacement using steady state Darcy flow experiments, similar to the studies by Chen et al. (2000) and Esaki et al. (1999). This method is in contrast to the commonly used pore pressure oscillation technique (Crawford et al., 2008; Faulkner and Rutter, 2000; Fischer, 1992; Kranz et al., 1990; Okazaki et al., 2013; Takahashi, 2003). Chen et al. (2000) and Esaki et al. (1999) used water as pore fluid; here, however, we will use various gases such as argon and carbon dioxide to study adsorption effects between the gases. The adsorption of CO_2 has large implications for carbon capture and sequestration as well as shale gas applications. According to Darcy's Law, fluid flow through a porous medium can be expressed as

$$Q = \frac{k A \Delta P}{\mu L} \quad , \qquad (11)$$

where Q is the flow rate through the sample, k is the permeability of the sample, A is the cross-sectional flow area of the sample, ΔP is the pressure drop through the sample, μ is the fluid viscosity, and L is the sample length. We realize that for gases Darcy's Law is more complicated and we need to assume that the real gas equation of state applies.

Because the permeability of the shale matrix will be orders of magnitude smaller compared to the fracture permeability, the permeability measured in this study will be mainly contributed by the fracture. In that case, k can be considered as the permeability of the fracture, under the condition that the flow area is substituted with the cross-sectional area of the fracture, and can be calculated as follows:

$$k = \frac{Q}{A}\frac{\mu}{\Delta P}\frac{L}{} \quad . \qquad (12)$$

One pump with enough volume to increase pore fluid pressure and perform flow tests under steady state conditions will be connected to each pore fluid inlet and outlet. Either a constant head or flow rate condition will be applied to the fault plane and the resulting flow rates or pressures will be measured, respectively. Using Darcy's Law and given the fault plane geometry and fluid properties, we can determine the fault permeability as a function of shear displacement. Performing these coupled shear-flow experiments at different pore fluid pressures will give insight into the effect of pore fluid pressure on fault permeability. Given the geometry of our sample assembly, permeability will be measured along the fault plane, parallel to the direction of slip. The mechanical and flow data will have to be corrected for the change in area overlap between the two sample pieces or aluminum forcing blocks during sliding.

Due to the elliptical shape of the thin fault plane, the flow path for fluid starts at the narrow end of the cylinder connected to the upstream reservoir, which then widens out before narrowing down where the fluid escapes to the downstream reservoir (Figure 70). Thus, our permeability measurements are "apparent" permeability values, which may deviate from the true, local, permeability values. However, relative changes recorded will not deviate, as the flow path does not change significantly during a single test. Computed tomography (CT) scanning of the samples before performing the coupled shear-flow experiments might help to identify large enough features that could potentially channelize the flow instead of sampling the entire fault surface during permeability experiments.

During shearing the sample assembly will be loaded within a conventional triaxial apparatus and sheared under a small, constant axial displacement rate of approximately 0.1 μm/s. Confining pressure will be increased in increments of 10 MPa up to 50 MPa, for example, resulting in effective stresses of 5, 15, 25, 35, and 45 MPa. Throughout each test confining and pore pressure will be held constant while axial load will be increased independently to induce shearing along the fault. Teflon shims on both ends of the sample assembly will accommodate sufficient decoupling between the sample assembly and the steel platens such that slip can occur along the fault.

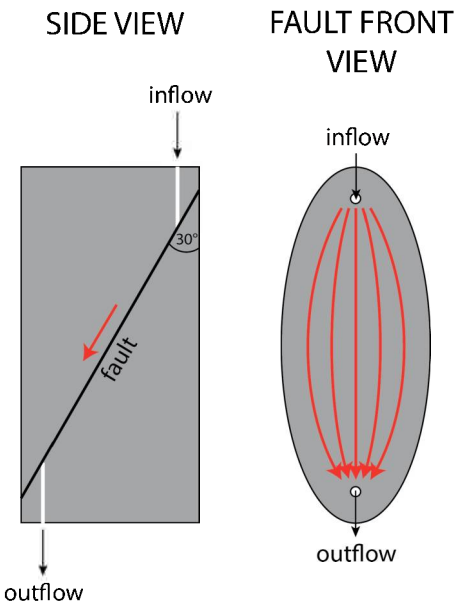

Figure 70. Schematic diagram showing the geometry of the sample and fluid flow paths within the sample.

Before and after each coupled shear-flow experiment we measure the surface roughness of the fracture using a three-dimensional scanning white light interferometer (WLI) at the University of California Santa Cruz in Emily Brodsky's laboratory. White light interferometry microphotography measures the topography of 3-D structures scale by using a microscope with a broadband white light source, which is coupled to an interferometer. Interferometry makes use of the wave superposition principle. For the device used, the maximum sample size is 89 x 203 x 203 mm, the field of view ranges from 0.03 to 14 mm, and the vertical scan range is 150 μm with a vertical resolution of < 0.1 nm. An example of a roughness profile perpendicular to slip measured with white light interferometry is shown in Figure 71 for the Corona Heights fault surface, California (Candela et al., 2012), where the authors compare the roughness profile on a millimeter scale with profiles at larger scales measured with a Light Detection And Ranging (LiDAR) apparatus and laser profilometer.

After the WLI measurements, both halves of each test specimen will be impregnated with thin section epoxy and cut along a plane normal to the fault plane to produce thin sections of the fault plane. We will prepare thin sections that will first be examined in a standard petrographic microscope and then mounted on aluminum sample posts and coated with gold under vacuum for examination in the scanning electron microscope (SEM). A reference area far away from the fracture (closer to the sidewall) will serve as an analog for the microstructure before shearing. Both the petrographic thin section and SEM analyses will provide microstructural information on the shearing mechanisms. More specifically, the thin section analysis will give insight into how the strain is accommodated along the fault as well as particle size distribution, potential development of cataclastic gouge and/or clay smear, and preferred orientation of particles. SEM analysis with an energy-dispersive (EDS) detector will allow for identification of the micro- and nanoscale fabric as well as elementary composition.

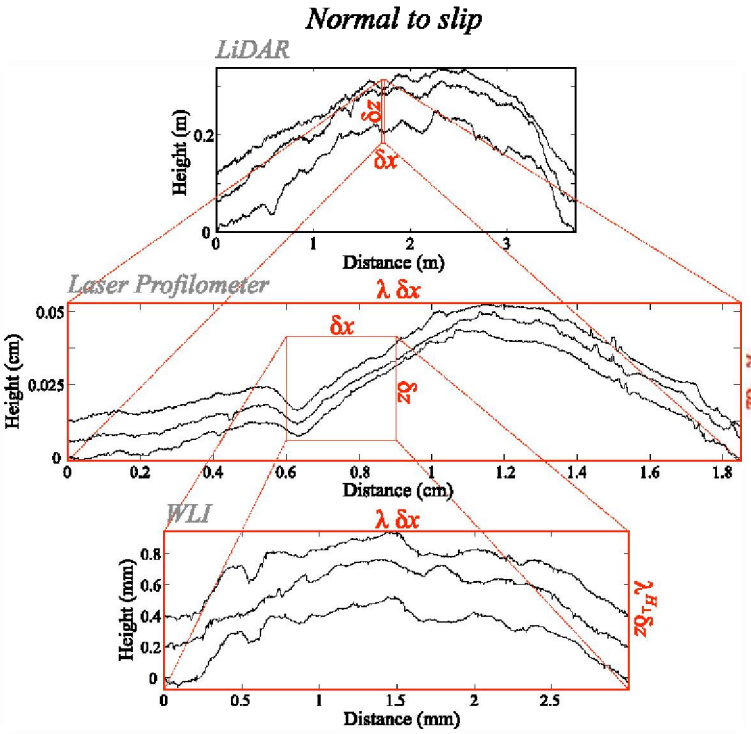

Figure 71: Roughness profiles perpendicular to slip from the Corona Heights fault surface in California (Candela et al., 2012). The bottom plot is obtained from white-light interferometry.

2.5: Shale swelling

Adsorption, Swelling and Viscous Creep of Synthetic Clay Samples

We are conducting laboratory experiments on synthetic clay samples to explore their adsorptive and swelling properties, as well as the effect of gas chemistry on their physical properties and viscous creep behavior. Synthetic samples were created of clays obtained from the Clay Minerals Society, including kaolinite, illite and montmorillonite.

Adsorption allows for significantly larger quantities of gas to be in place and possibly produced, which can be particularly important for low porosity shales in which the pore space for free gas storage is limited. However, one must take care to consider how desorption pressure, time, and alteration of reservoir stresses during production may affect the flow properties and production of the total system to know if desorbed gas will contribute significantly to production. Although it is rarely discussed, several authors have noted the adsorptive capacity of clay in addition to the organic component of gas shales (Ross and Bustin, 2008). Given that the organic fraction of most shales is less than 5%, and typical clay contents range from 30-50%, it may be appropriate to consider the clay content as a potentially significant storage reservoir.

While gas adsorption is ubiquitous in the coalbed methane literature, there is limited data available to predict the nature of gas adsorption in shales and the accompanying

volumetric strain caused by desorption during production or adsorption during gas injection. This research focuses on developing an understanding of the interrelation between the adsorptive, swelling and mechanical properties of pure clay in the context of the complex mineralogy that comprise gas shales.

Sample Description and Preparation

For two reasons, our first experiments were carried out on activated carbon (Filtrasorb 400, 12 x 40 mesh) purchased from Calgon Carbon. First, we wanted to study a material with which we could easily compare results obtained in our lab with those obtained in other labs. Second, it is helpful to produce a baseline set of data from our own laboratory, on a well understood material, with which to compare subsequent results on more complex samples. Kaolinite, illite, and montmorillonite clay standards were obtained from the Clay Mineral Society and sold to us as pure clay samples. The purity of these clay standards will need to be verified via X-ray diffraction at a later date.

Sorption experiments in this study were performed on powdered activated carbon, clay, and shale samples that were ground and sieved to approximately 100-250 μm using standard methods. The shale and activated carbon samples were dried by placing them in a vacuum oven at 125°C for 24-48 hours until constant mass was achieved. Experiments were performed on the clay samples without vacuum drying and will be hereafter referred to as being of "as received" (A.R.) moisture content. The experiments will be need to be repeated at a later date on vacuum dried samples in order to examine the effects of moisture.

After careful consideration, a dual-jacket method was chosen to isolate the sample and pore fluid from the confining fluid. A thin copper jacket was chosen for the inside in order to prevent the pore fluid from exiting the sample by diffusion. A viton jacket was chosen for the outside because of its compatibility with our confining oil, and the integrity of the seal it formed against the stainless steel coreholders.

Samples of 1.0 inch diameter and 2.0 inch length were cast inside of a 0.002 inch thick copper jacket that was cut from a sheet and soldered at the seam to form a cylinder. The cylinder was first slid over a stainless steel coreholder. A 40 μm aperture circular screen was then cut and placed at the ends of the cylinder to prevent particles from entering the system plumbing. The copper was then filled with small aliquots of material and tamped until completion, and a second screen was placed on top of the sample. Heat shrinkable viton tubing was then slid over the outside of the copper, and the top coreholder was placed on the sample. The tubing was then shrunk around the sample, and pre-positioned hose clamps were then tightened around the viton jacket.

In order to form a compact sample from crushed material that behaved as elastically as possible, all samples were first stressed to a confining pressure of 30 MPa, twice as high the maximum pressure to be reached during the experiment, in order to remove all plastic deformation. The confining pressure was then cycled back and forth between 1 and 30 MPa while the strain was monitored to check for repeatable behavior, which was typically achieved after about 15 cycles over a two-hour period.

Experimental Setup

Experiments were carried out using a conventional triaxial machine that has been modified to measure adsorption and gas permeability by incorporating a Quizix Series 1500 pump. Of primary relevance for this experiment is the plumbing of the pore fluid lines, consisting of a stainless steel sample cell (the coreholders, core sample and a short length of line), two stainless steel cylinders with servo controlled pistons inside them, two sets of independently controlled air actuated valves at either end of the reference cell (inlet and outlet), two high precision pressure transducers located inside of each cylinder, and two temperature thermistors. In this study the volumetric method was used to determine the adsorption capacities of the samples as a function of pressure as described previously in Section 2.4.

Methodology validation: activated carbon adsorption

The results of our adsorption experiments on activated carbon as compared to Sudibandryo *et al.* (2003) are shown in Figure 72.

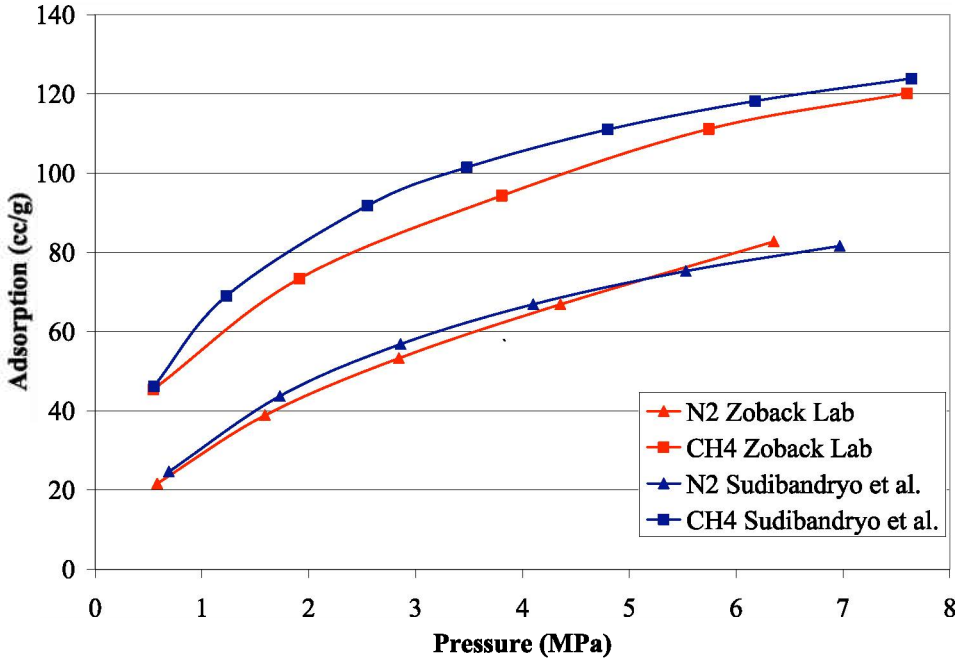

Figure 72. Comparison of adsoprtion of nitrogen and methane on activated carbon determined by Zoback 2010 and Sudibandryo *et al.* 2003.

For both nitrogen and methane, our results are slightly lower but very close to those attained by Subidandryo *et al.* (2003).

The relationship between adsorption and swelling strain is critical for understanding changes in permeability and stress in a reservoir during production or injection of gas. Figure 73 shows the total volumetric strain as a function of pore pressure at a constant effective stress as calculated by the true effective-stress law, with a calculated Biot

coefficient α = 0.876.

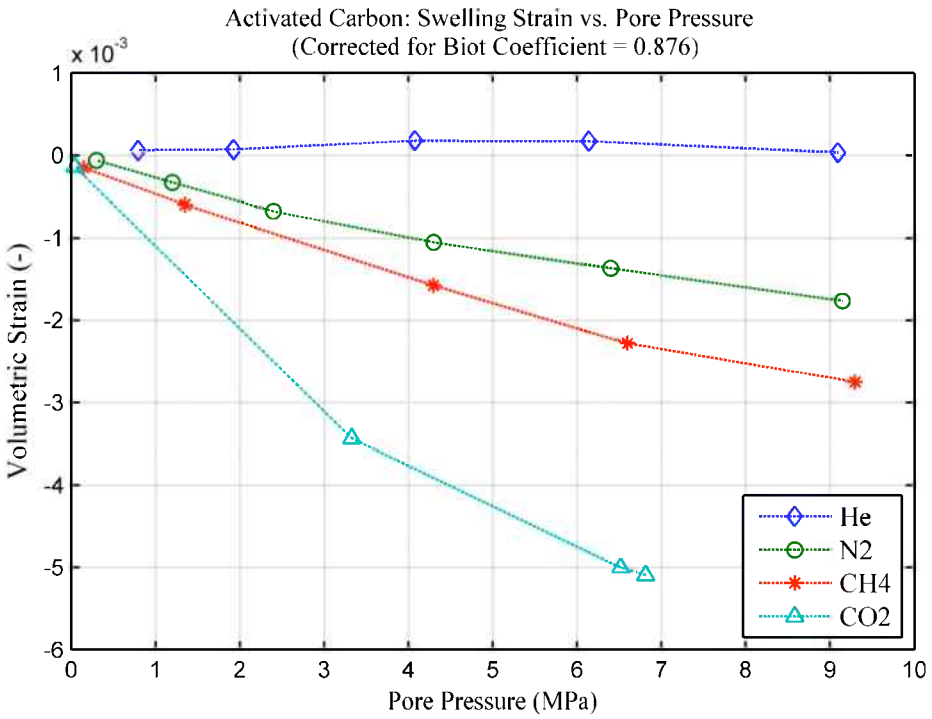

Figure 73. Activated carbon swelling strain as a function of pore pressure, with correction for Biot deformation.

As expected, we see that the greater the adsorption, the greater the swelling strain that is observed.

The results of adsorption experiments on activated carbon suggest that our modified laboratory equipment and methods are sufficient for simultaneously measuring adsorption and swelling strain.

Illite: Adsorption, Swelling and Creep Strain

As mentioned above, the adsorptive capacity of kaolinite, illite, and montmorillonite has been noted by several authors (Ross and Bustin, 2008, Busch *et al*, 2009). However, each of these clays can exist in a variety of forms with differing moisture content, cations, and degrees of cation coordination. Moreover, the relation between adsorption measurements on rock samples and those measured on the pure mineral and organic constituents is a gap in knowledge. It is the goal of our research to develop a better understanding of adsorption in gas shales, and in particular the potential contribution of the clays.

Preliminary results showing the adsorption of nitrogen, methane and carbon dioxide on dry (48 hours in a vacuum oven at 40 degrees C) illite is shown in Figure 74.

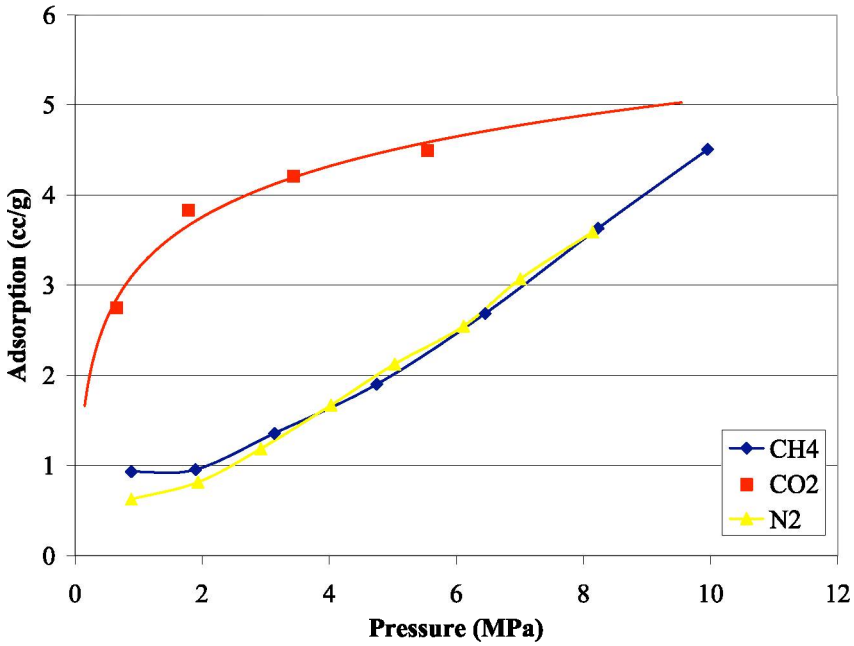

Figure 74. Adsorption of nitrogen, methane and carbon dioxide on dry illite.

There are several features worth noting about the illite adsorption curve. In the case of carbon dioxide acting as the adsorbent, we see a typical Langmuir curve. However, the isotherms for methane and nitrogen are nearly identical and linear, as opposed to exhibiting Langmuir shapes. Finally, one notices that carbon dioxide has a much greater capacity for adsorption at low pressures, but interestingly might be surpassed by methane and nitrogen at high pressures.

The swelling response to adsorption was also measured, as shown in Figure 75. There is an increase in swelling strain at higher pressures as the amount of adsorbed gas increases. The relation between adsorption, swelling and pore fluid is further examined in the discussion section.

Finally, the time-dependent, hydrostatic creep strain in illite was examined as a function of pore fluid. Hydrostatic creep strain was examined for both the clay and shale. For these experiments, samples were saturated with a pore fluid pressure of 2 MPa at an initial confining stress of 4 MPa. The confining pressure was then ramped up to 14 MPa over 20 minutes to produce a stress–strain curve from which the bulk modulus could be calculated. The confining pressure and pore pressure were then held constant for 8-16 hours, and strain was monitored over time.

The results show that carbon dioxide seems to increase the viscous creep strain of the illite by a factor of about 2-3 after 12 hours. This may have implications on the prospect of carbon dioxide injection and storage in gas shale reservoirs or reservoirs with shale acting as a seal, and will have to be the subject of further investigation.

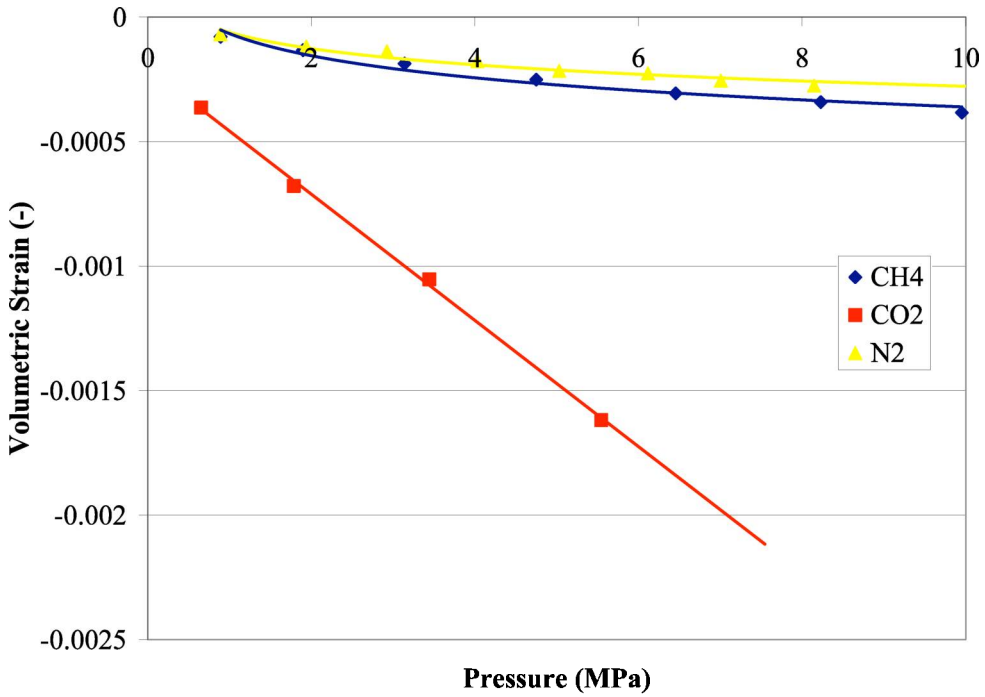

Figure 75. Adsorption of nitrogen, methane and carbon dioxide on dry illite.

Discussion of adsorption and creep

The measured amount of methane adsorption on dry illite is nearly equal to that measured in another lab (Ross and Bustin, 2008), however the shape that we have measured differs significantly. Adsorbents exhibiting Langmuir-shaped isotherms are so ubiquitous that exceptions require explanation. The theoretical amount of adsorption on the completion of a single monolayer can be approximated by making use of the molecular size and adsorbent surface area as follows:

$$A_{molecule} \approx \pi * r_{molecule}^2 \tag{1}$$

$$N_{ads,molecules} = \#layers * \frac{S.A.}{A_{molecule}} \tag{2}$$

$$V_{monolayer} = \frac{N_{ads.molecules} * R * T}{P * 6.02x10^{23}} \tag{3}$$

This back-of-the-envelope calculation depends on several assumptions and simplifications (molecules are spherical, all surface area is available to adsorbate, nearly all of the adsorbate is surrounded by adsorbent, etc.). However, it can be useful in interpreting adsorption data. To demonstrate the validity of this calculation, it was applied to surface area and adsorption data reported for nine Jurassic gas shale samples by Ross and Bustin, 2008. The results are presented in Table 6 and Figure 76 below.

Sample	Surface Area (m^2/g)	Measured Adsorption (cc/g)	Theoretical Monolayer (cc/g)
N376-1	6.2	0.4	0.55
N6080-1	18.5	0.4	1.66
N3773-2	28.8	2.1	2.58
N89-1	12.7	1.2	1.14
N230-1	11.4	1.3	1.02
N3793-1	40.3	3.6	3.6
N49-2	23.4	2	2.09
N91-1	15.3	1.3	1.37
N174-1	16.1	1.6	1.44

Table 6: Theoretical monolayer adsorption volume calculation for methane on Jurassic gas shale samples for Northwestern Canada. Surface area and adsorption data from Ross and Bustin, 2008.

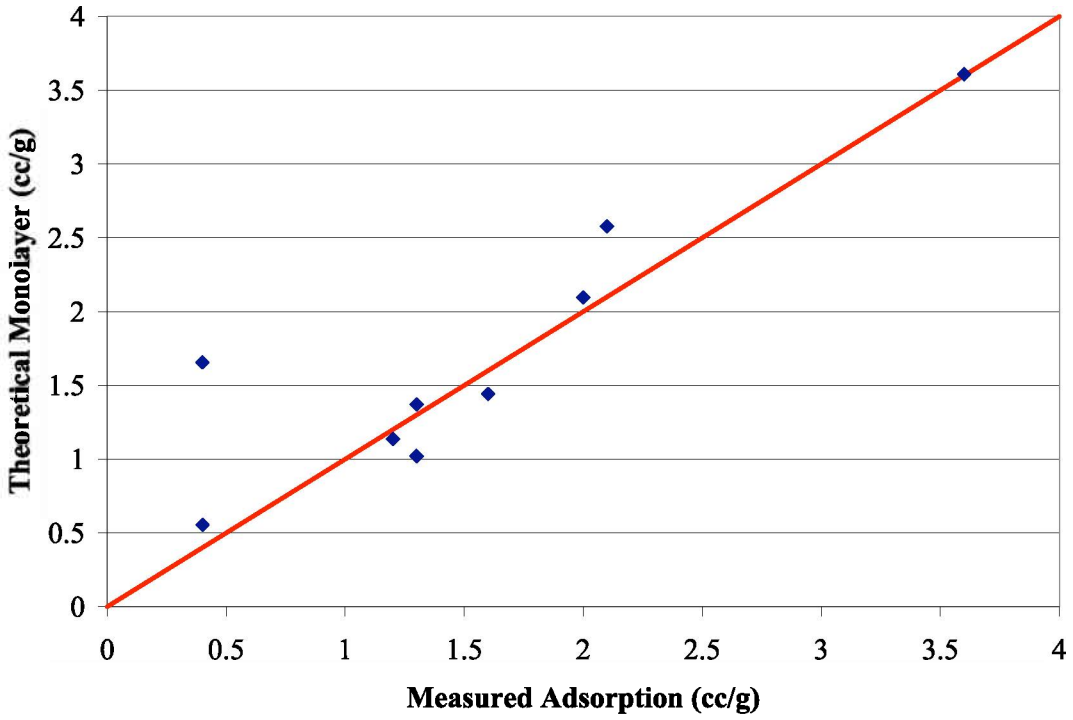

Figure 76: Theoretical monolayer amount of adsorption versus the measured amount on nine Jurassic gas shale samples. Red 1:1 line represents perfect agreement.

As seen in Figure 76, most of the data fluctuates about the 1:1 red line, suggesting that this is a valid method for interpreting adsorption data for gas shales. The theoretical monolayer was calculated for both activated carbon and illite. Surface areas were taken from vendor data for activated carbon and literature estimates for illite. The results are presented in Table 7.

	Act. Carbon	Illite
Surface Area (m^2/g)	1110	50
$N_{ads, CH4}$ (molecules/g)	$2.4x10^{21}$	$1.1x10^{20}$
$V_{monolaver, CH4}$ (cc/g)	99.4	4.5
$N_{ads, CO2}$ (molecules/g)		$1.5x10^{20}$
$V_{monolaver, CO2}$ (cc/g)		5.9

Table 7: Theroetical monolayer adsorption volume calculation for methane and carbon dioxide on activated carbon and illite.

In the case of activated carbon, one notices the agreement (within ~15%) between the theoretical methane monolayer and the data presented in Figure 73. This agreement suggests that Langmuir theory of monolayer adsorption is valid for activated carbon, as expected. In the case of illite, one notices that the measured amount of adsorption matches experimental data fairly well for carbon dioxide. However, the measured methane isotherm exceeds the theoretical monolayer amount and seems to show no signs of reaching an inflection point, even at pressures as high as 10 MPa.

A potential explanation for the illite methane and nitrogen adsorption data is presented here. First and foremost, the illite particles were approximately 2 microns in diameter, resulting in an extremely large external particle surface area (~1100 m^2/g, as compared to ~50m^2/g of intraparticle surface area). This external surface area does not exist within the clay content of real rock samples, and may be the primary location in which methane and nitrogen adsorption is taking place in our synthetic illite sample. This hypothesis may be further supported by the mechanical data. Figure 77 shows the volumetric swelling strain versus adsorption.

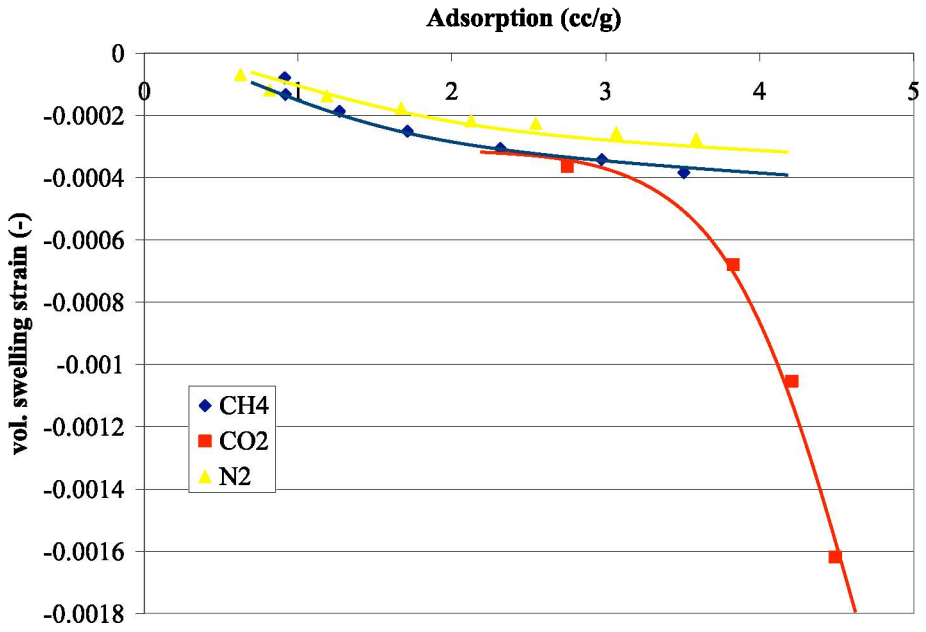

Figure 77: Volumetric swelling strain versus amount quantity of adsorbed methane, carbon dioxide and nitrogen on illite.

In Figure 77, one sees that swelling depends approximately linearly on adsorption for the cases of nitrogen and methane acting as adsorbates. However, there is an exponential increase in the amount of swelling for a given amount of adsorption when carbon dioxide is the adsorbing fluid. This suggests a fundamentally different mechanism behind the carbon dioxide adsorption. Many authors have reported that swelling in microporous materials is largely the result of the extremely high internal adsorption stresses resulting from adsorption in the smallest micropores (Kowalcyzk, 2010). This stress acts outward (normal to the pore walls) and results in sample swelling. If methane and nitrogen adsorption is largely occurring on the external surfaces of clay grains, swelling will be minimal (as the experimental data indicate). The smaller carbon dioxide molecules may be adsorbing in the microporous regions of the illite sample, which are inaccessible to methane and nitrogen, as supported by the large resultant swelling strain in response to carbon dioxide adsorption.

3.0: Transport and mobility of critical-state CO_2 in hydrofractures, natural fractures and pores

3.1: Transport simulation and permeability predictions using molecular dynamics

In addition to the adsorption isotherm predictions, transport of CO_2 in 3-D pore networks of carbon systems is also underway. Using known average estimates of porosities and pore size distributions of gas shale samples, we have created 3-D pore networks representative of the organic matrix of gas shale as shown in Figure 1. Periodic images of these 3-D pore networks are not meant to be representative of an entire gas shale, but rather, representative of the organic matrix comprising the porous kerogen in the shale. The porosity of the 1000 nm^3 represented in Figure 78 is 25%, which is much greater than the overall porosity of a given shale sample that will contain a combination and heterogeneous mix of kerogen and clay in addition to other mineral components. Using non-equilibrium grand canonical molecular dynamics simulations we have been able to predict the "local" permeabilities in these 3-D pore networks that may potentially represent that of the kerogen matrix. Future simulations will be needed to involve the addition of aluminosilicates representative of clay added to the carbon models to determine how the presence of the clay minerals may influence the permeability predictions.

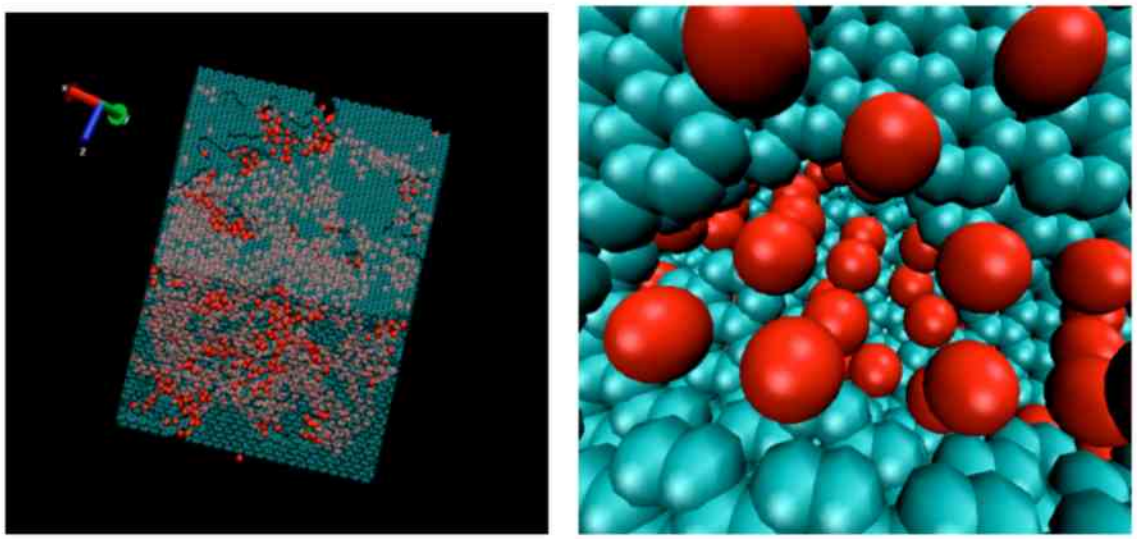

Figure 78. Snapshot (left) of CO_2 molecules in the 3-D pore network with porosity of 25% and average pore size of 1.2 nm with an example view of a CO_2-occupied pore (right).

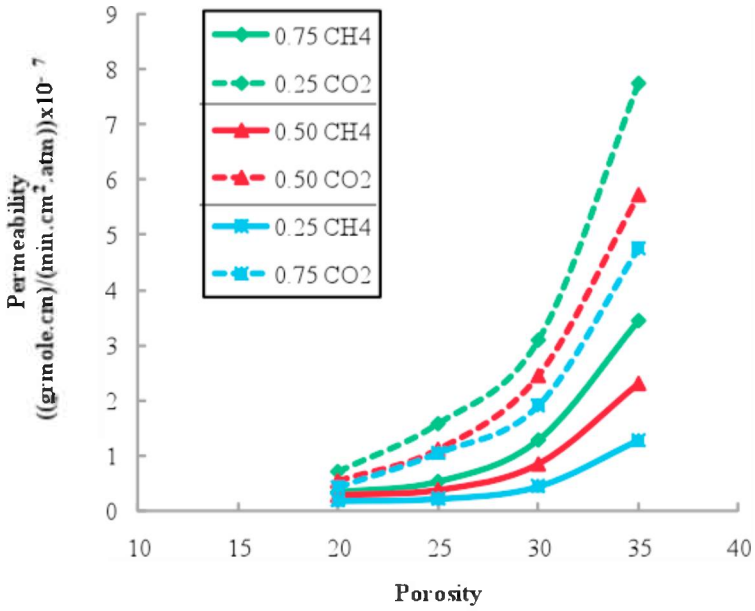

Figure 79. Permeability of CO_2 -CH_4 mixtures as a function of porosity in 1.2 nm pores.

Figure 79 shows the permeability predictions of three unique mixtures of CO_2 and methane as a function of porosity in a model 3-D pore network consisting primarily of micropores with an average diameter of 1.2 nm. In all cases CO_2 has a higher permeability than methane, which is likely due to a higher contribution to total transport through surface diffusion. Since surface interactions dominate in micropores it is likely that surface diffusion dominates the mechanism of transport in these cases. As the porosity decreases the permeability of both gases decreases likely due to pore blocking from adsorbed species and a decrease in pore connectivity.

Figure 80 shows time-averaged snapshots of CO_2 densities in straight-channel pores

ranging from 0.67 to 1.34 nm, within a 3-D pore network. As the pores increase in size transport is no longer dominated by CO_2-wall interactions, but will also take place via Knudsen diffusion in which CO_2-wall collisions will begin to play a role in determining the transport mechanism through the system.

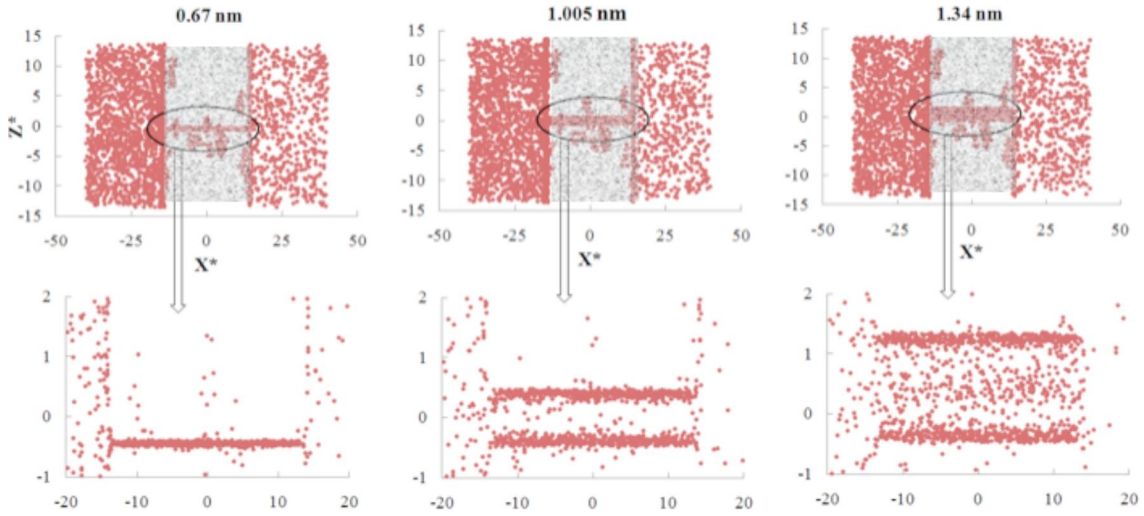

Figure 81. Transport of CO_2 in micropores with corresponding density particle densities

Carbon-based 3-D pore networks have been created to investigate CO_2 transport using NEMD simulations. Figure 82 (a) represents the dependence of CH_4 (diamonds), CO_2 (triangles), and N_2 (circles) permeabilities on the porosity in a pore network with a 12.6 Å average pore size. The results show that the permeability of all three components will increase with increasing porosity. In fact, as the porosity of the pore network becomes higher, having the same average pore size, the number and, therefore, the interconnectivity of the pores will increase, subsequently assisting molecular transport through the system. The permeability of all components is approximately zero when the porosity is low (e.g., < 20%), which implies that decreased connectivity inhibits molecular transport through the pore network. Figure 82 (b) represents the dependence of permeabilities of two components in a mixture of N_2 (solid curves) and CO_2 (dashed curves) on the porosity. The average pore size in the pore network is 12.6 Å, and the mole fractions of N_2 in the mixtures are 0.88 (circles), 0.75 (diamonds), 0.5 (triangles), and 0.25 (squares). The permeability of CO_2 is higher than N_2 for the same porosity due to the adsorption and shielding effect of CO_2. As the mole fraction of N_2 decreases in the feed gas, the permeability of N_2 will decrease. The permeability of N_2 is less affected by both the porosity and the feed composition, while the permeability of CO_2 appears to depend rather strongly on the porosity and feed composition.

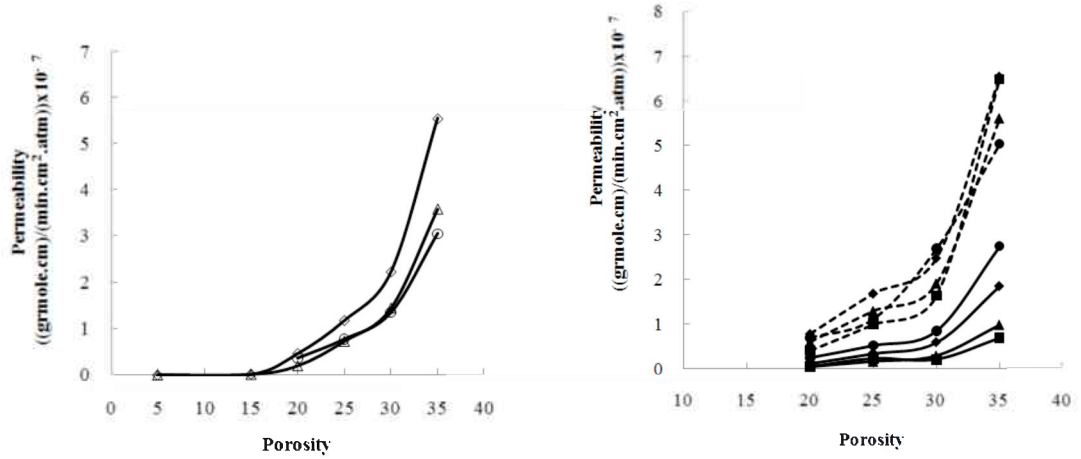

Figure 82. (a) The dependence of the permeability of CH_4 (diamonds), CO_2 (triangles), and N_2 (circles) on the porosity. (b) The dependence of permeability of N_2 (solid curves) and CO_2 (dashed curves) in the mixture on the porosity. The mole fractions of N_2 in the mixtures are 0.88 (circles), 0.75 (diamonds), 0.5 (triangles), and 0.25 (squares). The average pore size in the pore network is 12.6 Å in (a) and (b).

In addition to the adsorption isotherm predictions, transport of CO_2 and methane as a function of pore diameter using molecular dynamics (MD) simulations has also been carried out. These simulations were carried out in an attempt to determine at which pore size fluid-wall interactions versus purely fluid-fluid interactions become important in terms of playing a role in the mechanism of fluid transport in the pores of gas shales. The Klinkenberg effect is a result of gas slippage along the walls of a pore, in which fluid-wall interactions dominate over fluid-fluid interactions and can occur when the pore diameter approaches the mean free path of the gas. Conveniently, MD simulations can be carried out to determine at which pore diameter this effect becomes pronounced. Figure 83 shows the velocity profiles of pure CO_2 and CH_4 fluids in 1.9, 3.8, and 7.6-nm sized pores. As the pore size increases (i.e., pore diameter of 7.6 nm) it is evident that fluid-fluid interactions dominate resulting in the familiar Hagen-Poiseuille flow vs. the plug-flow behavior in smaller pores (i.e., pore diameter of 1.9 nm) where fluid-wall interactions dominate in the Knudsen regime. The transition between these two flow regimes occurs somewhere in the neighborhood of 4 nm. Therefore, since both micro (i.e., < 2 nm) and mesopores exist in gas shales, a combination of these two transport mechanisms is expected to occur.

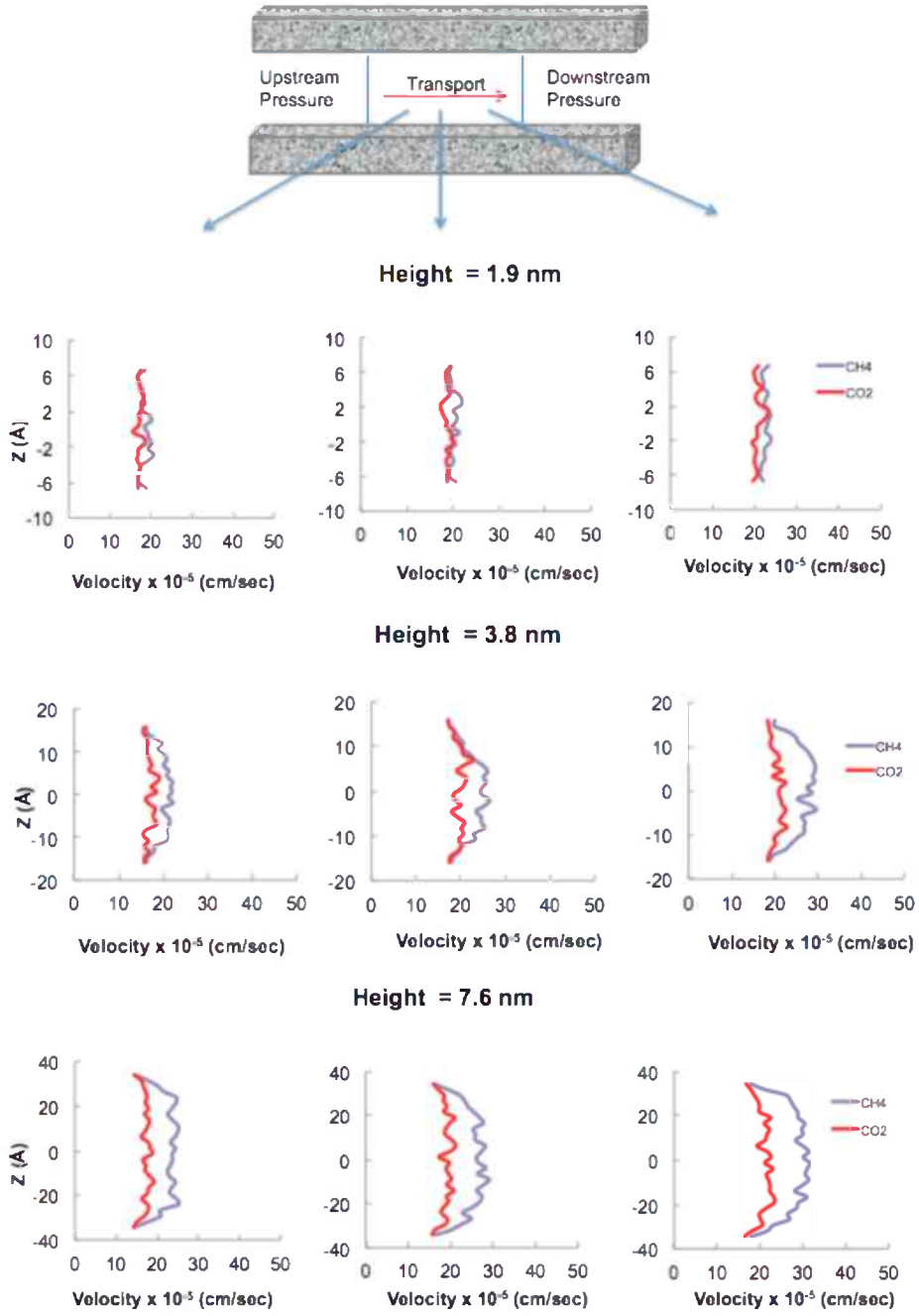

Figure 83. Velocity profiles of pure CO_2 and CH_4 in 1.9, 3.8, and 7.6 nm-sized carbon slit Pores exhibiting the relevance of the fluid-wall interactions at smaller pore sized.

Predicting Klinkenberg Constants from Molecular Dynamics Simulations Adsorption

We have investigated the Klinkenberg effect for a model fluid confined in micro and mesopores. The density and streaming velocity profiles of the fluid undergoing a pressure gradient along the pore have been examined in detail. Within the theory of Klinkenberg

porous media is approximated as a bundle of equidimensional pore capillaries of radius *r* with a diameter comparable to the mean free path of the fluid particles and that the interactions between the fluid particles and the capillary walls contribute to the forward movement of gas molecules in the transport direction, resulting in "gas slippage" that leads to reduced viscous drag and enhanced permeability (Klinkenberg 1941). Klinkenberg noted that in the pore capillary system the mean free path (λ) is inversely proportional to the mean pressure (P_m):

$$\frac{4c\lambda}{r} = \frac{b}{p_m} \tag{1}$$

where *c* is a constant approximated at unity in this case, and *b* is referred to as the gas slippage factor. Klinkenberg combined Poiseuille's Law for gas flow in capillaries (modified for gas slippage) with Darcy's Law for flow in porous media to obtain:

$$k_g = k_\infty \left(1 + \frac{4c\lambda}{r}\right) \tag{2}$$

Combining Equations 1 and 2, leads to the familiar Klinkenberg equation:

$$k_g = k_\infty \left(1 + \frac{b}{p_m}\right) \tag{3}$$

Non-equilibrium molecular dynamics simulations of pure methane and carbon dioxide and their equimolar mixtures were conducted. Figure 6 represents the time-averaged velocity profiles, v_i^x (z), for the two components in the yz planes (perpendicular to the direction of the applied pressure gradient) at 1/4, 1/2, and 3/4 of the pore length. As Figure 6 shows, the velocity profiles of both CH_4 and CO_2 components in the mixture deviate from Navier-Stokes hydrodynamic predictions. The parabolic profile is replaced with a uniform velocity profile (plug flow) at the center of the pore, as the molecular streaming becomes dominant transport mechanism due to the increased pore-wall effects (Akkutlu and Fathi, 2011).

Also, the velocity profiles of both CH_4 and CO_2 are equal in the pore and *non-zero* at the closest layer to the wall. We may then conclude that the particle-wall collisions likely influence the velocity profile and, due to the increased pore-wall effects, molecular streaming becomes dominant. A thin layer adjacent to the wall exists where only collisions of molecules with the pore wall occur and collisions among molecules may be ignored, which is consistent with Klinkenberg's theory (Bravo, 2007). In addition, as the fluid approaches the lower pressure along the pore the velocity of both components increases, as expected.

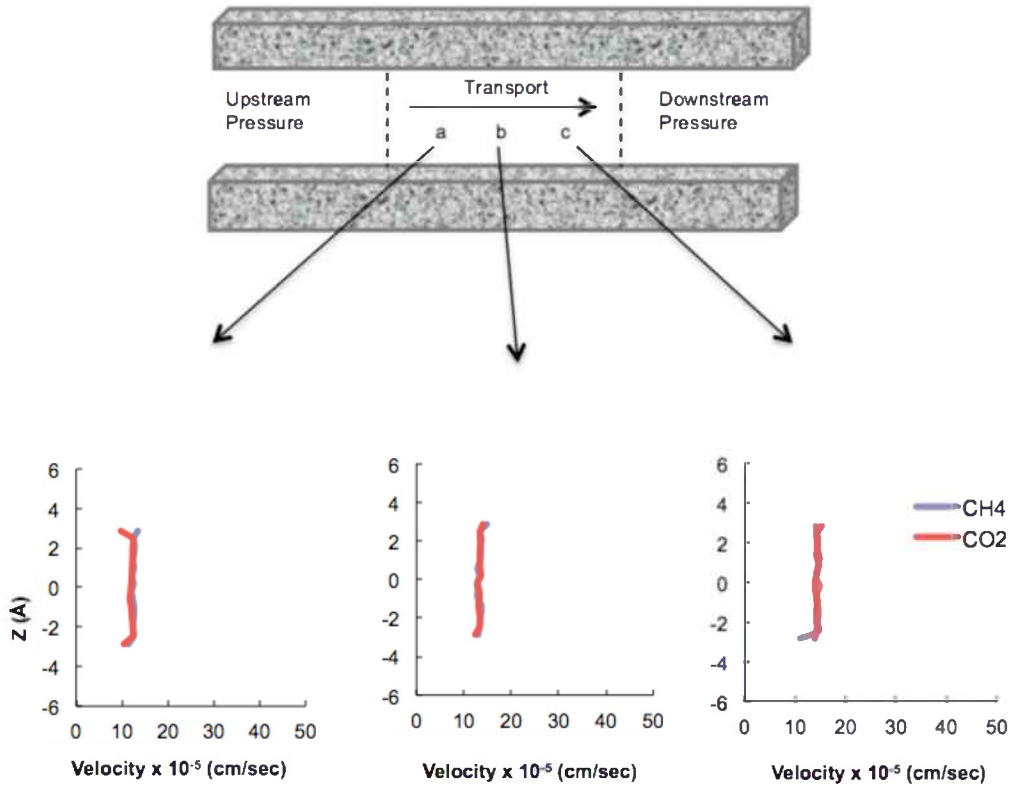

Figure 84. Velocity profiles $v^x(z)$ of CH_4 and CO_2 in the pore cross section at 1/4 (a), 1/2 (b), and 3/4 (c) of the pore length. The pore size is 11.4 Å and the upstream and downstream pressures are 3 and 1 atm, respectively.

To better understand the distributions of CH_4 and CO_2 in the pore, Figure 86 presents the time-averaged densities, $\rho_i^x(z)$, for the two components in the yz planes at 1/4, 1/2, and 3/4 of the pore length. As shown, each component in the fluid mixture forms only two adsorbed layers close to the walls, which indicates that most molecules are distributed near the walls, as is expected for a gaseous state in a pore. Another feature of Figure 85 worth mentioning is that the density of CO_2 is higher than that of CH_4, an effect caused by the adsorption affinity of the gases for the carbon surface. The energy contribution of CO_2-carbon interactions is greater than that of CH_4-carbon interactions, i.e., the carbon atoms comprising the pore surface are more attractive to CO_2 than to CH_4 molecules.

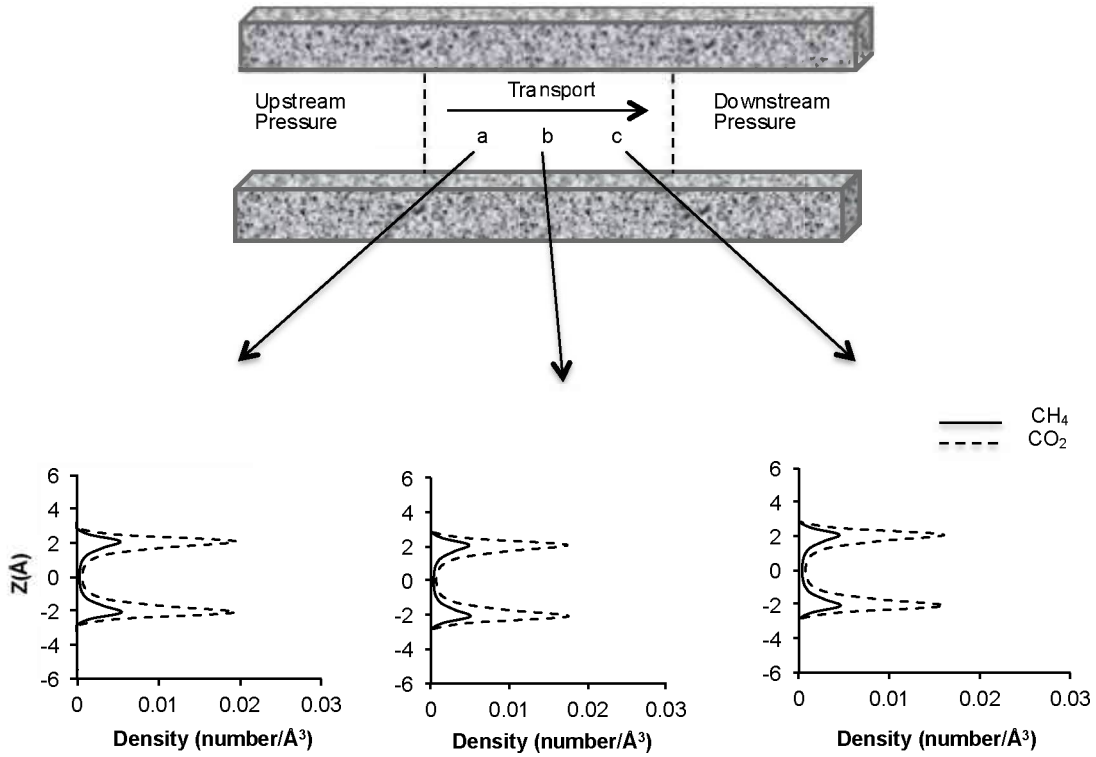

Figure 85. Density profiles $\rho^{\lambda}(z)$ of CH_4 (solid curves) and CO_2 (dashed curves) in the pore's cross sections at 1/4 (a), 1/2 (b), and 3/4 (c) of the pore length. The pore size is 11.4 Å and the upstream and downstream pressures are 3 and 1 atm, respectively.

It is important to determine the pore size depicting the transition from plug-flow to parabolic velocity profile. To study the effect of pore size on the velocity profiles, the pore size was increased from micro- to mesopores. Figure 86 shows the time-averaged velocity profiles, $v_i^x(z)$, for the two components at the center of the pore under precisely the same conditions as Figure 84, except that now the pore sizes are 19.0, 26.7, 38.1, and 57.1 Å. The results indicate that as the pore size increases, the pore becomes less packed and as molecular transport through the pore is less hindered, the velocity of the gases will increase. This is more noticeable for CH_4 molecules than CO_2 molecules as CH_4 is more evenly distributed throughout the pore. Moreover, it seems that as pore size increases, the fluid regime becomes more parabolic and classical flow behavior is approached. The velocity profile of CO_2 is affected only weakly by the change in pore size, while the velocity profile of CH_4 appears to depend rather strongly the pore size. These features should be compared with those encountered with smaller pores when the particle-wall collisions influence the velocity profile. In addition, by increasing the pore size, the velocity of CH_4 molecules becomes larger than that of CO_2, which can be attributed to the higher adsorption of CO_2 on the carbon surface, as described previously, and the higher mobility of CH_4 molecules in the larger pores.

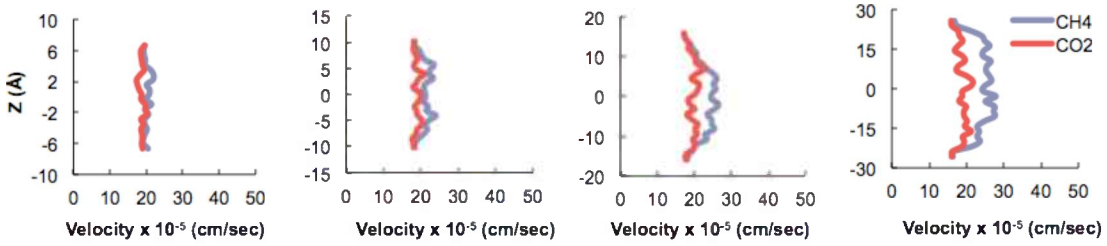

Figure 86. Velocity profiles $v^x(z)$ of CH_4 and CO_2 in the pore cross sections at the center of the pore. The pore sizes are 19.0, 26.7, 38.1, and 57.1 Å from left to right, respectively. The upstream and downstream pressures are 3 and 1 atm, respectively.

In addition to velocity profiles, CO_2 and CH_4 permeabilities may also be predicted using molecular simulation. The simulations results shown in Figures 84-86 are based upon fluid transport in a very idealized carbon-based slit pore. However, the real system is in fact a distribution of pores connected in a complex 3-D pore network. Therefore, estimating permeabilities using a slit-pore approach would result in an artificially high permeability estimate. For this reason the permeability predictions were carried out using a 3-D pore network model based upon a Voronoi tessellation approach, which is described in detail in our recently published work (Firouzi and Wilcox, 2012). In general, for petroleum applications the units of permeability are most often expressed in units of Darcy. In the membrane community the permeability units are generalized from the flux equation, in which the flux is equal to the mass-transfer coefficient multiplied by a pressure gradient driving force. In this case the mass-transfer coefficient is equal to the divided by the length scale over which the mass transfer takes place. The general permeability units in this case are mole/min·cm·atm. When converting these general permeability units to Darcy units, one has to assume a fluid viscosity. The fluid viscosity can be obtained from the bulk fluid viscosity at a given temperature and pressure, available in the NIST Webbook. However, it is not clear that the bulk fluid viscosity is equal to the viscosity of the fluid in the nanoconfinement of the pore. In previous studies it has been shown that the viscosity of confined fluids is dependent on the structure and pore diameter, which is often different from the viscosity of the bulk system (Sokhan et al. 2002; Thomas et al. 2008; Khademi et al. 2011).

To investigate the deviation of viscosity from bulk to the confinement of micro and mesopores, molecular simulations were carried out to determine self diffusivities, which were then used to predict fluid viscosities of CO_2 and CH_4. The self-diffusion coefficients may be calculated from the Green-Kubo relation in three dimensions using:

$$D = \frac{1}{3N}\sum_{i=1}^{N}\int_{0}^{\infty}\left\langle v_i(t)\, v_i(0)\right\rangle dt \qquad (4)$$

where N is the total number of molecules, and $v_i(t)$ is the velocity of molecule I at time t. The bracketed quantity represents the velocity autocorrelation function (ACF). The viscosity can then be estimated from the Einstein relation using:

$$\mu = \frac{k_B T}{3\pi d D} \tag{5}$$

where k_B is the Boltzmann's constant, T is the temperature, d *is* the diameter of the fluid molecule, and D is the self-diffusivity estimated from Equation (4).

Figure 87 presents the permeability of pure components, CO_2 and CH_4. The slippage factor b and k_∞ have been calculated based on Equation (3) described previously.

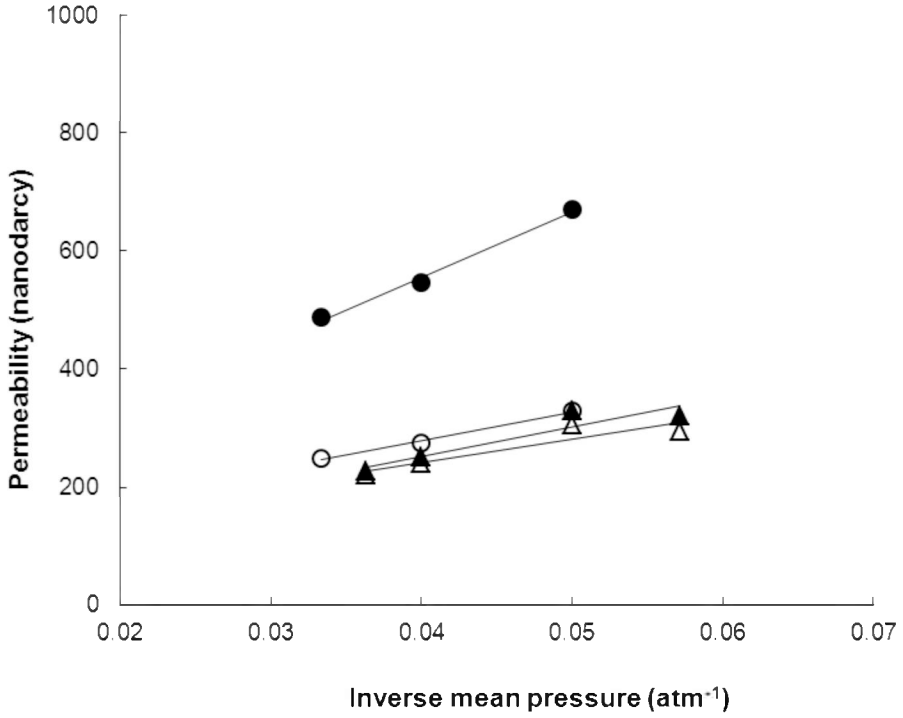

Figure 87. The dependence of the permeability of pure CH_4 (triangles) and CO_2 (circles) on inverse mean pressure applied to the 3-D pore network. The downstream pressures are fixed at 10 atm. The average pore size and the porosity of the pore network is 20 Å, and 20% respectively..

From Figure 87 it is clear that the use of the bulk-phase viscosity for estimating the permeability of CO_2 in a 3-D micropore network is not an appropriate assumption as it underestimates the CO_2 permeability significantly, i.e., between 200-300 nD compared to 500-700 nD. Through the use of the viscosity from molecular simulation can lead to permeability estimates 2 times that of the bulk-phase viscosity in the case of CO_2. On the other hand, the use of the bulk-phase CH_4 viscosity is a reasonable assumption for the permeability estimate in units of Darcy, which is consistent with the previous work that shows CH_4 is less influenced by the pore walls compared with CO_2.

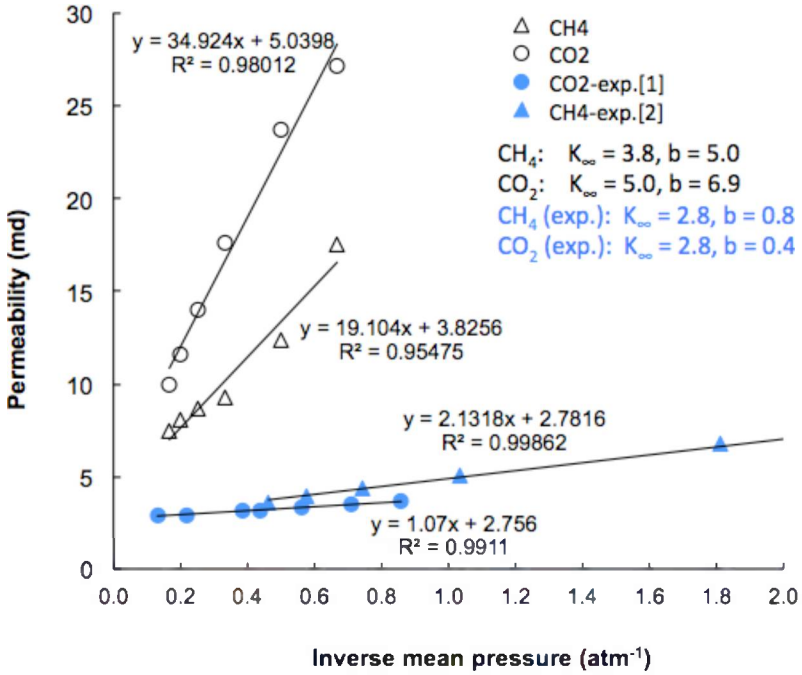

Figure 88. The dependence of the permeability of CH_4 (triangles) and CO_2 (circles) on the inverse mean pressure applied to a pore of size 11.4. The downstream pressure is 1 atm, while the upstream pressure increases. Ref [1]: Petroleum Reservoir Engineering (Physical Properties), J. W. Amyx, D.M. Bass, R.L.Whiting, McGraw-Hill 1960 and Ref [2]: J.C. Calhoun, S.J. Yuster, Drilling and Production Practice, 1946.

In addition to investigating the Klinkenberg effect using molecular simulation of CO_2, the study of the non-adsorbing gas, He, has also been carried out to compare to the permeability experiments carried out as discussed later in the report. To investigate the influence on permeability versus porosity, two 3D pore network models were investigated with porosities of 15% and 20%, with the lower porosity more applicable to the real samples investigated in the experimental permeability measurements. In addition, it is important to note that the simulations were carried out on a 3D pore network with an average pore size of 2nm, which is likely slightly smaller than present in the real shale samples. Figure 89 shows an example of the He permeability as a function of inverse mean pore pressure. The 15% 3D pore network resulted in an He permeability between 40-60 nD, while the 20% 3D pore network resulted in a significantly increased permeability of 600 to 800 nD.

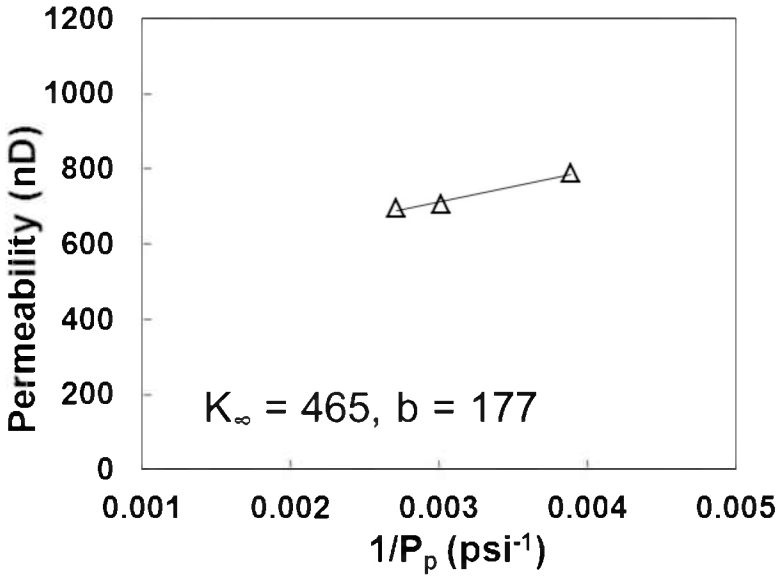

Figure 90. The dependence of the permeability of He on the inverse mean pressure applied to a 3D pore network with porosity of 20% and an average pore size of 2 nm. Decreasing the porosity down to 15% decreases the permeability to 40-60 nD.

Model Improvement for CO_2

In order to take into account the charge and flexibility of the CO_2 molecule, the MD simulation code was updated accordingly. These updates allow for a more accurate model of CO_2 as it interacts with pore walls and itself at elevated temperatures and pressures indicative of the subsurface conditions that the shale experiences. Carbon dioxide is modeled as a flexible molecule, with fixed bond lengths, but with a flexible bond angle, having three Lennard-Jones (LJ) sites, plus point charges to account for its quadrupole moment, centered on each atom.

The CO_2 molecules are represented by a united-atom (UA) model (Ryckaert and Bellemans, 1978; Van der Ploeg and Berendsen, 1982; Harris and Yung, 1995) in which the C and O atoms are considered as single interaction centers with their own effective potentials. The atoms and the UA centers are connected by harmonic potentials. The distance between the atoms is fixed at 1.16Å. The intramolecular interactions consist of the bond-bending (BB) forces in which the van der Ploeg-Berendsen potential (Van der Ploeg and Berendsen, 1982) is used:

$$U_{BB}(\theta) = \frac{1}{2} k_\theta (\theta - \theta_0)^2 \qquad (6)$$

where k_θ= 1275 kJ/mole/rad^2, θ_0=180°, and θ is the angle between the atomic bonds. The values of the molecular LJ parameters used in the simulations are listed in Table 8 where k_B is the Boltzmann's constant equal to 0.001987 kcal/mole/K.

Table 8. Lennard-Jones Parameters for CO_2 Molecules

	ε/k_B [K]	σ [Å]
$C(CO_2)$-$C(CO_2)$	26.2	2.824
$O(CO_2)$-$O(CO_2)$	74.8	3.027
$C(CO_2)$-$O(CO_2)$	44.8	2.922
C(graphite)-C(graphite)	28.0	3.400
$C(CO_2)$-C(graphite)	27.1	3.112
$O(CO_2)$-C(graphite)	45.8	3.214

The nonbonded interactions between interaction centers of different molecules are described with a cut-and-shifted LJ potential. The RATTLE algorithm was employed to solve the equations of motion. The configurational-bias Monte Carlo technique (CBMC) was used for the efficient generation of the CO_2 chain molecules since the direct generation of the CO_2 chain molecules and their insertion into the control volumes (CVs) that are connected to the pores greatly slows the simulations (De Pablo et al., 1992; Frenkel et al., 1991; Harris and Rice, 1988; Laso et al., 1992; Macedonia and Maginn, 1999; Mooij et al., 1992; Siepmann and Frenkel, 1992; Smit et al., 1995; Firouzi et al. 2004; Firouzi et al. 2007). We then combined the CBMC method with the grand-canonical MC technique to insert the CO_2 chains in the two CVs and subsequently in the pores. The atom-by-atom growth of the molecules is done in such a way that regions of favorable energy are identified, and the overlap with other molecules is avoided, hence speeding-up the computations greatly. Non-equilibrium molecular dynamics (NEMD) simulations with an external driving force imposed on the system was used. Simulations were conducted to determine the effect of pore size, temperature and exposure to an external potential on the pore filling and gas transport in carbon slit micro- and mesopores as well as 3-D pore networks.

Figure 91 shows the time-averaged CO_2 density profile (averaged in the *yz* planes) along the pore network. The vertical dashed lines indicate the boundaries of the pore network region. The density profiles are essentially flat in the two CVs, with numerical values that match those obtained by the GCMC method at the same conditions, indicating that the chemical potentials in the two CVs have been properly maintained during the NEMD simulations. As can be seen in Figure 91, the CO_2 density decreases along the 3D pore network in the transport region, which is expected. This feature is clearly seen in Figure 78, which shows the snapshot of the same pores and the distribution of CO_2 molecules for the same conditions as in Figure 91, obtained at steady state. From this figure it is evident that the CO_2 density decreases from left to right.

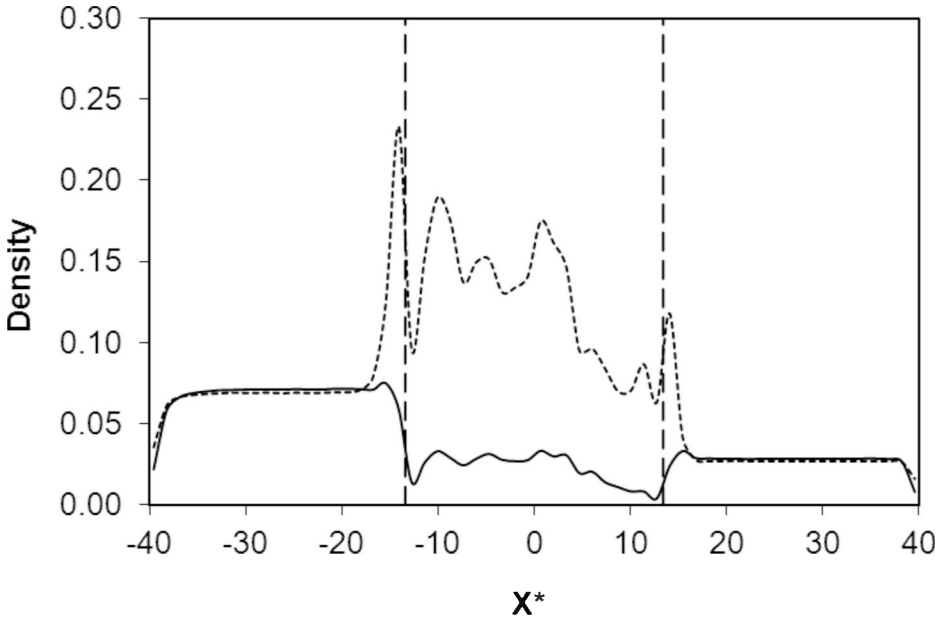

Figure 92. Time-averaged density profiles of flexible-quadrupole CO_2 (solid curve) and inflexible-neutralCO_2 (dashed curve) in the transport direction *x*. The average pore size and the porosity of the pore network is 12.5 Å and 30%, respectively. The upstream and downstream pressures are 50 and 20 atm, respectively. The temperature of the system is 25°C.

The dashed curve of Figure 92 shows the previous model in which the CO_2 molecule was neutral and inflexible. The previous model shows an overestimate in the density in addition to enhanced entrance and exit effects of the 3D pore network. These differences will be explored in future work. More complex molecular models will be used to model the graphite structures containing local charge and defect sites within the pores, in addition to the inclusion of chemical functional groups inside the cavities to generate a more realistic model of the complex shale system. These fundamental studies indicate the significance of molecular-scale phenomena, which lead to a greater understanding of the mechanisms associated with gas transport in the confined spaces.

Non-equilibrium molecular dynamics (NEMD) simulations have been carried out at similar conditions to establish a comparison between conventional permeability measurements at the core scale and permeability predictions using molecular dynamics simulations at the pore scale. The NEMD method is ideally suited for the experimental situation in which an external driving force, such as a chemical potential or pressure gradient, is applied to a given pore or pore network. To investigate gas permeability and predict Klinkenberg parameters using a more realistic model, a 3-D carbon-pore network structure is used by atomistically using the Voronoi tessellation method to represent the carbon-based kerogen porous structure of shale.

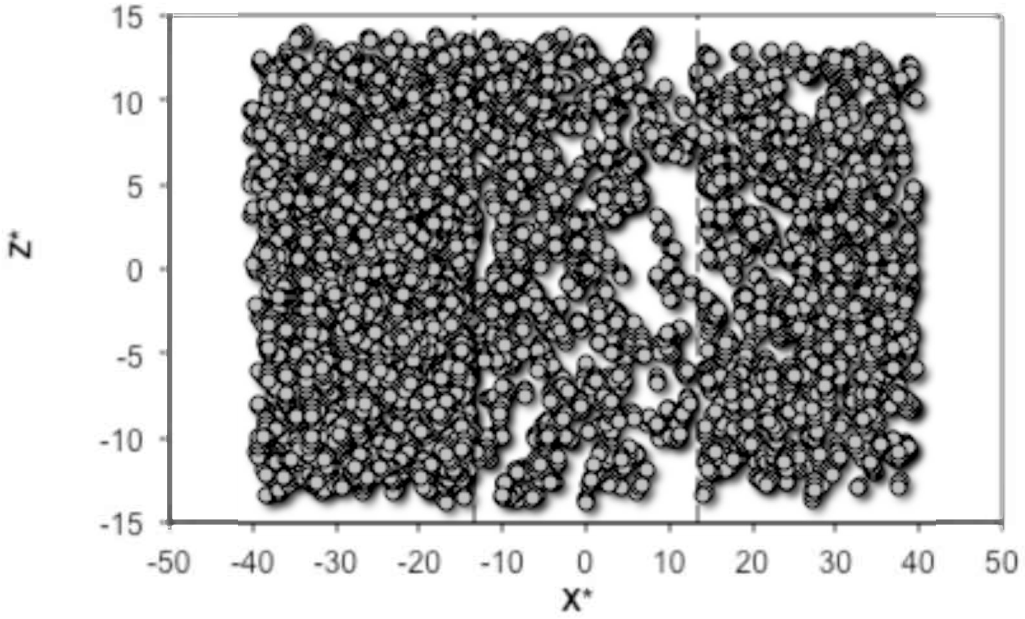

Enlarge

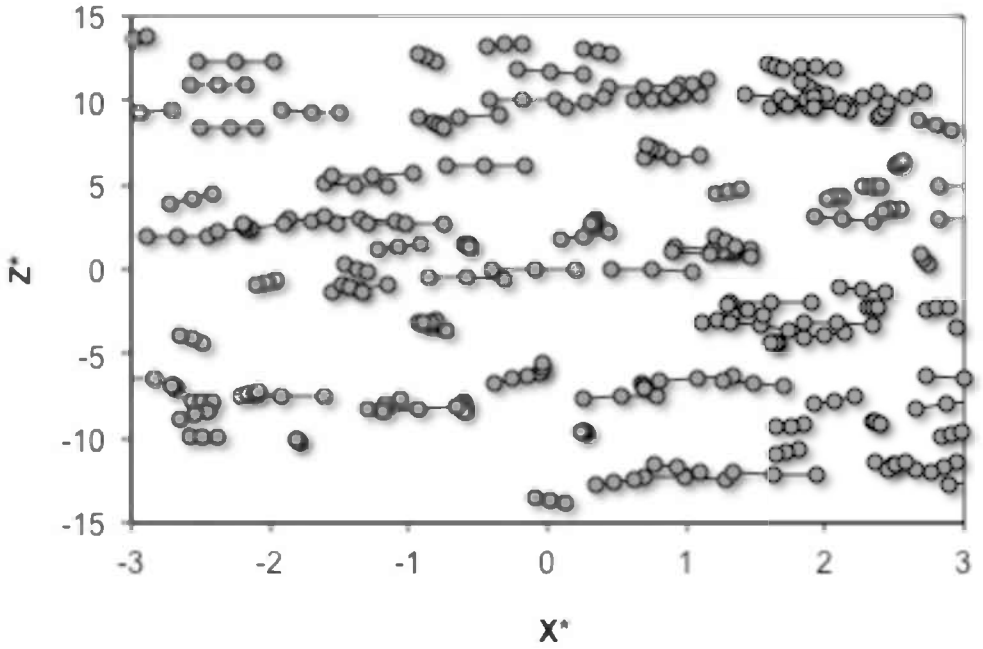

Figure 93. The distribution of CO_2 chain molecules in the pore network for the same conditions as Figure 83.

The size of the initial graphite cell in the model is 102, 103, and 103Å in x-, y-, and z-directions, respectively. The carbon atoms were packed with 31 layers of graphite. The total initial number of carbon atoms in each graphite layer and the simulation cell were 4,032 and 124,992, respectively. The porosity is 25% and the pores are selected randomly, with average pore sizes of 2 nm. The total number of carbon atoms in generated 3-D pore network matrix is 93,953. Although the porosity used for MD simulations may appear to be large, Vega et al., (2013) have imaged the spatial distribution of porosity in core-sized samples of Eagle Ford shale and have found localized volumes of shale with porosities similar to 25% in cores with an *average* porosity of 5.4%. Simulations are conducted to determine the effect of the pore structure and pressure gradient on helium permeability.

Figure 84 represents the dependence of the permeability of helium on the inverse mean pressure applied to the generated pore network model. The downstream pressure is fixed at 146.96 psi, while the upstream pressures are varied. By increasing the upstream pressure but maintaining the same downstream pressure along the pore, the permeability of helium decreases. This phenomena is described by the theory of Klinkenberg in that at the lower pressures the mean free path increases thereby increasing the slippage effect and leading to enhanced gas permeability, while at the larger mean pressures the slippage effect is suppressed leading to reduced permeability. The same behavior for CH_4 and CO_2 gases are found and discussed in detail in previous work (Firouzi and Wilcox, 2013).

The average pore size in the 3-D pore network used in the MD simulation is 2 nm, hence the calculated permeability represents flow in micro and mesopores. The gas permeability obtained by the pulse decay experiment is approximately an order of magnitude greater than that calculated by MD simulation. Gas transport is typically enhanced in micro and mesopores due to molecular streaming or Knudsen diffusion over Darcy flow where the gas velocity at the pore walls is non-zero and the "gas slippage" reduces viscous drag and increases permeability (Firouzi and Wilcox, 2013). The experimental permeability measurements of the intact core are greater than those obtained by the MD simulations because the core contains a broader distribution of pore sizes with likely differing connectivity including macro- and meso-pores. The MD simulations estimate accurately the gas flow in purely micropores. The experimental permeability is extracted from the early-time pressure profile that corresponds to macropores as indicated by the estimated apparent pore diameter. This permeability is referred to as Darcy permeability.

In addition, coal and the organic components of shale are comprised of extremely complex structures with surface functionality and natural fractures. More complex molecular models of graphite structures containing fractures, local charge and defect sites within the pores, in addition to the inclusion of chemical functional groups inside the cavities to generate a more realistic model of natural systems will be considered in future work.

To predict accurately gas transport in shale systems, it is important to study the transport phenomena of a non-adsorptive gas such as helium to investigate gas "slippage".

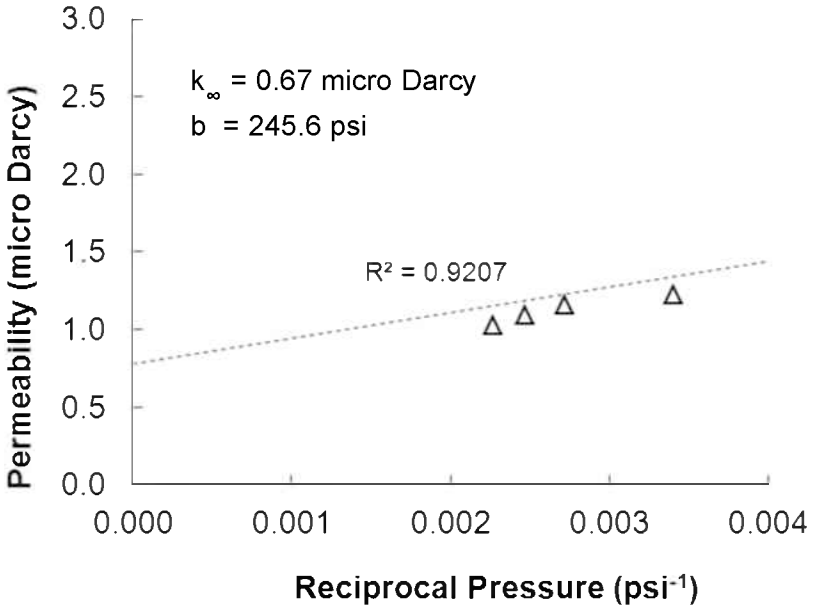

Figure 84. The dependence of the permeability of helium on inverse mean pressure applied to the pore network. The downstream pressures are fixed at 146.96 (psi) while the upstream pressure varies.

3.2: In-situ imaging of gas transport pathways

In the area of transport, we wish to image in real time the movement (by convection and diffusion) of gas through laboratory samples. Some gases, such as krypton or xenon, have markedly different X-ray attenuation properties in comparison to methane. Thus, such gases are useful for tracing the location and rate of gas transport as they replace methane or some other initial gas. Barnett, Eagle Ford, and Haynesville gas shale samples were studied. The pore connectivity of these samples was investigated using krypton as a high contrast gas injected and monitored with an X-ray computed tomography (CT) technique that enables the visualization of porosity and fracture.

CT scanning is a non-destructive imaging technique that provides two and three-dimensional images of opaque objects. It is relatively easy to apply, offers fine spatial resolution, and is adaptable to many types of experimental procedures. It has emerged as an important and powerful tool for non-destructive imaging because it is relatively easy and flexible to apply, offers fine spatial resolution and is adaptable to many types of experimental procedures and flow conditions (Akin and Kovscek, 2003). By using imaging techniques, the distribution of bulk density, fractures, and volumetric strain fraction can be defined and used to understand flow characteristics of gas in these naturally fractured, dual porosity reservoirs (Saites et al., 2006).

In this study, the object of interest is placed inside a circular array of X-ray detectors and a single X-ray source rotates around the sample. Because the X-ray tube moves around the apparatus in a circular path and reconstruction algorithms assume symmetric objects,

images display fewer artifacts when the scanned object has a circular cross-section (e.g., Le Guen and Kovscek, 2006). After the image is reconstructed, the computer converts the measured attenuation into CT (dimensionless Hounsfield) units normalized to the linear coefficient of water. Each Hounsfield unit represents a 0.1% change in density with respect to the calibration density scale. By definition, the CT numbers of air and water are -1000 and 0, respectively. Akin and Kovscek (2003) provide a comprehensive review.

Early adopters of CT imaging to rock characterization in the oil industry (Honarpour et al., 1985; Vinegar and Wellington, 1987; Withjack, 1988) offered reports on the measurements of rock properties such as porosity and flow visualization for a range of studies. Withjack, (1988) performed CT porosity measurements from two scans at the same location(s) of the sample under two different saturating fluids as

$$\frac{CT_{1r} - CT_{2r}}{CT_1 - CT_2} \tag{1}$$

where the subscripts 1 and 2 represent the saturating fluids, normally these are water and air, respectively. The subscripts 1r and 2r, in turn, represent the CT numbers of rock saturated with fluids 1 and 2, respectively.

With CT-scan imaging, there is a tradeoff between the spatial resolution and the sample size. Sample size is generally two to three orders of magnitude greater than the resolution. For example, to achieve roughly 20 nm spatial resolution, a sample size of about 60 μm is useful (Vega et al, 2013). For core-sized samples, greater voxel size is needed. In this work, we seek to measure the core-scale porosity distribution of tight, gas-bearing rocks where saturation with water is not practical. Saturation of samples with gas that provides sufficient attenuation to apply Eq. (1) does appear to be practical, however. For example Lu et al. (1992) used a dual-scan technique with a single energy, as proposed by Moss et al. (1992), to calculate porosity using Eq (1). They used krypton gas as the radio opaque agent and determined porosity of Devonian shale samples. Moss et al. (1992) went on to measure dual porosity distributions of Monterey and Bakken shale as well as coal using xenon for contrast. Lu et al. (1994) also examined Devonian shales to determine gas storage under dynamic flow conditions. Watson and Mudra (1994) characterized Devonian shales with X-ray tomography also using xenon and Eq. (1).

3.2.2 Samples

Both coal and shale samples were used. A group of gas shale core samples from the Barnett, Haynesville, and Eagle Ford formations were studied. The field sample plugs were 1 inch (2.5 cm) diameter and approximately 2 inches 5.1 cm) in length and were cut parallel to bedding. Sample porosity was estimated to be between 2 and 7% **(Table 9)**. Clay content varies between 27 and 39 percent. TOC ranges between 3.75 and 5.76, approximately. One of the Barnett samples displays a set of two calcite-filled fractures that run length-wise along the core. Dark-grey colored, the samples do not show any other visible markings.

3.2.3 Experimental

The experimental setup consisted of apparatus, core holders, and X-ray CT scanners as detailed next.

Shale imaging was completed on a GE HiSpeed CT/i fifth generation medical scanner operated in helical mode. The voxel dimension is 0.25 by 0.25 by 1 mm, the tube current is 120 mA, and the energy level of the radiation ranges from 80 to 120 keV. The images obtained display sufficient contrast among rock features and do not exhibit detectable positioning errors because of the large energy level and positioning system, respectively. An example resolution from the CT/i machine is shown in **Fig. 85.** The fine grid indicates voxel dimension projected in two dimensions and raw CT numbers are presented.

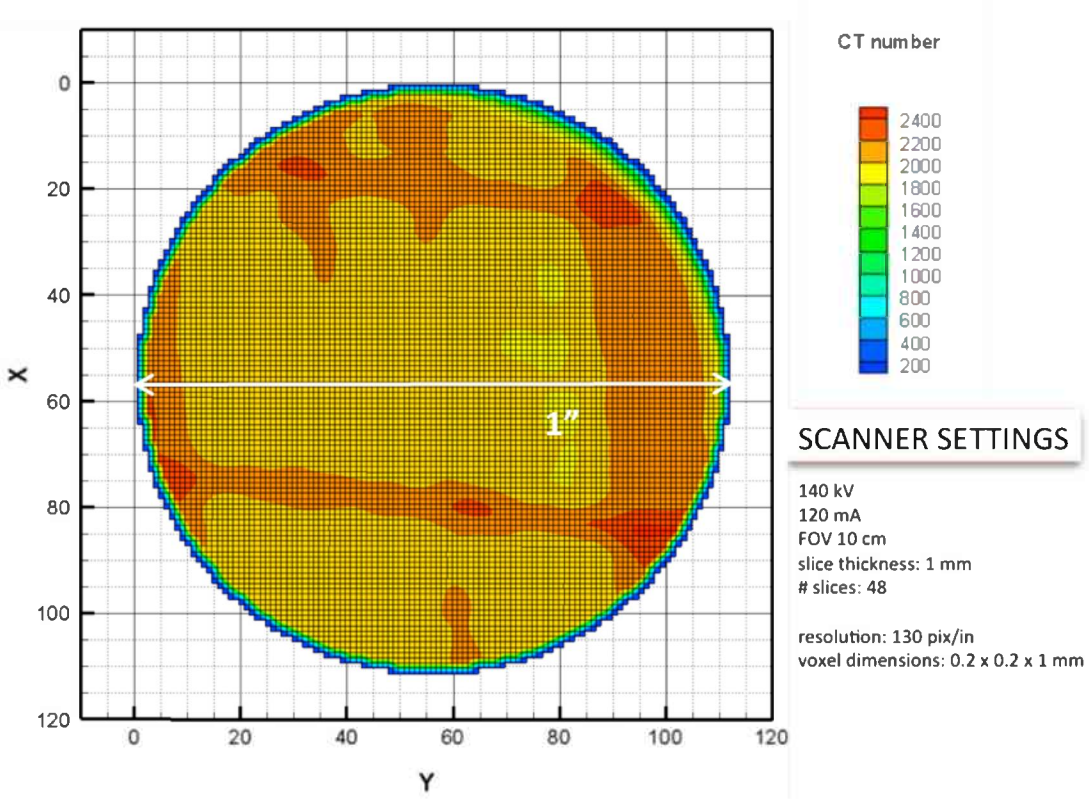

Figure 85. GE HiSpeed CTi X-ray CT scanner image resolution details for shale samples.

X-ray CT, as employed here, provides a fraction of a millimeter spatial resolution to measure porosity. Equation (1) demands sufficient contrast between scans of the sample filled with two different fluids. Hence, gases such as krypton that exhibit significant attenuation at the energy levels obtainable in our CT systems are needed.

Krypton gas has been used as the saturating fluid for Devonian shales (Lu et al, 1992) because of some similarities with natural gas, such as Lennard-Jones potential constant, polarizability and van der Waals radii. Lu et al. (1992) also speculate that krypton and methane may have similar storage properties on porous solids, so results found with

krypton may be translated (potentially) to natural gas estimates. Additionally, factors to choose krypton gas for our studies were that kinetic diameters of krypton and CO_2 are 0.3685 and 0.33 nm, respectively; and krypton gas provides significant contrast in attenuation as compared to vacuum, nitrogen, or air. **Figure 86** shows the CT numbers (H) of bulk krypton versus pressure (psi) and X-ray tube energy (keV) obtained in the CT/i scanner.

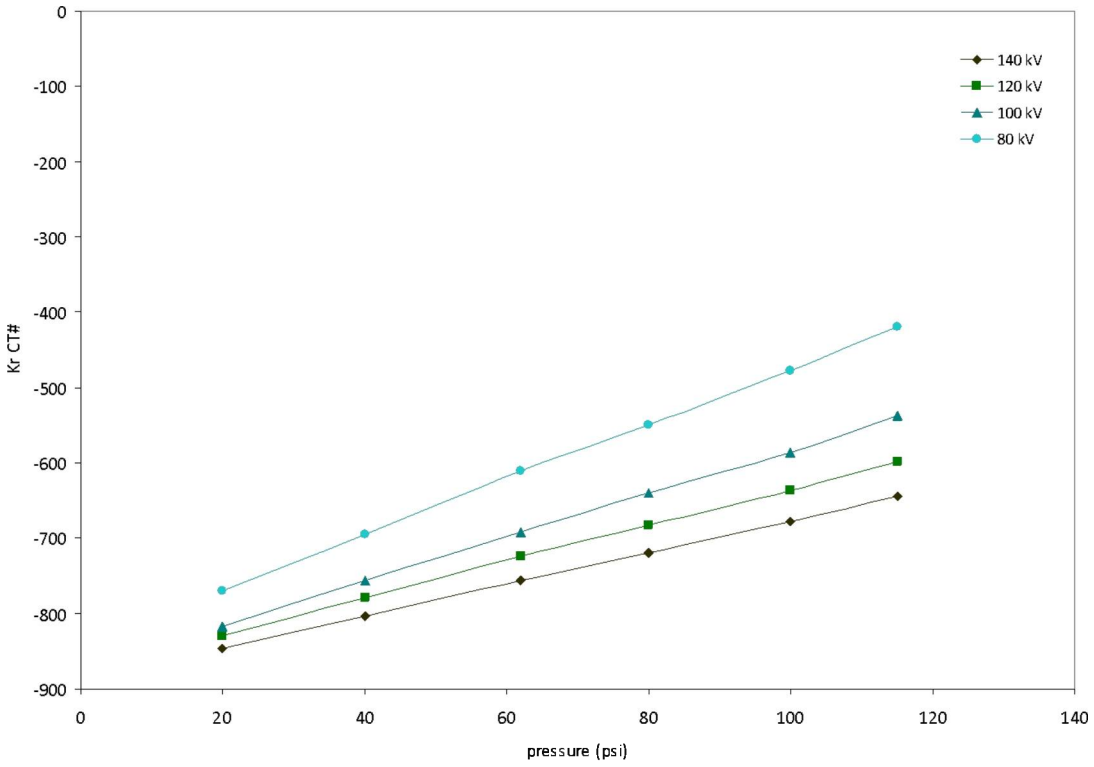

Figure 86. CT number of krypton gas versus pressure and CT scanner energy.

A coreholder system compatible with the reservoir material and the X-ray CT scanner was designed, fabricated and tested. The core samples were placed between two stainless steel end caps that contain fluid distribution channels that allow for gas circulation across the sample faces. The end caps provide access to a confining pressure system and to a pore pressure system. The samples were coated with a high temperature epoxy compound (730 Solvent Resistant Sealant, Dow Corning) and sleeved with heat-shrinkable Teflon (PTFE HS 2:1 Heat Shrink, Zeus). The core sleeve isolates the core from the confining fluid and allows realistic confining stress to be applied. The net effective stress applied to the samples was roughly 150-200 psi (1000-1400 kPa). An outer 1/6" thick aluminum sleeve slides over the core and seals via o-rings on the end caps. Threaded aluminum rods pass through the end caps and serve to hold the entire apparatus together when subjected to pressure. The apparatus is able to withstand pressures up to approximately 2,000 psi

(14,000 kPa). A sketch of the experimental setup is presented in **Fig. 87.** The assembled coreholder was oriented horizontally.

An experiment proceeds by first placing the core in a vacuum oven and heating to 70 °C until the weight of the sample stabilizes. The core is then jacketed (as described above) and placed in the coreholder. Confining pressure is applied. A vacuum pump is then used to remove any gas from the core. Gas injection occurs such that gas travels length-wise towards the production end of the core. The injection pressure is 100 psi (690 kPa). The valve at the production end is closed such that steady flow does not occur but rather pressure stabilization is sought. This mode of operation conserves the relatively expensive krypton. Pressure transducers send data to an acquisition system. Pressure stabilization is achieved when the pressure at the production end equals the injection pressure. The core is evacuated using the vacuum pump for subsequent experiments.

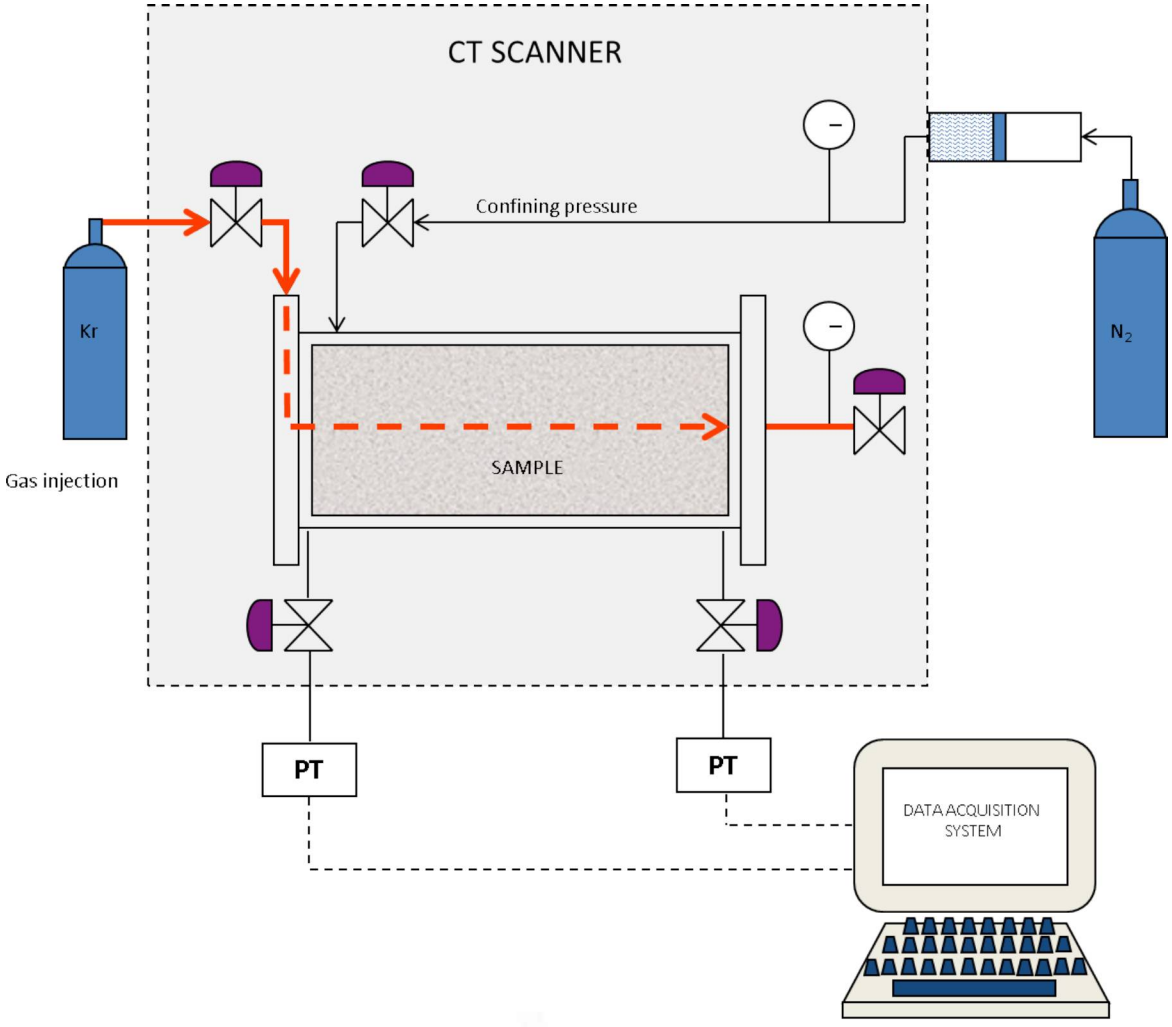

Figure 87. Shale imaging apparatus.

3.2.4 Results & Discussion—Constant Effective Stress

Figure 88 shows the principle of the porosity calculation. An evacuated and then gas-saturated sample is scanned, and a number of cross sectional slices are obtained. The cross-sectional images are then subtracted to obtain the difference in mass coefficient attenuation of the two states (represented by the CT number). The resulting group of images highlights the pore space penetrated by the gas and porosity follows from Eq. (1). These images, when reconstructed in three dimensions, depict the spatial distribution of porosity within the sample, as illustrated in **Figs. 88 and 89.**

Several shale samples were subjected to similar experiments. Varying results were obtained in achieving pressure stabilization of the gas injected in the samples due to low permeability and heterogeneity. An example of one result with krypton injection in a Barnett core sample is shown in **Fig. 90.** Although microporosity and microfractures are present in the sample, (Vega et al, 2013), such details are averaged into the porosity (structural details) that we measure for each voxel. Red shading indicates a porosity of 0.5 whereas black is 0. Calcite-filled fractures are apparent during visual inspection of the sample and in the reconstructed porosity map. Matrix material adjacent to the fracture is also evident. Average calculated porosity for the sample was 6.5% **(Table 9).** Fractures that appeared to be healed or cemented closed (presumably with calcite) are outlined in green in the photograph of the core in **Fig. 56**. These fractures seem to have larger porosity than the rest of the matrix and are permeable to krypton because of an imperfect filling of the fractures or opening of the fracture in the drilling/coring process. Core heterogeneity and bedding are clearly demonstrated in **Figs. 88 and 89.**

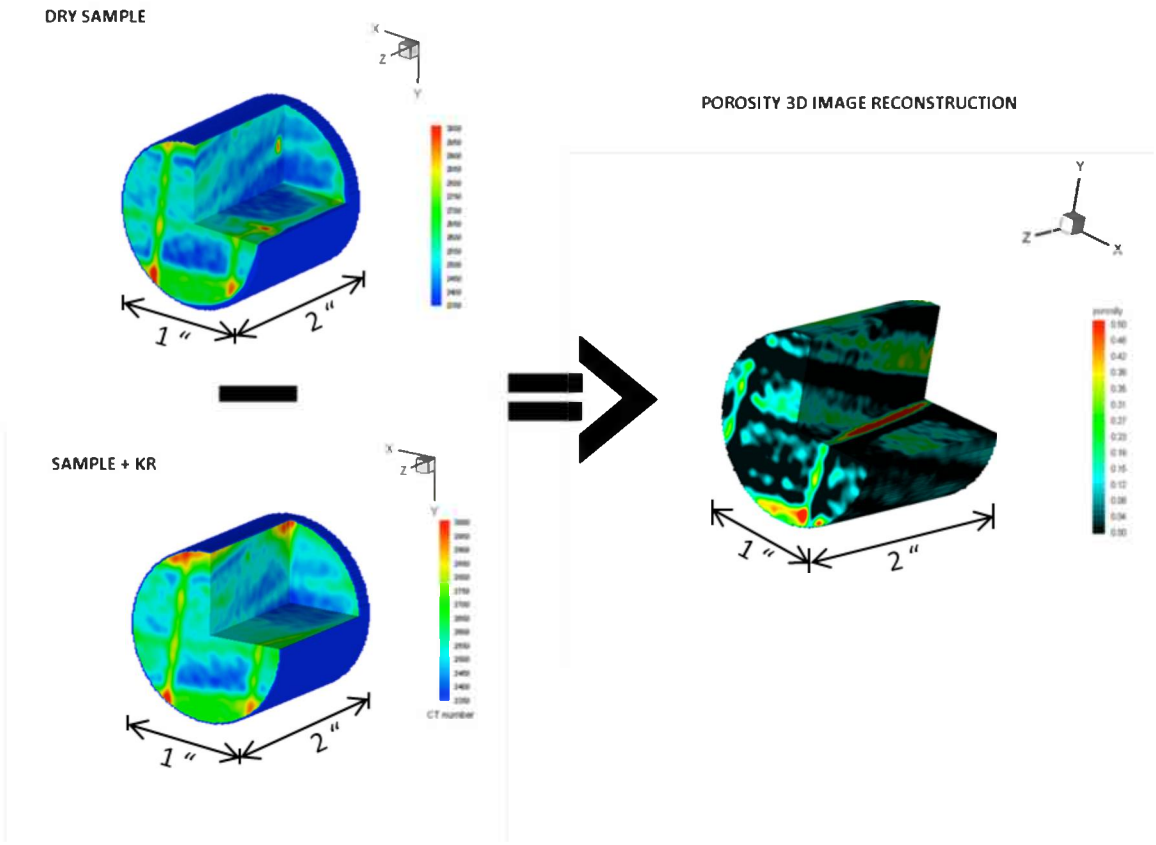

Figure 88. Image subtraction principle used to estimate porosity of a gas shale sample using CT images.

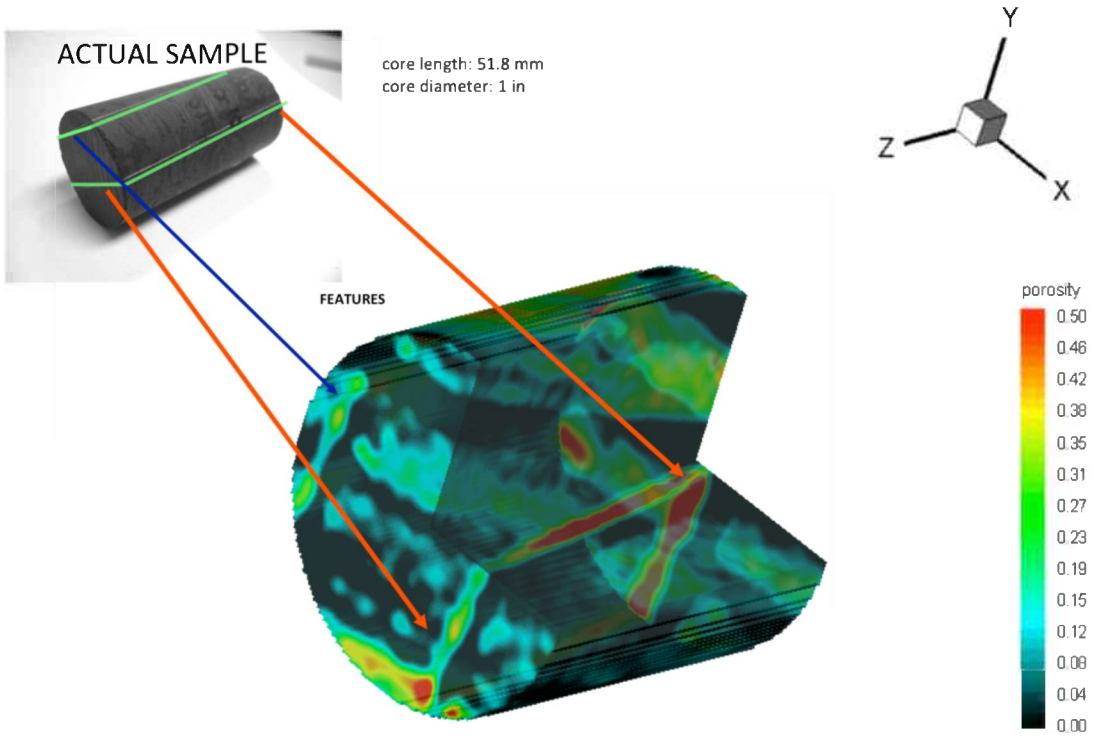

Figure 89. 3D porosity map reconstruction obtained for Barnett sample.

The 3D in-situ porosity images may be analyzed statistically. **Figure 90** shows the frequency (i.e., number of counts) of appearance of a particular porosity and gives a map of the three-dimensional porosity distribution as an inset, Barnett **(a)** and Eagle Ford **(b)**. The Eagle Ford sample has an average porosity of 0.054 but there is a long tail of greater porosity values. The average porosity of the core by CT scanning is obtained by summing the porosity measured in each voxel and dividing by the number of voxels. About 9% of the porosity measurements are greater than 0.15, but a significant fraction (43%) of the measured values are 0 as well.

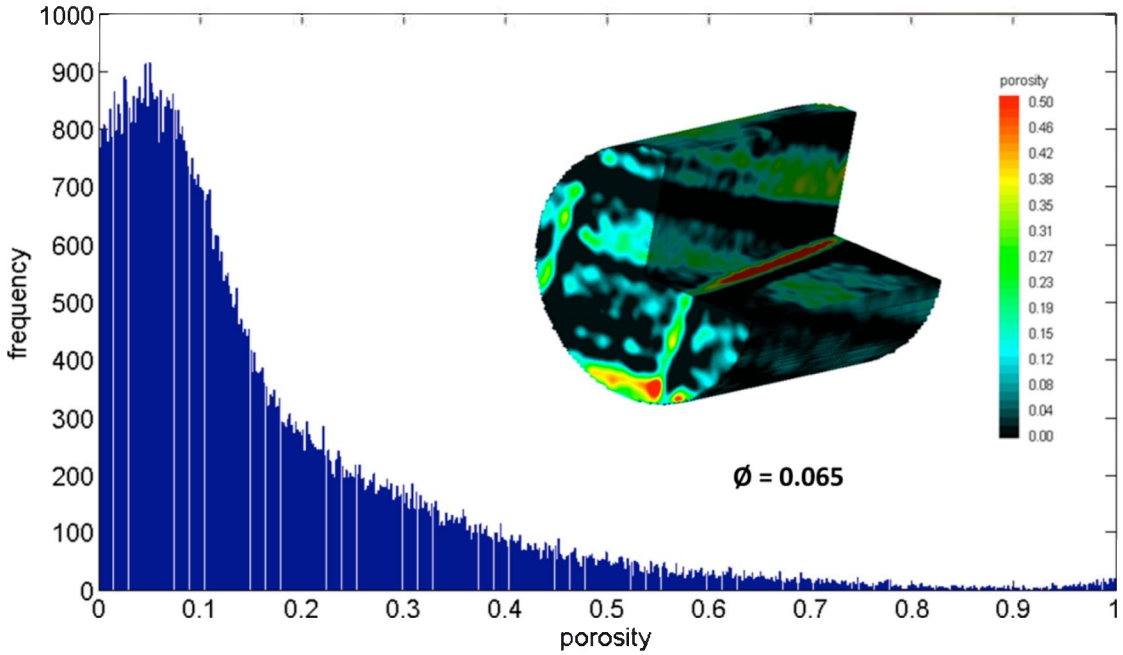

(a)

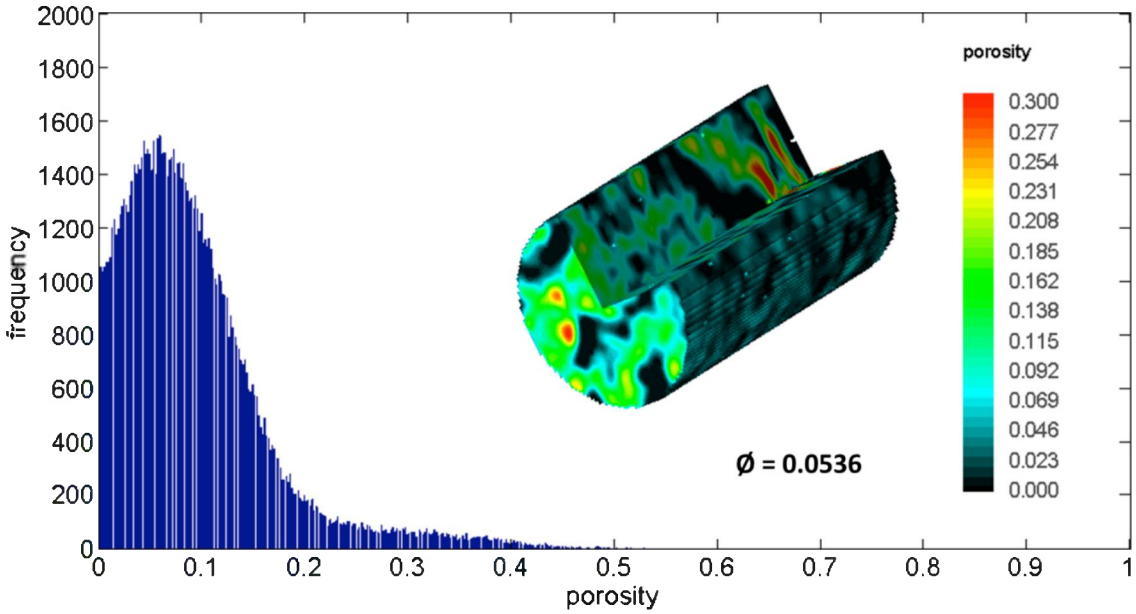

(b)

Figure 90. Porosity distribution for two of the samples represented in this study: (a) Barnett and (b) Eagle Ford.

Figure 89 also shows evidence of bedding structures in the sample, with at least three visible and alternating lower and higher porosity distribution areas. The black shaded volumes have zero porosity, according to CT measurements. In volumes of the core with nonzero porosity, porosity is in the range of 15%. These nonzero porosity regions may be connected kerogen and we are working on their identification. The central part near the cemented fracture has porosity in excess of 50%. These high porosities are in a very small volume and may represent incomplete cementing of the fracture.

The Barnett sample, **Figs. 89** and **90(a)** also has a long tail of fairly large porosity values that mostly originate from the fracture. The fracture and calcite filling were investigated using SEM and a small piece of the end trim from the core. **Figure** 91 shows the SEM images of the calcite. The first SEM BSE image in **Fig. 91(a)** shows the light gray (calcite) fracture surrounded by dark matrix. Bright white areas in the fracture are sulfate minerals such as barite and the white areas in the matrix are pyrite. The image in **Fig. 91(b)** is a close up view showing small pores and voids in the calcite fracture fill. These along with other images (to follow) support the higher porosity found in the fracture fill via krypton CT images.

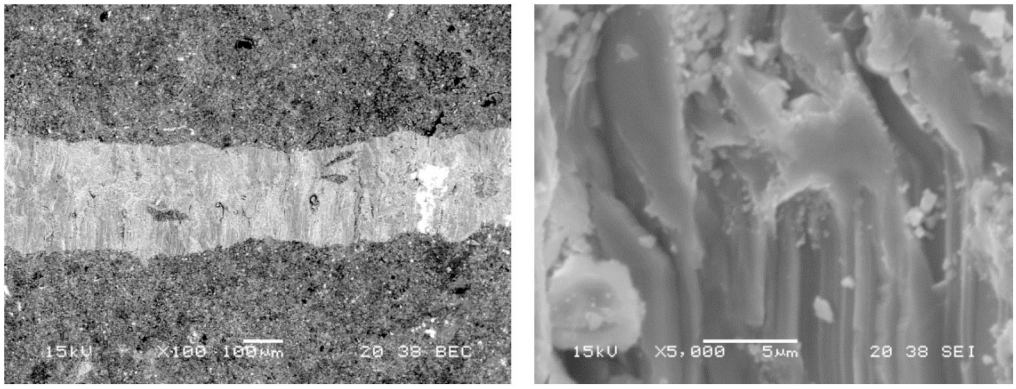

(a) **(b)**

Figure 91. SEM BSE images of the calcite-filled fracture on the Barnett sample (courtesy of C. Ross). (a) 100X and (b) 5000X. The fracture fill in (b) is oriented identical to that in (a).

Our initial imaging of a Barnett core sample, revealed significant gas porosity in a fracture that appeared visually to be healed with white fracture fill, presumably calcite. The 3D reconstructed porosity image is given in Fig. 89(a). Measurements indicate that some portions of the fracture have porosity that reaches about 50%. Our recent work has been in the area of characterization of the fracture fill. We hope to understand if the observation in Fig. 89(a) is representative of in-situ conditions or are an artifact of core preparation for laboratory work. Our primary tools in this characterization have been SEM (scanning electron microscopy) using SEI (secondary electrons), BSE (backscattered electrons), and CL (cathodoluminescence detectors) along with EDS (energy dispersive spectroscopy) and EPMA (electron microprobe analysis) with both EDS and CL capabilities.

These characterization tools teach us that the composition of the fracture fill is mainly calcite ($CaCO_3$) and dolomite ($CaMg(CO_3)_2$). There are lesser amounts of quartz, albite, sulfates, and sulfides (such as pyrite). With SEM-based imaging tools, fracture fill composition can be observed in BSE images where the relative brightness correlates with the average atomic number as shown in Figure 59 (left). Dense minerals such as pyrite are white in the image whereas silicates (e.g., clays and quartz) are dark gray. The relationship between gray scale values and elemental composition is determined using EDS measurements made at known points within the image. Another method is by using the EDS system to construct maps of selected elements (Fig. 92, right). In this false-color composite elemental map, the distribution of silicon (Si - red), calcium (Ca - aqua), magnesium (Mg - green), sulfur (S - yellow), and phosphorus (P - blue) are shown. The shale matrix shown in red is populated with silicates (such as clay, quartz, and albite) whereas the fracture fill is predominantly carbonates (calcite and dolomite, aqua and green respectively). Within the fracture fill, shale matrix remnants are isolated (in 2D) corresponding to fracture reactivation features and crack-seal texture as described by Gale and others (2007). In this particular image, the yellow sulfur-bearing regions are sulfides (pyrite). In other images (not shown), yellow corresponds to sulfates such as celestite ($SrSO_4$) and barite ($BaSO_4$). Blue areas are small particles of calcium phosphate. Other elements mapped and not shown include aluminum (Al), barium (Ba), carbon (C), iron (Fe), nitrogen (N), sodium (Na), oxygen (O), and strontium (Sr).

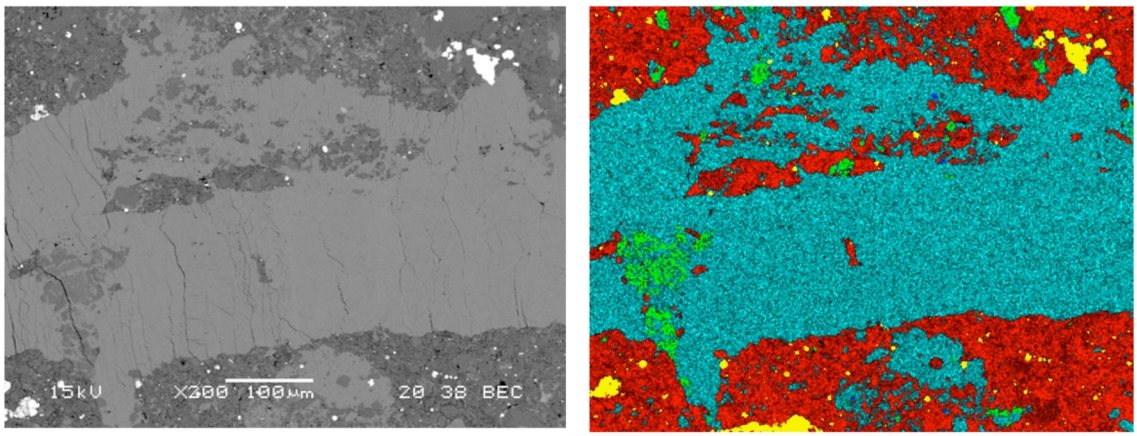

Figure 92: SEM BSE image and elemental map for Barnett fracture fill.

Significant zonation is observed in the fracture fill as illustrated in Fig. 93. In this figure, the SEM image is obtained using a cathodoluminescence (CL) detector that detects the total luminescence of the sample. The image on the left is the original image whereas the image on the right has red lines added to delineate the outermost parallel calcite crystals extending from the fracture wall toward the center of the fracture from the smaller, randomly oriented calcite crystals in the center of the fracture. Carbonate minerals are problematic in that their luminescence persists (phosphorescence) causing streaking and

blurring as described by Reed and Milliken (2003). Another method of viewing calcite zonation is via EPMA-based color CL as it collects the wavelength spectra enabling select portions of the spectra to be displayed (Fig. 94). In this manner, the UV-violet portion of the spectrum arising from carbonate luminescence is enhanced and the red-orange portion attributed to phosphorescence is either minimized or removed. This is the first time this tool has been used at Stanford University and we expect the technique to be further refined showing greater contrast in carbonates.

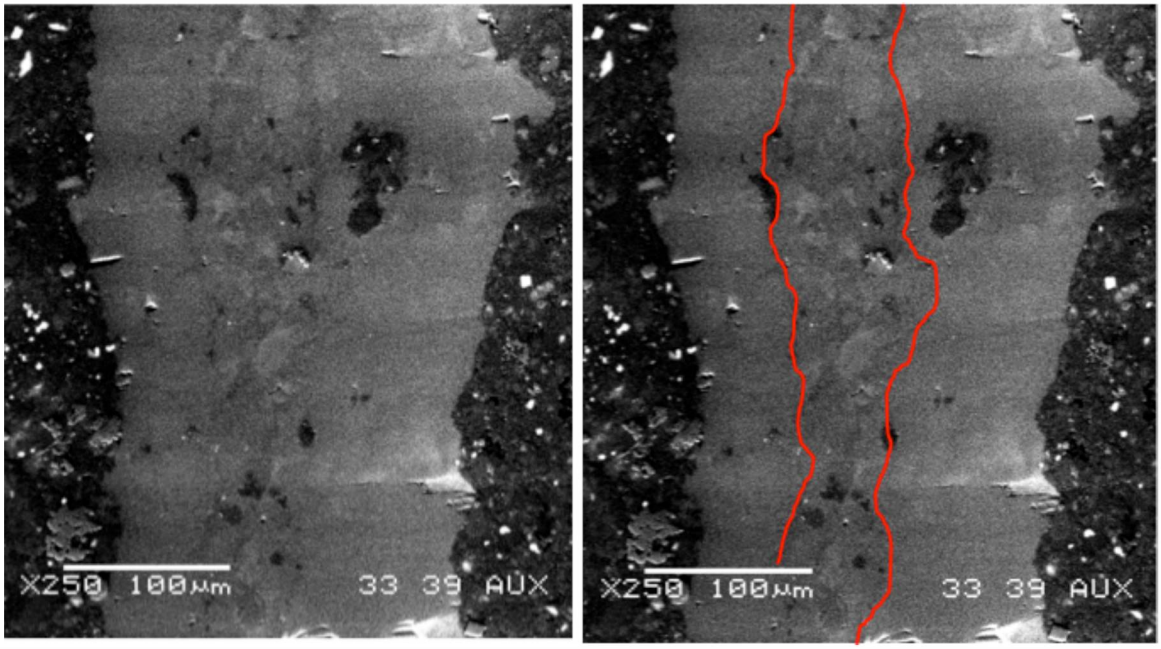

Fig. 93 SEM CL image at 250X showing zonation within the calcite fracture fill. On the right, red lines have been added to distinguish between zones.

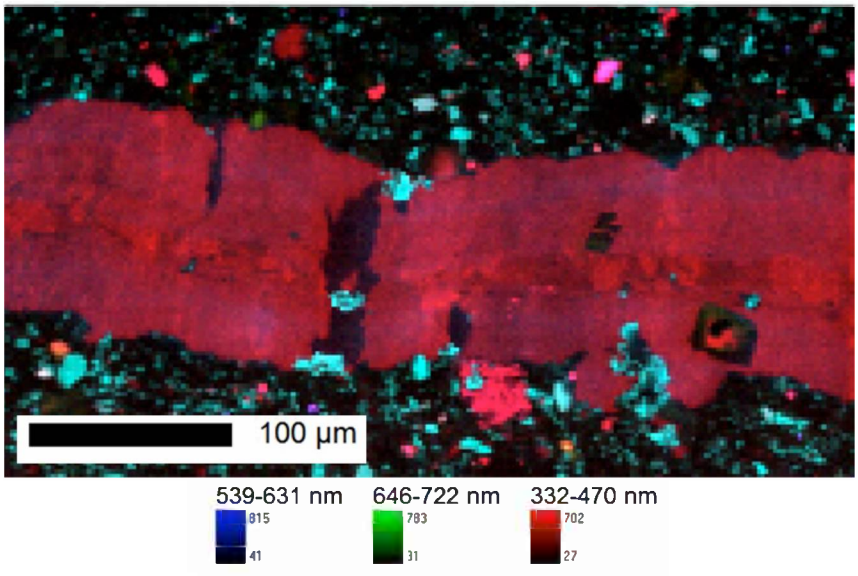

Fig. 94 EPMA color CL image at 200X showing zonation of calcite fracture fill.

Previous SEM results on small chips did not account for the high porosity values (40-50%) observed using CT imaging (Fig. 90(a)). For a definitive explanation, the core was removed from the core holder and a circular section corresponding to front portion of the core shown in the 3D porosity map (Fig. 90(a)) was cut from it. The entire disk was polished for SEM imaging whereas the remainder of the core was returned to its core holder for further testing. Porosity characterization of fractures and their fill are based on this sample in addition to smaller chips embedded in epoxy and polished.

SEM analysis of the fracture fill corresponding to the regions indicated by the lowermost red arrow and the blue arrow (Fig. 90(a), front portion of the core) and other Barnett samples indicates the presence of sheet pores and micropores within the fill. In this report, sheet pores include intercrystalline pores (which are most likely naturally occurring) and similarly-sized and somewhat larger fractures that may be natural, induced, or both. Examples of these larger, induced fractures can be seen in Fig. 59. The frequency and width of the fractures increase as you approach the edge of the sample, which in this case is at the left side of the image. Intercrystalline sheet pores occur between calcite crystals as identified using CL imaging (Fig. 93) and are mostly oriented across the width of the fracture. The majority of fractures included with the sheet pores in the fill are also oriented across the width of the fracture and are not confined to either crystal boundaries or obvious cleavage planes. These findings are consistent with coring induced damage. Micropores occur between two minerals within the fracture fill, along cleavage planes, and are most abundant in localized regions with both calcite and dolomite cements, such as the green region in Fig. 59.

Comparison of the 3D porosity map (Fig. 90(a)) with SEM images of the core end provided long sought answers. Localized porosity values of 5% were measured in microporous fracture fill regions; however, the small area imaged at high magnification thus far may not be representative of the overall fracture fill. In a few areas, a thin longitudinal fracture between the fracture fill and matrix was observed. In the 3D map (Fig. 90(a)), the porosity associated with the calcite filled fractures is much lower at the front compared to the back of the core. The only high porosity region at the front face of the cores is the yellow and red region at the base of the 3D core image (approximately perpendicular to the calcite-filled fractures). The high porosity is due to open fractures that are roughly parallel to each other and bedding planes (Fig. 95). Micron-size euhedral crystals can be seen in the fractures, but they might also occur throughout the matrix. In addition, the sample is quite robust despite the many fractures in this region. Our initial interpretation is that these are either induced or enhanced naturally-occurring fractures with preference for the latter. Once testing has been completed, the other end of the core can be evaluated in a similar fashion.

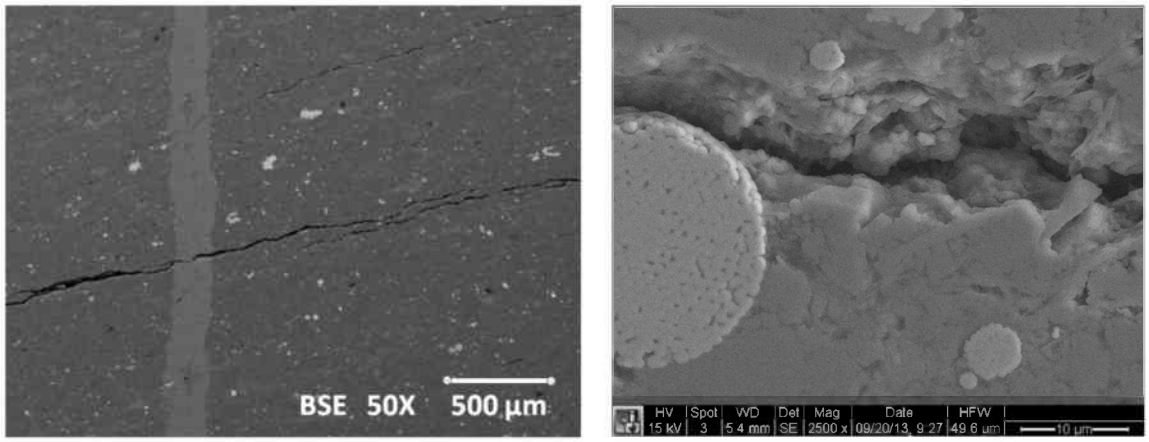

Fig. 95 Open fractures in Barnett sample.

Table 9. Comparison of image-calculated and database estimated[1] porosities for the examined samples.

Sample	Depth (ft.)	Image-calculated ϕ	Estimated ϕ
Barnett	8,562.10	6.50 %	5-6 %
Haynesville	11,283.90	6.40 %	5-7 %
	10,661.55	3.71 %	2.42 %
	11,102.45	1.40 %	2.77 %
Eagle Ford	12,753.30	4.80 %	5-7%

[1]Estimates as provided by the service company that prepared core samples.

To establish that the high X-ray contrast gas technique is widely applicable, additional samples were analyzed following the procedures given above. **Figure 96** shows additional porosity maps of unfractured Haynesville samples. Distinct features are observed such as regions of larger porosity distributed within a small porosity matrix. Differences in the porosity distributions of these three samples are apparent on these maps, and the average porosity values calculated through Kr injection reasonably match the porosity values estimated for the samples from related databases or otherwise measured with methods such as He pycnometry.

A comparison of the estimated porosity values with porosity values obtained from other sources for some of the samples is offered in **Table 9.** The heterogeneity of each core is clearly apparent as is the tortuous path followed by krypton in order to saturate the cores. These results are consistent with theories of a dispersed, medium low porosity matrix within a connected, low porosity inorganic matrix. However, evidence of microfractures was not found for the image resolution of these studies, probably due to a mismatch of

scales between the equipment (sub-millimeter) and the probable size of these features (microns to nanometers).

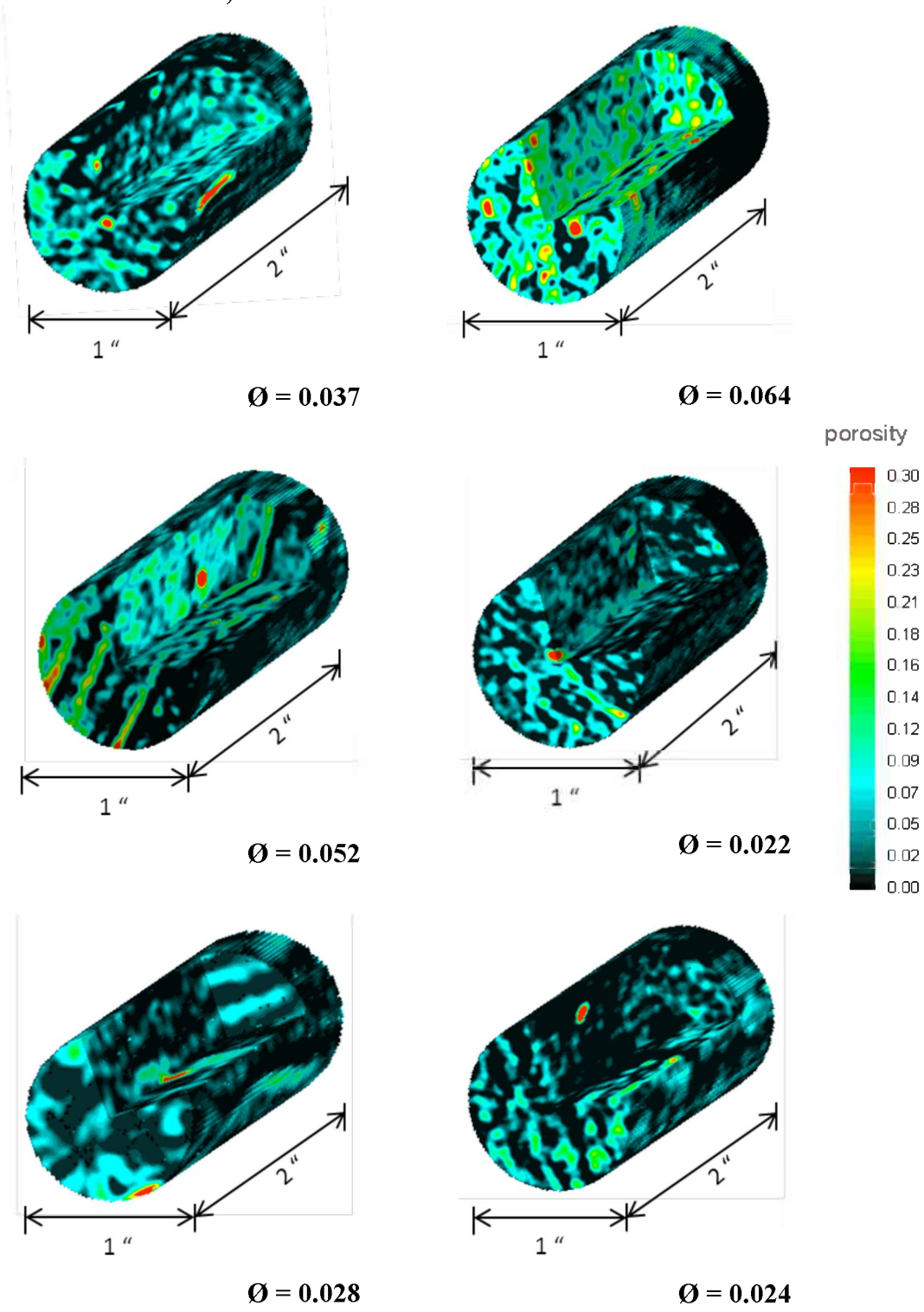

Figure 96. 3D porosity map reconstruction obtained for six additional Haynesville samples.

3.2.5 Results—Increasing Effective Stress

Figure 97 presents the core average porosity versus confining pressure for three Haynesville core samples. Here, the average porosity is obtained by summing all of the CT voxel porosity measurements and dividing by the number of voxels. Generally, the average porosity decreases as the confining pressure increases.

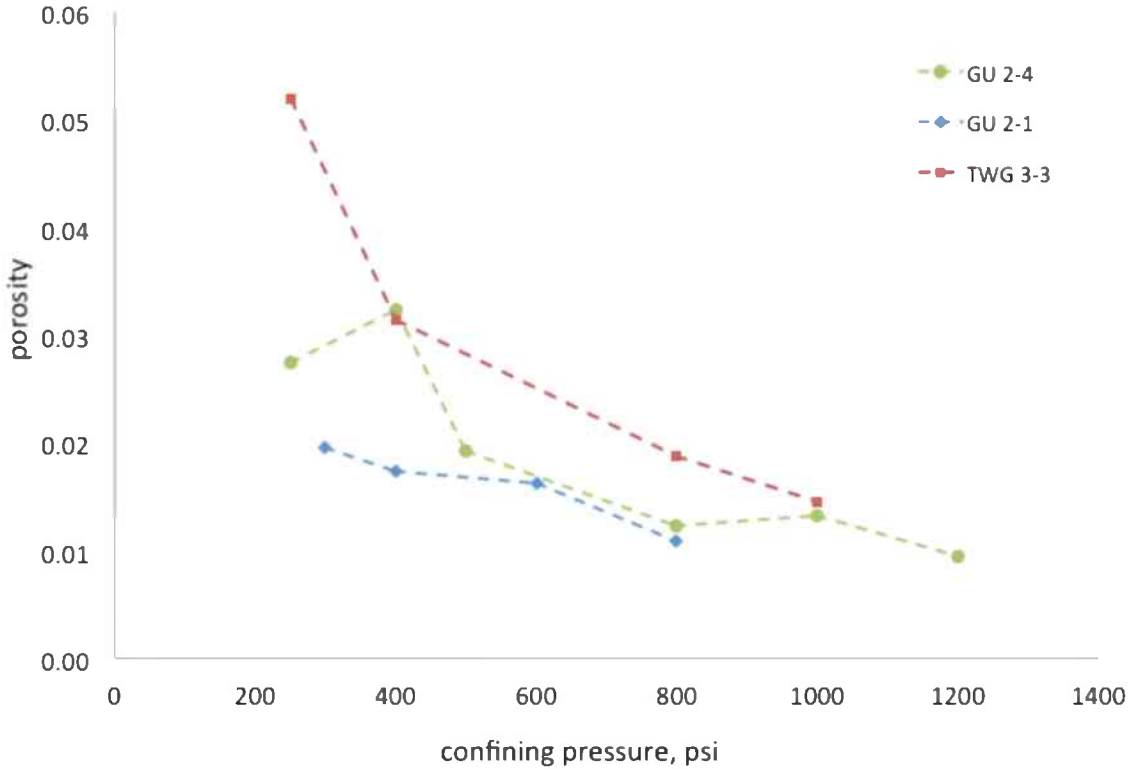

Figure 97: Average X-ray CT derived porosity as a function of confining pressure for 3 Haynesville

Detailed porosity maps as a function of effective stress were also plotted for each of these cores. Figure 98 gives an example of the results obtained for sample TWG 3-3. Significant differences in the spatial distribution of the porosity values are not seen as the confining pressure (effective stress) is increased. The results indicate, however, gradual closing of gas pathways and gradual reduction in porosity as the effective stress increases. At a confining pressure of 1000 psi it is evident that the gas carrying pathways have reduced dramatically in number.

Figure 56 also gives a photograph of the core. Fractures that appeared to be cemented closed (presumably with calcite) are outlined in green. The porosity image and visual inspection of the core shows clear bedding structures. The black shaded volumes have zero porosity, according to these measurements. In volumes of the core with nonzero

porosity, those porosity values are in the range of 15%. These nonzero porosity regions may be connected kerogen and we are working on their identification. The central part near the cemented fracture is showing porosities in excess of 50%. These high porosities are in a very small volume and are subject to repeat measurement for verification. They may represent incomplete cementing of the fracture or perhaps an artifact arising by the presence of moisture.

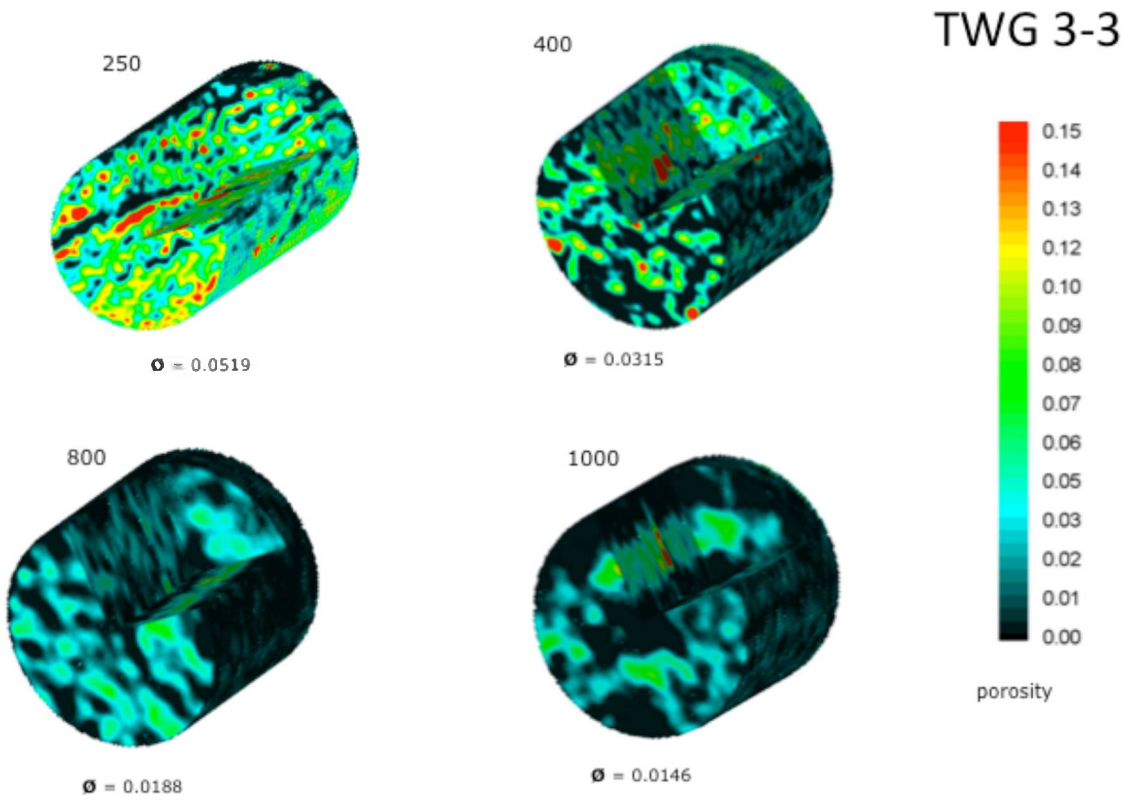

Figure 98: Porosity maps at increasing confining pressure (effective stress) for sample TWG 3-3. Average core porosity is given below each figure. Pore pressure is 100 psi and the confining pressure is given next to each image.

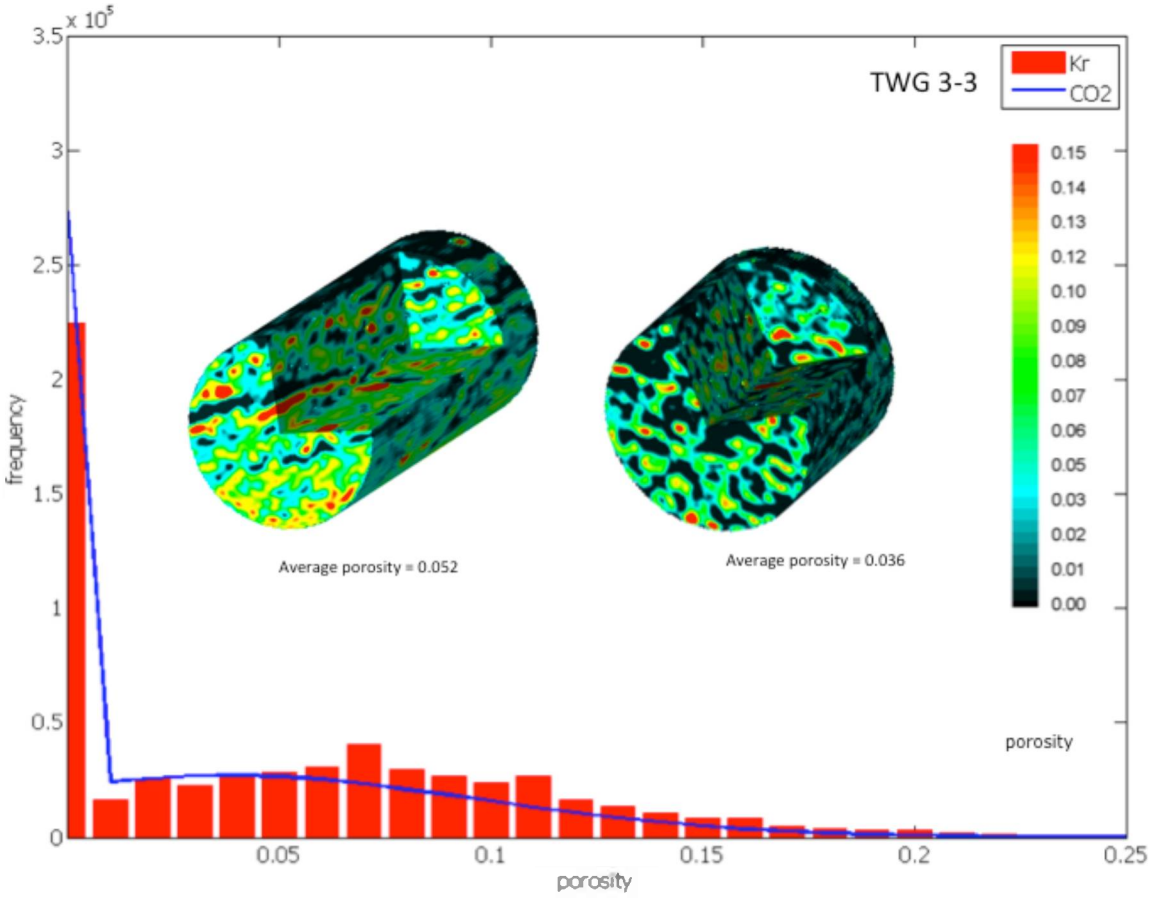

Figure 99: Porosity map obtained using CO_2 as the saturating fluid compared to krypton results for sample TWG 303.

We also considered the invasion of gas shale pore space by liquid CO_2 (pressure is 800 psi and temperature is 22 °C). We have concerns that sufficient contrast in X-ray attenuation might not be obtained using CO_2. Figure 66 gives example images of the porosity obtained using CO_2 and krypton. Both samples are at a similar effective stress of roughly 200 psi. The average porosity obtained with krypton is 0.052 whereas it is 0.036 with CO_2. This difference may be due to different pore occupancy for the different gases or due to the poor X-ray attenuation characteristics of CO_2 or both effects may be in play. Figure 11 also presents a plot of the frequency of the various values of porosity in each image. The shape of the frequency versus porosity relationship is similar for both images.

3.2.6 Summary of CT Imaging

Imaging of the porosity distribution within low permeability media was accomplished and enhanced by implementing a high X-ray contrast gas imaging technique. The method uses X-ray CT imaging of the sample of interest under vacuumed and tracer gas-saturated stages. Imaging of the gas-accessible pore space is possible through an image subtraction algorithm. It is thus possible to obtain sub-millimeter resolution images and 3D reconstructions that represent the average porosity spatial distribution of the core sample.

Porosities calculated with krypton injection in shale matched approximately the porosities predicted for samples of similar origins or measured through different means. Calcite-filled fractures were observed with the naked-eye and sub-millimeter resolutions. These fractures displayed larger porosity values than the rest of the shale. Krypton injection combined with CT scanner imaging seems to produce enough signal to be detectable and achieve reasonable porosity values with this non-destructive technology. Large, connected low porosity areas enveloping spotted, medium-low porosity zones consistently appear in the sample porosity maps studied. This observation supports theories of medium low porosity organic matrices dispersed within low, connected inorganic matrices as the probable pore network distribution for gas shale rocks similar to the subjects of the study.

3.3: Shale permeability to CO_2

Permeability Measurements in Shales Using Different Gases

A series of measurements are currently underway in which gas permeability of Barnett, Haynesville, Eagleford and Marcellus are being measured at different confining pressures and pore pressures. These measurements are intended to document the permeability of the shales at different effective pressures in the reservoir and to investigate the onset of the Klinkenberg effect in which slippage along flow path boundaries contribute appreciably to permeability.

Permeability is being measured first with helium, then with methane, then with CO_2 and then with helium again. The purpose of these measurements is to investigate permeability with both adsorbing (methane and CO_2) and non-adsorbing (helium) gases and to investigate whether swelling associated with CO_2 adsorption results in a permanent change in porosity and permeability.

Measuring the Klinkenberg Effect in Gas Shales

Estimating in-situ matrix permeability of gas shales reservoirs is a major challenge to reservoir characterization and accurate production forecasting. While fracture properties (both natural and induced) dominate reservoir performance early on in the life of a well, it is the matrix properties that control how a well will perform over long periods of time. Predictions and forecasts from reservoir simulators can only be as accurate as the underlying rock properties, rock behavior and physics used to build them. Laboratory studies are an effective way to improve upon these model inputs.

The Klinkenberg Effect

At low pore pressures and/or in small pores, the assumption that particle velocity is zero at the pore walls (the "no slip" assumption) may become invalid due to the fact that molecules may begin to interact more frequently with the pore walls than each other and skip through the pore, as depicted in Figure 100.

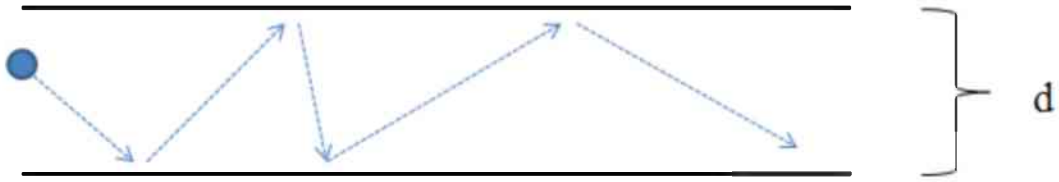

Figure 100: Cartoon illustrating the Knudsen diffusion mechanism, in which molecules more frequently collide with the pore wall than with each other the reducing invalidating the no slip boundary assumption and enhancing overall permeability (Figure taken from unknown internet source).

Within the petroleum industry, this is referred to as gas slippage or the Klinkenberg effect after the scientist who investigated the phenomena in low permeability sandstones in 1941 (Klinkenberg, 1941). The physical phenomenon responsible for this behavior is a diffusive process termed Knudsen diffusion, which uses the kinetic theory of gases to predict this behavior. As a pore diameter approaches the same distance as the mean free path (average distance a molecule travels before it collides with another molecule, a function of pressure/density) of molecules flowing through it, this diffusive flux becomes important. The mean free path is defined by the following equation:

$$\lambda = \frac{K_B T}{\sqrt{2}\pi d^2 p} \qquad (1)$$

where K_B is the Boltzmann constant, T is the temperature, d the molecular diameter and p the pressure. The mean free path is plotted as a function of pressure for several molecules of interest below in Figure 102.

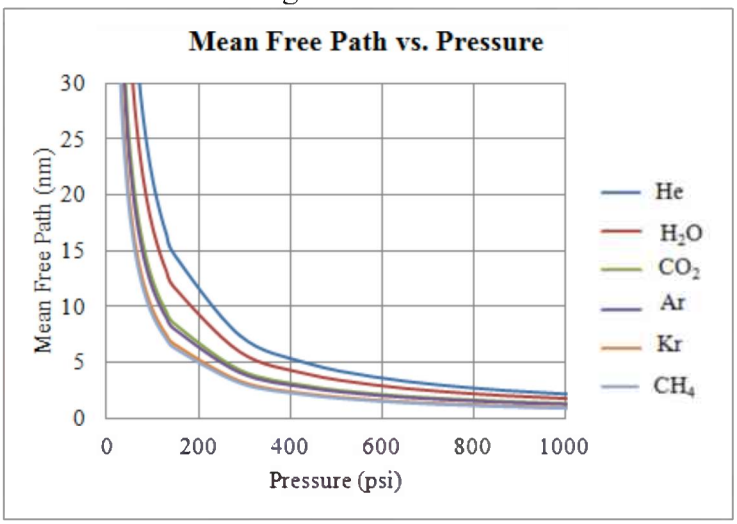

Molecule	Diameter (nm)
He	0.25
H_2O	0.28
CO_2	0.33
Ar	0.34
N_2	0.36
Kr	0.37
CH_4	0.38
C_2H_6	0.40
C_3H_8	0.43
C_4H_{10}	0.50
C_5H_{12}	0.65

Figure 102: Mean free path of gas molecules as a function of pressure. Note the large increase in mean free path at low pore pressures. Highlighted gases are discussed in a subsequent section.

It is clear that at low pressures (low gas densities) the mean free path becomes significantly larger than at elevated pressures. In addition we see that the smaller the molecule the larger the mean free path at a given pressure.

Klinkenberg's primary objective was to develop a way of converting gas measured permeability to liquid permeability. In the process of accomplishing this objective he showed that the apparent dependency of permeability on pressure was a function of a changing mean free path with pressure. Moreover, he showed that it could be quantified and corrected for. The equation he eloquently derives in his paper is as follows:

$$k_a = k_\infty \left(1 + \frac{b}{\overline{P}}\right) \tag{2}$$

where k_a is the apparent permeability (permeability measured with gas), k_∞ is the permeability at infinite pressure (liquid permeability), k_b is the Klinkenberg parameter and $\overline{P}$ is the mean flowing pressure across a sample. A standard Klinkenberg plot is made by plotting permeability versus one over pressure. The intercept (infinite pressure) is the estimated liquid permeability of the rock, and the slope of the line is dependant on the size of the mean free path relative to the effective pore size. While Klinkenberg cared mainly about getting k_∞, in the context of gas shales (with the exception of liquid plays) the parameter k_b is of more importance/use since it essentially tells us the extent to which our permeability will increase due to slippage as a function of pressure.

Moreover, with a few simple assumptions we can use the Klinkenberg parameter to estimate the effective aperture of the flow paths. Suppose we assume that the total mass flow is the sum of the viscous flow plus some empirical constant times the Knudsen flow. Let's also assume a slit-shaped pore geometry. If we model the viscous flux using the Poiseuille equation, we can write the following:

$$F = \frac{w^3 M \overline{P}}{12 \mu L R T} \Delta P + c \frac{4}{3} \left(\frac{2M}{\pi R T}\right)^{1/2} \frac{w^2}{L} \Delta P \tag{3}$$

where the first term is the viscous mass flow rate, the second is the Knudsen mass flow rate, F is the total mass flow rate (kg/s), M is the molar mass (kg/mol), c an empirical constant and w is the slot width. Dividing by the molar mass and molar density we get the following:

$$Q = \frac{w^3 P}{12 \mu L} \Delta P + c \frac{4}{3} \rho \left(\frac{2M}{\pi R T}\right)^{1/2} \frac{w^2}{L} \Delta P \tag{4}$$

where we now have converted the mass flow rate into a volumetric flow rate. If we combine this with Darcy's Law:

$$Q = \frac{kA}{\mu L} \Delta P \tag{5}$$

and then solve for permeability, we get the following:

$$k = \frac{w^3}{12A} + c \frac{4}{3} \frac{\rho \mu w^2}{A} \left(\frac{2M}{\pi R T}\right)^{1/2} \tag{6}$$

which we can then rewrite as:

$$k = \frac{w^3}{12A}\left[1 + \frac{16c\mu}{w\bar{P}}\left(\frac{2RT}{\pi M}\right)^{1/2}\right] \tag{7}$$

Equation 6 has the same form as the Klinkenberg equation (Equation 7). Thus, this simple model yields the following relation for the Klinkenberg constant, k_b:

$$k_b = \frac{16c\mu}{w}\left(\frac{2RT}{\pi M}\right)^{1/2} \tag{8}$$

which can easily be solved for w:

$$w = \frac{16c\mu}{k_b}\left(\frac{2RT}{\pi M}\right)^{1/2} \tag{9}$$

providing us with a direct linkage between the empirical Klinkenberg constant and pore aperture.

In addition to estimating the effective pore width, we can also estimate the Knudsen diffusivity based on the kb and k∞. Thorstenson and Pollock, 1989 demonstrated the magnitude of the Klinkenberg effect to be related to the Knudsen diffusivity via the following relationship:

$$D_K = \frac{k_\infty b_k}{\mu} \tag{10}$$

where both parameters in the numerator are derived from the Klinkenberg plot and μ is the viscosity.

Finally, we are measuring permeability with a variety of gases other than helium including methane, krypton, carbon dioxide and argon. In the table located within Figure 102 we have highlighted the fact that, conveniently, non-adsorbing analogues exist to the gases that we're interested in knowing the permeability of. Krypton is a non-adsorbing analogue to methane, and argon to carbon dioxide. By measuring permeability with both the adsorbing gases and the non-adsorbing gases, we hope to distinguish between the molecular size effects and adsorbing effects on permeability.

Results are presented below from two Eagle Ford shale samples (located in South Texas) and one Marcellus sample (Appalachian Basin). Both of the Eagle Ford samples were oriented horizontally with respect to the surface (parallel to bedding), and the Marcellus sample was oriented vertically (perpendicular to bedding). The exact core plug measurements and core photos are shown below in Figure 103.

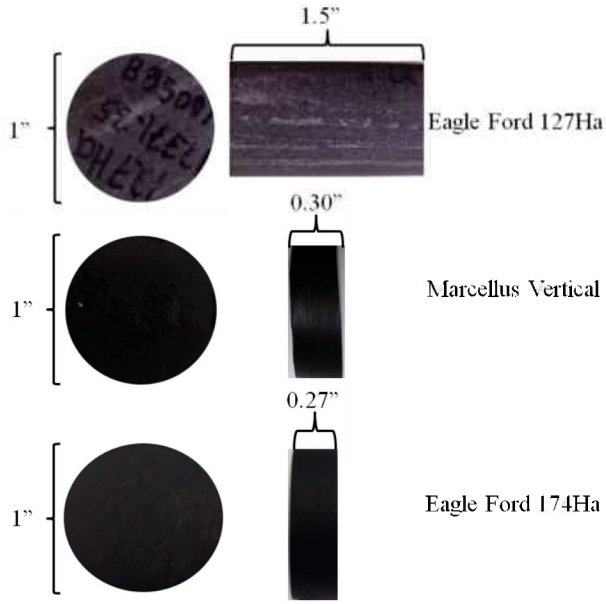

Figure 103: Sample photos and dimensions.

In Eagle Ford sample 127Ha one can clearly see a calcite filled vein that extends through the length of the sample. Complete mineralogical, SEM and pore size characterization of the samples is currently in progress.

Each sample was placed in a vacuum oven at 45°C until constant mass was achieved to remove any water and/or residual hydrocarbons from the core. The temperature was chosen so as to be above the boiling point of water in near vacuum conditions, but not so high as to remove clay-bound water and alter the clay properties.

The most common approach used within the oil and gas industry is to conduct measurements on either intact core plugs or crushed core. The benefits of measuring permeability on intact core plugs as opposed to crushed core are numerous, and include: straightforward and established methods for interpreting data, sampling a large (and perhaps more representative) volume of rock and the ability to test the influence of confining stress on permeability. All measurements discussed in this paper were made on intact core plugs as opposed to crushed samples. However, after the intact core samples were later ground for crushed permeability measurements (this data is still being processed). All measurements were conducted on 1" diameter core plugs in a hydrostatic pressure system shown in Figure 104.

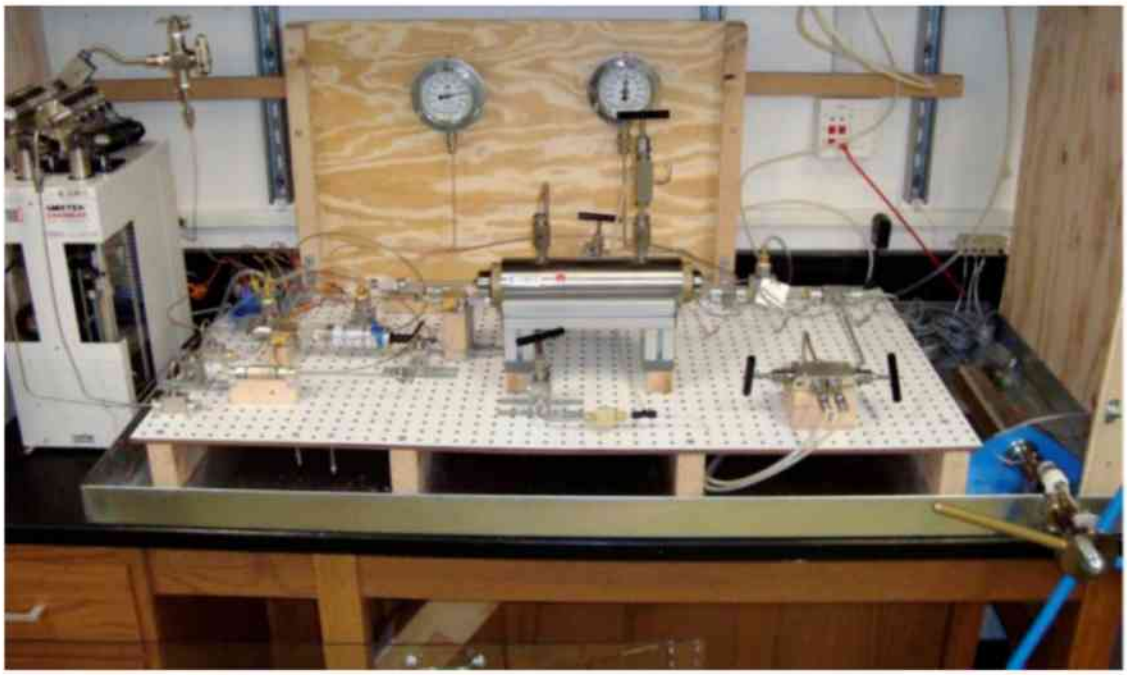

Figure 104: Photograph of hydrostatic permeability system. Quizix pump is on far left, Temco core holder is in the middle, and manual pressure generator is on the far right.

The sample is wedged between two floating plugs attached to pore lines inside of a Viton jacket. Confining pressure is controlled manually using the high pressure generator shown on the far right of Figure 104. Confining pressure is measured using a Heise DXD pressure transducer accurate to +/- 0.1% up to 10,000 psi. Pore pressure is controlled by a Quizix QX-6000 pump, equipped with two pistons capable of multiple operating modes including constant pressure, constant flow rate and a variety of paired operating modes. The maximum pressure the pump is capable of is 6,000 psi, and the pressure is measured using pressure transducers inside of the pump accurate to +/- 0.01%. All flow rates were measure via the Quizix system, capable of flow rates as low as 0.001 ml/min accurate to within +/- 0.1% of the set flow rate. Temperature within both the upstream and downstream pore lines as well as the confining pressure lines is measured with thermocouples. In order to maintain temperature stability, a custom heat control system was built using a heat lamp and a feedback algorithm implemented via LabView. All data was recorded using LabView as well.

Depending on the permeability of the sample, either a static, Darcy flow method or a dynamic, pressure pulse method was employed. Our system is capable of accurate Darcy flow measurements to approximately 1 microdarcy for a 1.5 inch sample. Of the three samples discussed in this paper, only one (Eagle Ford 127Ha) was permeable enough for the Darcy flow method. The pressure pulse method was used for both of the others (Marcellus and Eagleford174Ha). For details of both techniques see Vermylen, 2011.
Permeability is plotted versus pore pressure for a nominal effective stress of 1000, 2000, 3000 and 4000 psi in Figure 105.

There are several features in Figure 105 that are worth pointing out. First, note the scale difference for the Eagle Ford 127Ha sample (microdarcy as opposed to nanodarcy) and recall the calcite vein extending through this sample. It appears as if this vein is quite permeable, and results in a high permeability relative to a typical Eagle Ford sample. Second, notice that for a given nominal effective stress permeability seems to increase rather significantly at low pore pressures. This is the case in all samples however the effect is particularly apparent in the two lower permeability samples. Finally, notice that for a given pore pressure permeability varies as a function of nominal effective stress (C_p-P_p).

The next step in this workflow is to fit the data to a permeability effective stress law, as shown in Figure 106. The ratio of slopes method was used to determine the permeability coefficient (Kwon et al, 2001).

In this figure (106) all permeability data was fit to a unique permeability effective stress law for each rock. In all cases, χ was found to be less than 1, in agreement with the results of Vermylen, 2011. The light grey trend line indicates the general permeability effective stress trend, which was fit quite well by the high pore pressure data. However, notice the measurements made at low pore pressure deviate from this trend significantly. All of the data has been shifted in true effective stress space such that the high pore pressure data points form a trend. We can now select a constant true effective stress and investigate how permeability varies as a function of pore pressure due to non-stress-related (Klinkenberg) effects. We can select several values of true effective stress (indicated in Figure 106 by the red-dashed lines) and create Klinkenberg plots for each. The results are shown in Figure 107.

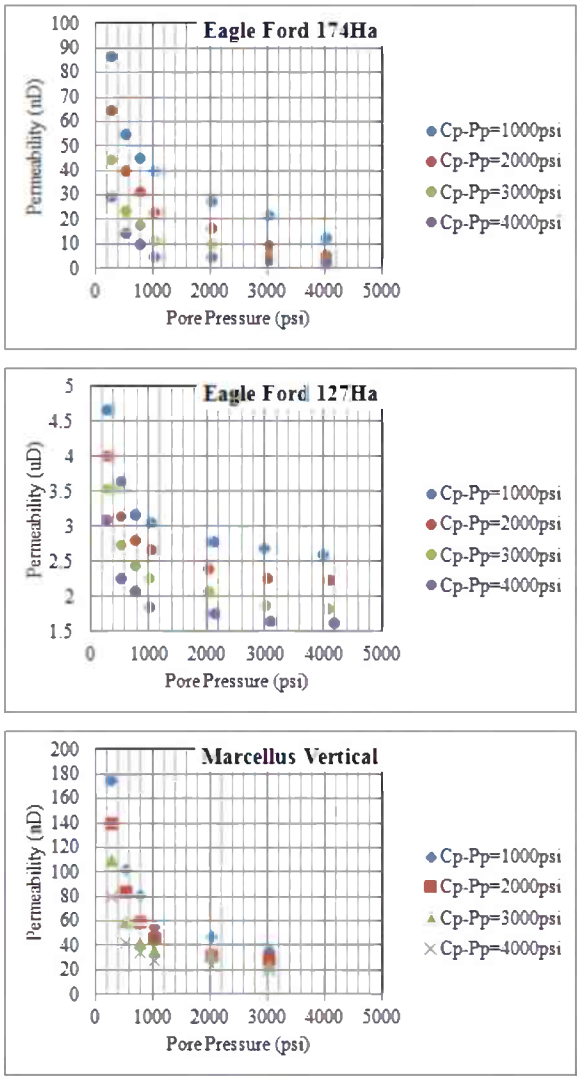

Figure 105: Permeability versus pore pressure at nominal effective stress values of 1000, 2000, 3000 and 4000 psi. Note permeability scale is in microdarcy for Eagle Ford 127Ha sample, and nanodarcy for the other two samples.

Figure 107 shows standard Klinkenberg plots for three different values of true effective stress. Note the increase in K_b with increasing effective stress. With these parameters established, we are now able to use the Equation 9 to calculate the effective size of the flow paths. Moreover, because we also now know how K_b varies with effective stress, we can estimate how the effect size of the flow paths varies with effective stress as well. These results are shown in Figure 108.

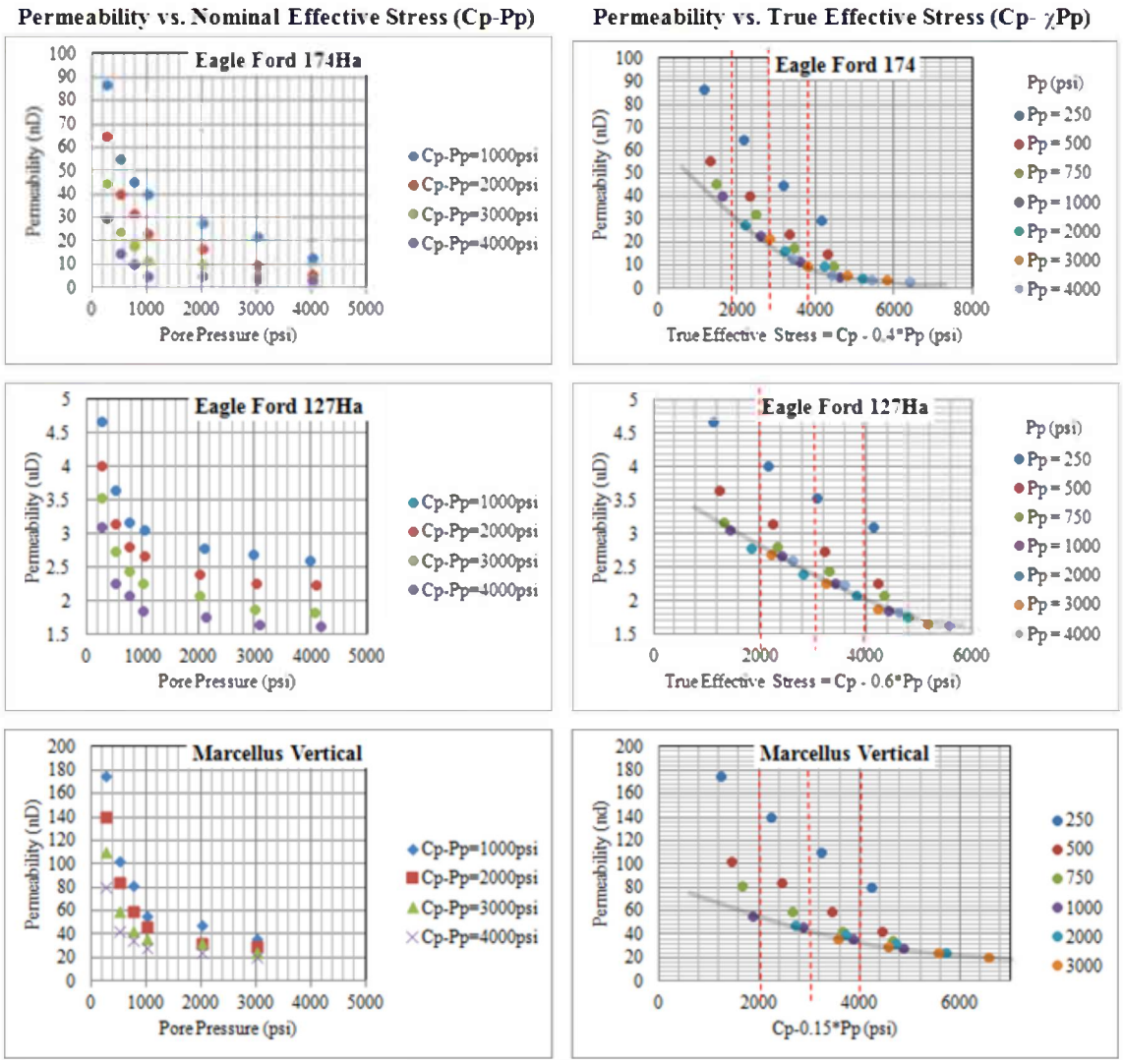

Figure 106. Permeability versus nominal effective stress (left) and permeability versus true effective stress (right). Light grey trend line indicates the permeability effective stress trend, which is fit well by measurements at high pore pressures. Note the deviation from the permeability effective stress trend by the low pore pressure points. Red-dashed lines indicate permeability isolines used for generating Klinkenberg plots.

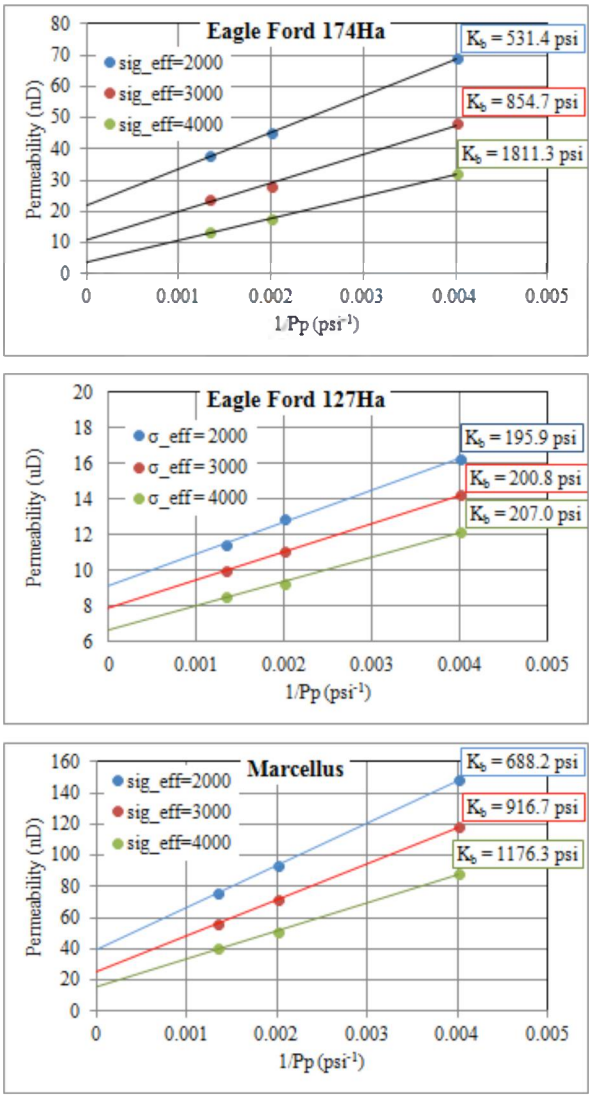

Figure 107: Standard Klinkenberg plots (permeability versus $1/P_p$). Permeability points selected for true effective stress values of 2000, 3000 and 4000 psi. Notice increase in K_b value (slope/intercept) with increasing effective stress.

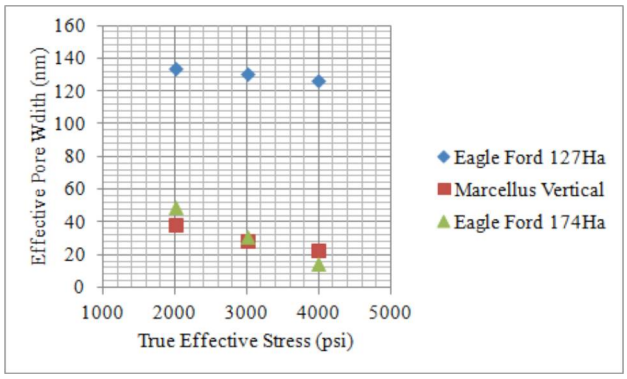

Figure 108: Effective pore width versus true effective stress, as estimated for the Klinkenberg parameter (K_b).

Figure 108 suggests that the effective pore size varies moderately with effective stress (about 5% in the case of Eagle Ford 127Ha, factor of 2 in the case of Marcellus, and a factor of about 5 in the case of Eagle Ford 174Ha). While many assumptions went into these estimates, the results seem plausible based on the apertures of pore sizes commonly observed in SEM photos. In addition to estimating the effective pore width, we are able to estimate the Knudsen diffusivity of the samples based on the Klinkenberg parameter.

Finally, permeability has been measured using a variety or test gases other than helium including methane, carbon dioxide, krypton and argon. By measuring permeability with both the adsorbing gases and the non-adsorbing gases, we hope to distinguish between the molecular size effects and adsorbing effects on permeability.

We carried out an extensive set of laboratory permeability measurements on gas shales examining the effects of confining stress, pore pressure and pore fluid type on permeability. Experiments were carried out on intact core plugs from the Eagle Ford and Marcellus shale reservoirs. Preliminary results suggest that the effective permeability of the rock is enhanced at low pore pressures (<1000 psi) due to slippage effects. A methodology is introduced by which one can separate the effects of stress and slippage on permeability. By separating these effects, we are able to make standard Klinkenberg permeability plots. From this we estimate the effective size of the flow paths within the sample. Preliminary results suggest the effective flow paths of the samples investigated to be on the order of tens of nanometers to slightly larger in a high permeability sample. Additionally, we calculate the Knudsen diffusivity, which may be used in reservoir simulation to perhaps more accurately predict the long-time production behavior of these shales.

We carried out an initial set of permeability experiments with different gases. We found that in a high permeability shale sample, the permeability of the shale to CO_2 was about 30% lower than that with helium. However, in a more typical shale sample with low permeability, the permeability to CO_2 was found to be immeasurably small, much less than 1nd. The cause of this phenomenon is still being investigated.

Permeability Measurements in Shales with Different Gases

Many physical properties of porous rocks (volumetric strain, porosity, permeability, etc.) vary as a function of confining pressure and pore pressure according to an effective pressure law. This is known as Terzaghi's Principle, and the Terzaghi effective stress (or simple/nominal effective stress) is defined as $\sigma_{Terzaghi} = C_P - P_P$, where C_p is the confining pressure and P_p is the pore pressure. This nominal effective stress law (as it will be referred to hereafter) is frequently modified to include a coefficient in front of the pore pressure term so that the relative importance of the two can be described in a single parameter. When describing how volumetric strain varies with effective stress, this coefficient is referred to as the Biot coefficient and the variable α is most commonly used. When describing how permeability varies as a function of effective stress, it is common to change the variable to χ (also used in this paper) to avoid confusion.

Many efforts have been made to describe how permeability depends on effective stress (Zoback and Byerlee, 1975; Kwon et al., 2001). The objective of these experiments has been to fit all permeability data to a function $k(\sigma_{eff})$ such that given a confining pressure and pore pressure combination, the permeability of a rock can be predicted. Most rocks have been shown to have $\chi \leq 1$, indicating that the rock is more sensitive to changes in confining pressure than pore pressure. However, there have been a handful of studies in which χ was found to be greater than 1, implying that changes in pore pressure have a larger impact on permeability than confining pressure (Zoback and Byerlee, 1975; Walls and Nur, 1979). A simple conceptual model for this observation is presented in Figure 9. In this model, fluid flows through a soft compressible matrix whereas the external stresses are supported by a stiff granular framework. Therefore if pore pressure and confining pressure were to increase by the same amount, for example, the compressible nature of the flow paths relative to the incompressible frame allows the change in pore pressure to have a greater effect on the pore size aperture than the external stress, increasing the overall permeability of the rock.

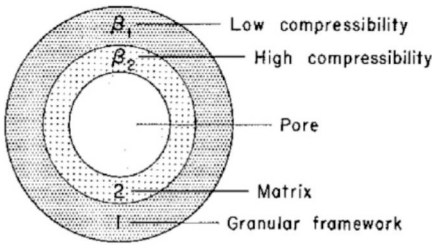

Figure 109: Conceptual model of a compressible pore space within a stiff granular framework (Zoback and Byerlee, 1975).

Based on observations of $\chi > 1$ in high clay sandstones and recent SEM images of gas shales showing the tendency for porosity to exist primarily in organic matter, Vermylen, (2011) hypothesized that χ might be greater than 1 in shales if gas was moving primarily through porosity located with soft kerogen. However, the study ultimately showed $\chi \leq 1$ on several Barnett shale samples, thus suggesting that perhaps there is no connectivity between pores within isolated pockets of kerogen and that flow was occurring primarily through some other porosity system, such as microcracks, for example.

In this work we followed up the Vermylen, 2011 study in a number of ways. First, we measured permeability as a function of effective stress for rocks from additional shale reservoirs in order to verify that the observation of $\chi \leq 1$ is not unique to the Barnett. The second and primary contribution of this study is to examine the influence of gas slippage effects on the permeability of shales, and to use the magnitude of this effect to estimate flow path size and Knudsen diffusivity (as previously described).

Major Upgrade of Permeability Measurement System

The hydrostatic pressure cell, pump and measurement system has undergone a major upgrade. The key objectives of the upgrade were to achieve improved thermal insulation of the measurement system and improved thermal stabilization. Precise temperature

control is necessary to accurately constrain the equation of state of the gases being used to measure permeability and to prevent pressure changes caused by temperature variations.

As shown in Figure 10 (left), the entire system (except for the computer which controls the tests and records data) is now enclosed in a thermal insulated compartment. This required the entire system to be disassembled and rebuilt within the insulated compartment.

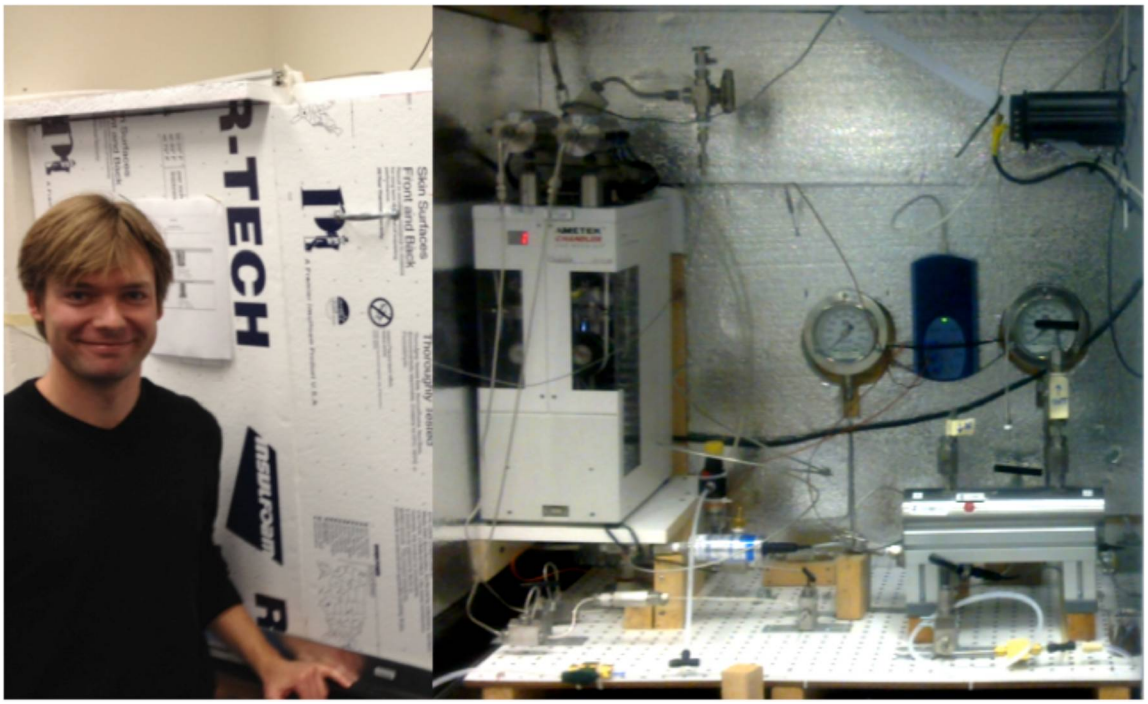

Figure 110: The hydrostatic pressure system used for permeability measurements has undergone a major upgrade including improved thermal insulation (left), moving the Quizix pump and flow lines into the insulated compartment (right) and installing an active thermal stabilization system within the compartment.

A second aspect of the upgrade to achieve improved thermal stabilization is to put the precise Quizix pump Figure 110 (Right) and all flow lines within the stabilized compartment. Flow lines from gas bottles (which supplied the pore fluids used in the permeability measurements) pass through a thermal bath (not shown) before entering the insulated compartment.

The third major step undertaken to stabilize temperature within the compartment was to install an active thermal stabilization system within the insulated box that consisted of a heat lamp, fan and sophisticated temperature sensing and control system. The result of these improvements allowed us to control temperature to less than 1° C over 8 hours.

These important upgrades of our pulse permeability measurement system were to enable measurements in samples with extremely low permeability. Great efforts were taken to minimize sources of error to the pressure time-data. Nevertheless, our data is not without

error, and there is certainly room for improvement. In the table below, we summarize what we believe to be some of the key technical challenges standing in the way of higher-quality data, and the approaches that we have already taken or are considering for future experiments.

On the basis of our experimental results to date and the areas for improvement suggested in Table 10, two significant modifications have been made. First, burst discs present in the downstream line have been removed to further reduce the number of connections. It is worth noting that this action does not impact the safety of the system. The burst discs were a redundant precaution, and other mechanisms are in place for ensuring the pressure rating of the lines is not exceeded. Second, the thermal stability of the system has been greatly improved. This was achieved by enclosing the entire system in an insulated chamber, as well as improving the heating mechanism and feedback algorithm for maintaining temperature control. The temperature control window of the system has now been improved to +/- 0.1°C. As a result of these improvements, we are now confidently measuring permeability in the nanodarcy to sub-nanodarcy range with a high degree of accuracy.

Table 10: Table summarizing experimental challenges, actions that have been taken to address those challenges as well as potential future improvements.

Technical Challenge	Action Taken	Level of Influence	Potential Improvements
Helium leaking out of upstream volume	Infinite upstream volume boundary condition (imposed using QX pump) renders leaks irrelevant on upstream side	None	N/A
Helium leaking out of downstream volume and/or through jacket	Leak rate low; corrected for lowest observed. Relatively large downstream volume reduces significance of leak rate.	Low	Switch from helium to argon gas for measurements. Further reduce connections on downstream side
Helium bypassing sample	Control experiment with steel plug in place of sample showed no evidence of this (see Figure 11).	None	Repeat control experiment regularly to monitor for issues related to sample bypass.
Confining stress fluctuations with temperature impacting shape of $\Delta P(t)$ curve	Pressure data analyzed where confining pressure and temperature stable.	Moderate	Thermal stability of system has been improved. An electronic pump could be installed to ensure confining pressure stability
Non-uniform fluid properties across length of core sample	Minimized by using smaller pulses at low pressures, where fluid properties vary more significantly with pressure.	Dependent on gas	Other approaches for data analysis (ex. numerical simulations of pressure-time data).

Thus, despite the challenges associated with measuring permeability in the nanodarcy range, we have built a system and devised a methodology that has allowed us to overcome many of these obstacles. While not devoid of error, we have considerable

evidence to suggest that our results are reliable and certainly not dominated by leaks. Supporting evidence includes the low leak rate and complete absence of sample bypass (presented in Figure 111), the minimal impact of leak rates and pressure corrections at early times where the slope is measured, the considerable variation in permeability measured between samples, as well as the systematic and geologically reasonable variation in permeability with confining pressure and pore pressure. Finally, we have recently made further improvements to the thermal stability and system leak rate such that we have even greater confidence in our capabilities moving forward.

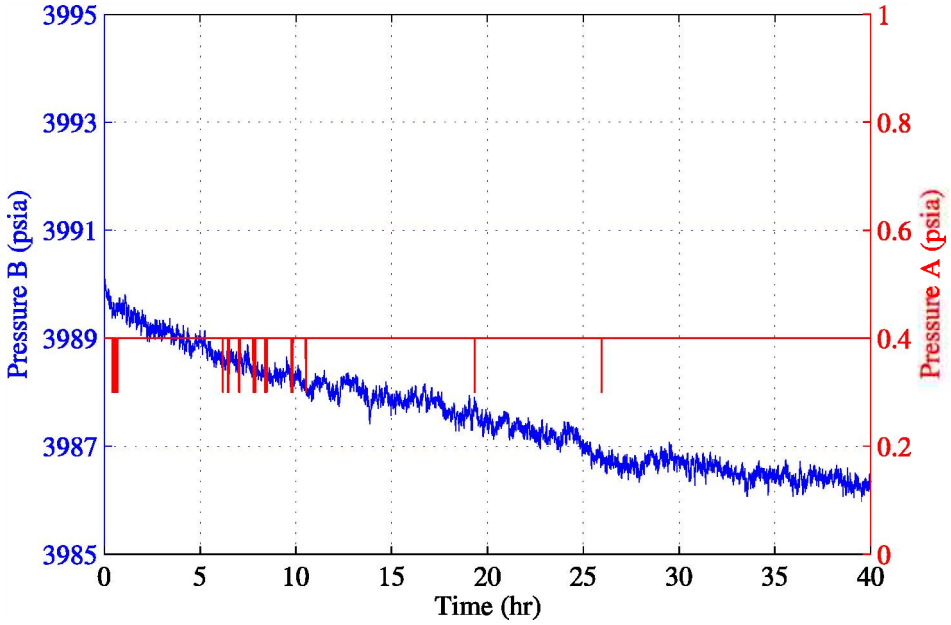

Figure 111: Pressure test with plug in place of sample. Side B, used as the downstream side in our experiments, was pressurized with ~3900 psi of helium, and side A was not pressurized at all. The results show that after 40 hours, no measurable quantity of gas has bypassed the plug into the other chamber. Pressure B has been corrected for temperature fluctuation.

Refinement of Shale Permeability Measurements

For six shale samples, permeability was measured at pore pressures from 1000 to 4000 psi, confining pressures from 2000 to 8000 psi and simple effective stresses ranging from 1000 to 4000 psi. This data was fit to an effective stress law. Of those six samples, three were chosen for additional permeability measurements at pore pressures below 1000 psi. The results for the high pore pressure data (all six samples) will be presented first, followed by a more in depth look at the rocks for which low pressure permeability measurements were also made. Some of these measurements were reported previously and are presented again here after further analysis.

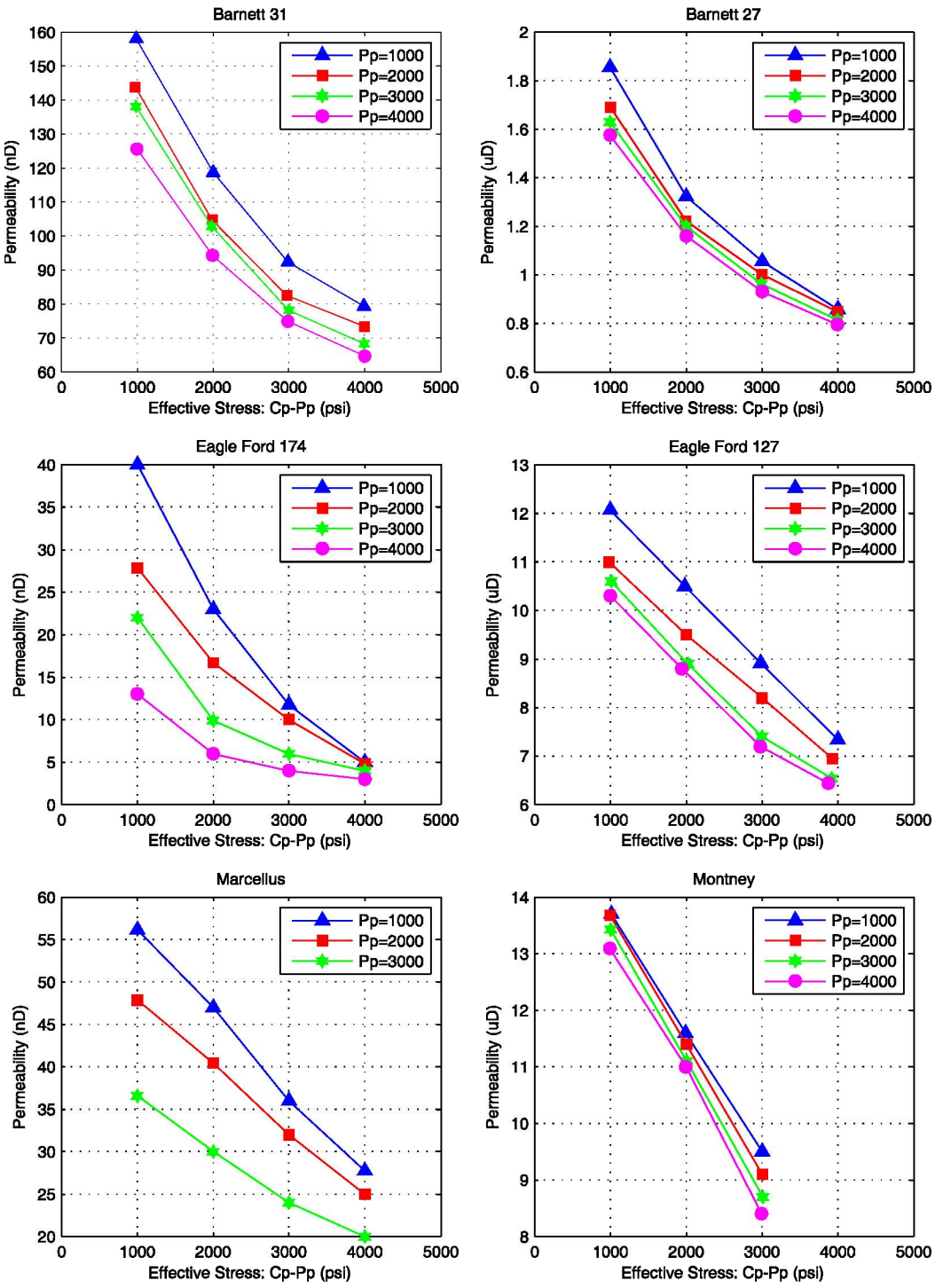

Figure 112: Permeability versus simple effective stress (Cp-Pp). Note permeability units for samples Barnett 27, Eagle Ford 127 and Montney samples (right column) are in microdarcy; all other samples are in the nanodarcy range.

Permeability as a function of simple effective stress (Cp – Pp) is shown for all six samples in Figure 112. There are several features worth pointing out. First, note the scale difference for the Barnett 27, Eagle Ford 127 and Montney samples (microdarcy as

opposed to nanodarcy) and recall that each of these core plugs contained an anomalous through-going feature. Both the Barnett 27 and Eagle Ford 127 samples contained a carbonate layer extending through the core plugs. We believe these carbonate layers are highly permeable relative to the rest of the shale matrix, resulting in a larger than typical plug permeability value in these two samples. The Montney sample contained what appeared to be a very minor crack oriented along its axis, which seems to have enhanced permeability relative to typical Montney plug. Finally, notice that for each sample permeability varies as a function of simple effective stress (C_p-P_p) in a similar way, allowing for a single function to be fit to the whole data set.

The data for each rock was fit to a unique permeability effective stress law as described previously. These results are presented in Figure 113. In all cases, χ was found to be less than 1, indicating that the rocks are more sensitive to changes in confining pressure than changes in pore pressure. By plotting all permeability data as a function of the true effective stress we have essentially shifted all data in effective stress space such that it forms a trend. The fact that we were able to do this suggests that we are successfully able to attribute all permeability variation observed thus far (Pp > 1000 psi) to effective stress effects.

As previously mentioned, three of the six samples were chosen for further characterization at lower pore pressures (Pp < 1000 psi). A typical permeability sample (Eagle Ford 174), a high permeability sample (Eagle Ford 127) and a vertical sample (Marcellus) were selected for variation. Permeability versus effective stress is plotted on the left in Figure 114 using the same effective stress law (same χ) as previously found to fit the high pressure data. It is apparent in this figure that the measurements made at low pore pressure deviate from the trend fit by the high pore pressure data. We attribute this permeability enhancement (relative to what one would predict given the effective stress) to slippage (*i.e.*, Klinkenberg) effects.

Given that all of the data have been shifted in effective stress space (with the appropriate value of χ), we can investigate how permeability varies as a function of pore pressure due to non-stress-related (Klinkenberg) effects. We select several values of true effective stress (indicated in Figure 114 by the black-dashed lines) and create Klinkenberg plots for each by moving vertically along the line and selecting points of intersection with the pore pressure trend. The results are shown on the right half of Figure 114.

There are several aspects of these Klinkenberg plots worth pointing out. First, note the increase in K_b with increasing effective stress for a given rock. This parameter essentially represents the magnitude of gas slippage that is occurring in the rock. This follows intuition given that one would expect increasing effective stress to narrow flow paths, thereby increasing the Knudsen number and the expected contribution from slip flow. It is also worthwhile to compare the magnitude of K_b between samples. Both the Eagle

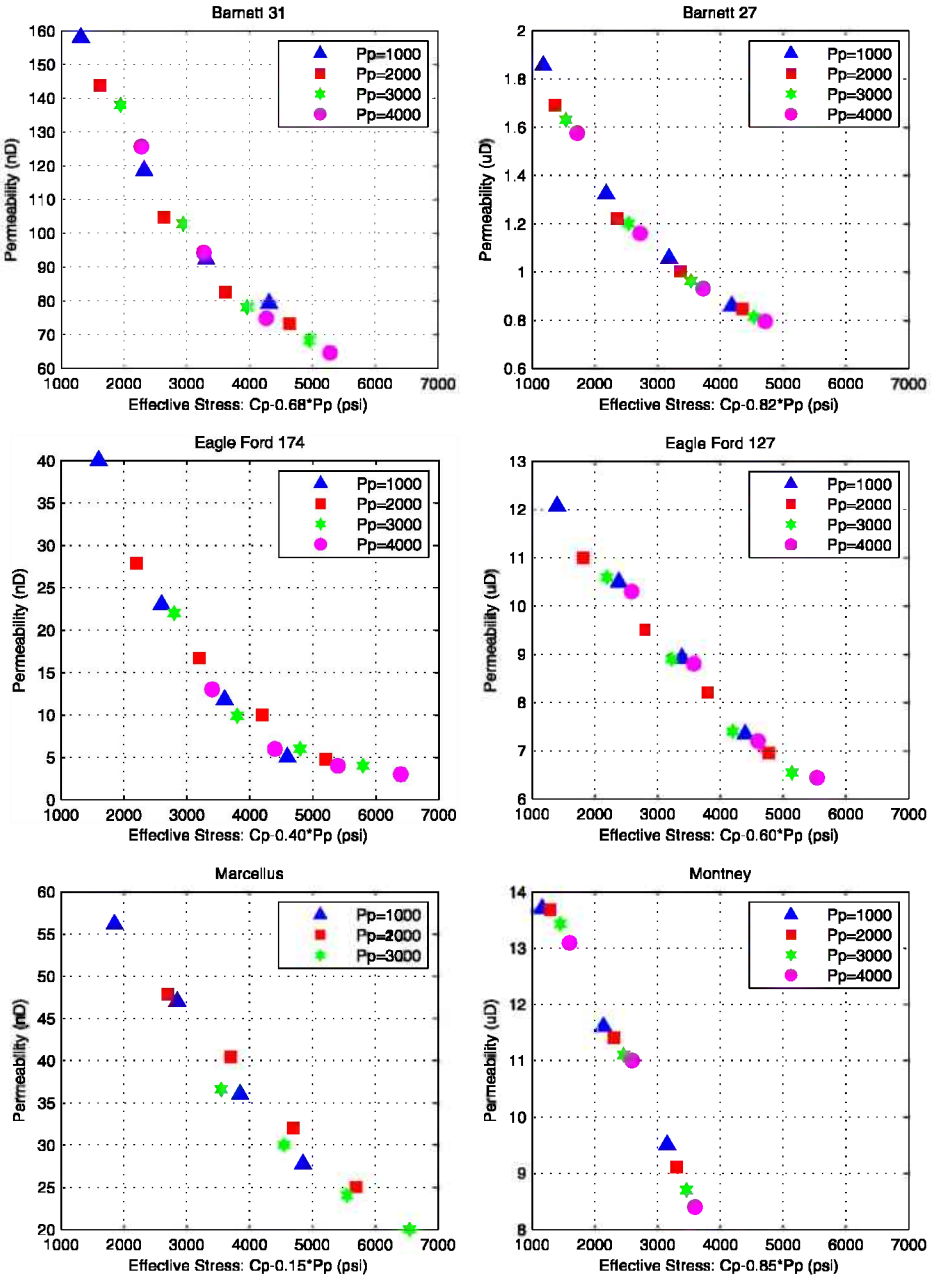

Figure 113: Permeability versus true effective stress after data fit to effect stress law for each sample.

Ford 174 and Marcellus samples are characterized as having a similar permeability, as well as similar contributions from slip flow as evidenced by the similar K_b values. This contrasts with the higher permeability Eagle Ford 127 sample, which has a lower K_b and thus a smaller overall contribution of slip flow to total flow.

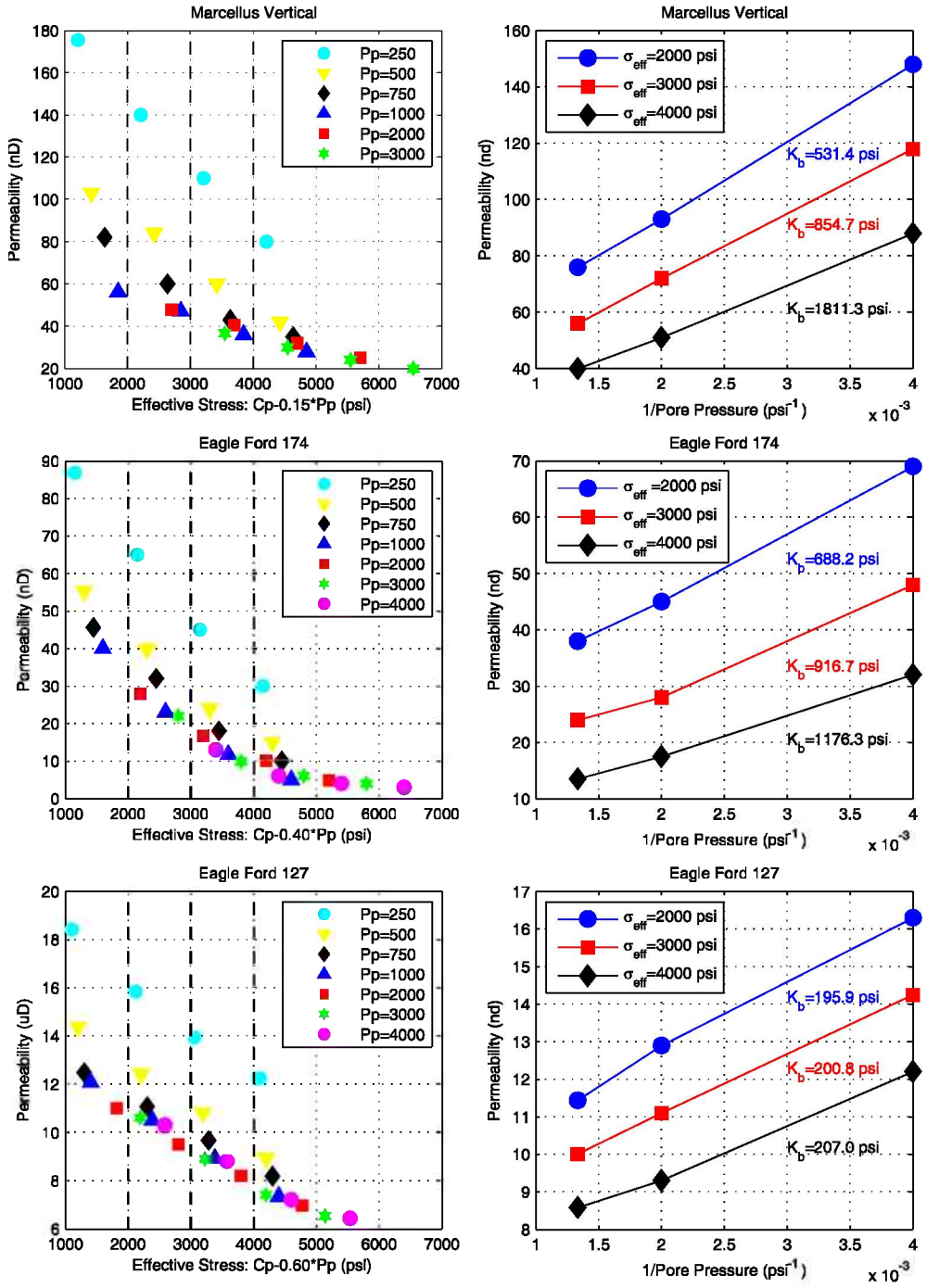

Figure 114: Left: Permeability versus true effective stress with low pore pressure data. Note the deviation from the high pore pressure trend by the low pore pressure points. Black-dashed lines indicate effective stress isolines used for generating Klinkenberg plots by selecting their intersection with the permeability trend for several pore pressures (Pp = 250, 500 and 750 psi). Right: Standard Klinkenberg plots (permeability versus $1/P_p$). Permeability points selected for true effective stress values of 2000, 3000 and 4000 psi. Notice increase in K_b value (slope/intercept) with increasing effective stress.

With Klinkenberg parameters established for each sample, we are now able to calculate the effective size of the flow paths. Moreover, because we also now know how K_b varies with effective stress for each rock, we can estimate how the effective size of the flow paths varies with effective stress as well. These results are presented in Figure 15. Our calculations suggest that the effective pore size varies moderately with effective stress (about 5% in the case of Eagle Ford 127Ha, factor of 2 in the case of Marcellus, and a factor of about 5 in the case of Eagle Ford 174Ha). While many assumptions went into these estimates, the results seem plausible based on the apertures of pore sizes commonly observed in SEM photos in the shale gas literature (Loucks and Reed, 2009).

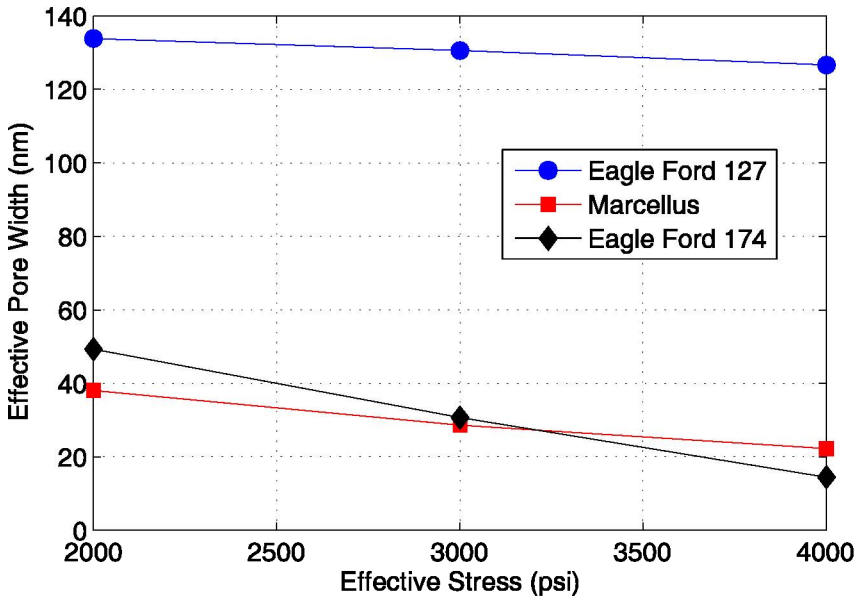

Figure 115: Effective pore width versus true effective stress, as estimated for the Klinkenberg parameter (K_b).

Shale Permeability with Different Gases

Preliminary permeability results have been obtained for several shale samples utilizing different gases as pore fluids. Figure 116 shows permeability as a function of confining pressure for Eagle Ford Sample 127Ha. This sample has unusually high permeability (on the order of 10 microdarcies) when compared with most gas shales with a permeability of 50-500 nanodarcies.

In this sample, the effect of confining pressure reduces the He permeability from 16 μd to about 10 μd. This degree of change is typical of shale gas samples (as discussed previously). When methane and krypton on used as pore fluids, there is a slight reduction in permeability (about 10%) with respect to that when measured with helium. This is likely due to the adsorption of methane. As the pore size in this sample associated with gas transport is about 100nm in size, adsorption of ~0.3 nm size molecules has little effect on permeability. When CO_2 is the pore fluid, the permeability reduction is more significant (about 30%), presumably because CO_2 adsorbs more strongly than methane or krypton.

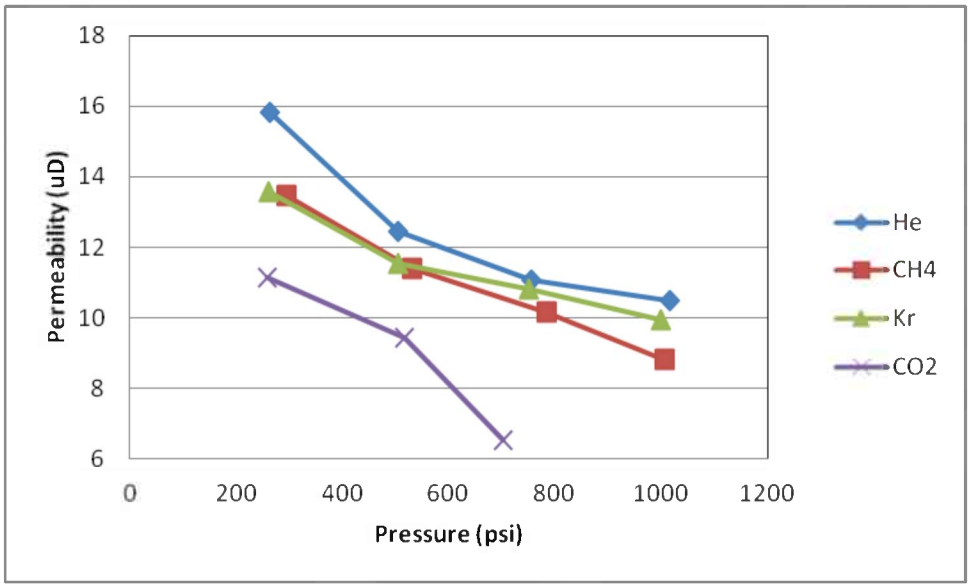

Figure 116: Permeability measurements on a sample of Eagle Ford Shale (sample 127Ha) with unusually high permeability. In this case, the decrease in permeability with adsorbing gases is relatively minor (see text).

In marked contrast, Figure 117 shows that no measureable CO_2 flows through a shale sample with relatively typically low matrix permeability. This sample, a Marcellus shale sample is being measured perpendicular to the bedding. Its permeability with He is about 40 nd. However, when both a 25 and 50 psi pulse of CH_4, Kr or CO_2 are applied to the sample, essentially no pressure response is observed. The upper panel in Figure 117 shows what happens with a 25 psi pulse of pressure CO_2. The pressure drops almost 2 psi in about 16 hours although it should have gone up (see Figure 117). In fact, the observed pressure drop is simply the result of the temperature change of the gas. Similarly, the slight increase in downstream pressure observed on the downstream side of the Marcellus sample in response to a 50 psi pulse (lower part of Figure 117), also reflects the temperature change of the pore gas, not CO_2 flowing through the sample.

The results in Figure 118 basically indicate that permeability to an adsorbing gas is immeasurably small in low permeability shales, perhaps because the pores are extremely small in such formations and adsorption essentially blocks the pores. This phenomenon is still being investigated. At face value, the results shown in Figure 118 imply the permeability to CO_2 is much less than 1 nd.

A new series of tests are planned to further investigate this phenomenon.

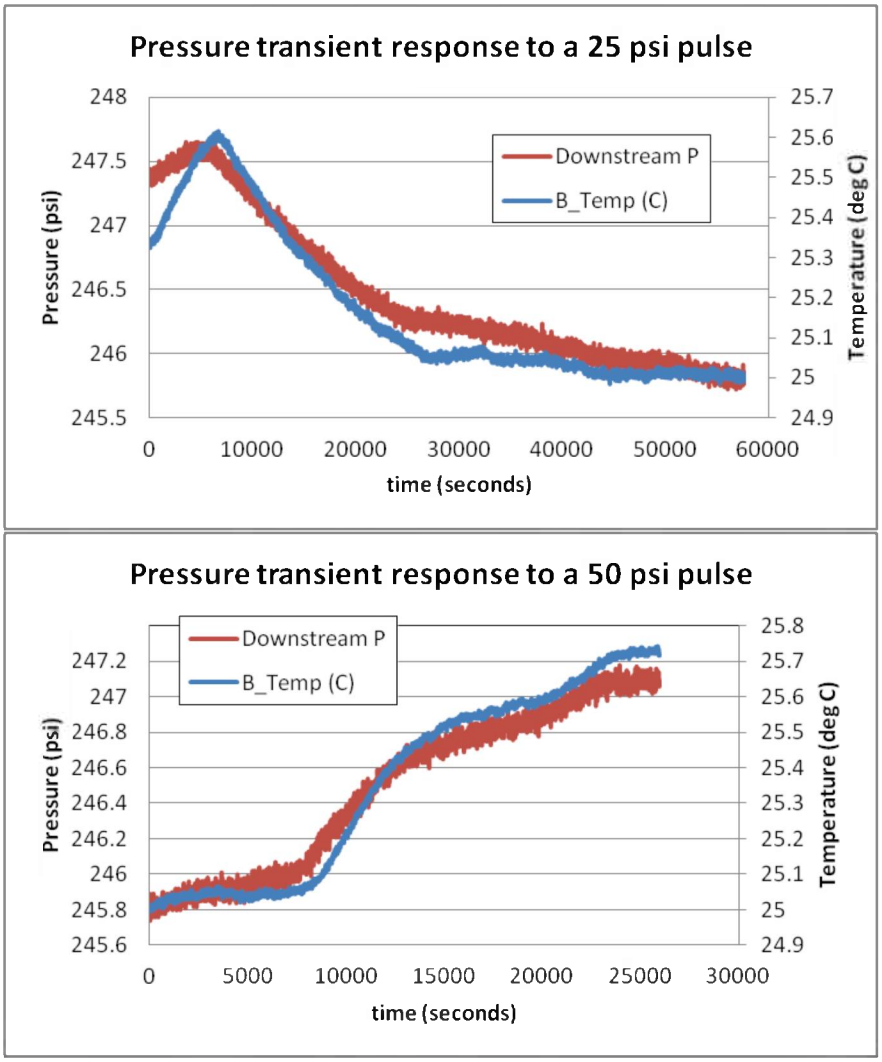

Figure 117: Pressure transient response in Marcellus shale sample in which permeability is being measured perpendicular to the direction of bedding. In this case no discernable flow through the sample occurred. The extremely small pressure change that occurred in response to either a 25 or 50 psi pressure pulse was simply the result of the small change in temperature of the measurement system. No detectable pressure change was detected downstream from the upstream pressure pulse.

A series or permeability of measurements with multiple gases has been conducted on a sample of Eagle Ford shale perpendicular to the bedding planes. We have previously described similar permeability measurements in which a sample of Marcellus shale with a He permeability of about 40 nd, had un-measureable permeability (estimated to be less than 1 nd) when CO_2 was used as a pore fluid. In the experiment shown in Fig. 119, we are finding a similar result.

The experiment began using He at a confining pressure of 3000 psi and pore pressure and 2000 psi. When the confining pressure increased to 6000 psi and then reduced, a decrease in permeability was observed that was mostly recovered when confining pressure was decreased to 3000 psi. A second set of measurements with He at a pore pressure of 500 psi, similar behavior was seen but the unrecoverable permeability decrease was larger, apparently due to the higher effective pressure. When the pore fluid was switched to CO_2

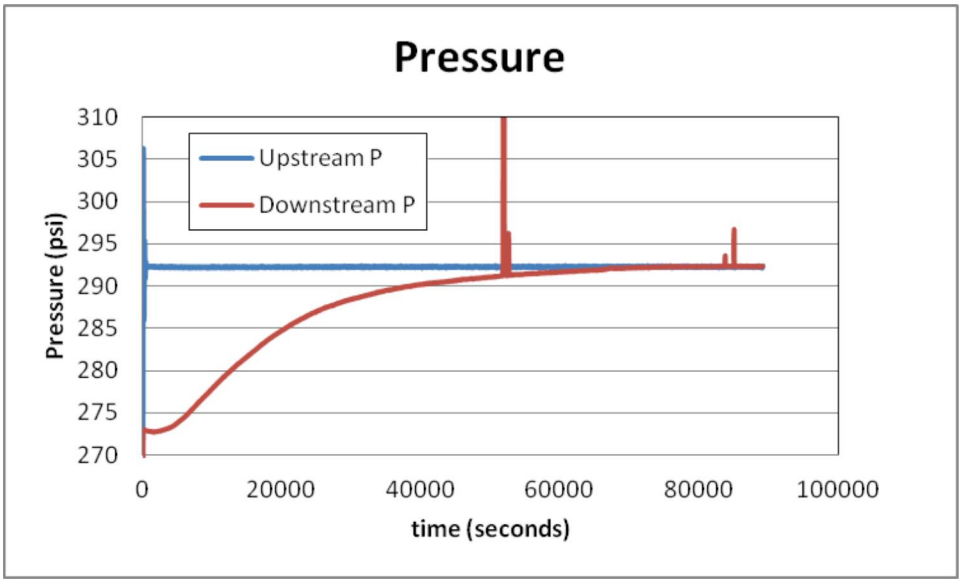

Figure 118: The downstream response of the same Marcellus sample as in Figure 17 to a 25 psi pulse of He. In about the same time shown in the upper panel of Figure 117, the pressure increases by almost 20 psi.

at a pore pressure of 377 psi, the permeability decreased dramatically to about 1 nd. This is seen at confining pressures of both 1500 and 3000 psi.

We attribute this marked decrease in permeability to CO_2 adsorption blocking pore throats in this very low permeability sample. As the experiments with He at 500 psi pore pressure and CO_2 at 377 psi have approximately the same mean free path (see Fig. 119), it seems to confirm the adsorption hypothesis. It is not yet known what will happen at higher confining pressure or whether the permeability loss with CO_2 will be reversible.

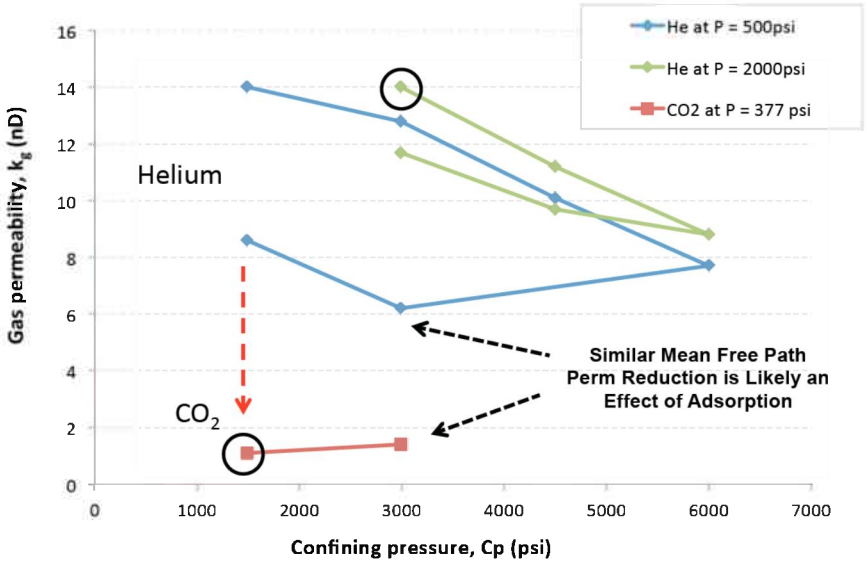

Figure 119. Permeability measurements in a sample of Eagle Ford shale with different pore pressures, confining pressures and gases. As described in the text, the permeability to CO_2 is extremely low, as seen in previous experiments.

3.4: A step-decay method for core characterization

Characterization of the permeability, porosity, and sorption of shale cores is laborious. We have modified with good success the pulse decay method of permeability characterization and developed interpretation techniques to understand the transport properties of helium, carbon dioxide, methane, and nitrogen. This new apparatus also aids in the interpretation of gas transfer from more permeable microfractures to less permeable matrix of shale.

Traditionally, methods as attributed to Brace et al., (1968), Amaefule et al. (1986), Dicker and Smits (1988), and Jones (1997) have been used for gas permeability measurements of low permeability samples. They are still used in laboratory measurements for shale samples. The Brace et al. (1968) approximate solution assumes a linear pressure gradient at all times that may lead to significant errors (Yamada and Jones, 1980; Bourbie and Walls, 1982). It also ignores the gas sorption effect that restricts the solution to only non-adsorptive gases (Amaefule et al., 1986). Jones (1997) developed an analytical solution to calculate the permeability after taking into the account the criticisms imposed by several authors such as Dicker and Smits (1988), Bourbie and Walls (1982), Yamada and Jones (1980), and Lin (1977) regarding the Brace et al. (1968) solution. Jones (1997) included the effect of compressive storage of the sample's pore volume to correct for the permeability measurements.

In our work, gas permeability measurements, however, are intended to include adsorptive gases such as carbon dioxide and methane. Therefore, the gas permeability is additionally analyzed by solving the mass balance equations numerically. This research simulator aids interpretation of experimental results, mainly permeability. For example, the fine-scale porosity maps from above are useful as part of the input to a core-scale simulator. This is a platform to examine various physics as well as a means to integrate the smaller scale predictions. Current commercial simulation tools appear to be lacking in all of the physical mechanisms that we might wish to examine. A conventional simulator may not include gas slippage, sorption and diffusion effects. Commercial simulators, however, do provide a means of verification of research codes under limiting conditions.

3.3.1 Apparatus and Experimental Procedure

The pressure pulse decay apparatus is shown in Fig. 120 and it relies on placing a sample core inside a holder made of stainless steel that is connected to closed upstream and downstream volumes. Because the system is capable of running a series of pressure pulses without vacuum evacuation of the apparatus, we refer to the procedure as a step decay measurement.

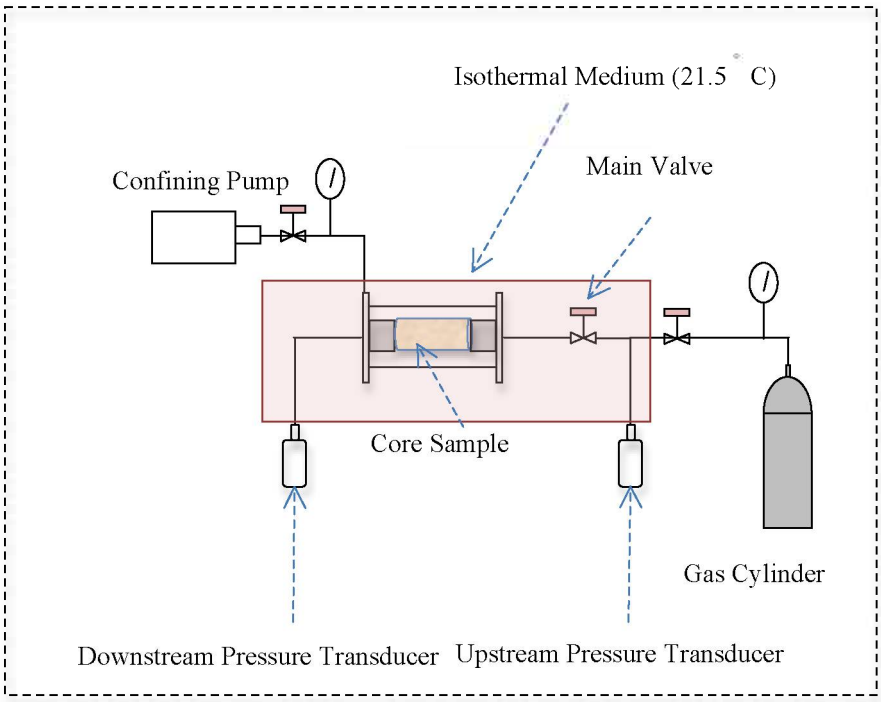

Figure 120: Schematic of the experimental setup.

Initially, the pressure exerted is identical throughout the system. The main valve that separates the upstream volume from the core and the downstream volumes is closed initially. The upstream pressure is increased to a value 5% greater than the initial pressure in the core and downstream volumes. The main valve is opened and gas is allowed to flow into the core and the downstream volume. The pressure is monitored and recorded using pressure transducers (Super TJE Model). Once the pressure equilibrates in the system, upstream and downstream pressure profiles are obtained and used for permeability measurements. Temperature is also monitored and controlled (Omega CN8200 Series) throughout the system to ensure flow stability.

To demonstrate the capabilities of the step-decay apparatus, a core plug from the Eagle Ford shale play is used, see Fig. 121(b). The sample has a clear calcite filled fracture that propagates along in width and length. It is a horizontal core and is sampled from a depth of 12,753.3 ft. The XRD composition of the sample is provided in Table 10. The sample mainly contains calcite with a relatively low clay content of 12.3 wt%. The total organic content of the sample is about 4.8 wt%. Wang et al. (2009) showed a linear relationship between TOC and free and adsorbed gas content. The greater the TOC, the greater the sorption.

The sample was heated in a vacuum oven for three days at 65.5°C to remove any residual moisture. The sample is placed on the bottom cap and a Teflon heat-shrink tube wraps the sample. The inside of another piece of heat-shrink tube is coated with a white silicone material and placed around the sample. The sample, then, is wrapped with both aluminum foil and nickel foil as a diffusion barrier to prevent gas from escaping the core to the confining volume. This wrapping order is made twice and allowed to dry for three days.

Table 10: XRD composition of Eagle Ford core sample.

XRD Composition, %					
Quartz	Feldspar	Calcite	Pyrite	Clay	TOC
22.7	1.2	53.3	4.7	12.3	4.8

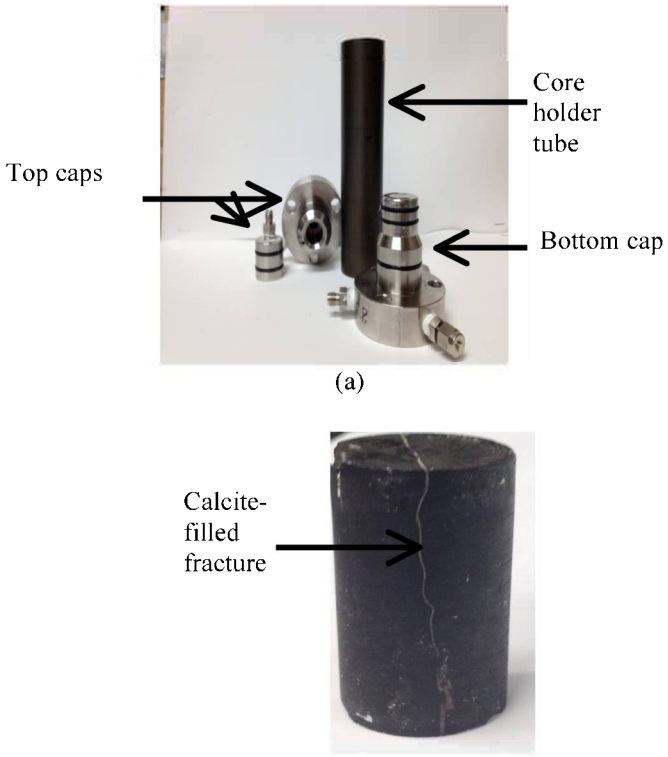

Figure 121: (a) Core holder apparatus and (b) core sample.

After putting together the core system apparatus, two pressure transducers and a temperature controller are used. The temperature of the sample is kept constant at 21.5 °C. A water pump is used to apply confining pressure on the sample and constant net effective stress. Table 11 lists the core and apparatus volumes.

Table 11: Core and apparatus volumes.

Upstream Volume, cm^3	12.1
Downstream Volume, cm^3	5.7
Core Length, cm	4.6
Core Diameter, cm	2.5
Pore Volume, cm^3	1.4

3.3.2 Numerical Simulation

While Darcy permeability is an intrinsic rock property, the permeability of gas flow through micropores depends on the rock, gas type, and operating conditions (Javadpour, 2009). The diffusive flow of gas in micropores is believed to be dominant over viscous

flow (Roy et al., 2003). Recently, several authors such as Javadpour (2009), Akkutlu and Fathi (2011), Shabro et al. (2011) and Darabi et al. (2012) have coupled Darcy flow with Knudsen diffusion to describe gas transport in shale reservoirs. The contribution of Knudsen diffusion increases as the Knudsen number increases, i.e. the gas mean free path becomes comparable to the pore diameter.

Numerical flow simulation and history matching is one technique to infer gas apparent permeability. A fully implicit 2-D, single-phase, compressilble-gas simulator was written to study gas flow characteristics of shale cores and to be used as a means of inferring gas permeability via matching of pressure history. This research simulator allows us the freedom of adding/subtracting various physical mechanisms of transport and sorption. The simulator uses the black oil model and a standard upstream-weighted finite volume approach (Aziz and Settari, 1979). The Newton Raphson method was used to solve the non-linearity in pressure terms. The flux of gas is described by Darcy's law without diffusion. The permeability in the model is a constant property and represents the average apparent Darcy permeability for the given pressure drop. The pressure drop difference is fixed at 5% to allow comparison between other simplified analytical methods of data interpretation as well to keep the net effective pressure constant. The gas properties, i.e. viscosity and compressibility, are dynamic and are estimated using NIST (NIST Webbook, 2013) and the Peng Robinson equation of state (Peng and Robinson, 1976), respectively.

The numerical scheme is fully implicit. The gas compressibility makes the transmissibility terms very sensitive to pressure change and therefore explicit schemes cannot be used for this problem. The general equation solved in discretized form is

$$\frac{\partial}{\partial x}\left(\alpha\frac{A_x k_x}{\mu_g B_g}\frac{\partial p}{\partial x}\right)\Delta x+\frac{\partial}{\partial y}\left(\alpha\frac{A_y k_y}{\mu_g B_g}\frac{\partial p}{\partial y}\right)\Delta y=V_b\frac{\partial}{\partial t}\left[\emptyset\frac{1}{B_g}+(1-\emptyset)\rho_m V_g\right], \quad (1)$$

where α is the transmissibility conversion factor, A is the cross-sectional area, k is the measured gas permeability and is assumed the same in the x and y directions, μ_g is the gas viscosity, B_g is the gas formation volume factor, V_b is the block volume, ϱ_m is the rock density and V_g is the volume of adsorbed gas. Sorption is assumed to be at equilibrium.

The 2-D model is in Cartesian form and simulates the physical dimensions of the pressure pulse decay experiment, is represented in Fig. 122.

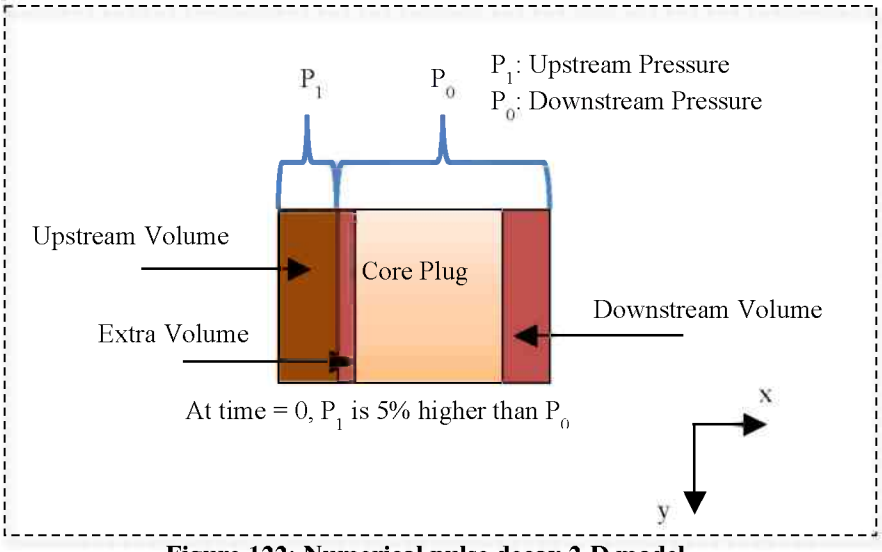

Figure 122: Numerical pulse decay 2-D model.

In this model, four volumes were created: one for the upstream volume, one for the volume between the main valve and the core (called extra volume), one for the core sample and one for the downstream volume. The extra volume is separated from the upstream volume by a closed valve prior to the start of the experiment. The initial upstream pressure is 5% greater than the core and downstream pressure. The pressures in the extra volume, core sample, and the downstream volumes are initially the same, P_0. Once the upstream valve is opened, the pressure in the extra volume rises instantly to the upstream pressure. The pressure decline in the upstream volume during the experiment is uniform. The boundary conditions of the system are no-flow. No source/sink terms are needed. The simulator was validated by comparison with a commercial simulator for gas flow without sorption. Grid and time step refinements were conducted to minimize numerical dispersion caused by the truncation errors due to PDE discretization.

The in-situ porosity distribution of the core was measured using CT-scan imaging as described in section 3.2 and shown in Fig. 123. CT-scan results of the sample understudy and several other shale samples are found in Vega et al. (2013). The average porosity of the sample is about 6.2%. The porosity profile incorporated in this 2-D model was extracted from the middle layer of the CT scan image, see Fig. 123 below. The map shows a clear high-porosity pathway through the sample. This is a calcite filled fracture that is visible by to the naked eye, Fig. 68(b).

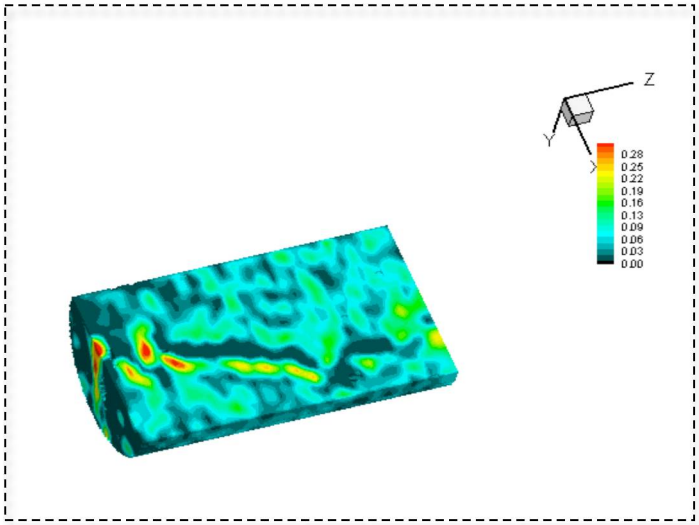

Figure 123: A 2-D slice of the Eagle Ford core using CT scan, (Vega et al., 2013).

The overall porosity map used in the numerical model including the porosity of the upstream volume, extra volume, core, and downstream volumes are shown in Fig. 71. Note that the scale used for Figs. 123 and 124 is not the same. The porosity values in the upstream and downstream volumes, in Fig. 5, are assumed to be 1 while the porosity in the small extra volume is adjusted to represent the measured volume of the flow lines. The permeability in the open volumes is set to 8000 mD while the core permeability is in the tens of micro-Darcy range.

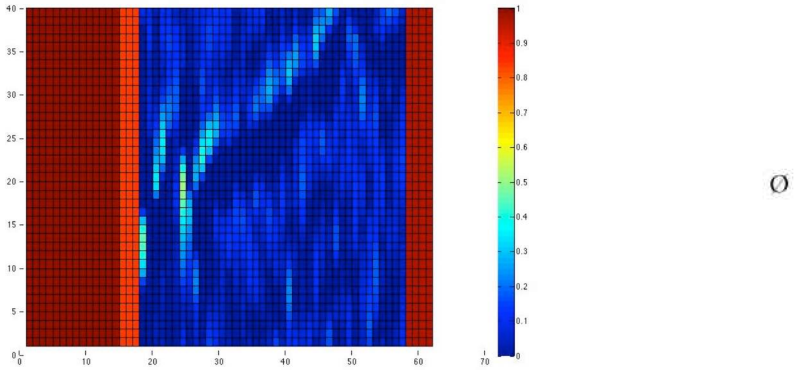

Figure 124: Porosity profile used in the numerical model.

In all the numerical experiments the same porosity profile is used because the net effective stress applied to the core sample was the same for all the cases. The apparent permeability is inferred by matching the simulated and measured upstream and downstream pressure history simultaneously.

3.3.3 Sorption measurements

In addition to low-pressure sorption analysis, high-pressure sorption measurements were conducted on CH_4 and CO_2 at the core level using the transient pressure pulse decay apparatus. The measurements are based on tracking the number of moles in the upstream and downstream volumes during gas transport. As the gas transports downstream, the

number of moles of gas in the core is estimated by subtracting the total number of moles in the downstream volume from the upstream moles. The pore volume of the sample is estimated using He and Boyle's law. Specific Gibbs excess isotherms are generated and converted to absolute isotherms as indicated in Eqs. 2 and 3, respectively.

$$N_{excess} = N_{total} - V_{system}\ \rho_{gas}, \tag{2}$$

$$N_{absolute} = \frac{N_{excess}}{1 - \frac{\rho_{adsorbed}}{\rho_{gas}}}, \tag{3}$$

Where N_{excess} is the Gibbs excess sorption, N_{total} is the total number of moles in the upstream while the downstream is at vacuum, V_{system} is all the volume occupied by gas, ϱ_{gas} is the gas molar density at equilibrium , $N_{absolute}$ is the absolute sorption and $\varrho_{adsorbed}$ is the adsorbed phase gas molar density.

After estimating the absolute isotherms for CH_4 and CO_2, a Langmuir model (Langmuir, 1918) (Eq. 4) and BET model (Brunauer et al., 1938) (Eq. 5) were fitted, respectively.

$$V_g = \frac{V_L P}{P + P_L}, \tag{4}$$

$$V_g = \frac{V_m C \left(\frac{P}{P_o}\right)}{1 - \left(\frac{P}{P_o}\right)} \frac{1 - (N+1)\left(\frac{P}{P_o}\right)^N + N\left(\frac{P}{P_o}\right)^{N+1}}{1 + (C-1)\left(\frac{P}{P_o}\right) - C\left(\frac{P}{P_o}\right)^{N+1}}, \tag{5}$$

Where V_g is the volume of adsorbed gas, V_L is Langmuir volume at which maximum monolayer occurs, P is the pore pressure, and P_L is the Langmuir pressure. In the BET model, V_m is the BET maximum monolayer volume of adsorbed gas, C is the BET equilibrium constant that controls the sorption isotherm behavior at lower pressure values, P_o is the saturation pressure and N is the maximum number of adsorbed layers. The results section discusses the sorption isotherms obtained.

3.3.4 Sorption results

The absolute sorption isotherms of CH_4 and CO_2 for the Eagle Ford core sample are shown in Fig. 125. The applied net effective stress in all the sorption experiments is 500 psi and is kept constant at all times. The sorption of CH_4 is fit with a Langmuir isotherm. Sufficient pressure was not applied to reach a plateau of sorbed CH_4; therefore, Langmuir isotherm parameters are not reported. CO_2 shows greater sorption in comparison to CH_4 and the shape of the isotherm is decidedly nonLangmuir. The shape of CO_2 sorption isotherms appears to be suitable for the n-layer BET isotherm, as seen in Fig. 125. The measured sorption data are incorporated in the numerical simulator.

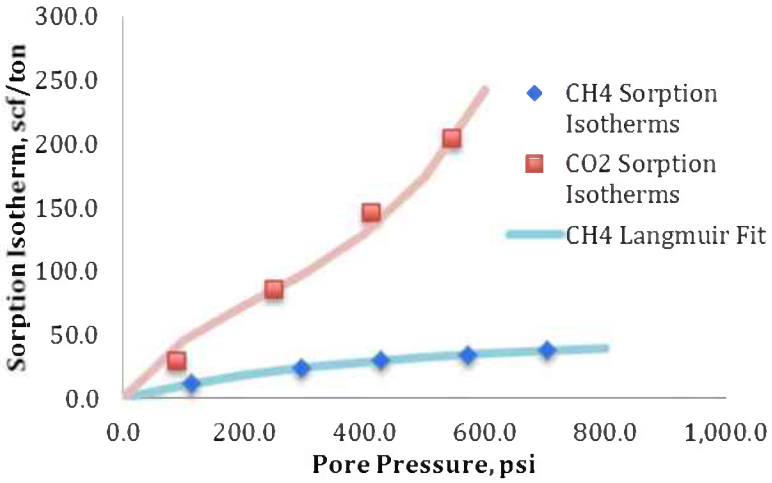

Figure 125. High-pressure gas sorption in the core sample.

3.3.5 Permeability Results

Three sets of permeability measurements are discussed here. Prior to running the experiment, the shale sample was exposed to high effective stress, about 30% greater than the maximum operating effective stress in all the experiments to eliminate poroelasticity effects. The applied net effective stress in all the sorption experiments is 500 psi and is kept constant at all times. When trying to match the experimental and simulated pressures, the upstream and downstream pressures are matched simultaneously. This is achieved by matching the pressure difference. Figure 125 shows an example of the match between the upstream and downstream experimental and numerical pressures. Figure 126 shows another example of how to match the pressure difference between the experiment and the simulation model.

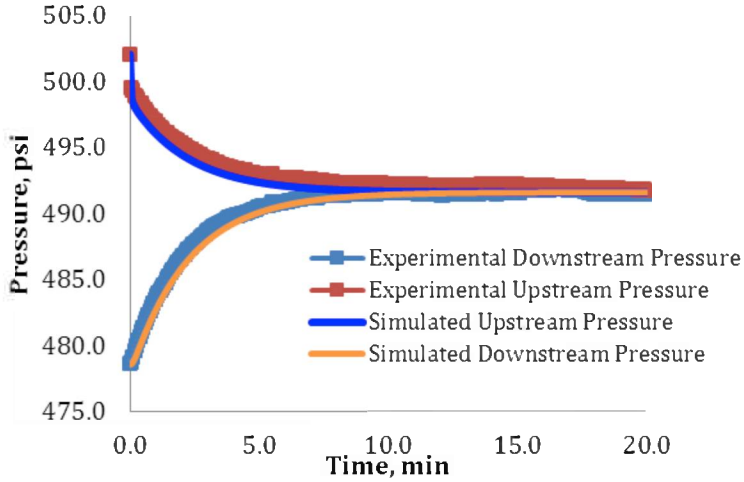

Figure 126. An example of the upstream and downstream pressure responses.

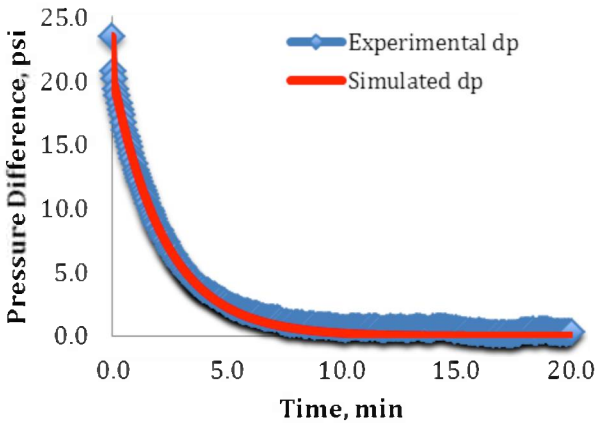

Figure 127: Example of matching the pressure difference between the experiment and the model.

Figure 128 shows the permeability estimated using the history-match as well as the Jones (1997) and Brace et al. (1968) methods. Brace et al. (1968) permeability values are clearly lower than the history-match and Jones (1997) solutions. The Brace et al. (1968) solution matches only the upstream pressure of the experiment while Jones (1997) and the history-match models match upstream and downstream pressure simultaneously. This preserves mass balance. Also, the Brace et al. (1968) solution assumes a core porosity of zero, hence no compressive gas storage in the core, only in the upstream and downstream volumes. Jones (1997) and the history-match methods, on the other hand, account for the compressive gas storage in the system. Accordingly, the permeability obtained by Brace is underestimated. The work done by Rowe (1985) has also indicated that Brace et al. (1968) solution underestimates the permeability values. Jones (1997) and the history-match results are very close to each other. The error bars in Fig. 76 represent permeability values obtained from selecting different pressure range when applying Jones (1997) and Brace et al. (1968) solutions. The error bar associated with the Jones (1997) method is too small to be visible. The error associated with the Brace et al. (1968) method is large compared to the other methods. This permeability fluctuation is also discussed in Brace et al. (1968) original manuscript.

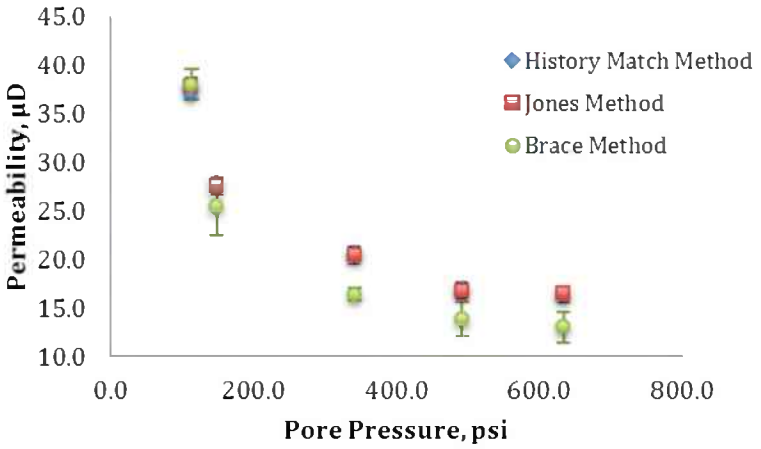

Figure 128: Measured permeability using history-match, Jones (1997) and Brace et al. (1968) solutions.

The sample permeability was additionally tested using CH_4 and CO_2. Figure 128 shows the permeability versus reciprocal pressure plot for He, CH_4, and CO_2 as generated by the history-match method. The error bars in the data found in Fig. 128 and 129 represent ±5% uncertainty in the volumetric measurements of the apparatus. The measured permeability using CH_4 is slightly greater or similar to He permeability for large pressures (i.e., small 1/p). This result was unexpected; however, the sample is considerably permeable for shale. If the dimensions of the pore space were narrow, sorption takes place simultaneously as the gas transports through the rock, and therefore, the measured gas permeability is strongly dependent on sorption. The measured gas permeability reflects Darcy flow in conductive zones in the core. The molecular diameter of CH_4, 0.38 nm, is larger than the diameter of He, 0.26 nm. Therefore, the transport of CH_4 takes place in larger pores while He can additionally access smaller conduits. We offer a conceptual model that partially explains these results. The system can be thought as gas transport in various layers with different permeabilities arranged in parallel, see Eq. 6.

$$k_{avg} = \frac{\sum_{i=1}^{3} k_i h_i}{\sum_{i=1}^{3} h_i}, \qquad where\ k_1 > k_2 > k_3 \tag{6}$$

Here k is permeability and L is the thickness. The average permeability using He is estimated based on gas access to three different volumes, as an example, with three permeabilties. Due to the size of the CH_4 molecule, this gas only accesses two different volumes with two permeabilites, k_1 and k_2. The resulting averaged permeability would, accordingly, be greater for CH_4 due to the fact that it only accesses two volumes. In the case of He, we take the sum over 3 layers whereas for CH_4, we take the sum over two layers. The sorption of CH_4 to shale surfaces tends to reduce permeability and tends to negate the larger permeability in this specific case that results from gas penetration of

intermediate to large-sized pores. The Klinkenberg effect on He and CH_4 measured permeabilities is lower at larger pressures as well.

The measured permeability of CO_2 is the smallest among all gases. CO_2 is an extremely adsorptive gas compared to CH_4 and He, see Fig. 129. A straight-fit line is fit for each gas to estimate the slip factor (i.e., b_{slip}) and rock intrinsic permeability (i.e. k_∞). The intrinsic permeability values for the three gases are close to each other. The slip factor of He is the greatest while the value of CO_2 is the lowest. This is because He is a non-adsorptive gas and therefore is expected to have greater slippage along pore walls in comparison to CO_2. The CH_4 slip factor falls in between the other two gases.

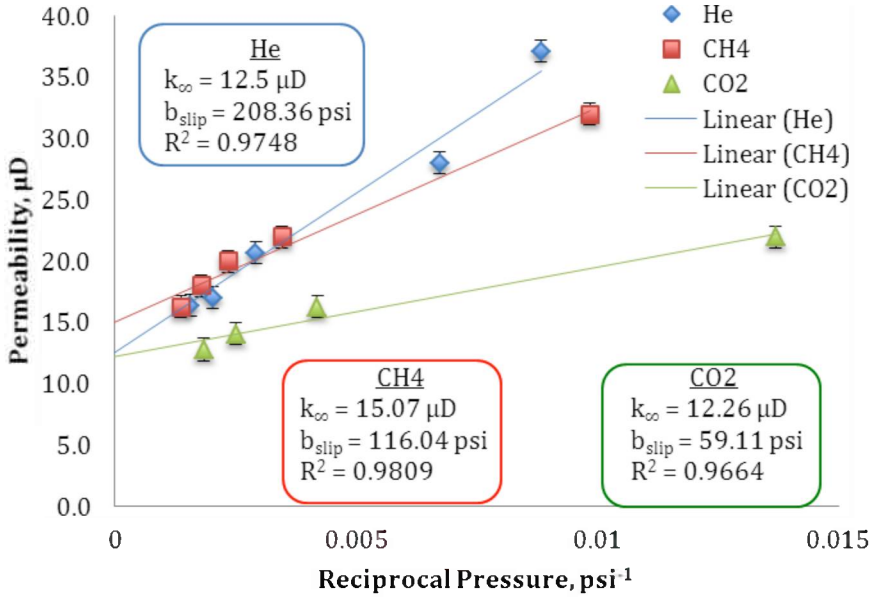

Figure 129: Permeability versus reciprocal pressure for He, CH_4 and CO_2 gas.

If a straight-fit line for the CH_4 permeability points is made by excluding the permeability at the lowest pressure (largest 1/p), all gases have nearly the same intrinsic permeability, see Fig. 129. This result may indicate very low influence of sorption on gas permeability for this particular sample. This might be attributed to gas transport in the most conductive conduits that are the least affected by sorption. It may also indicate that CO_2 did not cause swelling to the sample. A recent publication by (Aljamaan et al., 2013) showed a significant reduction to the CO_2 intrinsic permeability of core samples of Barnett shale that mainly was attributed to large sorption effects.

From the knowledge of intrinsic permeability and slip factor, the apparent pore radius and gas mean free path are calculated. The apparent pore diameter as estimated using Eq. 5 for He is about 54.14 nm, i.e. pore diameter of 108.28 nm. This averaged pore size lies in the macropore region. This might be attributed to the existence of a high porosity region as shown in the CT-scan image of the sample. Also, the applied net effective stress of 500 psi on the sample might not be enough to close permeable conduits in the core. The pore size estimated for He is used for CH_4 and CO_2 interpretation as discussed previously.

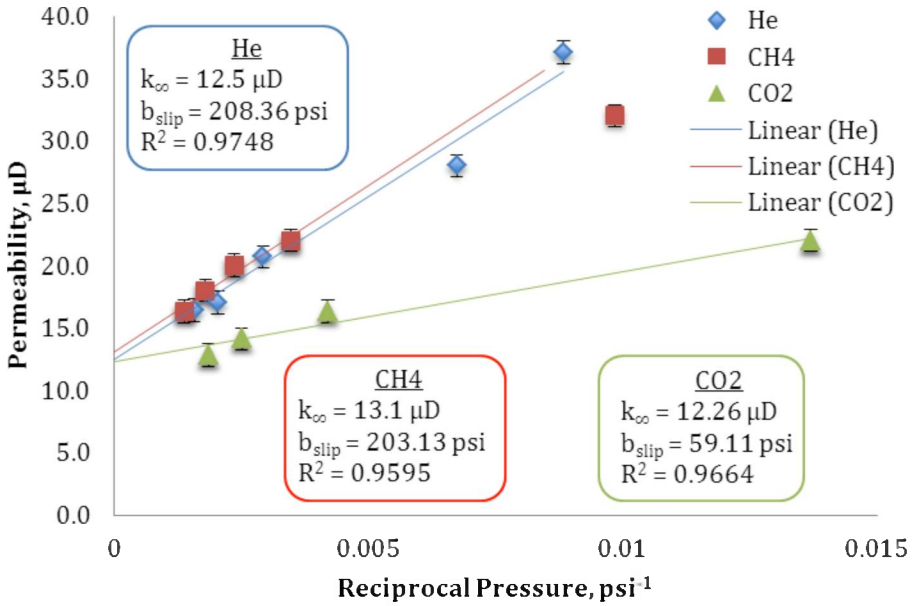

Figure 130: Adjusted linear fits for permeability versus reciprocal pressure for He, CH_4 and CO_2 gas.

The pore diameter estimated from the low-pressure sorption analysis, 13.9 nm, is significantly smaller than that estimated from permeability measurements, 108.28 nm. This difference is attributed to the sample nature and the operating conditions. Grinding the sample to a powder removes the larger sized pores. Powder samples have more uniform micropores and mesopores than intact cores. The intact core can additionally have macropores and microcracks. The CT-scan images indicate a clear porous channel in the rock that might be responsible for the high permeability flow and therefore high apparent pore diameter. In addition, the experimental pressure in the transient pressure pulse decay is substantially larger than the maximum pressure of the low-pressure analysis. The larger the pressure, the smaller the mean free path of the gas. This may restrict gas access to smaller pores in the micropore range during gas transport through the core. The flow is forced into larger pores and may leave some micropores unvisited. Adsorptive gases, however, access smaller pores due to their sorptive characteristics and eventually yield a smaller apparent pore radius. This effect, however, for this sample occurs only after the downstream and upstream pressures equilibrate.

The mean free paths of the gases used in the experiment and the corresponding Knudsen numbers are calculated. The mean free paths of CH_4 and CO_2 are lower than He due to their larger densities and molecular masses. Knudsen number is analyzed using the estimated mean free path and pore diameter from the experiments and is depicted in Fig. 79. For most of the pressure points investigated in this work, the flow regime for the particular sample and flow conditions lies in the slip regime, see Table 11. It is essential to develop a consistent framework that involves pore radius and mean free path measurements to predict accurately the transport regime. Such an analysis would include the Darcy approximation and suggest corrections to permeability estimation when flow lies in the transition or free molecular flow regimes. The method introduced by Javadpour

(2009) combines continuum and Knudsen diffusion and can be used to predict measured permeability for high Knudsen numbers. The estimation of the pore size and mean free path values also can be used for comparison with imaging results obtained from SEM/STEM or with transport results obtained from MD.

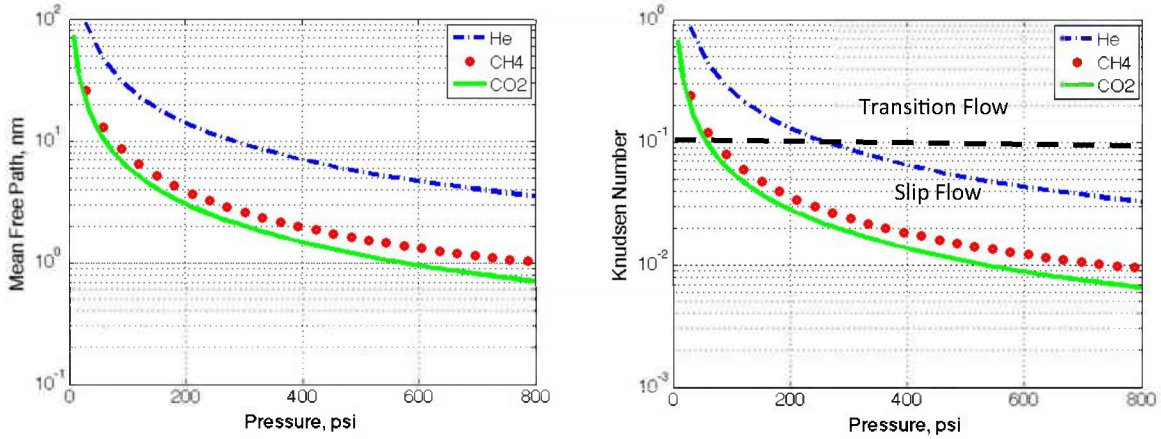

Figure 131: Estimated mean free path (left) and Knudsen number (right) for He, CH_4 and CO_2.

3.3.6 Multiple porosity information from step-decay tests

We have had good success in using the step-decay apparatus and the interpretation techniques developed to understand the transport properties of helium, carbon dioxide, methane, and nitrogen. Our research, as well as that of others, has shown that the gas-carrying pore system in shale exhibits a variety of length scales. With decreasing length scale comes decreasing permeability. Given the quite low permeability of regions of shale with nanometer-sized pores coexisting with fracture-like conduits, we have examined carefully pressure histories from step-decay experiments to understand if there is additional information in the history that might be analyzed. Figure 132 presents a pressure history from an Eagle Ford core with an expanded pressure axis. Both upstream and downstream pressure are given. It is notable that the upstream and downstream pressures converge relatively rapidly and then both decline somewhat over an extended time period. As the figure indicates, we compute that the porosity occupied by gas when the upstream and downstream pressure histories converge is about 6%. Given longer time, the helium penetrates additional pore space and the total porosity reaches about 7.8%. Thus, we interpret the late time pressure decline (increase in porosity) as gas penetrating the most impermeable and hard to reach pores within the shale matrix. Note that helium is a nonadsorbing gas.

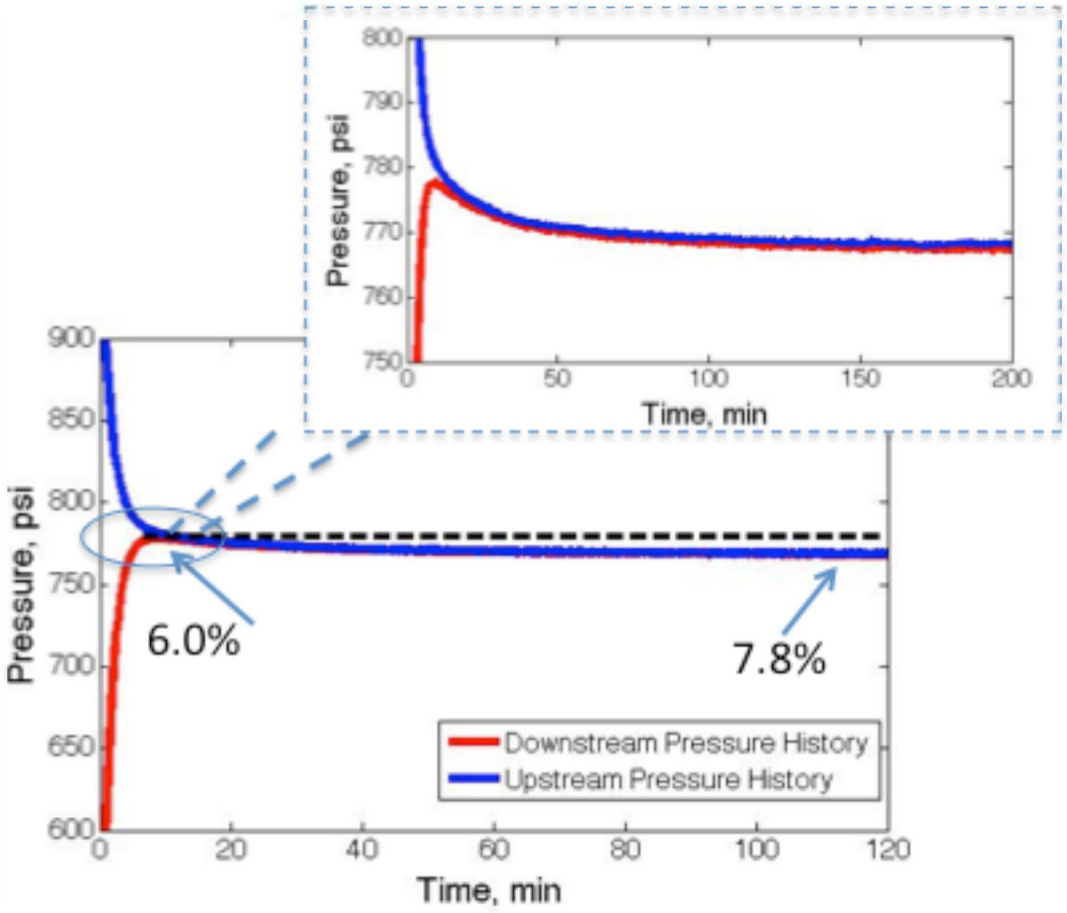

Figure 132. Example pressure history with expanded pressure scale. The effective stress is 2000 psi.

3.3.7 Summary step-decay

Permeability determination using a history-match method for low permeability transient pressure decay experiments provides reliable measurement when exactly matched to the experimental pressure history. Such a method yields minimal errors when measuring the intrinsic permeability and slip factor for estimating the effective pore radius. The numerical model incorporates pressure-dependent gas properties and non-ideal phase behavior including the case of CO_2 as the saturating gas. The simulator can be extended to study transport behavior at larger pressure drops and permeability corrections incorporated for the given flow regime. Comparisons with Jones (1997) and Brace et al. (1968) methods showed that the latter method yields lower permeability values that can reach up to a 25% difference. Jones (1997) solution has smaller error bar and yields results closer to the history-match method.

The high-pressure sorption isotherms were measured for the sample core using CH_4 and CO_2. CO_2 showed greater sorption compared to CH_4 at all pressures, as expected. At the modest pressures of investigation, CO_2 sorbed more than five times as much in comparison to CH_4. The CH_4 isotherm shows a Langmuir-like behavior while the isotherms obtained with CO_2 is described by n-BET behavior. The measured isotherms

were incorporated in the simulator to estimate the gas permeability. Unlike extremely low permeability shale samples, this sample shows large permeability that might be attributed to the calcite-filled fracture that was captured by the CT-scan imaging and is visible to the eye. Permeability measurements for the different gases showed that values obtained using He and CH_4 are close to each other. The permeability measured using CO_2 gas was the lowest. In general, the intrinsic permeability values obtained for the three gases are somewhat close to each other. The effect of sorption on permeability measurements is not as high as expected and this is likely due to the high rock permeability.

References

Akin, S., Kovscek, A.R., 2003. "Computed Tomography in Petroleum Engineering Research." *Applications of X-ray Computed Tomography in the Geosciences.* Geological Society, London, Special Publications, 215, 23-28.

Akkutlu, I. Y. and Fathi, E., (2011). "Multi-scale Gas Transport in Shales with Local Kerogen Heterogeneities", SPE 146422, presented at the SPE Annual Technical Conference and Exhibition held in Denver, Colorado, USA, 30 October-2 November.

Aljamaan, H., Alnoaimi, K., Kovscek, A., (2013). "In Depth Experimental Investigation of Shale Physical and Transport Properties", SPE 1582146, presented at the Unconventional Resources Technology Conference held in Denver, Colorado, USA, 12-14 August.

Amaefule, J. O., Wolfe, K., Walls, J. D., Ajufo, A. O., Peterson, E., (1986), "Laboratory Determination of Effective Liquid Permeability in Low-Quality Reservoir Rocks by the Pulse Decay Technique", SPE 15149, 493-502.

Amyx, J.W., Bass, D.M., Whiting, R.L., Petroleum Reservoir Engineering (Physical Properties), McGraw-Hill, 1960.

Aziz, K., Settari, A., (1979). "Petroleum Reservoir Simulation", printed by Blitzprint Ltd., Calgary, Alberta.

Bagri, A.; Grantab, R.; Medhekar, N. V.; Shenoy, V.B. Stability and formation mechanisms of carbonyl- and hydroxyl-decorated holes in graphene oxide. *J. Phys. Chem. C* 2010, 114, 12053–12061.

Barton, N., Bandis, S., and Bakhtar, K., Strength, deformation and conductivity coupling of rock joints: Int. J. Rock Mech. Min. Sci. Geomech. Abstr., 22(3), 121-140 (1985).

Beroza, G.C. et al. (2009), Deep Tremors and Slow Quakes. *Science*. 1025, 324.

Bird, P. (1984), Hydration-phase diagrams and friction of montmorillonite under laboratory and geologic conditions, with implications for shale compaction, slope stability, and strength of fault gouge, *Tectonophysics* 107**,** pp. 235–260.

Blanpied, M. L., C. J. Marone, D. A. Lockner, J. D. Byerlee, and D. P. King (1998), Quantitative measure of the variation in fault rheology due to fluid-rock interactions, *J. Geophys. Res.*, 103(B5), 9691–9712.

Bourbie, T., Walls, J., (1982), "Pulse Decay Permeability: Analytical Solution and Experimental Test", SPE Journal 9477, 719-721.

Brace, W. F., Walsh, J. B., Frangos, W. T., (1968). "Permeability of Granite Under High Pressure". Journal of Geophysical Research, Vol. 73, No. 6, March 15.

Bravo, M.C., Journal of applied physics 102 (2007) 074905.

Brunauer, S., P. H. Emmett, and E. Teller, 1938, Adsorption of Gases in Multimolecular
Layers: Journal of the American Chemical Society, v. 60, p. 309-319.

Busch, A., S. Alles, Y. Gensterblum, D. Prinz, D. N. Dewhurst, M. D. Raven, H. Stanjek,and B. M. Krooss (2008), Carbon dioxide storage potential of shales, *Int J Greenh Gas Con, 2(3),* 297-308.

Busch, A., Alles, S., Krooss, B., Stanjek, H., Dewhurst, D., 2009, Effects of physical sorption and chemical reactions of carbon dioxide in shaly caprocks: Energy Procedia, **1,** 3229-3235.

Bustin, R. M., A. M. M. Bustin, A. Cui, D. Ross, and V. M. Pathi (2008), Impact of Shale Properties on Pore Structure and Storage Characteristics, in *SPE Shale Gas Production Conference,* edited, Society of Petroleum Engineers, Fort Worth, Texas, USA.

Byerlee, J. D. (1978), Friction of rocks, *Pure Appl. Geophys*., 116, 215– 626.

Calhoun, J.C., Yuster, S.J., Drilling and Production Practice, 1946.

Candela, T., Renard, F., Klinger, Y., Mair, K., Schmittbuhl, J., and Brodsky, E.E., Roughness of fault

surfaces over nine decades of length scales: J. Geophys. Res., 117, B08409, doi:10.1029/2011JB009041 (2012).
Chen, Z., Narayan, S.P., Yang, Z., and Rahman, S.S., An experimental investigation of hydraulic behavior of fractures and joints in granitic rock: Int. J. Rock Mech. Min. Sci., 37, 1061-1071 (2000).
Chiaramonte, L., Zoback, M.D., Friedmann, J., Stamp, V., Seal integrity and feasibility of CO2 sequestration in the Teapot Dome EOR pilot: Geomechanical site characterization: Environ. Geol., 54, 1667-1675 (2008).
Crawford, B.R., Faulkner, D.R., and Rutter, E.H., Strength, porosity, and permeability development during hydrostatic and shear loading of synthetic quartz-clay fault gouge: J. Geophys. Res., 113, B03207, doi:10.1029/2006JB004634 (2008).
Darabi, H., Ettehad, A., Javadpour, F., Sepehrnoori, K., (2012). "Gas Flow in Ultra-Tight Shale Strata". Journal of Fluid Mechanics **710**: 641-658.
Das, I., and M.D. Zoback (2010), Long-period, long duration seismic events during hydraulic fracture stimulation of a shale gas reservoir, The Leading Edge, July 2011, 778-786.
Das, I., and M.D Zoback, Long-period, long-duration seismic events during hydraulic stimulation of shale and tight gas reservoirs — Part 1: Waveform characteristics, *Geophysics, v.*78, no.6, 1–12 (2013a).
Das, I., and M.D Zoback, Long-period long-duration seismic events during hydraulic stimulation of shale and tight gas reservoirs — Part 2: Location and mechanisms, *Journal of Geophysics, , v.*78, no.6, 1–12, (2013b).
Dicker, A. I., Smits, R. M., (1988). "A Practical Approach for Determining Permebility From Laboratory Pressure-Pulse Decay Measurements". Paper SPE 17578, presented at the SPE International Meeting on Petroleum Engineering, held in Tianjin, China, November 1-4.
De Pablo, J.J., Marianne, B., Prausnitz, J.M., Fluid Phase Equilibria 73 (1992) 187.
Ertekin, T, King, G.R., and Schwerer, F.C. (1986). "Dynamic Gas Slippage: A Unique Duel-Mechanism Approach to the Flow of Gas in Tight Formations," SPE 12045 Proceedings of the SPE Annual Technical Conference and Exhibition, San Francisco, CA, Oct 5-8.
Esaki, T., Du, S., Mitani, Y., Ikusada, K., and Jing, L., Development of a shear-flow test apparatus and determination of coupled properties for a single rock joint: Int. J. Rock Mech. Min. Sci., 36, 641-650 (1999).
Faulkner, D.R. and Rutter, E.H., Comparisons of water and argon permeability in natural clay-bearing fault gouges under high pressure at 20°C: J. Geophys. Res., 105, 16,415-16,426, (2000).
Firouzi, M., Molaai Nezhad, Kh., Tsotsis, T.T., Sahimi, M., Journal of Chemical Physics 120 (2004) 8172.
Firouzi, M., Tsotsis, T.T., Sahimi, M., Chemical Engineering Science 62 (2007) 2777.
Firouzi, M., Wilcox, J., Molecular modeling of carbon dioxide transport and storage in porous carbon-based materials, J. Microporous and Mesoporous Materials, 158 (2012) 195-203.
Firouzi, M., Wilcox, J., Journal of Chemical Physics 138, 064705, (2013).
Fischer, G.J., The determination of permeability and storage capacity: Pore pressure oscillation method: in Fault Mechanics and Transport Properties of Rocks, edited by B. Evans and T.-F. Wong, 187-212, Academic, San Diego, Calif. (1992).
Ford, D.M., Heffelfinger, G.S., Molecular Physics 94, 673, (1998).
Frenkel, D., Mooij, G.C.A.M., Smit, B., 1991, Journal of Physics: Condensed Matter 3 (1991) 3053.
Gale, J. F. W., R. M. Reed, and J. Holder, 2007, Natural fractures in the Barnett Shale and their importance for hydraulic fracture treatments: AAPG Bulletin, v. 91, n. 4 (April 2007), p. 603-622.

Haenel, M. W. Recent progress in coal structure research. *FUEL* 1992, 71, 1211-1223.

Hashimoto, A.; Suenaga, K.; Gloter, A.; Urita, K. Direct evidence for atomic defects in graphene layers. *Nature* 2004, 430(19), 870-873.

Harris, J.G., Yung, K.H., Journal of Physical Chemistry 99 (1995) 12021.
Harris, J., Rice, S.A., J. Chemical Physics 88 (1988) 1298.
Heffelfmger, G.S., Ford, D.M., Molecular Physics 94, 659, (1998).
Honarpour, M.M., Cromwell, V., Hatton, D., Satchwell, R., 1985. "Reservoir Rock Descriptions Using Computed Tomography (CT)." paper SPE 14272 presented at the SPE Annual Technical Conference and Exhibition held in Las Vegas, NV. 22-25 Sep.
Ikari, M. J., D. M. Saffer, and C. Marone (2007), Effect of hydration state on the frictional properties of montmorillonite-based fault gouge, *J. Geophys. Res.*, 112, B06423.

Ikari, M. J., D. M. Saffer, and C. Marone (2008), Frictional and hydrologic properties of clay-rich fault gouge, *J. Geophys. Res.*, 114, B05409.
Jagiello, J., Thommes, M., Comparison of DFT characterization methods based on N_2, Ar, CO_2 and H_2 adsorption applied to carbons with various pore size distribution, Carbon 42 (2004) 1227-1232.
Javadpour, F., Fisher, D., Unsworth, M., (2007). "Nanoscale Gas Flow in Shale Gas Sediments". Journal of Canadian Petroleum Technology **46** (10): 55-61.
Javadpour, F., (2009). "Nanopores and Apparent Permeability of Gas Flow in Mudrocks (Shales and Siltstone). Journal of Canadian Petroleum Technology **48** (8): 16-21.
Jia, L., C. M. Ross, and A. R. Kovscek, 2007, A Pore Network Modeling Approach to Predict Petrophysical Propoerties of Diatomaceous Reservoir Rock, SPE Reservoir Engineering and Evaluation. 10 (6), 597-608. DOI: 10.2118/93806-PA.

Jones, S. C.(1997). "A Technique for Faster Pulse-Decay Permeability Measurements in Tight Rocks". Paper SPE 28450, presented at the SPE Annual Technical Conference and Exhibition held in New Orleans, 25-28 September.
Kang, S. M., E. Fathi, R. J. Ambrose, I. Y. Akkutlu, and R. F. Sigal, 2010, CO_2 Storage Capacity of Organic-Rich Shales: SPE Annual Technical Conference and Exhibition, 134583-MS.
Khademi, M., Sahimi, M., Journal of Chemical Physics 135 (2011) 204509.
Klinkenberg, L.J., The permeability of porous media to liquids and gases, Drilling and Production Practice, API (1941) 200-213.
Kohli, A. H. and M.D. Zoback, Frictional properties of shale reservoir rocks,
Journal of Geophysical Research, Solid Earth, v. 118, 1-17, doi: 10.1002/jgrb. 50346,
(2013).
Kowalcyzk, P., Furmaniak, S., Gauden, P. and Terzyk, A., 2010. Carbon dioxide adsorption-induced deformation of microporous carbons. J. Phys. Chem. C, 114, 5126-5133.
Kostov, M. K., Santiso, E. E., Gubbins, K. E., and Nardelli, M. B. Dissociation of water on defective carbon substrates. *Phys. ReV. Lett.* 2005, 95, 136105.
Kovscek, A. R., G.-Q. Tang, and K. Jessen (2005), Laboratory and Simulation Investigation of Enhanced Coalbed Methane Recovery by Gas Injection, in *SPE Annual Technical Conference and Exhibition,* edited, Society of Petroleum Engineers, Dallas, Texas.
Kranz, R., Saltzman, J.S., and Blacic, J.D., Hydraulic diffusivity measurements on laboratory rock samples using an oscillating pore pressure method: Int. J. Rock Mech. Min. Sci. Geomech. Abstr., 27, 345-352, (1990).
Kudin, K. N.; Ozbas, B.; Schniepp, H. C.; Prud'homme, R. K.; Aksay, I. A.; Car, R. Raman spectra of graphite oxide and functionalized graphene sheets. *Nano Lett.* 2008, 8(1), 36-41.
Kwon, O., Kronenberg, A.K., Gangi, A.F., and Johnson, B., 2001, Permeability of Wilcox shale and its effective pressure law: Journal of Geophysical Research, v.106, p. 19339-19353.
Laso, M., de Pablo, J.J., Suter, U.W., 1992, J. Chemical Physics 97 (1992) 2817.
Langmuir, I., 1916, The constitution and fundamental properties of solids and liquids, Part I.: Journal of the American Chemical Society, v. 38, p. 2221-2295.
Lin, W. (2009), Gas Sorption and the Consequent Volumetric and Permeability Change of Coal, Stanford University Dissertation.
Loeb, Leonard B. (2004) [1927], *The Kinetic Theory of Gases*, Dover, p. 293, ISBN 978-0-486-49572-9
Loucks, R. G., R. M. Reed, S. C. Ruppel, and D. M. Jarvie (2009), Morphology, Genesis, and Distribution of Nanometer-Scale Pores in Siliceous Mudstones of the Mississippian Barnett Shale, *Journal of Sedimentary Research, 79(12),* 848-861.
Lu, X.-C., F.-C. Li, and A. T. Watson (1995a), Adsorption Studies of Natural Gas Storage in Devonian Shales, *SPE Formation Evaluation, 10(2),* 109-113.
Lu, X.-C., F.-C. Li, and A. T. Watson (1995b), Adsorption measurements in Devonian shales, *Fuel, 74(4),* 599-603.
Liu, Y.J., and Rice, J.R., (2007), Aseismic slip transients emerge spontaneously in three-dimensional rate and state modeling of subduction earthquake sequences. *J. Geophys.Res.* v. 110, B08307.

Liu, Y., Wilcox, J. CO_2 adsorption on carbon models of organic constituents of gas shale and coal. *Environ. Sci. Technol.* 2011, 45 (2), 809–814.

Liu, Y., J. Wilcox, Molecular Simulation of CO_2 Adsorption in Micro- and Mesoporous Carbons with Surface Heterogeneity, Int. J. Coal Geol., 104, 83-95 (2012).
Liu, Y., J. Wilcox, Molecular Simulation Studies of CO_2 Adsorption from CO_2/N_2, CO_2/CH_4, and CO_2/H_2O Mixtures by Carbon for CCS Applications, Environ. Sci. Technol. 47(1), 95-101 (2012).
Macedonia, M.D., Maginn, E.J., Molecular Physics 96 (1999) 1375.
Matteucci, S., Yampolskii, Y., Freeman, B. D. and Pinnau, I., 2006, transport of gases and vapors in glassy and rubbery polymers, in Materials Science of Membranes for Gas and Vapor Separation (eds Y. Yampolskii, I. Pinnau and B. Freeman), John Wiley & Sons, Ltd, Chichester, UK.
Mooij, G.C.A.M., Frenkel, D., Smit, B., Journal of Physics: Condensed Matter 4 (1992) L255.
Moss, R.M., Pepin, G.P., Davis, L.A., 1992. "Direct Measurement of the Constituent Porosities in a Dual-Porosity Matrix." *The Log Analyst.* 33(2), 126-135.
NIST (2007), NIST Reference Fluid Thermodynamic and Transport Properties Database (REFPROP): Version 9.0, edited.
NIST—National Institute of Standards and Technology (2011). from http://physics.nist.gov/PhysRefData/XrayMassCoef/tab3.html
Noda, H., Shimamoto, T., (2009), Constitutive properties of clayey fault gouge from the Hanaore fault zone, southwest Japan, *J. Geophys. Res.*, 114, B04409
Nuttall, B. C., C. F. Eble, J. A. Drahovzal, and R. M. Bustin, 2005, Analysis of Devonian
Black Shales in Kentucky for Potential Carbon Dioxide Sequestration and Enhanced Natural Gas Production, Kentucky Geological Survey.
Okazaki, K., Katayama, I., and Noda, H., Shear-induced permeability anisotropy of simulated serpentinite gouge produced by triaxial deformation experiments: Geophys. Res. Lett., 40, doi:10.1002/grl.50302, (2013).
Paterson, M.S. and Wong, T.-F., Experimental Rock Deformation – The Brittle
Field: Springer, 2nd edition, 347 p., (2005).
Peacock, D.C.P., Knipe, R.J., and Sanderson, D.J., Glossary of normal faults: J. Struct. Geol., 22, 291-305, (2000).
Peng, D., Robinson, D., (1976). "A New Two-Constant Equation of State". Industrial Engineering Chemistry Fundamentals **15** (1): 59-64.
Peters, K. E. (1986), Guidelines for evaluating petroleum source rock using programmed pyrolysis, *Aapg Bull, 70(3),* 318-329.
Peters, K. E., and M. R. Cassa (1994), Applied Source Rock Geochemistry, in *The Petroleum System: From Source to Trap,* edited by L. B. Magoon and W. G. Dow, AAPG Memoir.
Ravikovitch, P. I., Neimark, A. V., Characterization of nanoporous materials from adsorption and desorption isotherms, Colloids and Surfaces A: Physicochem. Eng. Aspects 187-188 (2001) 11-21.
Reed, R. M., and Milliken, K. L., How to Overcome Imaging Problems Associated with Carbonate Minerals on SEM-Based Cathodoluminescence systems: J. of Sedimentary Research v. 73, n.2, March, p. 328-332, (2003).
Roy, S., Raju, R., (2003). "Modeling Gas Flow Through Microchannels and Nanopores". Journal of Applied Physics **93** (8): 4870-4879.
Saites. F, Wang, G., Guo, R., Mannhardt, A., Kantzas, A., 2006. "Coalbed Characterization Studies With X-Ray Computerized Tomography (CT) and Micro CT Techniques", paper 2006-027 presented at the Canadian International Petroleum Conference held in Calgary, Canada. 13-15 Jun.
Reinen, L. A., and J. D. Weeks (1993), Determination of Rock Friction Constitutive Parameters Using an Iterative Least Squares Inversion Method, *J. Geophys. Res.*, 98(B9), 15,937–15,950.
Ross, D. J. K., and R. M. Bustin (2007), Impact of mass balance calculations on adsorption capacities in microporous shale gas reservoirs, *Fuel, 86(17-18),* 2696- 2706.
Ross, D. and Bustin, M., 2008, The importance of shale composition and pore structure upon gas storage potential of shale gas reservoirs: Marine and Petroleum Geology, **44,** 233-244.
Ryckaert, J.-P., Bellemans, A., Faraday discussions of the Chemical Society 66 (1978) 95.
Rubin, A. M. (2008), Episodic slow slip events and rate-and-state friction, *J. Geophys. Res.*, 113, B11414.
Ruina, A. (1983). Slip Instability and State Variable Friction Laws. *J. Geophys. Res.* Vol. 88, pgs. 10,359-10,370.
Saffer, D. M., and C. Marone (2003), Comparison of smectite- and illite- rich gouge frictional properties: Application to the updidp limit of the seismogenic zone along subduction megathrusts, *Earth Planet. Sci. Lett.*, 215, 219– 235.

Sagidullin, A.I. and I. Furo, 2008, Langmuir 24, pp. 4470-4472.
Segall, P. and J.R. Rice (1995), Dilatancy, compaction, and slip instability of a fluid saturated fault, *J. Geophys. Res.*, v.102, 155-221.
Segall, P. and J.R. Rice (2006), Does shear heating of pore fluid contribute to earthquake nucleation?, *J. Geophys. Res.*, 111, B09316.
Segall, P., Rubin A.M., Bradley, A.M., and J.R. Rice (2010), Dilatant Strengthening as a Mechanism for Slow Slip Events, *J. Geophys. Res.,* 115, B12305.
Shabro, V., Torres-Verdin, C., Javadpour, F., (2011). "Numerical Simulation of Shale-Gas Production: from Pore-Scale Modeling of Slip-Flow, Knudsen Diffusion, and Langmuir Desorption to Reservoir Modeling of Compressible Fluid". Paper SPE 144355, presented at the SPE North American Unconventional Gas Conference and Exhibition held in the Woodlands, Texas, USA, 14-16 June.
Shibazaki, B., and T. Shimamoto (2007), *Geophys. J. Int.* 171, 191.
Shimamoto, T., and J. M. Logan (1981), Effects of simulated clay gouges on the sliding behavior of Tennessee sandstone, *Tectonophysics*, 75, 243– 255.
Siepmann, J.I., Frenkel, D., Molecular Physics 75 (1992) 59.
Smit, B., Karaborni, S., Siepmann, J.I., Journal of Chemical Physics 102 (1995) 2126.

Smith K. L.; Smoot, L. D.; Fletcher T. H.; Pugmire R. J. *The structure and reaction processes of coal.* Springer, 1994.

Sokhan, V.P., Nicholson, D., Quirke, N., Journal of Chemical Physics 117 (2002) 8531.
Sondergeld, C. H., R. J. Ambrose, C. S. Rai, and J. Moncrieff (2010a), Micro-Structural Studies of Gas Shales, in *SPE Unconventional Gas Conference,* edited, Society of Petroleum Engineers, Pittsburgh, Pennsylvania, USA.
Sondergeld, C. H., K. E. Newsham, J. T. Comisky, M. C. Rice, and C. S. Rai (2010b), Petrophysical Considerations in Evaluating and Producing Shale Gas Resources, in *SPE Unconventional Gas Conference,* edited, Society of Petroleum Engineers, Pittsburgh, Pennsylvania, USA.
Sone, H., Zoback, M.D., (2010), Strength, creep and frictional properties of gas shale reservoir rocks. 44th US Rock Mechanics Symposium and 5th US-Canada Rock Mechanics Symposium, Salt Lake City, Utah. *ARMA* 10-463.
Sone, H and Zoback, M.D., Mechanical properties of shale-gas reservoir rocks—Part 1: Static and dynamic elastic properties and anisotropy, *Geophysics,* v. 78, no. 5, D381-D392, 10.1190/GEO2013-0050.1 (2013).
Sone, H and Zoback, M.D., Mechanical properties of shale-gas reservoir rocks—Part 2: Ductile creep, brittle strength, and their relation to the elastic modulus, *Geophysics,* v. 78, no. 5, D393-D402, 10.1190/GEO2013-0051.1 (2013).
Sudibandryo M., Pan Z., Fitzgerald, J., Robinson, R. and Gasem, K. 2003, Adsorption of methane, nitrogen, carbon dioxide, and their binary mixtures on dry activated carbon at 318.2 K and pressures up to 13.6 MPa: Langmuir, **19,** 5323-5331.
Takahashi, M., Permeability change during experimental fault smearing: J. Geophys. Res., 108(B5), 2235, doi:10.1029/2002JB001984 (2013).
Tembe, S., Lockner, D.A., and Wong, T.-F., Effect of clay content and mineralogy on frictional sliding behavior of simulated gouges: Binary and ternary mixtures of quartz, illite, and montmorillonite: J. Geophys. Res., 115, B03416, 22 p., doi:10.1029/2009JB006383 (2010).
Teufel, L., Permeability changes during shear deformation of fractured rock: 28th US Symposium on Rock Mechanics, Tuscon, 29 June – 1 July, 473-480, (1987).
Thomas, A., McGaughey, A.J.H., Nano Letters 8 (2008) 2788.
Thorstenson, D.C., Pollock, D.W.: Gas transport in unsaturated zones: multicomponent systems and adequacy of Fick's laws. Water Recourses Res. **25**(3), 477–507 (1989)

Van Krevelen, D.W. *Coal*, 3rd completely revised edition; Elsevier, Amsterdam, The Netherland, 1991.

Vega, B., Dutta, A., Kovscek, A. R., " CT Imaging of Low Permeability, Dual-Porosity Systems Using High X-Ray Contrast Gas", submitted to Transport in Porous Media (2013).
Vega, B., J. C. Andrews, Y. Liu, J. Gelb, A. R. Kovscek, 2013. "Nanoscale Visualization of Gas Shale Pore and Textural Features," Proceedings of the Unconventional Resources Technology Conference held in Denver, Colorado, USA, 12-14 August.
Vermylen, J.P. (2011). "Geomechanical Studies of the Barnett Shale, Texas USA," PhD Thesis, Stanford University.

Vinegar, H.J., Wellington, S.L., 1987. "Tomographic Imaging of Three-Phase Flow Experiments." *Review of Scientific Instruments,* **58,** 96-107.
Walls, J., and Nur, A., 1979, Pore pressure and confining pressure dependence of permeability in sandstone: 7th Formation Evaluation Symposium, Can. Well Logging Soc.
Wang, F., Reed, R., John, A., Katherine, G., (2009). "Pore Networks and Fluid Flow in Gas Shales". SPE 124253, presented at the Annual Technical Conference and Exhibition held in New Orleans, Louisiana, USA, 4-7 October.
Warren, B. E. (1969), *X-ray diffraction,* Reading, Mass., Addison-Wesley.
Watson, A.T., Mudra, J., 1994. " Characterization of Devonian Shales With X-Ray Computed Tomography." *SPE Formation Evaluation*. September. 209-212.

White, C. M.; Smith, D. H.; Jones, K. L.; Goodman, A. L.; Jikich, S. A.; LaCount, R. B.; et al. Sequestration of carbon dioxide in coal with enhanced coalbed methane recovery-a review. *Energy Fuels* 2005, 19, 659-724.

Whithjack, E.M., 1988. "Computed Tomography for Rock Property Determination and Fluid Flow Visualization." *Society of Petroleum Engineers Formation Evaluation,* **3,** 696-705
Whithjack, E., Devier, C., Michael, G., 2003. "The Role of X-Ray Computed Tomography in Core Analysis" paper SPE 83467 presented at the SPE Western Regional/AAPG Pacific Section Joint Meeting held in Long Beach, CA. 19-24 May.
Yamada, S. E., Jones, A. H., (1980). "A Review of a Pulse Technique for Permeability Measurement", SPE Journal 8760, 20, 357-358.
Zoback, M.D., and Byerlee, J.D., 1975, Permeability and Effective Stress: AAPG Bulletin, v. 59, p. 154-158.
Zoback, M.D. and Gorelick, S.M., Earthquake triggering and large-scale geologic storage of carbon dioxide: Proc. Natl. Acad. Sci. USA, 109(26), 10164-10168, doi:10.1073/pnas.1202473109 (2012).
Zoback, M.D., Kohli, A., Das, I., and McClure, M., The importance of slow slip on faults during hydraulic fracturing stimulation of shale gas reservoirs: Paper SPE-155476, SPE Americas Unconventional Resources Conference held in Pittsburgh, Pennsylvania, USA, 5-7 June 2012, (2012).